SLAC-R-609
November 2002

SPEAR 3 Design Report

Stanford Synchrotron Radiation Laboratory

Stanford Linear Accelerator Center, Stanford University, Stanford, CA 94309

Work supported by Department of Energy contract DE–AC03–76SF00515.

SPEAR 3

Design Report

draft revision 8/31/99

Stanford Synchrotron Radiation Laboratory

Authors:

P. Bellomo, R. Boyce, J. Corbett (Deputy Editor), P. Corredoura, E. Daly, D. Dell'Orco, T. Elioff, I. Evans, A. Fisher, R. Hettel (Editor), N. Kurita, J Langton, G. Leblanc, C. Limborg, D. Martin, Y. Nosochkov, T. Rabedeau, S. Park, J. Safranek, H. Schwarz, J. Sebek, J. Tanabe, C. Wermelskirchen, K. Wille, R. Yotam, F. Zimmermann

Prepared for the Department of Energy, Office of Basic Energy Sciences, Division of Chemical Sciences, under contract number DE-AC03-76SF00515 by Stanford Linear Accelerator Center, Stanford University, Stanford, California.

Acknowledgments

In addition to the authors of this Design Report, the present state of the SPEAR 3 design is the result of contributions from many people.

Special appreciation is due to H.Wiedemann, who first proposed the SPEAR 3 upgrade project and continues to advise the design group on accelerator physics issues; to A. Bienenstock and B. Richter, who recognized the scientific merit of the upgrade project in the early stages and worked to achieve it; to J. Dorfan for his continuing advocacy of the project; and to K. Hodgson, who has worked tirelessly to secure the support needed to realize SPEAR 3 and to maximize its capabilties.

Contributors from other SSRL staff members include S. Brennan, S. Carlsen, B. Choi, M. Dormiani, D. Dungan, L. Dunn, R. Emanuel, B. Evanson, D. Gough, R. Gould, E. Guerra, D. Keeley, P. Kuhn, N. Li, B. McSwain, J. Montgomery, H.-D. Nuhn, P. Pianetta, H. Rarback, M. Rowen, L. Shewchuk, B. Scott, T. Slater, A. Terebilo, A. Trautwein, T. Troxel, H. Winick, and K. Zuo. The SPEAR 3 design group is indebted to M. Cornacchia for his guidance in accelerator physics and design decisions.

Contributors from other divisions of SLAC include D. Baltazar, G. Bowden, Y. Cai, R. Cassel, W. Davies-White, J. Davis, T. Donaldson, A. Fasso, J. Fox, L. Giannini, R. Humphrey, N. Ipe, J. Judkins, T. Knight, R. Larsen, G. Leyh, J.J. Lipari, D. Macnair, D. Mostowfi, C. Pappas, P. Rodriguez, D. Rogers, M. Ross, R. Ruland, B. Skaggs, S. Smith, J. Steiber, R. Tighe, R. Wilkins, and D. Wright, and Y. Yan.

Recognition is due to many people from other institutions, including L. Bertolini (LLNL), M. Borland (APS/ANL), J. Byrd (LBNL), J. Carwardine (APS/ANL), J. Corlett (LBNL), G. Decker (APS/ANL), R. Dejus (APS/ANL), L. Emery (APS/ANL), A. Garren (LBNL, retired), A. Hofmann (CERN, retired), K. Kennedy (LBNL, retired), A. Lumpkin (APS/ANL), R. Rimmer (LBNL), D. Robin (ALS/LBNL), R. Schlueter (LBNL), and Ron Yourd (LBNL). The design group is grateful for the comprehensive technical review and recommendations from J. Galayda (APS/ANL).

Acknowledgment is due to members of the SPEAR 3 Director's Review Committee (November 1997), the DOE "Lehman Review" Committee (July 1998), and the SPEAR 3 Advisory Committee. The members include R. Damm (APS/ANL), R. DiGennaro (LBNL), J. Galayda (APS/ANL), K. Halbach (consultant), D. Harding (FNAL), A. Jackson (LBNL), B. Kincaid (LBNL), L. Klaisner (SLAC), S. Krinsky (NSLS/BNL), D. Lehman (DOE), J. Murphy (NSLS/BNL), J. Noonan (APS/ANL), M. Nordby (SLAC), M. Osinski (DOE), J Rees (SLAC, retired), R. Schwartz (DOE), H. Schwarz (SLAC), J. Seeman (SLAC), P. Stefan (SSRL, previously NSLS), and R.Yourd (LBNL).

The contributions of W. Franzwa, R. Hirsch, H. Lee, J. Muhlestein, W. Oosterhuis and P. Smith from the Department of Energy are gratefully acknowledged. Special recognition is due to P. Dehmer, M. Krebs, and R. Marianelli, who worked to launch the SPEAR 3 project within the DOE.

The support of H. Varmus from the National Institutes of Health, and of M. Cassman and J. Norvell from the National Institute of General Medicine has been instrumental for the successful start of the SPEAR 3 project.

Finally, the authors are indebted to present and past members of the SLAC Technical Publications Department for their excellent work in assembling the Design Report under sometimes demanding conditions. These members include V. Akkaraju, T.Anderson, M. Arcenal, N. Bock, K. Henniss, J. Masek, R. McDunn, P. Myers, C. Tilghman, J. Wahl and S. West.

Table of Contents

Appendices

Introduction 1

The Stanford Positron Electron Asymmetric Ring (SPEAR 2) was commissioned in 1972 as a 2.4 GeV colliding beam facility. Although designed for high-energy physics experiments, the original construction included a single bending magnet beam line, which enabled SPEAR to emerge as a productive and respected center for synchrotron radiation experiments.

With the SPEAR 2 upgrade in 1974, the maximum energy for high-energy physics operations reached 4 GeV. Operations related to the colliding beam program at energies ranging from 1.5 to 4 GeV, revealed 3 GeV and 100 mA as the optimal operating parameters for synchrotron radiation applications. These parameters represent the trade-off between energy and current necessitated by limits in RF power, vacuum-chamber photon absorption capacity, and beam stability. Since 1990, SPEAR 2 has operated successfully in this mode as a dedicated synchrotron radiation source.

Within the last 10 years, the synchrotron radiation user community at SPEAR has grown exponentially. Currently, more than 1,600 researchers participate in the various proposals for beam time accepted by SPEAR annually. In the past decade, the facility's operational efficiency has improved from about 50% to the current 95%. These recent successes have spurred demands for enhanced technical performance capable of supporting the next generation of experiments.

In January of 1997, following an initial upgrade proposal by Helmut Wiedemann [1] and subsequent discussions with the SSRL users, a study group began designing "SPEAR 3," a lower emittance, higher current storage ring optimized for synchrotron radiation operation. In May 1997, an SSRL users' workshop examined the benefits of SPEAR 3 in terms of enhanced photon flux density and new scientific opportunities [2]. Their conclusions and recommendations stressed:

- The important new opportunities for Science and Technology afforded by SPEAR 3 provide compelling reasons to proceed as rapidly as possible.
- The use of undulators in SPEAR 3 will provide unparalleled capabilities in the 1-4 keV spectral region. This new technology promises to foster scientific advances in many fields.
- The SSRL users' workshop gives its strongest possible endorsement to the SPEAR 3 project.

During 1997, The DOE Basic Energy Sciences Advisory Committee (BESAC) formed a special committee (Birgeneau-Shen) to investigate the current status of synchrotron light facilities as well as their potential for the future. The committee report endorsed government support for the SPEAR 3 upgrade [3].

The performance goals for SPEAR 3 include:

- 20 nm-radian beam emittance, a reduction from 160 nm-rad.
- 200 mA stored beam initially, a factor of two increase, with future increases towards 500 mA as beam lines are upgraded; 500 mA initial operation possible with beam lines closed.
- 3 GeV injection energy, an increase from the current 2.3 GeV.

These goals will be met by installation of: a double-bend achromat lattice (DBA) with new magnets and power supplies, a new vacuum chamber, and a 500 mA RF system. The existing wigglers and undulators will not change position, but the bending magnet beam lines will undergo minor angular alteration. The existing accelerator tunnel and its support buildings will continue to house all components, with only minor modifications to their utilities.

The SPEAR 3 upgrade will increase by an order of magnitude the focused photon flux density from insertion device beam lines. Due to higher critical energy, the photon flux density from bending magnet beam lines will increase by up to two orders of magnitude. As a result, the SSRL user community will benefit greatly from the major performance enhancements SPEAR 3 provides for all existing experimental stations. The increased flux density will extend experimental capability in a variety of applications that includes: x-ray absorption studies of speciation in environmental samples; powder and thin film diffraction studies of materials; protein crystallography; topographic studies of material structures; surface microcontamination on Si wafers; and x-ray tomographic analysis. New experiments in environmental and materials science as well as biological studies also become possible.

The opportunities engendered by SPEAR 3 have special import for the rapidly growing user community. SPEAR 3 serves as a cost-effective way to preserve and enhance the significant public and private investment at SSRL ---as well as a vehicle for expanding the world class services and technological capabilities provided by modern synchrotron radiation facilities.

The SPEAR 3 upgrade is planned as a 4-year project. Technical system design will commence in FY 99, so as to facilitate the procurement of major items (e.g. magnets and vacuum system components) in FY 2000. Preparatory work will take place during the normal 2-3 month shutdown periods in FY 2000 and FY 2001. This stage includes modifications to the booster, ring shielding, AC power systems, and ring cabling systems.

The removal of SPEAR 2 hardware and the main installation of SPEAR 3 will take place during the last six months of FY 2002. A check-out and commissioning period follows immediately, since the project design emphasizes the quick resumption of experimental operations by users.

The sections that follow discuss the accelerator physics issues associated with SPEAR 3. Thay also provide detailed descriptions of the technical modifications required to complete the upgrade. The total project costs are estimated at 53.1M$ (in FY 1999 dollars). Further details of cost and schedule appear in Chapter 8.

References

[1] H. Wiedemann, "High Brightness Lattice for SPEAR," SSRL/ACD 84, Nov. 1988.

[2] "SPEAR 3 Workshop: Making the Scientific Case," May 29-30, 1997, SLAC Pub SLAC-R-513.

[3] "Report of the Basic Energy Sciences Advisory Committee Panel on DOE Synchrotron Radiation Sources," Nov. 1997.

Overview 2

The SPEAR storage ring was originally designed for electron-positron colliding beam experiments spanning an energy range of 1-4 GeV per beam. A racetrack lattice was chosen to create two long straight sections in the East and West "pits" (Figure 2.1). A modified FODO lattice was chosen for the arcs, with the FODO cells separated by 3.1 m straight sections. Special matching-cell magnet configurations were required on either side of the East and West pits. Electrons and positrons were injected into the ring from the main SLAC linear accelerator (LINAC) at a maximum energy of 2.4 GeV, a level limited by the ratings of the transport line and SPEAR septum magnet.

In 1972, SPEAR I was commissioned with an operating energy of 2.4 GeV, a level limited by the RF and magnet power supply systems. In 1974, these systems were upgraded for approximately 4 GeV operation. Soon after the 'SPEAR 2' upgrade became operational, the charmed Ψ/J-particle was discovered at an energy of 1.5 GeV (per beam). SPEAR continued to operate at or near that energy for colliding beam experiments until the end of the high-energy physics program in the late 1980's. Two Nobel Prizes were awarded for work done at SPEAR: one for the discovery of the Ψ/J (B. Richter, jointly with S. Ting, 1976), and another for discovering the electron-like τ particle in 1975 (M. Perl, 1995).

The first synchrotron radiation experiments took place in 1973 as part of the Synchrotron Radiation Pilot Project [1]. The first Stanford Synchrotron Radiation Project (SSRP) beam line was commissioned in 1974, operating parasitically with the high-energy physics program. As more beam lines were added, and the experimental program gathered momentum, SSRP evolved into a full-fledged laboratory. In 1977, under the aegis of NSF funding, SSRP became known as SSRL. Two years later, SPEAR operation was divided between the high-energy physics and the synchrotron radiation physics communities. SSRL operated in the 3-3.5 GeV energy range so as to produce a higher-energy photon spectrum, and at currents up to 100 mA (at 3 GeV), a level limited by photon-absorber power ratings. The straight sections in the modified FODO lattice proved fortuitous for the development of synchrotron radiation technology as the first wiggler [2] and undulator [3] insertion devices used for synchrotron radiation experiments were installed in SPEAR 2.

In 1982, SSRL became a DOE-funded laboratory. SPEAR was operated by SLAC until the end of the 1980's, with SSRL officially an experimental user of the facility. At the end of the high-energy physics program, SPEAR became a fully dedicated synchrotron radiation source, SSRL became a department within SLAC, and SSRL took over responsibility for SPEAR operations.

By the late 1980's, the availability of the SLAC LINAC for SPEAR injection had become limited by the SLAC Linear Collider (SLC) project, which required full-time LINAC operation. In 1991, the problem was resolved by the completion of a dedicated electron injector composed of a LINAC pre-injector and a synchrotron booster [4]. While the booster was designed for 3 GeV operation, the transport line and SPEAR septum magnet ratings still limit the SPEAR injection energy to a maximum of 2.4 GeV; the routine injection energy is now 2.3 GeV.

A new SPEAR lattice configuration, which lowered the emittance from 470 nm-rad to 160 nm-rad by altering ring-magnet strengths, was also implemented in 1991 [5]. Two previous attempts to reduce emittance, one in 1976 [6] and one in 1985 [7], were unsuccessful because the lattice configurations were not compatible with the two-kicker injection bump then in use. The problem was resolved during the 1991 lattice re-configuration by adding a third electron injection kicker. In 1994, the magnet strengths were altered again, without changing emittance, to reduce the strength of the strong-focusing quadrupole magnets in the East and West pits [8].

Currently, SPEAR operations benefit from an ongoing accelerator improvement program that has increased accelerator reliability and beam quality. However, certain user experiments could profit from improvements in flux, focused flux density, and brightness. To reach the performance level expected of third-generation synchrotron light sources, SPEAR 3 would need to increase photon brightness by at least an order of magnitude. The SPEAR 3 upgrade project will achieve this increase by replacing 1) the existing magnet lattice, 2) the vacuum chamber and 3) the RF system. The new lattice will reduce beam emittance by an order of magnitude. As beam lines are upgraded, stored beam current will increase - first by a factor of two, and later by as much as fivefold. Although beam lines must be modified to accept higher power densities, the majority of the beam line infrastructure (including insertion devices) will be reused for SPEAR 3 to minimize the total downtime.

References

[1] I. Lindau, W.E. Spicer, J. Electron Spectroscopy 3, 409 (1974).

[2] M. Berndt et al., IEEE Trans. Nucl. Sci. 26, 3812-3815 (1979).

[3] K. Halbach et al., IEEE Trans. Nucl. Sci. 28, 3136-3138 (1981).

[4] H. Wiedemann et al., Proc. of the 1991IEEE Particle Accel. Conf., San Francisco, 2688-2690.

[5] J. Safranek, Ph.D Thesis, Stanford University, 1991.

[6] A. Garren, M. Lee, P. Morton, "SPEAR Lattice Modifications to Increase Synchrotron Light Brightness," SPEAR Pub. 193, 1976.

[7] L. Blumberg, J. Harris, R. Stege, J. Cerino, R. Hettel, A. Hofmann, R. Liu, H. Wiedemann, H. Winick, Proc. of 1985 IEEE PAC, 3433.

[8] H.-D. Nuhn, Proc. of the 4th European Particle Accel. Conf., London, 1994, 642-644.

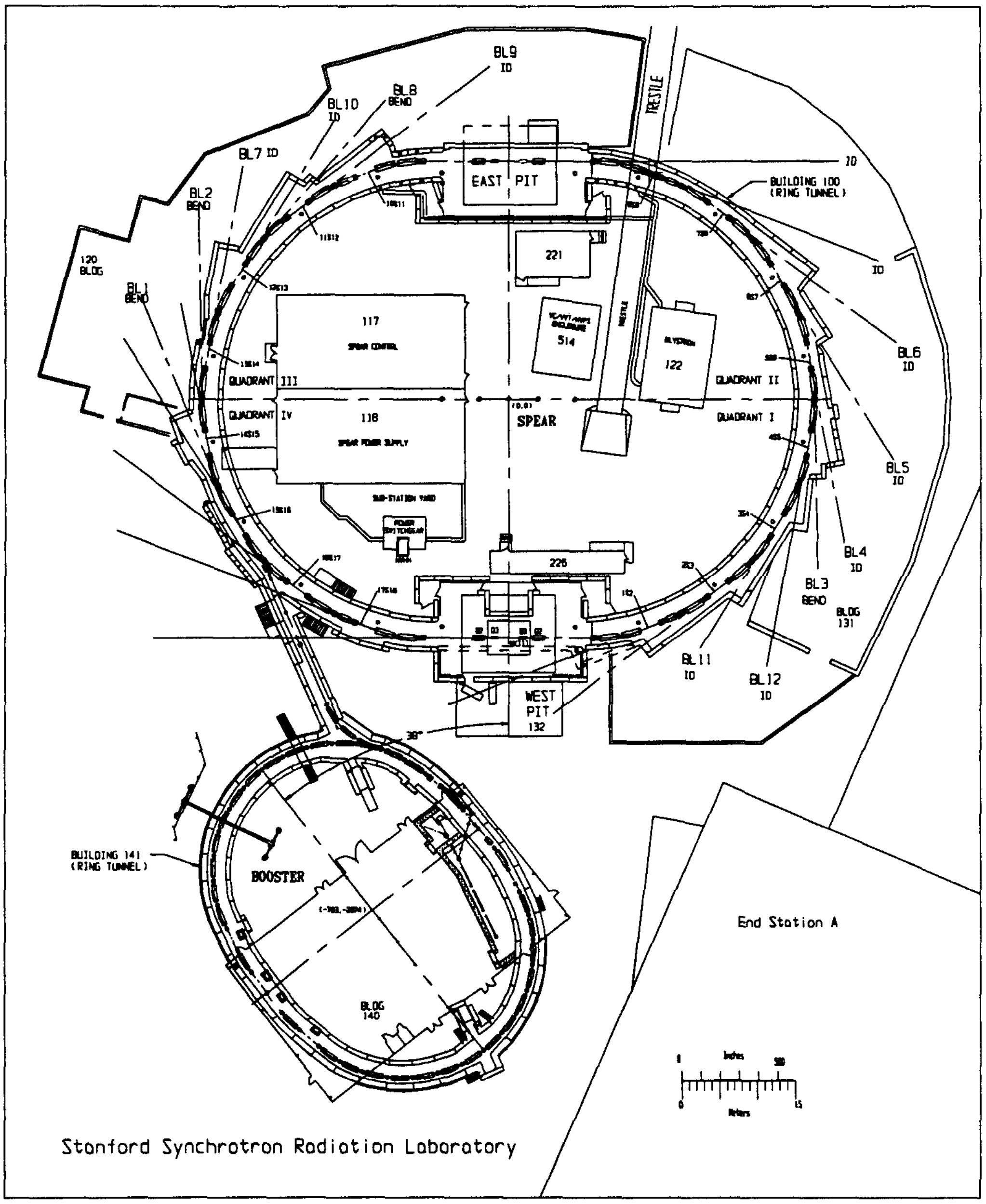

7-98
8413A203

Figure 2.1 The SPEAR accelerator facility.

2.1 SPEAR 2 Operational Overview

The SPEAR 2 accelerator complex (Figure 2.1) includes the 234.1 m electron storage ring and a 10 Hz synchrotron injector with 120 MeV LINAC pre-injector. Ten main beam lines, with a total of 25 experimental stations (plus 3 more under construction), receive synchrotron radiation from six insertion devices and four dipole magnets. For typical user operation, 100 mA is injected into SPEAR at 2.3 GeV and ramped to 3 GeV once per day (twice per day for the first few weeks following a ring shut-down period). The maximum injection energy is limited to 2.3 GeV by the SPEAR septum magnet (and some transport-line magnets).

The natural beam emittance of SPEAR 2 is 130 nm-rad at 3 GeV. This emittance is increased to 160 nm-rad by the wiggler magnets located in straight sections having non-zero dispersion. The SPEAR 2 machine parameters and beam dimensions at beam line source points are summarized in Tables 2.1 and 2.2, respectively.

To maintain operational stability, the electron LINAC remains on-line 24 hours a day. To establish stable accelerated beam conditions, the booster synchrotron is turned on approximately 2 hours prior to injection; it is turned off approximately 1 hour after a stable beam has been delivered to users. Approximately 15 minutes before injection, the beam is extracted from the booster and brought down the BTS transport line to a Faraday cup upstream of the SPEAR septum.

To fill the storage ring, the beam lines are closed and magnet currents are cycled to zero and back to their 2.3 GeV configuration to minimize hysteresis effects. The ring is filled to 100 mA at an average rate of approximately 20 mA/min. The magnets are then ramped to 3 GeV, tuning and orbit corrections are performed, and the beam lines are re-opened. The entire process normally takes less than 30 minutes.

After ramping to 3 GeV, the beam orbit is corrected to compensate for orbit non-reproducibility from magnet hysteresis. During the beam delivery period a global orbit feedback system using electron beam position monitors works in tandem with local vertical feedback systems using beam line photon position monitors to reduce slow orbit fluctuations and to stabilize photon beam positions.

Careful control of the cavity temperature and the tuner positions prevents coupled-bunch motion driven by higher-order modes in the 5-cell RF cavities. Nevertheless, transverse coupled-bunch motion is observed sporadically. The bunch pattern (approximately 50 RF buckets having 3-bucket spacing, filling about half the ring circumference) helps to reduce the excitation of higher-order modes (HOMs).

Following a scheduled vacuum venting, the ring is conditioned within a few weeks of operation. At that point, the beam lifetime is approximately 40 h at 100 mA. The product of instantaneous beam current and lifetime, called the "vacuum quality factor," remains roughly constant (approximately 4 A-h) during the beam delivery period. The high vacuum quality permits once-a-day injection, with the beam decaying from 100 mA to 60-70 mA during the 24-hour delivery period.

2.2 SPEAR 3 Performance Goals

The SPEAR 3 project will enhance the synchrotron radiation beam properties and improve the overall performance of the SSRL accelerator facility by reducing the beam emittance by an order of magnitude and increasing the beam current by a factor of five (to 500 mA). The focused flux density and brightness of the photon beam will be increased by at least an order of magnitude for insertion device beam lines (Figure 2.2). Due to the higher critical energy, the relative performance gain for dipole sources is further enhanced for photon energies above 10 keV. Table 2.1 compares SPEAR 2 and SPEAR 3 machine parameters, while Tables 2.2, 2.3, and 2.4 provide photon beam parameters. It should be noted that the BL 4 electromagnet wiggler will be replaced in 2002 by a permanent magnet wiggler similar to the BL 9 device. The BL 7 electromagnet wiggler may also be replaced in 2002 (not indicated in Table 2.3).

While the operating current will be limited initially to <500 mA by power limitations in some of the beam lines, SPEAR 3 will be capable of 500 mA operation when the photon beam lines are closed. Full 500 mA operation will be approached as the beam lines are upgraded.

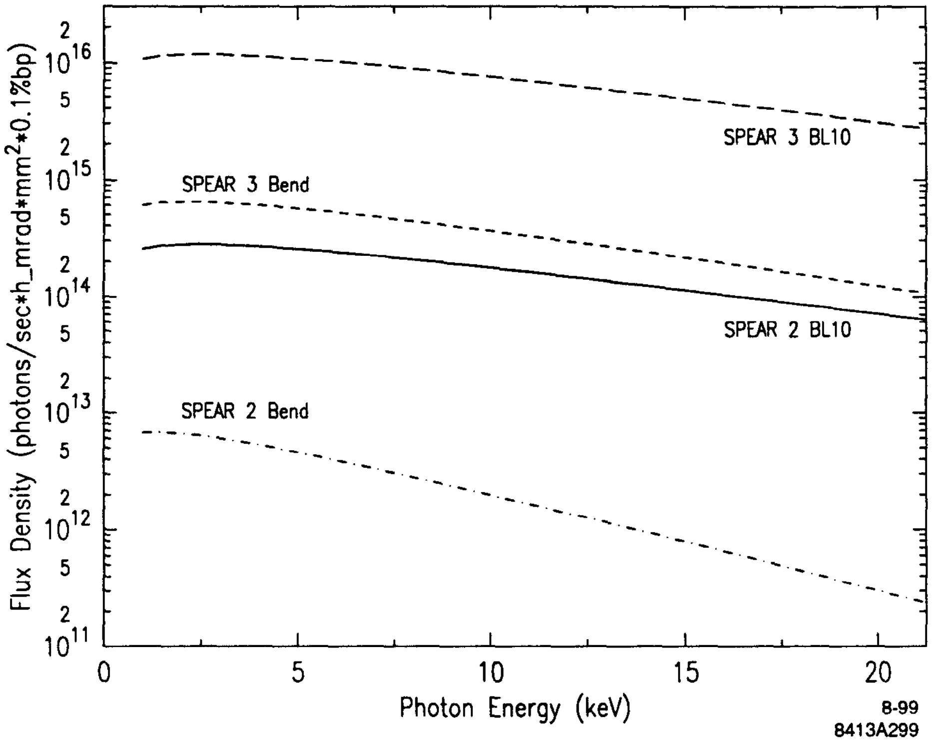

Figure 2.2 Comparison of SPEAR 2 (100 mA) and SPEAR 3 (500 mA) flux density for a representative insertion device (BL10) and a bend magnet beam line.

Table 2.1 Machine performance parameters for SPEAR 2 and SPEAR 3.

	SPEAR 2	SPEAR 3
Emittance (with IDs)	160 nm-rad	18 nm-rad
Energy	3 GeV	3 GeV
Current	100 mA	200/500 mA†
Lifetime	40 h @ 100 mA	>15 h @ 500 mA
Critical energy	4.8 keV	7.6 keV
Injection energy	2.3 GeV	3 GeV

†. Initial 200 mA operation will be limited by some beam line components. The ring will be capable of 500 mA operation with beam lines closed.

Table 2.2 Photon beam source point sizes for SPEAR 2 and SPEAR 3.

	ID		Bend Magnet	
	SPEAR 2	SPEAR 3	SPEAR 2	SPEAR 3
σ_x	2000 μm	427 μm	790 μm	160 μm
σ_y	53 μm	30 μm	200 μm	50 μm
σ_s	23 mm (75 ps)	5.7 mm (19 ps)	23 mm (75 ps)	5.7 mm (19 ps)

Table 2.3 Increase in focused flux density (1:1 imaging) and horizontal brightness for SPEAR 3 insertion device beam lines at 500 mA with a new wiggler installed on BL 4. (Values scale linearly with beam current. BL 4 values are at 12 keV).

beam line	4	5	6	7	9	10	11
Focused flux density	x103	×43	×43	×25	×38	×43	×42
Horizontal brightness	x58	×24	×24	×14	×21	×24	×23

Table 2.4 Increase in focused-flux density and horizontal brightness for SPEAR 3 bend magnet beam lines at 500 mA, including the increase due to a higher critical photon energy. (Values scale linearly with beam current).

Photon energy	1 keV	10 keV	20 keV
Focused flux density	×93	×189	×425
Horizontal brightness	×24	×48	×108

The smaller beam size in SPEAR 3 can be fully exploited once the electron beam orbit position and angle at beam line source points is stabilized to within 10% of the photon beam size and divergence, respectively. Closed orbit motion as well as single- and multi-bunch motion will be minimized by 1) controlling the temperature and reducing the motion of critical accelerator components, 2) minimizing the impedance of vacuum chamber components, and 3) using feedback systems. The goal for horizontal and vertical beam stability at insertion device source points is <40 μm RMS and 5 μm RMS, respectively. For dipole source points, the goal is 15 μm RMS and 5 μm RMS, respectively.

Limitations on the floor plan and tunnel geometry led to careful consideration of the trade-offs between beam line performance and the accelerator design (Appendix A1). The decision to operate SPEAR 3 at 3.0 GeV rather than at a higher energy arose from the condition that the maximum operating current at 3.5 GeV must be reduced by a factor of ~2 (relative to 3 GeV operation) to stay within the power rating of the photon absorbers (power density $\propto IE^4$). For the most common operating range at SSRL (i.e., 3 GeV and photon energies below 10 keV), flux, focused flux density, and brightness are dominated by ring current which decreases at higher electron beam energies.

Another consideration is that at 3 GeV, the 74 h Toushek lifetime for 500 mA operation is sufficiently greater than the dominant gas-scattering lifetime of ~30 h. Operation at a higher electron energy will not significantly prolong the total lifetime. On the other hand, the end station photon spectrum above ~20 keV improves as ring energy increases. Therefore, the ring magnets and power supply systems are designed to operate at beam energies up to 3.3 GeV (with reduced current) to take advantage of the improved hard x-ray spectrum.

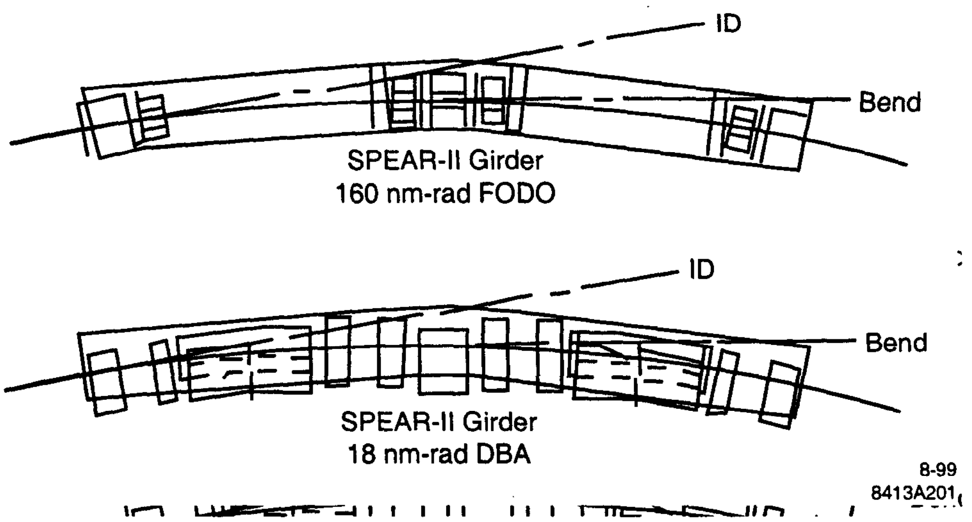

Figure 2.3 SPEAR 2 and SPEAR 3 lattice cells.

Additional SPEAR 3 upgrade goals include:

- 3 GeV injection energy (up from 2.3 GeV) for greater fill-to-fill orbit reproducibility and to permit top-off injection.
- Unchanged insertion device beam line alignment and minimally realigned bend magnet beam lines.
- Stable beam properties at high current.
- High operational reliability.
- Provision for future accelerator and beam line upgrades.
- Minimal SPEAR 3 conversion downtime.

To achieve these goals, the SPEAR 3 upgrade calls for replacing the existing FODO magnet lattice with a Double Bend Achromat (DBA) lattice (Figure 2.3). New magnets, power supplies, vacuum chamber, and RF systems will be installed. Systems for monitoring, controlling and stabilizing the beam lines will be implemented, and the power handling capability of the beam lines will be increased. The injector and BTS transport line will be upgraded for 3 GeV operation as a separate project. To minimize the installation downtime, the magnets and the vacuum chamber will be preassembled on new support girders prior to installation in the ring tunnel. Most of the new cable plant will be installed prior to the downtime. The downtime will last 6-months, and be proceeded by three normal 2- to 3-month downtimes, during which preliminary installation and preparatory work can be performed.

The SPEAR 3 lattice provides four new 4.7 m straight sections, together with two 7.6 m racetrack straight sections (Figure 2.4). At least two of the 4.7 m straight sections and one 7.6 m straight are designated for future IDs; the other long straights will be used for RF cavities, beam diagnostics, and potentially, more beam lines. A hypothetical 4 m undulator operating in one of the long straights and optimized for 1-4 keV operation would have a brightness approaching 10^{19} (Figure 2.5) [1].

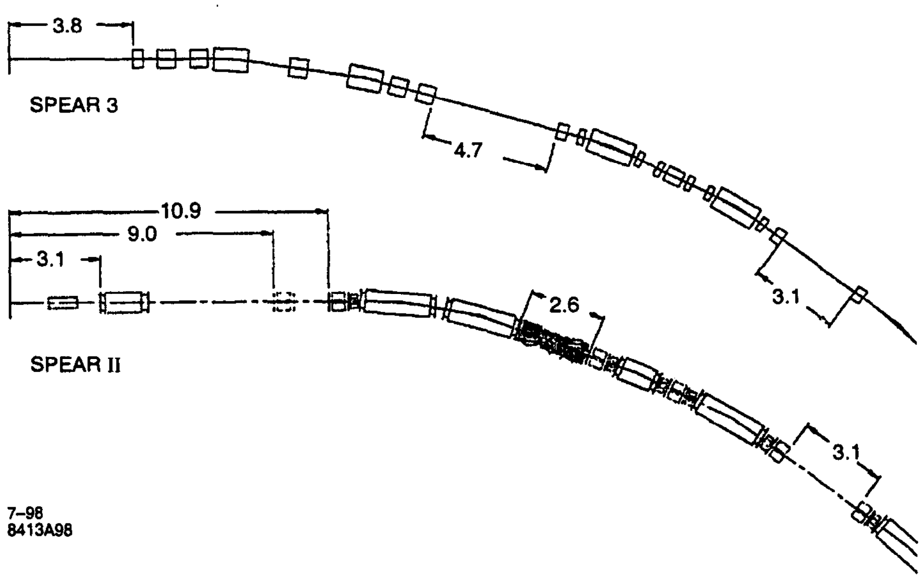

Figure 2.4 Matching cell straight sections for SPEAR 2 and SPEAR 3.

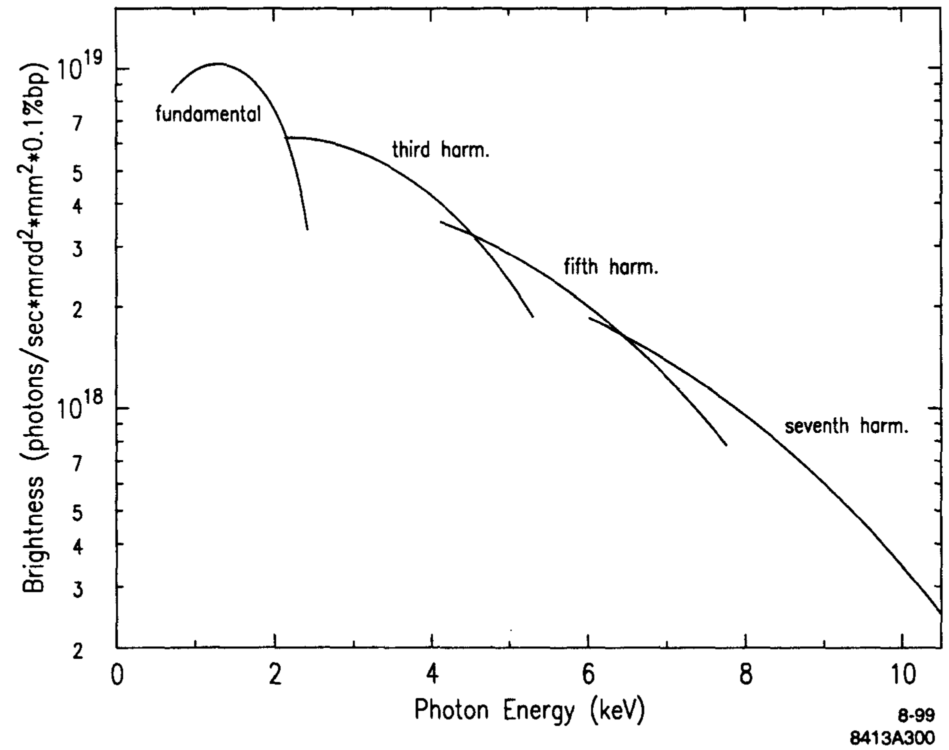

Figure 2.5 Tuning curves of an undulator optimized for 1–4 keV operation on SPEAR 3 (500 mA, 0.1% electron energy spread). The curves are calculated assuming a 100–period (3.2 cm) ID with a 10–mm gap and realistic magnetic parameters.

References

[1] R. Dejus, APS, 1997.

2.3 Scientific Opportunities

The scientific opportunities with the SPEAR 3 upgrade have been summarized in "SPEAR 3 Workshop: Making the Scientific Case" [1], the product of a two-day workshop held at SSRL on May 29-30, 1997. An excerpt from the report's executive summary appears below:

"The most immediate impact would be improvements in capabilities on all of the operational experimental stations on SPEAR. By decreasing the emittance of SPEAR by a factor of 7 and increasing the beam current to 200 mA, existing insertion device end stations would experience an increase of focused photon flux density at the sample of approximately a factor of 10. As the radius of curvature of the bending magnets would be reduced with the new lattice, the critical energy of those beam lines would increase from the present 4.8 keV to 7.1 keV. Bending magnet beam lines equipped with focusing mirrors would see an increase in focused flux ranging from approximately 30 at low energies up to a factor of 200 at 20 keV. Therefore, one consequence of the upgrade is that the focused flux density of focused bending magnet beam lines would nearly equal that of existing BL 10-2 (Figure 2.2). This would have a major impact on the usefulness of these bending magnet lines, since they would then become workhorses in a variety of disciplines including protein crystallography, thin film diffraction studies and applications of x-ray absorption spectroscopy.

"The improved brightness would also have a significant impact on the potential of SSRL for future developments in undulator beam lines. Although not explicitly included in the SPEAR 3 storage ring upgrade, an undulator line optimized for the photon energy region 1-4 keV would provide potential for spectroscopy experiments which require very small focal spots in this energy region. The potential impact for experiments in environmental science (Mg, Al, Si, K, and Ca K-edges) and biologically important elements (P, S, Cl, K, Ca) is very exciting.

"Finally, the potential for producing micro-focussed beams (with dimensions in the range of just a few microns) would open up SSRL for a range of element specific imaging and local probe spectroscopies which would have a major impact on a wide range of applications, particularly in the environmental and biological sciences."

As the report demonstrates, the attendees were excited by the prospects of SPEAR 3 at SSRL. The report goes on to detail the impact of the upgrade on the fields of biological macro-molecular crystallography; biological small angle x-ray scattering; biological x-ray absorption spectroscopy; molecular environmental science; materials x-ray absorption spectroscopy; imaging/tomography/ topography; condensed matter, materials science and technology; and VUV and Soft x-ray science.

References

[1] SLAC publication SLAC-Report-513, 1997.

2.4 Upgrade Project Summary

The SPEAR 3 project includes the modification of the storage ring, injection transport line, beam-line front ends, and conventional facilities to meet the upgrade goals outlined above.

Certain beam line components will initially limit SPEAR 3 operation to approximately 200 mA when beam lines are open. When beam line front ends are closed, however, the ring can run at the full 500 mA design current.

The following sections summarize the project scope and tasks.

2.4.1 Lattice

A double bend achromat (DBA) magnet lattice having 14 standard cells and 4 matching cells has been selected to:

- Meet specifications for emittance, dynamic aperture, lifetime, beam stability, and photon beam parameters.
- Exhibit acceptable injection and machine operation properties.
- Meet stringent beam steering and stabilization requirements.
- Preserve the current insertion device beam line alignment and require only minor realignment of the bending magnet beam lines.
- Provide adequate space between magnets for necessary vacuum system components, beam position monitors, RF cavities, etc.

2.4.2 Magnets and Supports

Upgrading the magnet system requires the provision of:

- Ring magnets with acceptable mechanical and magnetic properties at 3 GeV operation (with > 10% overhead rating).
- A magnet inventory that includes:
  - 36 gradient dipoles (8 @ 3/4 length)
  - 94 quadrupoles
  - 72 sextupoles (with skew quad trims)
  - 72 corrector yokes, 36 of which have both horizontal and vertical corrector coils; 18 of which have just horizontal coils; and 18 of which have just vertical coils (i.e 54 correctors per plane).
  - 1 injection septum
- Magnet alignment struts and fixtures.
- Measurement and fiducialization of the magnets to guarantee field quality and alignment tolerances.
- New magnet girders (both standard and matching cell) with supports to improve load distribution and reduce mechanical vibration.

Figure 2.6 shows the SPEAR 3 magnet and vacuum chamber assembly mounted on a new girder.

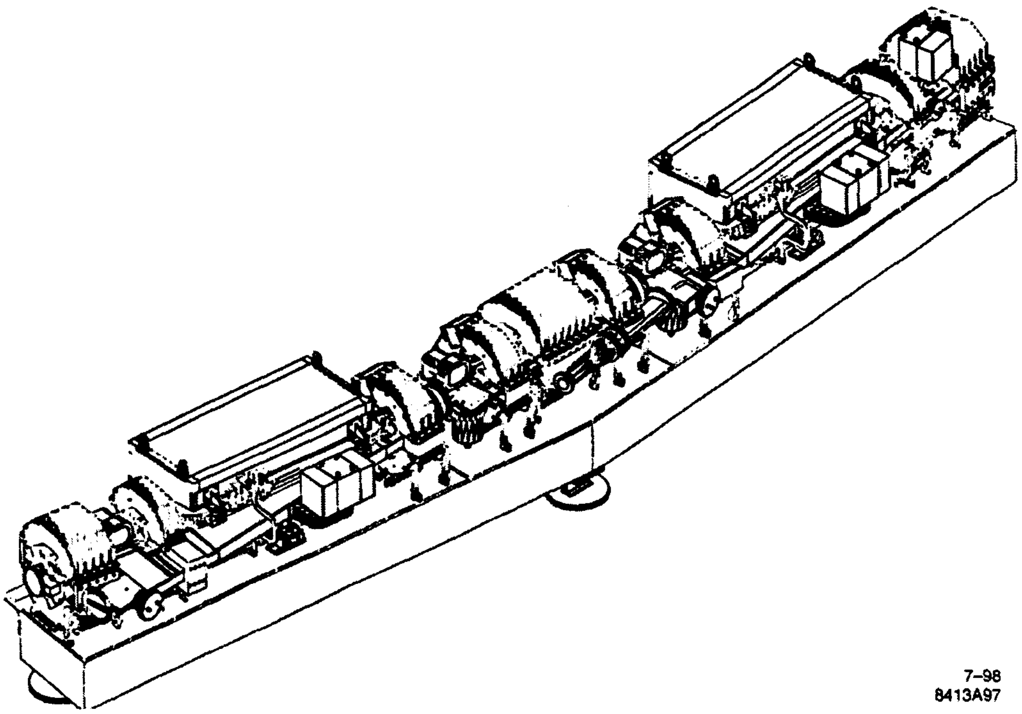

Figure 2.6 SPEAR 3 standard cell magnet girder.

2.4.3 Vacuum system and beam line front ends

The SPEAR 3 vacuum system will feature an ante-chamber geometry with discrete photon absorbers. It will be constructed of copper to increase its capacity to dissipate the power load from mis-steered photon beams. The insertion-device vacuum chambers for beam lines 5, 6, 7 (unless replaced), 9, 10, and 11 will be reused. Vacuum system requirements and components include:

- Vacuum chamber components rated for 3 GeV, 500 mA operation.
- Minimum wall thickness at magnet locations (Figure 2.2).
- Discrete photon absorbers, located in the vacuum antechambers, capable of handling the synchrotron radiation power load associated with a 500 mA stored beam.
- <50 mA passively safe operating current for full-field insertio device synchrotron radiation (without orbit interlock). Passively safe operation for dipole radiation at 500 mA.
- Resistive CuNi inserts in the Cu chamber at orbit corrector sites to reduce the eddy-current attenuation and the distortion of AC magnetic fields generated by the orbit feedback system.
- Shielded bellows, pumping ports and manifolds, synchrotron radiation masks, and impedance-reducing transition components for the new and reused chamber sections.
- Three low-impedance, in-vacuum injection kicker magnets.
- 90 (i.e., 5 per magnet-cell chamber) beam-position monitors (BPMs), stable to 5 μm RMS vertically and 15–40 μm RMS horizontally (depending on location), during 24 h accelerator temperature excursions.
- Stripline pickup and kicker assemblies (both horizontal and vertical) for tune monitoring and transverse-beam excitation systems.
- A synchrotron light mirror and visible light port.
- Upgraded beam scraper assemblies.
- A ceramic chamber break for the DCCT current monitor.

- New beam safety stopper assemblies
- New sector isolation vacuum valves.
- beam line front-end masks and absorbers rated for 500 mA operation.
- New insertion device vacuum chambers for BL 4 (and possibly BL 7).
- A vacuum pumping and monitoring system, including titanium sublimated pumps (TSPs) and ion pumps, capable of maintaining <2 nT N_2-equivalent gas pressure at 500 mA.

A cross-section of the SPEAR 3 vacuum chamber in a quadrupole magnet is shown in Figure 2.7.

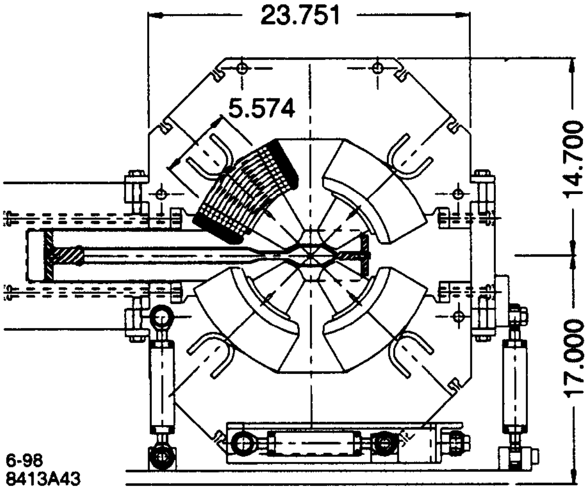

Figure 2.7 SPEAR 3 vacuum chamber cross-section in a quadrupole magnet.

2.4.4 RF System

The present SPEAR 2 RF system consists of two 5-cell RF cavities, each powered by a 500 kW klystron operating at 358.53 MHz. With this system, it would only be possible to operate SPEAR 3 at a maximum current of 260 mA at 3 GeV. Also, beam destabilizing HOMs in these cavities must be avoided assiduously through precise control of the cavity temperature and tuner positions, and with a feedback system to suppress zero-mode longitudinal beam oscillations.

The limitations of the SPEAR 2 RF system will be circumvented through installation of four new PEP-II style, mode-damped cavities that are capable of stable electron beam operation at 500 mA. The new cavities will operate at 476.3 MHz, only slightly different from the PEP-II frequency of 476 MHz. This setting yields a harmonic number of 372 for the 234.126 m circumference of SPEAR 3. The PEP-II style cavities will be installed in the West racetrack straight section. RF power will be provided by two 650 kW klystrons powered by the existing HV power supplies employing new low-level controls.

RF system implementation tasks include:

- Fabricate and install four mode-damped 476.3 MHz RF cavities and related waveguide network.
- Install two 650 kW, 476.3 MHz klystrons in existing tube locations using existing HV power supplies.
- Install circulators, Magic Tees, and RF loads for the new RF power system.
- Provide connections to the LCW cooling system for cavities, klystrons and circulators.
- Provide connections to the high-conductivity water (HCW) system for RF loads.
- Upgrade the low-level RF control system and install new cabling

2.4.5 Power Supply Systems

All of the SPEAR 2 magnet power supplies will be replaced. Power supplies for the BL 7 electromagnetic wiggler and most BTS transport line supplies will be reused. Table 2.5 lists the new power supplies.

Table 2.5 New power supplies needed for SPEAR 3.

Power Supply	Qty	Volts	Amps	kW
Dipole	1	1200	775	930
QF, QD, QFC strings	4	750	100	75
QF, QD individuals	40	100	100	10
QFY, QFX, QFZ, QDX, QDY, QDZ	6	400	100	40
SD, SF	2	650	250	163
SDI, SFI	2	125	150	19
Septum	1	65	275	18
Correctors	108	50	30	1.5
ID, Skew Quad, QMS Trims	25	50	30	1.5
BTS B7H, B8V	2	45	525	24

Other power-supply system tasks include:

- Replace the AC power-switch gear and the distribution for the power supplies, as needed.
- Install new cabling for all ring magnets, except the dipole main coils.
- Reuse the existing magnet current bus for the dipole magnets; reroute the busses in the pit areas as needed.
- Replace the three kicker pulsers and their HV supplies with new systems.
- Implement a digital-control interface for the power supplies.

2.4.6 Beam Stabilizing Measures and Feedback Systems

Sources of beam instability will be reduced through careful mechanical and electrical component design and by controlling temperature in the accelerator tunnel. Feedback systems will be used to further stabilize beam motion within 10% (or less) of beam size. Feedback systems will also minimize divergence at the photon-beam source points.

Measures for reducing the sources of beam noise include:

- Stabilizing the diurnal excursion of ring tunnel air temperature to ± 1° C (or less) by 1) thermally insulating the East and West pit straight sections, 2) limiting the exchange of tunnel air with external air sources, and 3) applying reflective paint to all concrete shielding blocks exposed to direct sunlight.
- Maintaining LCW input temperature variation to ± 0.3° C (or better).
- Reducing the amplitudes of magnet girder vibration modes through improved supports.
- Using discrete, water-cooled photon stops to absorb synchrotron radiation power, thus minimizing beam-dependent vacuum chamber motion.
- Water-cooled copper vacuum chambers to stabilize temperature against heating from restive chamber wall impedance or high-order modes.
- Limiting BPM-pickup motion to <15–40 μm RMS horizontally, depending on location, and <5 μm RMS vertically at the BPM locations.
- Using highly regulated, low-ripple power supplies.

- Minimizing the RF impedance of vacuum chamber components.

Active systems used to further stabilize beam motion include:

- A digital orbit feedback system, expanded from the SPEAR 2 system, to stabilize the electron beam orbit across a bandwidth from DC to >60 Hz.
- Feedback systems that minimize harmful HOMs by regulating cavity temperature and tuner position.
- A Mode-Zero RF feedback system to stabilize common-mode, longitudinal, bunch oscillations.

Transverse and longitudinal multibunch feedback systems will not be required.

2.4.7 Instrumentation and Control Systems

SPEAR 3 instrumentation and control systems include the computer control system, the beam and lattice diagnostic systems, and the injection timing system.

Upgrade tasks for the computer control and timing systems include:

- Expand the computer database and control system software and hardware to accommodate the new power supplies; BPMs; diagnostic equipment; feedback systems; vacuum monitors and pump supplies; temperature sensors; water flow switches; and other protection system components.
- Development of accelerator application software.
- Support of CAMAC and VME hardware-interface platforms.
- Implement high-speed digital control links for the fast-orbit corrector and other power supplies.
- Integrate the SPEAR-II low-level RF control system that employs EPICS control software and the VxWORKS real-time operating system.
- Modify the injection timing system to achieve single-bucket filling, from the booster (RF frequency 358.53 MHz).

Diagnostic systems for SPEAR 3 include:

- An electron BPM processor system, expanded from the present 36 BPMs to 90+ BPMs, having a 2 kHz orbit acquisition rate.
- Upgrades for the following: the DCCT current monitor, the tune monitor, the injection monitors, the scrapers and the console instrumentation.
- An operator monitoring interface to the Beam Loss Monitor system used by the Beam Containment System.
- A synchrotron light monitoring system to measure beam size, bunch length, and beam stability.
- Transverse turn-by-turn bunch-position and longitudinal phase-monitor systems from SPEAR 2.
- A quadrupole modulation system for measuring BPM offsets and lattice parameters.

2.4.8 Protection Systems

The following machine and personnel protection systems are required for SPEAR 3:

- Expanded vacuum protection and magnet cooling water protection systems to accommodate the new accelerator magnet, vacuum and power conversion systems.
- A new orbit interlock system that will protect against damage to vacuum chamber components caused by mis-steered synchrotron radiation.

- A modified beam containment system that will accommodate the new Long Ion Chamber (LION) beam-loss monitors in the ring tunnel and the BTS transport line.
- A modified and expanded personnel protection access control system to accommodate new power supply systems.

2.4.9 Cable Plant

A new cable plant will be installed to improve system reliability and to facilitate the installation of SPEAR 3 components within a 6-month period. Cable plant components and requirements include:

- Cable trays installed outside and above the ring tunnel, connecting with existing external cable tray routes.
- New cable penetrations through the ring tunnel roof, three each for the North and South arcs.
- New cables, pre-terminated as much as possible, installed in trays prior to the 6-month conversion period.
- Reused cables, including some machine protection and most personnel protection system cables, and a water-cooled bus for the dipole magnets and the BL 7 electromagnet wiggler magnet (if used).

Prior to the 6-month accelerator installation period, new cables will be coiled in the new external trays near the shielding penetrations. Magnet and vacuum chamber girder assemblies will be pre-wired, with wiring terminated at consolidated connection points to simplify connection to the new cables after the girders are installed.

2.4.10 Injection System (separate AIP Project)

Only minor upgrades of the booster resonant-magnet power supply system (White circuit) and BTS transport line components are required for reliable 3 GeV operation. They include:

- Installing water cooling for the booster DC bias and pulser power supply SCRs and improving the overall cooling of the pulser power supply.
- Installing a new charging choke for the White circuit pulser network.
- Increasing the power rating of connections to the White circuit charging and pulse chokes, as needed for 3 GeV operation.
- Upgrading the White circuit pulser firing circuit components and protection interlock.
- Improving the mechanical support and bracing of the magnet and choke coils as well as the cores.
- Increasing voltage of the RF high-voltage power supply for 3 GeV operation by raising AC transformer input taps for 42 kV output (up from 37 kV) and by upgrading soft-start and AC protection circuits.
- Modifying the booster-to-SPEAR (BTS) transport-line magnets near the SPEAR septum, together with their support components and power supplies as needed.
- Installing 6 new BTS steering magnets.
- Upgrading BTS insertable screens and current-monitoring systems.

2.4.11 Accelerator Facilities

The following accelerator facility upgrades are required for SPEAR 3:

- New radiation shielding for the roofs and walls (where needed) in the East and West pit regions.
- Local radiation shielding components.

- Thermal insulation in the East and West pits along with sealing of the shielding penetrations, as needed, to stabilize the tunnel air temperature within of ±1° C (or better) across a 24 h period.
- Reflective paint on shielding blocks exposed to direct sunlight to improve tunnel temperature stability.
- An upgraded accelerator LCW-distribution system and increased LCW capacity to accommodate new magnets, vacuum chambers, and photon absorbers.
- A new, stand-alone, high-conductivity water (HCW) system for RF loads.
- New and/or relocated AC distribution transformers, breaker panels, and outlets in the ring tunnel.
- Improved ring tunnel lighting.
- An upgraded fire protection system.
- Modified air plumbing as needed, to accommodate the upgraded components.

2.4.12 Installation

The installation of the majority of SPEAR 3 components will take place during a shutdown period of approximately six months. Some component installation and site preparation work will be done during the normal two-to-three month SPEAR shutdown periods that precede the extended shutdown.

Tasks for the extended shutdown include:

- Replacement of the accelerator magnets.
- Replacement of the vacuum chambers, kickers, valves and gauges, associated support assemblies.
- Installation of the power supplies, related cabling, and the AC distribution system
- Installation of the BTS components near the SPEAR septum.
- Installation of the MPS, PPS, and LION system components.
- Installation of new cables and cable trays.
- Modification of the beam line front ends and realignment of the four bending magnet beam lines.
- Survey and alignment of the accelerator vacuum chamber components and magnets.

Tasks that will be accomplished in prior 2- to 3-month shutdown periods include:

- East and West pit shielding modifications.
- Tunnel AC power and lighting changes.
- LCW distribution upgrades.
- All cable plant installation outside the tunnel
- BPM processor expansion.
- Corrector and trim magnet power supply installation.
- Installation of improved magnet girder supports.
- 3 GeV injector upgrade (separate AIP project).

2.4.13 Schedule

The SPEAR 3 storage ring, injector, transport line, and conventional facility upgrade tasks are planned on a three-year time scale, preceded by a year of R&D, pre-engineering, and design preparation. More detailed schedule information is included in Section 8.3.

Storage Ring Design Parameters 3

The SPEAR 3 upgrade project will replace the current 160 nm-rad FODO lattice with an 18 nm-rad DBA lattice. To facilitate rapid, cost-effective hardware conversion, the new lattice and vacuum chamber will be pre-assembled on steel girders and will direct synchrotron radiation down existing beamlines. The complete design utilizes robust, conventional technology with the aim to 1) minimize installation and commissioning time, 2) produce long beam lifetime, and 3) deliver stable x-ray beams. The resulting 3 GeV storage ring preserves twelve 3.1 m straight sections, increases four straight sections to 4.7 m, and contains two 7.6 m straight sections.

To conform to the existing tunnel geometry and constraints imposed by the RF system, and to satisfy the needs of the user community, the lattice must satisfy the following conditions:

- a 234.126 m storage-ring circumference
- magnets on the existing girder pattern (wherever possible)
- synchrotron radiation delivered to existing photon beamlines
- < 20 nm-rad emittance at 3.0 GeV
- low dispersion between lattice cells

These requirements can be satisfied with a relatively simple DBA lattice. The DBA is operationally robust, entails minimum engineering risk, and provides factors of 10-200 increase in focused-flux density to the beamlines with only 200 mA circulating current.

This chapter provides an overview of the SPEAR 3 storage-ring lattice and its anticipated performance including 1) dynamic aperture, 2) orbit stability, 3) collective effects, and 4) beam lifetime. Factoring in realistic, yet conservative magnet errors, the horizontal dynamic aperture is about 18-20 mm in the 3.1 m straights, large enough to capture the injected beam and provide Touschek lifetimes of up to 50 hr at 500 mA. Based on an average pressure of 1.8 nT (N_2 equivalent), the net beam lifetime is about 18 hr at 500 mA.

3.1 Storage Ring Lattice and Beam Parameters

Section 3.1 is divided into several subsections covering lattice design and beam parameters. The basic lattice, with seven standard cells leading into the racetrack straights, is shown to fit neatly in the tunnel and to produce radiation-source parameters competitive with many 3rd generation light sources. Single-particle dynamics and dynamic aperture simulations (including the effect of magnet errors) are presented. A satisfactory dynamic aperture is demonstrated in the presence of conservative multipole errors and energy oscillations exceeding 3%. It is shown that insertion devices do not significantly affect dynamic aperture, and that alternative lattice configurations are possible that either lower the electron beam emittance or reduce β-functions in the racetrack straights.The coupling correction scheme, based on 14 skew quadrupole windings on the sextupole cores, is discussed. Section 3.1 concludes with discussions of lattice tuning, electron beam-stay-clear, the safe photon beam steering envelope and ion effects.

3.1.1 Storage Ring Geometry

Figure 3.1 illustrates the racetrack shape of SPEAR with 18 magnet cells arranged in a 234.126 m circumference. The racetrack configuration adds both complexities (periodicity breaking, unique components) and opportunity (long straight sections) to SPEAR 3. Fortunately, the current arrangement of magnet girders allows a straightforward conversion from the ~4.5 GeV FODO lattice to a 3 GeV DBA lattice. The fourteen standard cells closely resemble the footprint of the current lattice, while the four matching cells require a new geometry. In order to minimize the hardware conversion time, the new lattice and vacuum chamber will be pre-assembled on steel girders.

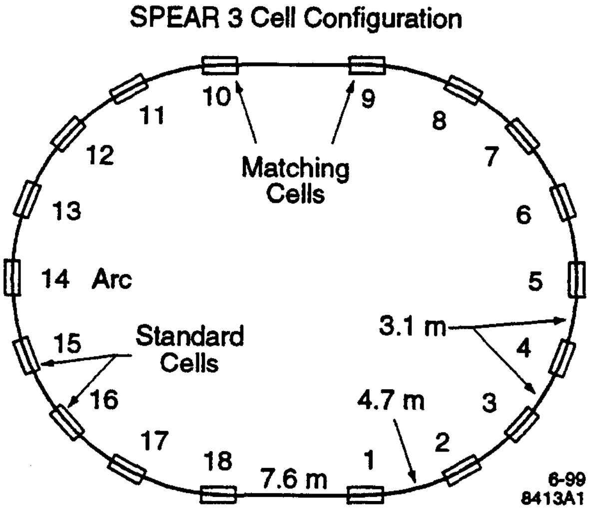

Figure 3.1 SPEAR storage ring configuration.

For reference, Figure 3.2 illustrates the lattice and electron-beam optics for SPEAR 2. Each standard cell contains two 10.5° dipole magnets embedded in a split-QF FODO cell arrangement. The dipole layout in the matching cells was designed for dispersion control and quadrupole locations were optimized for collider applications. Note that in SPEAR 2, cells 1,9,10,18 each contain two back-to-back full-angle dipoles, while cells 2,8,11,17 contain one full-angle dipole and one half-angle dipole.

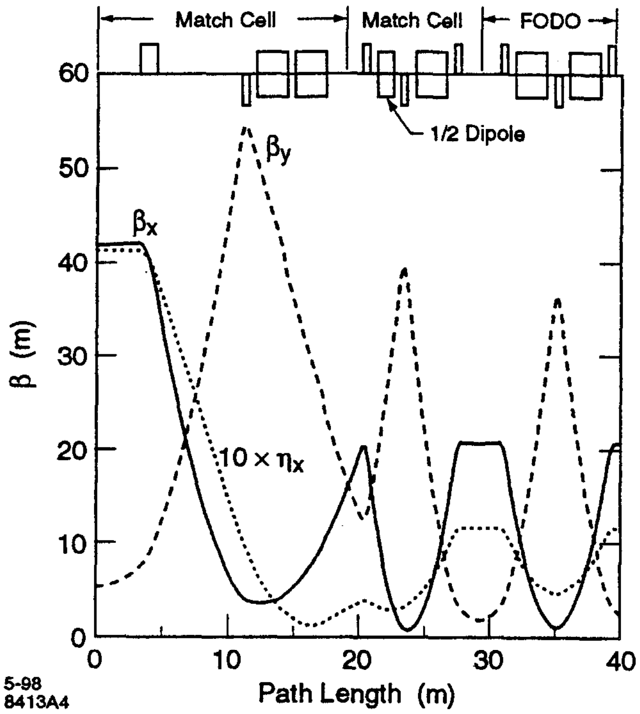

Figure 3.2 SPEAR 2 lattice and electron beam optics.

In SPEAR 3, the FODO cells and matching cells on girders 2,8,11,17 are replaced with standard DBA cells to extend the periodic structure of the lattice. The remaining bend angle is achieved with pairs of 3/4-angle dipoles in matching cells 1,9,10 and 18. These cells also provide the transition optics from the arcs to the racetrack straights.

As discussed below, the standard SPEAR 2 FODO cells have a slightly longer path length than the standard SPEAR 3 DBA cells. As a result, the matching cells in SPEAR 3 were configured to make up the path length difference.

3.1.2 Standard Cells

The standard arc cells have a gradient-dipole DBA structure with β_x=10.2 m and β_y =4.7 m in the 3.1 m straights. Figures 3.3 and 3.4 show how the compact lattice design yields relatively low β-functions throughout the cell. This helps to decrease sensitivity to magnetic field errors, and to reduce demand on the vacuum pumps. Figure 3.3 also demonstrates how vertical focusing in the gradient dipoles tends to shift the peak vertical betatron function toward the center of the cell. The shift in β_y creates a more FODO-like optics, which improves separation of the β-functions at the SD sextupoles. The use of gradient dipoles also decreases the β-functions in the straight sections, and reduces the integrated strength of the QD quadrupoles.

Table 3.1 lists the key optical parameters for the standard DBA cells:

Table 3.1 SPEAR 3 standard cell parameters

Cell Parameter	Value
Path length (m)	11.691
Horizontal cell phase advance (2π)	0.79
Vertical cell phase advance (2π)	0.26

Table 3.1 SPEAR 3 standard cell parameters

Cell Parameter	Value
Natural horizontal cell chromaticity ($\Delta\nu_x/\delta$)	–1.2
Natural vertical cell chromaticity ($\Delta\nu_y/\delta$)	–0.79
β_x (insertion straight, m)	10.16
β_y (insertion straight, m)	4.72
β_x (peak, m)	11
β_y (peak, m)	16

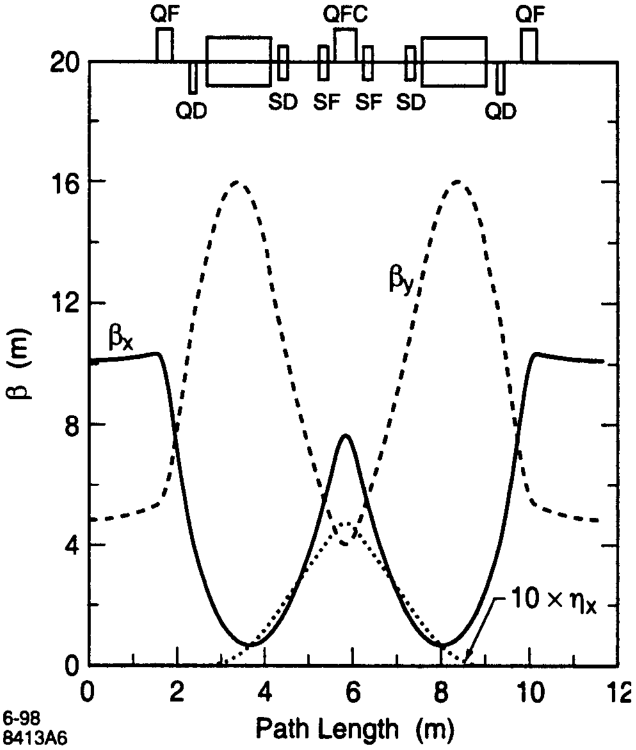

Figure 3.3 SPEAR 3 cell optics.

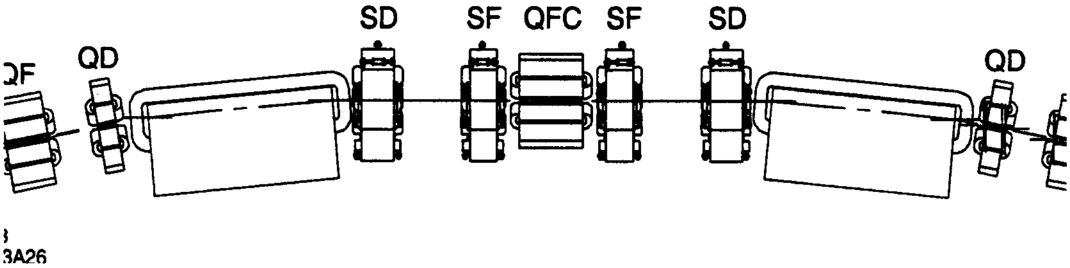

Figure 3.4 SPEAR 3 cell geometry.

One of the main cell design issues involved the specification of the dipole lengths, dipole field gradients, and dipole locations. ANSYS calculations of flux in the iron core were used to determined the minimum dipole length for a range of field gradients. The dipole positions were then determined by taking into account both optical and engineering constraints: if positioned too near the cell center, the dipoles drove up the strength of QFC and increased chromaticity. Moving the dipoles apart relaxed QFC and the sextupoles, and lowered the β-functions in the straights. The drawbacks to separating the dipoles included the tendency to push the quadrupole doublets into the insertion straights and move the dipole beamline source points away from the current locations. Given these constraints, the dipole magnets were separated by the maximum possible distance without compromising the length of the insertion device straights or alignment of the beamlines. The final dipole field gradient ($-0.33\ \mathrm{m}^{-2}$) was determined by balancing engineering constraints against optical considerations and design of the QF/QD doublet.

Other constraints on the cell design included the relative positioning of the quadrupole and sextupole magnets to provide space for field coils, photon stops, BPMs, correctors and flanges, and the adjustment of the quadrupole lengths to equalize field gradients within each magnet family. With similar field gradients, no single magnet family limits the upper energy of the storage ring (3.3 GeV).

The final cell design took into account all the physical constraints while restricting the betatron phase advances near $\phi_x=0.75$, $\phi_y=0.25$ per cell. These phase advances help to cancel chromatic quadrupole aberrations and geometric sextupole aberrations. The actual phase advance, $\phi_x=0.79$, $\phi_y=0.26$, was based on global tune-optimization and tracking studies. In practice, in-situ lattice tuning will dictate the optimum phase-advance values.

3.1.3 Matching Cells

Similar to the standard cells, the matching cells have a DBA configuration with zero dispersion in the straights. In the matching cells, however, two 3/4-angle dipoles† replace the 1/2-angle dipoles used by SPEAR 2. The new configuration is shown in Figure 3.5.

The location of the 3/4-angle dipoles was determined by two constraints: 1) the 234.126 m storage ring path length, and 2) the distance from the racetrack straights to the first cell in the main arcs. The path length constraint was set by the need for a 7:4 circumference ratio between SPEAR 3 and the injector (Section 4.8.4). The translation distance from the racetrack straights was necessary to position the electron beam in the insertion device straight sections.

Figure 3.5 also shows the optical functions in the matching cells. To match the β-functions in the arcs to the racetrack straights, a quadrupole doublet was used on the arc side of the matching cells, and a quadrupole triplet was used on the racetrack side.The triplet improved optics control through the long straights (Section 3.1.10.2) leaving open the possibility for a lower β configuration. A single quadrupole (QFY) located between the dipoles produces achromatic focusing. With the exception of QFX, the matching cell quadrupoles have the same core length as those used in the main arc cells. Each matching cell quadrupole family operates on an independent power supply.

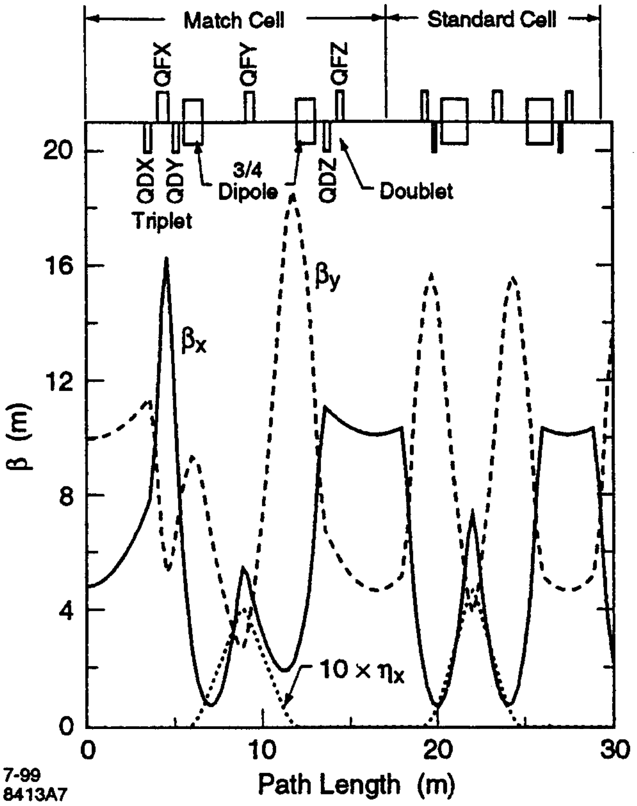

Figure 3.5 SPEAR 3 matching cell.

†The 3/4-angle dipoles use the same lamination pattern as the full-length dipoles. This 3/4-angle design allows excitation of the entire dipole string by a common power supply.

The complete matching-cell design was based on a multi-parameter optimization intended to minimize peak β-function values and create long drift spaces on either side of the cell. In the process, the separation of the 3/4-angle dipoles and strength and position of the quadrupoles were systematically varied. The phase advance through the matching cells was adjusted to optimize on-energy dynamic aperture, and the strength of the two sextupole families (SFI/SDI) was adjusted to maximize off-energy dynamic aperture. Tracking studies favored sextupole strengths slightly below the value needed to correct local chromaticity.

3.1.4 Storage Ring Lattice

The complete SPEAR 3 lattice contains 18 magnet girders with 14 standard cells and four matching cells. The lattice provides twelve 3.1 m straights, four 4.7 m straights, and two 7.6 m straights. Each straight section has zero dispersion by design, but the dispersion can be tuned slightly positive to reduce horizontal emittance (Section 3.1.10.1). Figure 3.6 shows the β-functions and dispersion for one quarter of the lattice.

As shown in Figure 3.7, the storage ring tunes (ν_x=14.19, ν_y=5.23) are located away from strong resonances. The working point was chosen to provide an efficient horizontal phase advance for injection as well as a comfortable dynamic aperture over a range of tunes within the working diagram (Section 3.1.7). The integer tune in the horizontal plane, ν_x~14, generates a natural horizontal emittance of 18.6 nm-rad. With insertion devices active, the horizontal emittance decreases to about 16 nm-rad. The bare lattice parameters (without insertion devices) are listed in Table 3.2.

Note that the dipole bending radius in Table 3.2 (ρ=7.86 m) applies to all lattice dipoles assuming an average B-field of 1.27 T and 1.45 m path length through the full-angle dipoles.

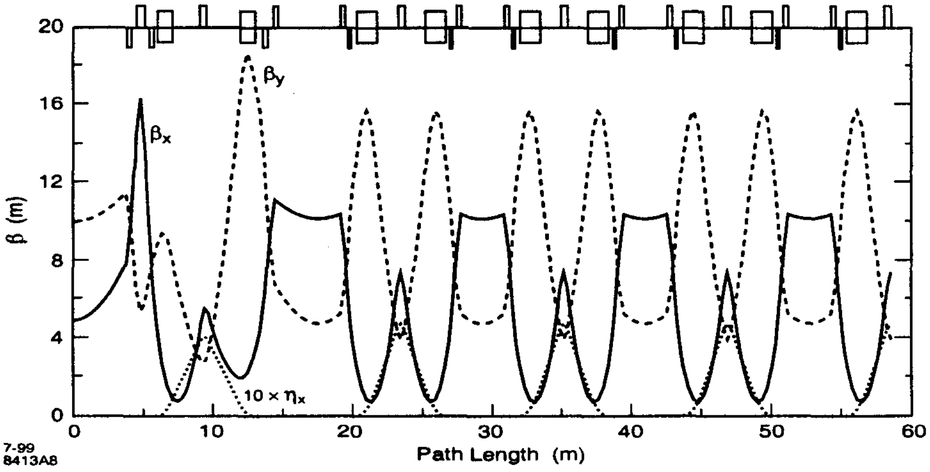

Figure 3.6 Optical functions for one-quarter of the SPEAR 3 lattice.

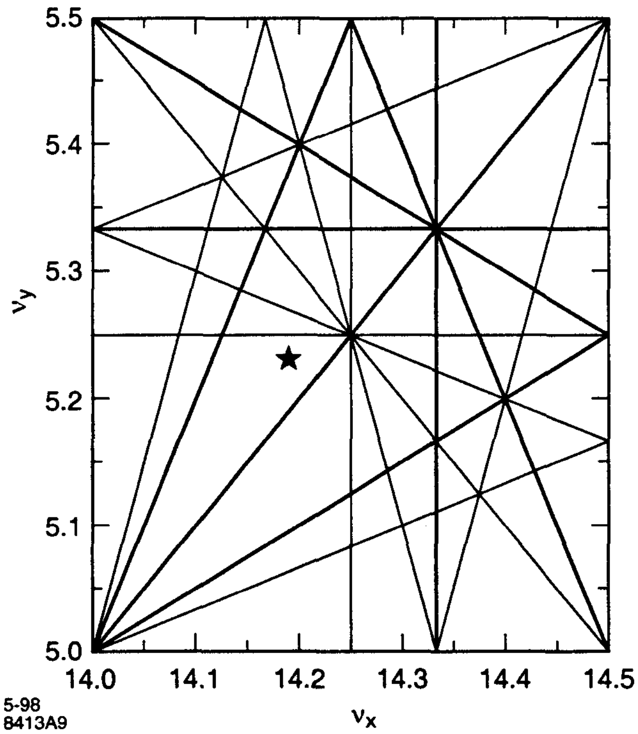

Figure 3.7 SPEAR 3 tunes in the working diagram

Table 3.2 SPEAR 3 lattice parameters (no wigglers).

Parameter	Symbol	Value
Nominal Energy	E (GeV)	3.0
Current	I (A)	0.2 ⇒ 0.5
Circumference	C (m)	234.126

Table 3.2 SPEAR 3 lattice parameters (no wigglers).

Parameter	Symbol	Value
Number of Cells	N_c	18
3.1 m Straights	$N_{L=3.1}$	12
4.7 m Straights	$N_{L=4.7}$	4
7.6 m Straights	$N_{L=7.6}$	2
Emittance	ε_x(nm-rad)	18.6
Energy Spread	σ_E/E (%)	0.097
Horizontal Tune	ν_x	14.19
Vertical Tune	ν_y	5.23
β_x at Insertions	β_x (m)	10.16
β_y at Insertions	β_y (m)	4.73
x-Chromaticity	$\xi_x=\Delta\nu_x/\delta$	-21.9
y-Chromaticity	$\xi_y=\Delta\nu_y/\delta$	-14.3
Momentum Compaction	α_c	0.00113
RF Frequency	ν_{rf} (MHz)	476.3366
Synchronous Phase	ϕ_s (degrees)	163
RF Voltage	V_{rf} (MV)	3.2
Harmonic Number	h	372
Synchrotron Tune	ν_s	0.008
RF Bucket Size	$(\sigma_E/E)_{RF}$ (%)	3.08
Dipole Field	B (T)	1.27
Dipole Radius	ρ (m)	7.86
Critical Energy	E_c (keV)	7.62
Energy Loss/Turn	U_o (keV)	912

Table 3.3 lists parameters for the main magnets. Each quadrupole has a 35 mm pole tip radius and a field gradient of < 18.5 T/m at 3.0 GeV. A 20% power supply overhead is available for configuration changes, energy ramping, and optics control. More overhead is available for the matching-cell triplet quadrupoles to provide optics control in the racetrack straights. The dipole magnets have acceptable multipole content to >110% field excitation, and the sextupoles are designed to operate with k-values up to 50 m^{-3} at 3.0 GeV. The dipole, QFC, matching-cell quadrupoles, and sextupole

families are each gang-connected to common power supplies. Most of the QF and QD magnets have separate power supplies for local optics control.

Table 3.3 SPEAR 3 magnet parameters

Magnet Family	Length (m)	k-value
Full Dipole	1.45	- 0.33 (m^{-2})
3/4 Dipole	1.09	- 0.33
QF	0.34	+1.81576
QD	0.15	- 1.58041
QFC	0.50	+1.78661
QDX	0.34	- 1.42157
QFX	0.60	+1.58443
QDY	0.34	- 0.46267
QFY	0.50	+1.47212
QDZ	0.34	- 0.86973
QFZ	0.34	+1.45627
SF	0.21	+30 (m^{-3})
SD	0.25	- 37
SFI	0.21	+15
SDI	0.21	-17

3.1.5 Electron Beam Parameters

SPEAR 3 will initially operate with approximately 200 mA at 3 GeV. As beamline upgrades permit, the current will increase by about 100 mA/year until the maximum current of 500 mA is reached. At this stage, the beam will be stored in 280 contiguous RF buckets with a 92 bucket (200 ns) ion-clearing gap. The single-bunch current will be 1.8 mA (8.7×10^9 particles/bunch) with a 2.1 ns bunch separation (0.63 m). At 500 mA, The total stored energy is 1.2 kJ, and the total radiated power from the dipole magnets is 456 kW.

Alternatively, SPEAR 3 can operate at a maximum beam energy of 3.3 GeV. In this mode, the beam current must be reduced to control the radiation power load. According to the power scaling law ($P \sim IE^4$), the maximum operating current is 340 mA so the net photon flux is less at the lower end of the spectrum. Further, in order to operate at higher energy, the beamlines must be adjusted for narrowing of the photon beam fan width from insertion devices. For these reasons, the dominant mode of operation will be 3 GeV beam energy.

Beam stability is a high priority for SPEAR 3. Multi-bunch stability will be achieved, in part, by utilizing PEP-II style RF cavities. Based on calculations with damped high-order cavity modes (Section 3.5) the full beam current can be stored without longitudinal or transverse bunch-by-bunch feedback systems (Section 3.6). The broadband impedance ($Z_{||}/n$) will be on the order of 1 Ω. All main power supplies and trim supply modules will be replaced with high performance upgrades (Section ???) and the fast Orbit Feedback system will operate with a -3 dB closed-loop bandwidth of 100 Hz (Section ???). The goal of the Orbit Feedback system is to stabilize the electron beam to within 10% of the transverse beam size (~40 μm horizontal, ~5 μm vertical, Section 3.3).

In terms of beam lifetime, SPEAR 3 is expected to achieve a 16 hr e-folding time at 500 mA (8-9 A-hr). As explained in Section 3.7, to achieve these conditions the lattice must be carefully tuned for wide dynamic aperture and the vacuum system must be carefully conditioned to maintain an N_2-equivalent gas pressure of <2 nT. The injection schedule will depend on lifetime conditions and the needs of the user community. Calculations indicate a 500 mA fill will decay to ~200 mA in 24 hr (Section 3.7.4).

In the nominal lattice configuration, the horizontal emittance is 18.6 nm-rad. With wigglers active, the emittance decreases to about 16 nm-rad (Section 3.1.9). Further emittance reduction is possible by allowing finite dispersion in the 3.1 m straight sections (Section 3.1.10.1). With η_x=0.1 m dispersion in the straights, for example, the bare lattice emittance decreases to 12 nm-rad at 3.0 GeV. Since finite dispersion in the straight sections tends to reduce the dynamic aperture, this option is reserved as an upgrade path. In the vertical plane, the 14-magnet coupling-correction system is expected to achieve 1% coupling. The resulting vertical emittance will be on the order of 180 pm-rad.

Table 3.4 lists single-bunch electron beam parameters at 500 mA. Note that the gradient dipole magnets increase the horizontal partition number, thereby reducing the horizontal damping time.

Table 3.4 Single-bunch beam parameters.

Parameter	Value	Symbol
Energy	3.0	E (GeV)
Total Current	200 => 500	I (mA)
Bunch Current	1.8, 8.7x10^9	I (mA), Electrons
Horizontal Emittance	18.6	ε_x (nm-rad)
Energy Spread	0.097	σ_E/E (%)
Coupling	1	κ (%)
Bunch Length	16, 4.9	σ_x (ps), σ_l (mm)
x-Damping Time	4.24, 1.21	τ_x (ms), J_x
y-Damping Time	5.14, 1.00	τ_y (ms), J_y
s-Damping Time	2.87, 1.79	τ_s (ms), J_s
$I_{threshold}$	4.5	mA (energy widening)
$I_{threshold}$	28	mA (mode coupling)

Table 3.5 lists the lattice functions at the photon beam source points. The optical functions in the dipoles were calculated 24 mrad upstream from the end of a standard-cell B2 dipole. The insertion device parameters refer to the center of the 3.1 m straights. All values apply to the ideal bare-lattice machine optics.

Table 3.5 Electron beam parameters at the photon beam source points.

Source	β_x	α_x	β_y	α_y	η_x	η'_x
Dipole	0.804	-0.414	13.749	2.758	0.106	0.174
Insertion	10.16	0.000	4.73	0.000	0.000	0.000

Table 3.6 gives the corresponding electron beam size and angular divergence based on 1% emittance coupling (ε_y=0.01ε_x), η and η' aare the dispersion and its derivative and σ_E=0.1% energy spread. The formulas for the size and divergence of the electron-beam assume a Gaussian beam in the plane of interest:

$$\sigma = \sqrt{\varepsilon\beta + \eta^2\sigma_E^2} \tag{1}$$

$$\sigma' = \sqrt{\varepsilon\beta + \eta'^2\sigma_E^2} \tag{2}$$

where σ_E is the electron beam energy spread (0.1 %) and $\gamma = \frac{1+\alpha^2}{\beta}$. These values will be used in the following section to compute the photon beam size.

Table 3.6 Electron beam size and divergence at the photon beam source points.

Source	σ_x [μm]	$\sigma_{x'}$ [μrad]	σ_y [μm]	$\sigma_{y'}$ [μrad]
Dipole	160	236	51	11
Insertion	435	43	30	6

3.1.6 Photon Beam Parameters

To enhance focused flux density, a premium was place on generating low horizontal betatron functions in the insertion device straight sections. As a result, in conjunction with the order of magnitude emittance reduction (relative to SPEAR 2), the focused flux density from the SPEAR 3 IDs will increase by a factor of 10 at 200 mA and the flux density from dipole beamlines will increase by a factor of 100-200 in the 20 keV photon energy range at 200 mA.

The photon-beam parameters are determined by the electron-beam phase-space distribution and the radiation emission properties. To calculate the photon-beam size and divergence, one adds the electron-beam parameters in quadrature with the radiation angle at the wavelength-of-interest. For dipole and wiggler beamlines the vertical photon beam size and divergence at the critical wavelength $\lambda_c$are[1]:

$$\sigma^P = \frac{\lambda_c}{4\pi\sigma_{\psi'}} \tag{3}$$

$$\sigma_{y'}^P = \sqrt{\sigma_{y'} + \sigma_{\psi'}}^2 \tag{4}$$

where $\sigma_{\psi'} = \frac{2}{\gamma\sqrt{2\pi}}$ is the rms half-angle for emission of radiation (136 μrad). As Table 3.7 reveals, the photon beam size at the dipole source points is dominated by the electron beam size, while photon beam divergence is dominated by the radiation emission angle. The critical wavelength in the dipole beamlines is given by

$$\lambda_c[\text{Å}] = \frac{18.64}{B[T]E^2[GeV]} \tag{5}$$

where B is the dipole field and E is the beam energy. At 3 GeV, λ_c =1.6 Å in the dipole beamlines.

Table 3.7 also contains data for the insertion-device beamlines including 1) the peak field, 2) wiggler parameter (K=0.934•B[T]•λ_u[cm]), 3) critical energy, 4) critical wavelength, and 5) photon-beam phase-space parameters. For most SPEAR 3 IDs, K>> 1, so the effective horizontal size of the photon beam is a convolution of the RMS deflection ampltude in the wiggler and the cross-section of the electron beam. In the replacement wigglers for beamlines 4 and 7, for example, the RMS deflection is about ??? μm, so the effective source size is increased from 430 μm to about ??? μm.

Currently, only beamline 5 operates in the undulator mode. To achieve K=1, we chose the 10-period, λ_u=18.3 cm device with a peak field of 0.58 kG for Table 3.7. The radiation characteristics were computed using the wavelength at the first harmonic (evaluated on axis):

$$\lambda_1 = \frac{\lambda_\mu\left(1+\frac{K^2}{2}\right)}{2\gamma^2} = 39.8\text{Å} \quad (K=1) \tag{6}$$

The source properties, operating with K=1, are derived from the equations for an extended source [1]:

$$\sigma^p_{x/y} = \sqrt{\sigma^2_{x/y}+\sigma^2_r} \tag{7}$$

$$\sigma^p_{x'/y'} = \sqrt{\sigma^2_{x/y}+\sigma^2_{r'}} \tag{8}$$

where $\sigma_r = \sqrt{\frac{\lambda_1 L}{4\pi}}$, and $\sigma_{r'} = \sqrt{\frac{\lambda_1}{L}}$ and L is the total undulator length. In this mode, diffraction effects increase the photon beam divergence in the horizontal plane by about 50% ($\sigma^p_{x'}$ = 63 μrad).

Table 3.7 SPEAR 3 Photon beam parameters. ε_c and λ_c are the critical energy and wavelength..

Device	Periods	B(T)	ε_c (keV)	λ_c [Å]	K	σ_x^P [μm]	σ_y^P [μm]	$\sigma_{y'}^P$ [μrad]
Dipole	n/a	1.27	7.62	1.63	n/a	160	51	136
Beamline 4	4	1.8	10.77	1.15	75	435	30	136
Beamline 5	10	0.06	0.31	λ_1=39	1	435	30	47
Beamline 6	27	1.3	7.78	1.59	8	435	30	136
Beamline 7	4	1.8	10.77	1.15	75	435	30	136
Beamline 9	8	1.9	11.57	1.07	47	435	30	136
Beamline 10	15	1.45	8.68	1.43	18	435	30	136
Beamline 11	13	1.98	11.85	1.05	32	435	30	136

References

[1] H.-D. Nuhn, SSRL Internal Note, SSRL-ACD-118, 1992.

3.1.7 Single Particle Dynamics

Section 3.1.7 presents single-particle dynamics data and results from dynamic aperture studies for SPEAR 3. The discussion begins with tune shift as a function of betatron amplitude and energy. The dynamic aperture is shown for the error-free lattice with zero chromaticity, and with magnet errors and energy oscillations up to 3%. The dynamic aperture with errors is roughly constant for all random-error seeds studied. The effect of operating with a positive chromaticity of a few units (unnormalized) is small. Section 3.1.9 covers both the effects of insertion devices including the impact of small-gap chambers.

3.1.7.1 Tune Shift with Amplitude

To avoid resonance crossings, the amplitude-dependent tune shift must remain within reasonable values. Figure 3.8 shows that in the case of SPEAR 3, the tunes do not approach the half-integer until the horizontal betatron amplitude x_β>20 mm.

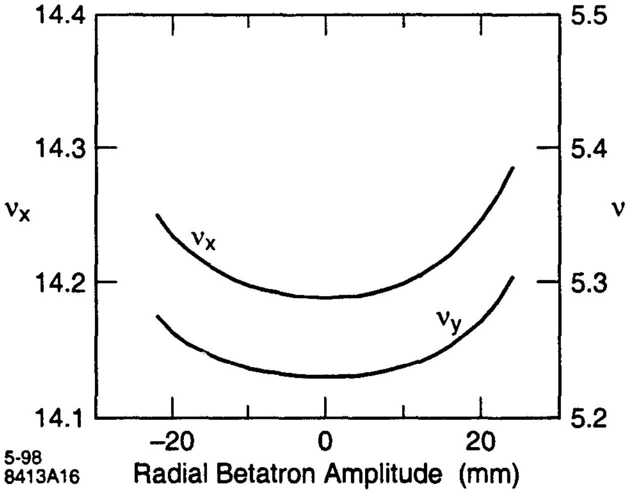

Figure 3.8 Horizontal and vertical tune as a function of horizontal betatron amplitude.

Figure 3.9, shows the vertical tune shift for vertical betatron amplitudes up to 15 mm. This behavior is confirmed by element-by-element tracking of the dynamic aperture.

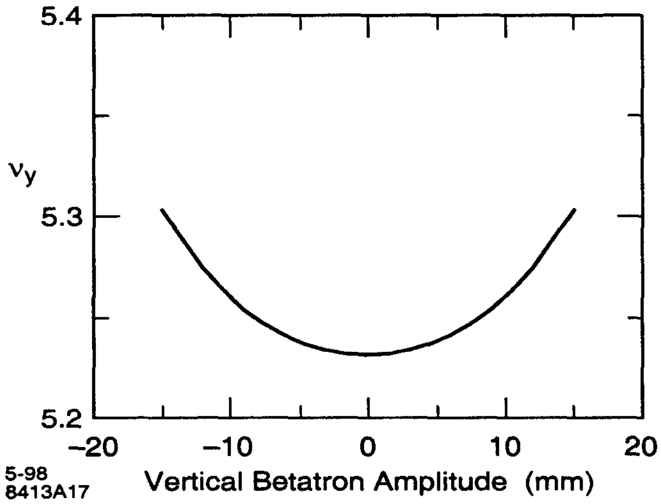

Figure 3.9 Vertical tune as a function of vertical betatron amplitude.

3.1.7.2 Off-Energy Effects

Since individual particles within the electron beam execute energy oscillations, it is important to minimize off-energy β-function distortions and tune shift. Optimization of the relative sextupole strengths in the standard and matching cells can be used to control these effects. Figure 3.10 shows the resulting peak β-function distortion as a function of energy. Figures 3.11 and 3.12 plot the momentum-dependent tune shift in the horizontal and vertical planes. The low chromatic variation of the β-functions and tune gives rise to an off-energy dynamic aperture in excess of 3%.

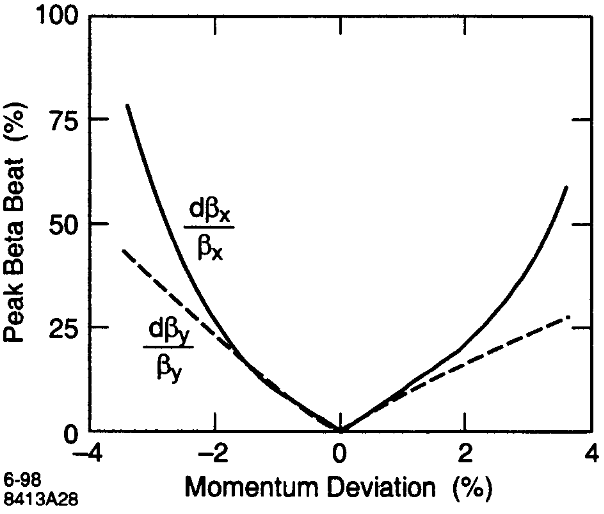

Figure 3.10 Peak β-function distortion as a function of particle energy.

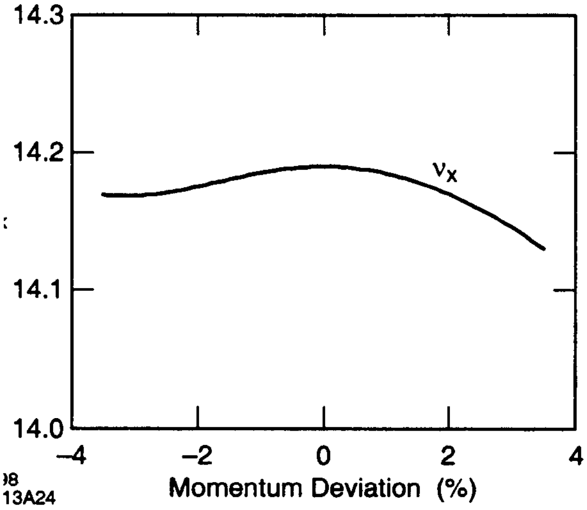

Figure 3.11 Horizontal tune shift as a function of particle energy.

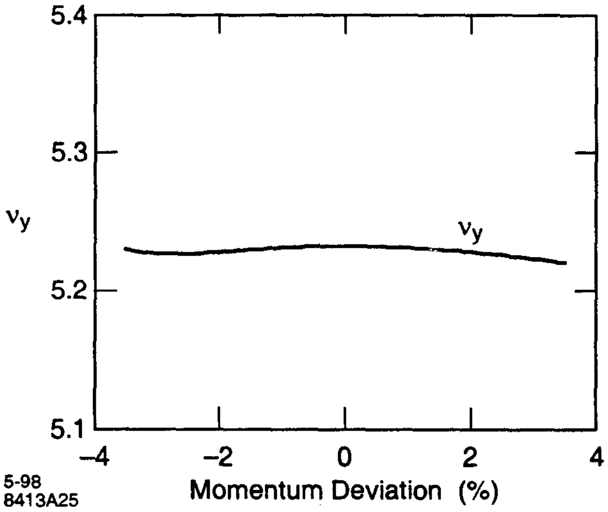

Figure 3.12 Vertical tune shift as a function of particle energy.

3.1.7.3 Dynamic Aperture

In most light sources, strong, non-linear sextupole fields limit betatron oscillation amplitudes. As a result, many sextupole families are often used to produce a large momentum-dependent dynamic aperture. For SPEAR 3, however, the main SF and SD families in the standard cells and a relatively small adjustment of the SFI and SDI families in the matching cells are sufficient to produce a dynamic aperture with up to 3% energy oscillations.

The dynamic aperture was simulated with LEGO [1], a modern tracking code designed to study single particle dynamics in PEP-II. Based on tracking simulations, Figure 3.13 plots the error-free dynamic aperture with electrons exhibiting up to 3% energy oscillations. For this plot, the dynamic aperture was evaluated in the 3.1 m straights which house the injection septum and the insertion devices (β_x=10.2 m, β_y=4.7 m). Particle trajectories were considered stable if they survived 1024 turns (not counting stable islands).

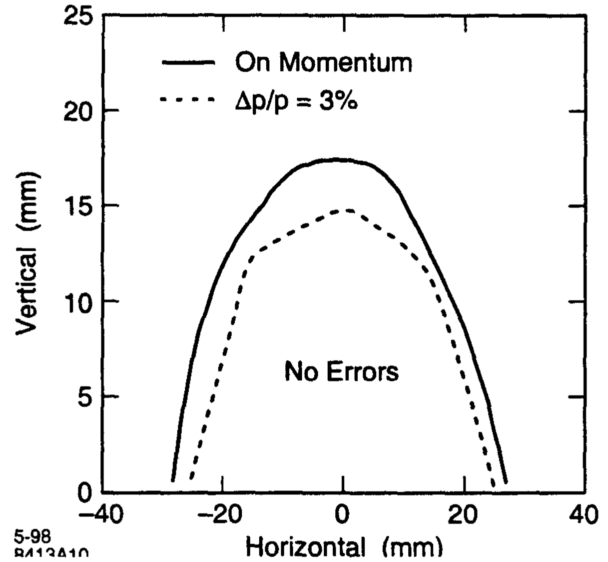

Figure 3.13 Dynamic aperture, no errors, $\delta p/p$ = 0% and 3%.

To simulate more realistic machine configurations, four separate categories of magnet errors were introduced: 1) alignment errors, 2) random errors on the main-field component of each magnet, 3) systematic multipole errors, and 4) random multipole errors. Section 3.1.8 provides details of the magnetic errors. After introducing errors, LEGO corrects the 1) betatron tunes, 2) orbit, 3) linear chromaticity, and 4) coupling. Then it initiates element-by-element trajectory integration.

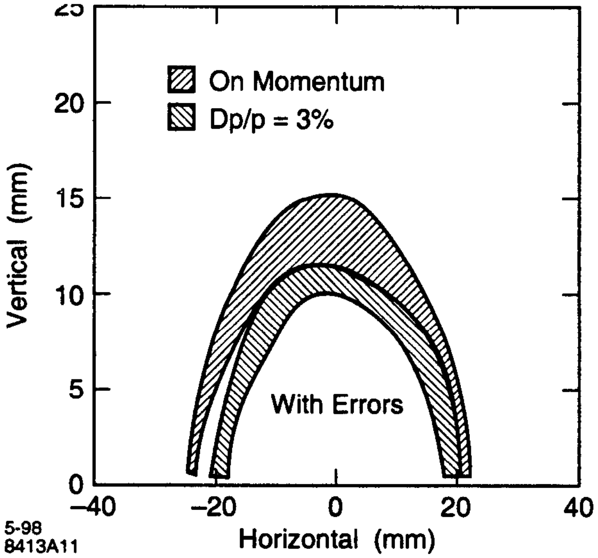

Figure 3.14 Dynamic aperture with errors, δp/p = 0% and 3%.

Many random seeds were used to develop machine-behavior statistics. The plot shown in Figure 3.14 gives dynamic aperture with errors for both on-energy electrons and electrons executing synchrotron oscillations with up to 3% energy error. The aperture envelopes were based on six random-seed configurations. The results demonstrate sufficient dynamic aperture for both injection (Sections 3.1.12 and 3.2) and beam-lifetime considerations (Section 3.7). Taking into account the effect of particle loss in the small-gap insertion-device chambers, we expect the on-energy dynamic aperture in the horizontal plane to be about ±18 mm. In Section 3.7, this value, with an aperture degradation of -1 mm-per-percent energy deviation, is used to calculate the Touschek lifetime of the beam.

To study dynamic aperture further, the working point was scanned in the tune diagram while the lattice was tracked with a single representative error set. Figure 3.15 displays the results, with the horizontal dynamic aperture plotted in terms of beam size. This plot was generated by taking the minimum horizontal dynamic aperture evaluated on either side of the beam centerline for each tune value. A dynamic aperture of 20 mm corresponds to about 45 σ_x.

Table 3.8 Dynamic as a function of working point in units of the horizontal beam size, σ_x. All magnetic field and alignment errors included.

0.30	49	49	49	49	51	46	47	47	46	44	41	38	36	49	48
0.29	51	46	52	51	48	46	47	47	47	44	41	39	46	49	48
0.28	49	49	50	51	49	48	51	49	46	44	42	40	36	48	48
0.27	50	49	49	51	50	48	46	49	46	42	40	40	37	38	37
0.26	49	46	47	51	49	46	44	47	43	42	42	41	41	39	41
0.25	47	47	49	51	49	48	44	43	46	45	42	42	37	41	49

Table 3.8 Dynamic as a function of working point in units of the horizontal beam size, σ_x. All magnetic field and alignment errors included.

0.24	47	47	46	50	47	49	45	44	48	46	43	41	45	43	50
0.23	48	49	46	$\boxed{49}$	48	48	46	50	48	45	44	49	47	42	42
0.22	48	48	45	44	49	48	50	48	48	45	46	42	42	43	43
0.21	49	45	46	46	48	50	50	51	48	46	44	44	46	46	44
0.20	48	48	44	46	41	47	44	50	48	45	46	42	47	48	45
0.19	48	46	45	50	48	45	47	49	46	47	47	48	47	47	45
0.18	47	45	47	51	49	47	47	42	46	47	43	49	46	43	40
0.17	53	49	48	49	50	48	47	45	45	43	46	40	45	44	42
0.16	51	49	48	50	49	50	47	47	44	42	41	36	42	41	40
υ_y / υ_x	0.16	0.17	0.18	0.19	0.20	0.21	0.22	0.23	0.24	0.25	0.26	0.27	0.28	0.29	0.30

To study the effect of increased sextupole strength, the dynamic aperture was simulated with positive chromaticity. As demonstrated in Figures 3.15 and 3.16, the horizontal and vertical apertures decrease as the chromaticity is raised. For un-normalized chromaticities of 4-5 units, the horizontal dynamic aperture for on-energy particles is reduced to about ±15 mm. At higher chromaticities, the linear component of the chromaticity begins to produce rapid particle loss for particles with 3% energy oscillations. Note that for these plots, both the horizontal and vertical chromaticities were set to the values indicated on the vertical axes.

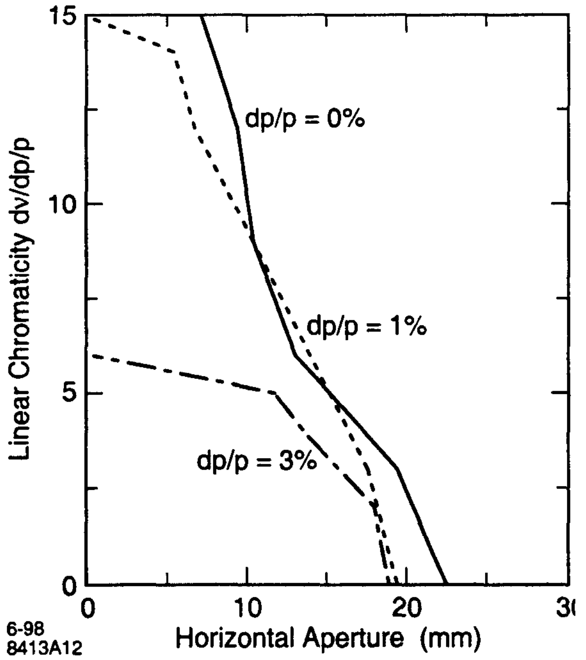

Figure 3.15 Horizontal dynamic aperture as a function of chromaticity.

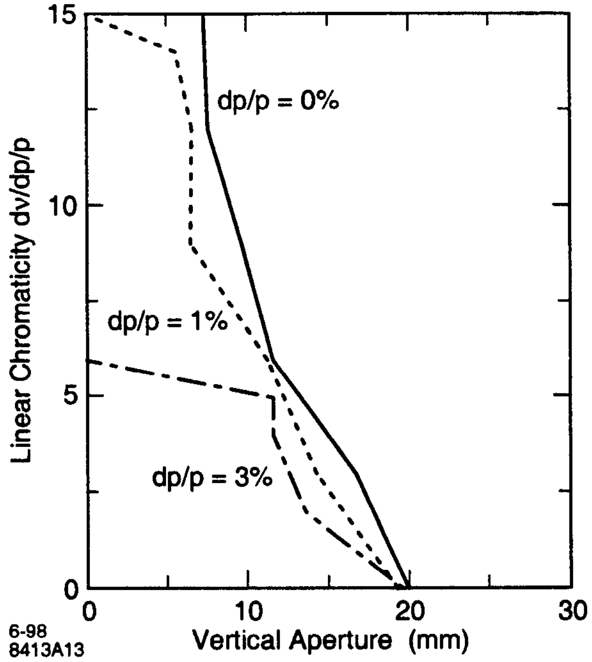

Figure 3.16 Vertical dynamic aperture as a function of chromaticity.

3.1.7.4 Large-Amplitude Coupling

In order to monitor the full extent of the dynamic aperture, most of the tracking simulations did not account for physical apertures. In practice, however, the vacuum chamber has horizontal and vertical apertures that can limit the lifetime of the beam. In the vertical plane, for example, SPEAR has two insertion devices, each with $y=\pm$ 6 mm vacuum chambers that define the vertical acceptance. Although the height of the ID chambers yields an acceptable gas-scattering lifetime, it can limit the Touschek lifetime if strong, large-amplitude coupling is present. In the presence of machine errors and strong sextupole fields, for instance, particles with large horizontal amplitudes can reach resonance levels that couple the horizontal motion into the vertical plane. This effect has been observed in several operational machines [ref???].

To study the effect of large-amplitude coupling, we launched particles with variable horizontal and synchrotron-oscillation amplitudes and monitored the maximum vertical betatron excusion. Figure 3.17 plots the degree of x-y coupling as a function of initial horizontal amplitude for particles with δ=0, 1, 2, and 3% energy oscillations. Each particle was launched with an initial vertical amplitude of 100 μm and its peak vertical amplitude was monitored at the ID location for 1024 turns. The plot shows the average value from six machines, each with a different error seed. Interpreted conservatively, these results predict an effective reduction of horizontal aperture from 20 mm to about 18 mm (or a reduction in acceptance from 39 mm-rad to 32 mm-rad). This coupling mechanism should not affect the ~10 mm injection oscillations in the horizontal plane.

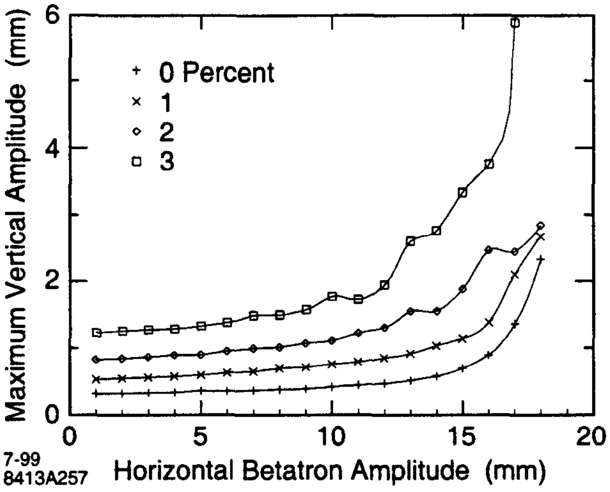

Figure 3.17 Maximum vertical betatron amplitude at insertion device position.

3.1.8 Alignment and Field Errors

Dynamic aperture simulations were made to test the specifications for magnet alignment and field errors. The resulting alignment tolerances are modest and will not require new alignment techniques. The tolerance on main field errors is also readily achieved. Similarly, the multipole content is conservative, leaving room for any discrepancy between 2-D magnet simulations and 3-D field effects or fringe field distortion.

3.1.8.1 Alignment Specifications

Table 3.9 lists the local rms alignment tolerances. Although modern laser tracking systems can achieve more accurate alignment, these values were used to simulate uncertainty between magnetic and mechanical centers, errors in the magnet fiducials, and creep. Note that, because the dipoles support a quadrupole field, the dipole alignment tolerance is the same as that used for quadrupoles.

Table 3.9 Local magnet alignment tolerances.

Element	x (μm)	y (μm)	roll (μrad)
Dipole	200	200	500
Quadrupole	200	200	500
Sextupole	200	200	500

3.1.8.2 Dipole Good Field Region

As Figure 3.18 illustrates, the ±16.6 mm trajectory sagitta through the straight dipole magnets requires a wide 'good field region' (GFR). In this case, we defined the GFR as existing 30 mm beyond the trajectory extrema (or at ± 46.6 mm). The multipole content of the straight field magnet was calculated with ANSYS at a 30 mm radius. For tracking purposes, two separate cases were studied: 1) a ± 30 mm GFR with constant multipole fields that follow the beam trajectory, and 2) a 'sliced' dipole model with multipole spill-down terms calculated at each slice to simulate the curved beam trajectory. In the second case, the spill-down terms simulate the actual field values seen by the electron beam. Further discussion can be found in Section 3.1.8.4.

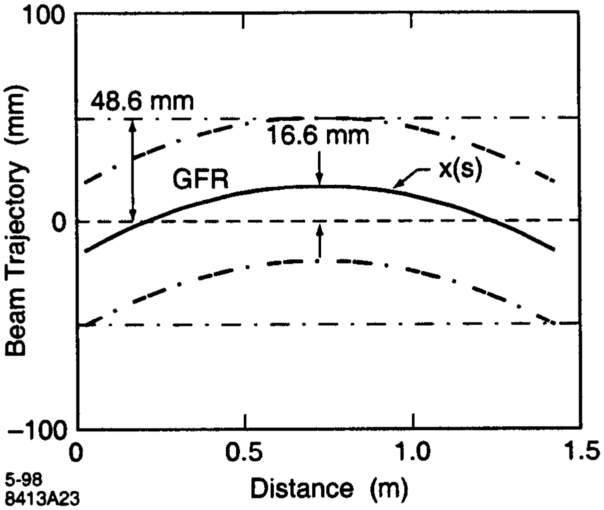

Figure 3.18 Electron beam trajectory through a SPEAR 3 dipole.

3.1.8.3 Quadrupole and Sextupole Good Field Region

The quadrupole magnets have a 35 mm pole tip radius. Their multipole content is evaluated at 32 mm to facilitate comparison to magnets used in other storage rings. The 32 mm normalization radius defines the boundary of the 'good field region'. Multipole fields in the 45 mm-radius sextupoles were also normalized to 32 mm.

3.1.8.4 Systematic Multipole Field Errors

Systematic multipole field errors are higher-order field components than the main field that apply to all magnets with a common core design. For SPEAR 3, a single lamination stamp will be used for the dipole, quadrupole, and sextupole magnets, respectively. Table 3.10 lists the systematic multipole field values used in these magnets for tracking studies. To allow for unknown fringe-field contributions, the tracking simulations used larger values than the 2-D values predicted by ANSYS simulations.

Table 3.10 Systematic multipole field components

Magnet	Multipole order	Radius (mm)	$\Delta B_n/B$
Dipole	2	30	1.00×10^{-4}
Dipole	3-14	30	5.00×10^{-4}
Quadrupole	6,10,14	32	5.00×10^{-4}
Sextupole	9	32	4.40×10^{-3}
Sextupole	15	32	1.21×10^{-3}

The skew quadrupole fields used for coupling correction will be superimposed on the sextupole magnets. A skew octupole field, with strength proportional to the skew quadrupole field, was also added to the sextupoles for simulation purposes. In terms of magnetic field strength, the skew octupole field is about 60% of the skew quadrupole field at a 32 mm radius. Tracking simulations show that the skew octupole field does not effect dynamic aperture.

To simulate the effect of systematic multipoles in the dipoles, we 'sliced' the dipoles and applied multipole spill-down terms in proportion to the electron beam trajectory offset in each slice. For these studies, since the beam sees only 2-D fields in the magnet core, we calculated the spill-down terms from multipole fields derived with ANSYS.

The spill-down terms are found by a Taylor-expansion of the multipole fields evaluated along a straight-line axis about the curved-beam trajectory. Along the straight reference axis, the total magnetic field is given by a power series expanded in terms of multipole coefficients

$$B(z) = \sum(B_n + iA_n)z^{n-1}, \tag{9}$$

where z=x-iy. Along the curved beam trajectory, z=x(s)-i0. For our case, with no systematic skew fields present,

$$B(z-x(s)) = \sum B_n(z-x(s))^{n-1} \tag{10}$$

Expansion of the exponent terms on the RHS of (Equation 10) leads to a table of binomial coefficients. At position 's', the multipole components seen by the beam were calculated by multiplying the vector of multipole coefficients B_n against a matrix of the binomial coefficients and trajectory offsets raised to the appropriate power [ref???]. Tracking studies show that the multipole spill-down terms do not degrade dynamic aperture.

3.1.8.5 Random Field Errors

Differences in magnetic core length can produce random main field errors. For tracking studies, we specified 0.1% random field error on the main field component of each magnet. Depending on the magnet type, this corresponds to a 0.25 - 0.5 mm core length error in the fabrication process. A 2-σ error truncation was used to simulate quality control in magnetic measurements.

Random multipole errors are introduced by magnet assembly imperfections which vary from magnet to magnet. The normalized random multipole specifications used for tracking studies are listed in Table 3.11. To achieve conservative tracking results, large random multipole components were specified for the n=3, 6, 10 and 14 terms on the quadrupole magnets. A 2-σ error truncation was used in tracking simulations.

Table 3.11 Random Multipole Field Errors[†]

Magnet	Multipole order	Radius (mm)	$\Delta B_n/B$
Dipole[†]	2	32	1.00×10^{-4}
Quadrupole	3,6,10,14	32	5.00×10^{-4}
Sextupole	5	32	3.30×10^{-3}
Sextupole	7	32	2.30×10^{-3}

[†]. assumes ± 1 mm error on gradient dipole-core length

3.1.9 Insertion Device Modeling

Many of the drift sections between magnet cells contain wigglers or undulators. The current machine, SPEAR 2, has seven such devices. To date, the insertion devices (IDs) have not affected machine performance negatively: SPEAR 2 readily injects to 100 mA at 2.3 GeV with insertion devices at full field[†]. For SPEAR 3, the lattice is expected to continue performing well, even after the installation of replacement devices or additional devices for future beamlines.

This section reviews the magnetic parameters for each of the seven IDs currently installed within SPEAR. These parameters include: 1) linear and non-linear tune shifts, 2) radiation effects, and 3) optical compensation with quadrupole trim windings. Tracking results show negligible impact on dynamic aperture.

3.1.9.1 Wiggler Parameters and Modeling

Table 3.12 lists the magnetic properties for each insertion device, and the dominant optical effects expected with the SPEAR 3 lattice. The parameter definitions and formulae used to compute these values appear in Table 3.12. Nominally, the IDs will reside in dispersion-free straights where β_x=10.2 m and β_y=4.7 m. Future devices are likely to be approximately 10-period wigglers similar to those for Beamlines 9 and 11. Such devices will replace the 4-period electromagnet wigglers on Beamlines 4 and 7, or illuminate new beamlines.

The most basic effects of an insertion device on the storage-ring optics can be understood from the field expression for a sinusoidal variation in z and infinitely wide wiggler poles [1].

$$B_y = B_0 \cosh\left(\frac{2\pi y}{\lambda}\right)\cos\left(\frac{2\pi z}{\lambda}\right) \qquad (11)$$

$$B_z = -B_0 \sinh\left(\frac{2\pi y}{\lambda}\right)\sin\left(\frac{2\pi z}{\lambda}\right) \qquad (12)$$

where ‘y’ and ‘z’ are the vertical and longitudinal coordinates, and z=0 is the center of a pole. Expanding (Equation) to first-order around the oscillating electron beam trajectory yields a vertical field gradient perpendicular to the orbit. This gradient results in a vertical tune shift and betatron

---

[†] Injection and 3.0 GeV beam dynamics studies are currently underway with the most recent wiggler (Beamline 11, 13 period, 2T).

beat [2]. Table 3.12 summarizes these effects for each device in SPEAR 3. Although the total tune shift in the ring increases proportionally to the number of wigglers, the pattern of the betatron beat depends on the distribution of wigglers within the ring. In the case of two identical wigglers separated by one optical cell, however, the betatron beat is partially cancelled by the 90° vertical phase advance between IDs. Section 3.1.9.3 discusses optical compensation using many wigglers.

The first higher-order wiggler field effect arises from the cubic dependence of the vertical field perpendicular to the beam trajectory, as seen in the power series expansion expressed of B_z. This octupole-like field generates a quadratically increasing vertical tune shift with amplitude. Using Smith's formula for vertical tune shift with amplitude induced by a wiggler [3], the tune shift was evaluated for the maximum vertical acceptance defined by the vacuum chambers at Beamlines 6 and 11 ($y=\pm 6$ mm, $\beta_y=4.7$ m, $A_y=7.7$ mm-mrad). The total octupole-induced tune shift for all seven wigglers is 0.002 for $y=6$ mm from the center of the wiggler (200-σ_y for 1% emittance coupling). This tune shift was considered an acceptable tune perturbation, since it is significantly smaller than the amplitude-dependent tune shift caused by the sextupoles.

Tracking simulations performed on an equivalent pure octupole field in the wiggler confirm that the vertical dynamic aperture stays outside the physical wiggler aperture. Non-linear wiggler effects, including a multipole field component to simulate the octupole-like field show only a small reduction in vertical dynamic aperture, from 12 mm to 9 mm. Even at 9 mm, the vertical aperture remains well outside the 6 mm physical aperture. Since the non-linear octupole-like field of an insertion device acts only in the vertical plane, no reduction of horizontal dynamic aperture is anticipated.

Table 3.12 Insertion Device Parameters†

ID	N	λ	B_0	ρ_0	K	$\int k_y ds$	$\Delta\nu_y$	$\Delta\beta_y/\beta_y$	$\Delta\nu_y$ (y=6mm)
4	4	0.45	1.8	5.56	75	0.029	0.011	7	0.4×10^{-4}
5†	10	0.18	0.9	11.1	15	0.007	0.003	2	0.6×10^{-4}
6	27	0.07	1.3	7.70	8	0.016	0.006	4	9.1×10^{-4}
7	4	0.45	1.8	5.56	75	0.029	0.011	7	0.4×10^{-4}
9	8	0.26	1.93	5.18	47	0.039	0.015	9	1.6×10^{-4}
10	15	0.13	1.45	6.90	18	0.021	0.008	5	3.4×10^{-4}
11	13	0.17	1.98	5.05	32	0.044	0.017	11	4.1×10^{-4}

†. N=number of periods, λ=period length (m), B_0=peak field (T), ρ_0=bending radius (m), K=wiggler parameter, $\int k_y ds$=integrated focusing (m^{-1}), $\Delta\nu_y$=linear tune shift, $\Delta\beta_y/\beta_y$= vertical betatron beat (%), $\Delta\nu_y$(y=6mm)= octupole induced tune shift at 6 mm amplitude.

The wiggler model used for optics calculations and tracking simulations is also accurate up to the second order. To model the wigglers, each wiggler pole was replaced by a constant field dipole with gaps between the poles. The pole field, $B_p=B_0\pi/4$, and pole length, $L_p=4\lambda/\pi^2$, produce the same bending and focusing effect as the actual wiggler field [2]. The model also yields the correct orbit excursion within an insertion device. In the Beamline 11 wiggler, for example, (N=13, B_0=2 T) the horizontal orbit excursion and dispersion are less than 0.3 mm, with the perturbations localized along the length of the ID. The total incremental path length is about 16 microns..

Table 3.13 Formulas used for insertion device parameters.†

Parameter	Formula
Bend radius	$\rho_0=3.33E/B_0$ (m)

Table 3.13 Formulas used for insertion device parameters.†

Parameter	Formula
K (wiggler parameter)	$0.934\ B_0(T)\lambda(cm)$
$\int k_y ds$ (integrated focusing)	$N\lambda/(2\rho_0^2)\ (m^{-1})$
$\Delta\nu_y$ (linear tune shift)	$\int\beta_y k_y ds/4\pi$ where β_y=4.7 m
$\max\{\Delta\beta_y/\beta_y\}$% (betatron beat)	$\int\beta_y k_y ds/(2\sin(2\pi\nu_y)$ where β_y=4.7 m, ν_y=5.23
$\Delta\nu_y$(y=6mm) (non-linear tune shift)	$\varepsilon_y\pi N\beta^2{}_y[1+2/3(N\lambda/2\beta_y)^2+1/5(N\lambda/2\beta_y)^4]\ /4\lambda\rho_0^2$

†. Beamline 5 contains five separate devices (1) N=10, λ=0.18, (2) N=15, λ=0.12, (3) N=24, λ=0.07, and (4) N=30, λ=0.06, and (5) an elliptically polarized undulator (EPU) . For this example, we chose the N=10, λ=0.18 device.

3.1.9.2 Radiation Effects

The quantum excitation from synchrotron radiation in the wigglers can increase the beam energy loss-per-turn (U), change the equilibrium emittance, and alter the beam energy spread. For each ID, the relative increase in energy loss-per-turn with respect to the bare lattice (without IDs) is [4]:

$$\frac{U-U_0}{U_0} = \frac{N^2\rho_B}{4\pi\rho_0^2} \tag{13}$$

where ρ_B=7.86 m is the effective radius of curvature in the main dipoles and U_0=912 keV/turn. With all seven of the present insertion devices at full field, the energy loss increases to U=1123 keV/turn (23% increase). In this case, the radiated power from the insertion devices totals 105 kW at 500 mA.

The relative change in beam energy spread due to each ID is[4]:

$$\left(\frac{\sigma_E}{\sigma_{E0}}\right)^2 = \frac{\left(1+\frac{2N\lambda\rho_B^2}{3\pi^2\rho_0^2}\right)}{\left(1+\frac{N\lambda\rho_B}{4\pi^2\rho_0^2}\right)} \tag{14}$$

With all seven wigglers at full field, the net energy spread increases by only 1.5%, from σ_{E0}/E=0.097% to σ_E/E=0.0985%. In terms of emittance reduction, radiation from Beamline 11 results in a decrease on the order of 0.6 nm-rad. With all wigglers active, the emittance decreases to about 16 nm-rad.

Table 3.14 Energy loss and energy spread due to insertion devices.

Beamline	4	5	6	7	9	10	11	Total
(U- Uo)/Uo (%)	3.64	0.9	1.99	3.64	4.84	2.56	5.54	+23%
$(\sigma_E - \sigma_{E0})/\sigma_{E0}$ (%)	0.35	-0.18	-0.13	0.35	0.64	0.0	0.84	+1.5%

3.1.9.3 Optics Compensation

To minimize betatron beats, the optical distortions induced by the insertion devices must be corrected. The independent power supplies on each QF and QD quadrupole make possible several options for correcting the focusing errors. In order of increasing complexity, three compensation techniques were explored.

3.1.9.3.1 Local Betatron Amplitude Correction

The QF/QD quadrupole doublets closest to the wiggler produce the most local correction, which is symmetric when the ID is in the middle of the drift space. This scheme compensates all the IDs independently, and the betatron perturbation remains small. The quadrupole trim values used to correct the wiggler on Beamline 11 are -1.2% and -7.8% for the QF and QD quadrupoles, respectively, but since the tune shift is not corrected locally, it must be adjusted globally.

3.1.9.3.2 Semi-Local Correction

Anti-symmetric excitation of the QF and QD quadrupoles on the girders to either side of an ID can reduce quadrupole trim strengths by a factor of two relative to the approach presented in Section 3.1.9.3.1. This technique, however, doubles the tune shift induced by the insertion device and quadrupole correction.

3.1.9.3.3 Betatron Amplitude and Phase Correction

The preferred scheme locally compensates for both the betatron beat and tune shift. It involves all four QF and all four QD quadrupole trims located on the girders to either side of each ID, and renders global tune control unnecessary. The trims required to correct the Beamline 11 wiggler are -1.0% and -6.7% for the QF and QD quadrupoles nearest the wiggler. The outer QF and QD trims, require settings of +0.2% and +1.2%, respectively.

In practice, this complete betatron-amplitude and betatron phase compensation scheme (Section 3.1.9.3.3) will be used. This technique was chosen for tracking studies. The results show that linear wiggler effects do not reduce the dynamic aperture.

References

K. Halbach, "Fields of Undulators and Wigglers," NIM, A187, p. 109-117, (1981).

[1] H. Wiedemann, Particle Accelerator Physics II, Springer-Verlag (1995).

[2] L. Smith, "Effects of Wigglers and Undulators on Beam Dynamics", LBL-ESG Tech. Note-24 (1986).

[3] A. Ropert, "High Brilliance Lattices and the Effects of Insertion Devices", CERN 90-03 (1990).

3.1.10 Optical Upgrade Paths

Several optical upgrade paths are possible with the SPEAR 3 lattice including a reduced emittance lattice via finite dispersion in the straight sections (or increased horizontal tune), or a reduction of the β-functions in the racetrack straights for vertically polarized insertion devices. In this Section, examples are given for a reduced emittance lattice and for optics control in the racetrack straights.

3.1.10.1 Low Emittance Lattice

Many 2nd and 3rd generation light sources relax the achromatic cell constraint to reduce horizontal emittance. The decrease in horizontal beam size more than compensates the increase from finite dispersion, resulting in brighter synchrotron radiation.

Tracking studies show, however, that lowering the emittance can lead to a reduction in dynamic aperture. Fitting η_x to 0.1 m in the insertion straights, for instance, reduces emittance by -37% and beam size by -22%, but also decreases the horizontal dynamic aperture by about 25%. The dynamic aperture values listed in Table 3.16, for instance, are for on-energy electrons, zero chromaticity, and no field errors. The data plotted in Figure 3.20 (horizontal dynamic aperture with errors) indicate that appreciable emittance reduction is possible with only modest loss of dynamic aperture. In practice, the straight section dispersion in the straight sections can be raised gradually to decrease emittance while monitoring dynamic aperture. Figure 3.19 shows the ring optics for η_x= 0.1 m (compare to Figure 3.6). Table 3.15 compares some of the key storage ring parameters with low emittance optics (η_x= 0.1 m) to those for the nominal optics (η_x = 0.0 m).

Table 3.15 Comparison of $\eta_x = 0.1$ m optics to $\eta_x = 0.0$ m optics.The quadrupole strengths are well within range of the magnets and power supplies (Table 3.15).

Parameter	$\eta_x = 0.1$ Optics	$\eta_x = 0$ Optics	Comparison
ε_x (nm-rad)	11.9	18.6	–36%
σ_x–ID (μm)	324	435	–25%
+x dynap (mm) (at y=0.65 μm)	+20	25	–20%
–x dynap (mm) (at y=0.65 μm)	–22	–30	–27%
β_x–ID (m)	8.8	10.2	–14%
β_y–ID (m)	4.6	4.7	–2%

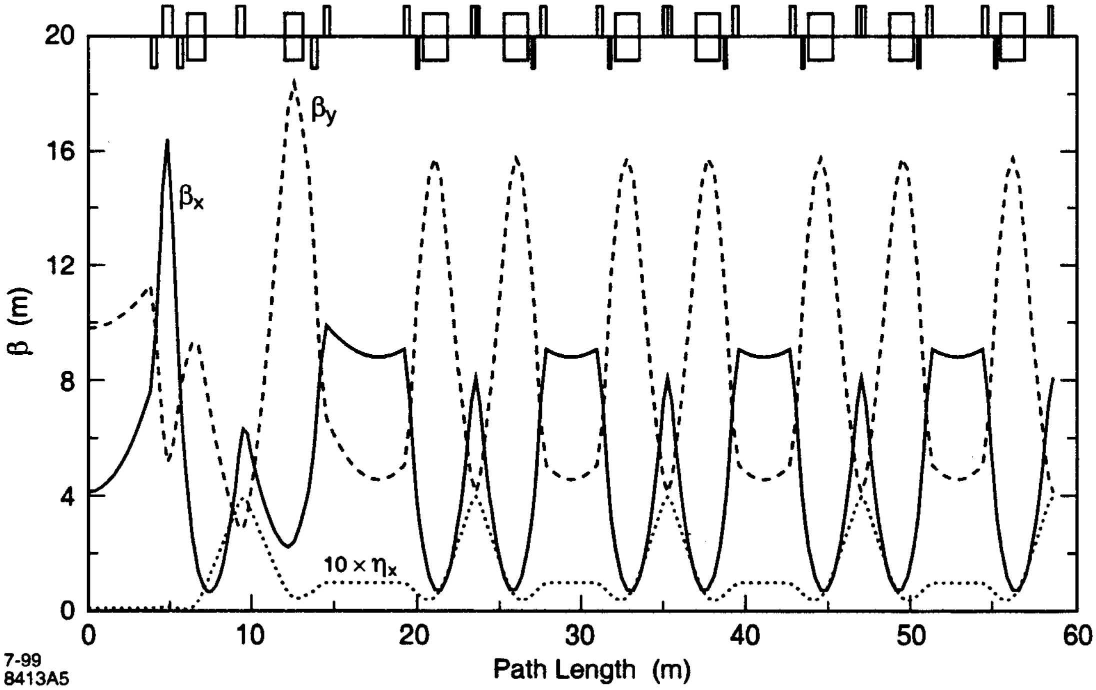

Figure 3.19 Reduced emittance optics for one quarter of SPEAR 3.

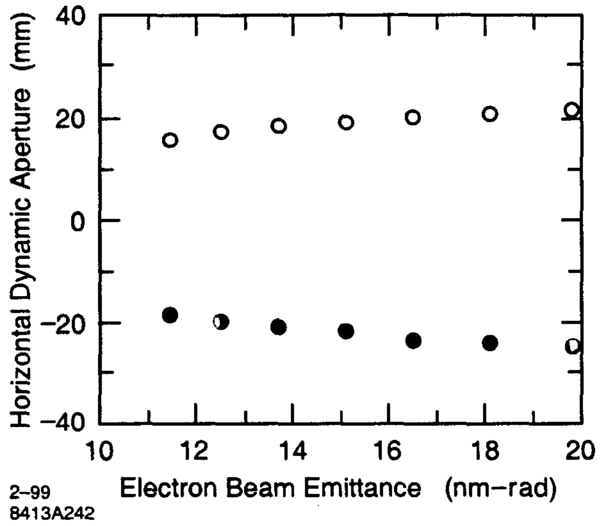

Figure 3.20 Dynamic aperature as a function of horizontal emittance.

In conclusion, dispersion reduction in the insertion straights promises to improve the performance of SPEAR 3. Tuning the lattice for reduced emittance requires no hardware modifications. However, since emittance reduction tends to decrease dynamic aperture, it is reserved as an upgrade path.

3.1.10.2 Optics Control in the Racetrack Straights

The 7.6 m free space regions in the racetrack straights have nominal β-function values of β_x~5 m and β_y~10 m in the center. To increase brightness, and potentially allow polarization experiments, it is possible to lower the β-functions locally. A reasonable value for the reduced horizontal β-function is on the order of 3-4 m. Values significantly below 3 m would increase the peak β-functions in the matching cell triplets and produce an hour glass-shaped beam in the insertion device.

To control the β-functions in the racetrack straights, the six independently powered quadrupole families in the matching cells provide a complete optical match to arcs (five quadrupole families match the Twiss parameters and the QDX quadrupoles cancel dispersion). Since lowering the β-functions changes the matching cell phase advance and chromaticity, the QF and QD quadrupoles in the arc cells need a small adjustment to keep the tune constant. The SF, SD sextupole families are used to control chromaticity.

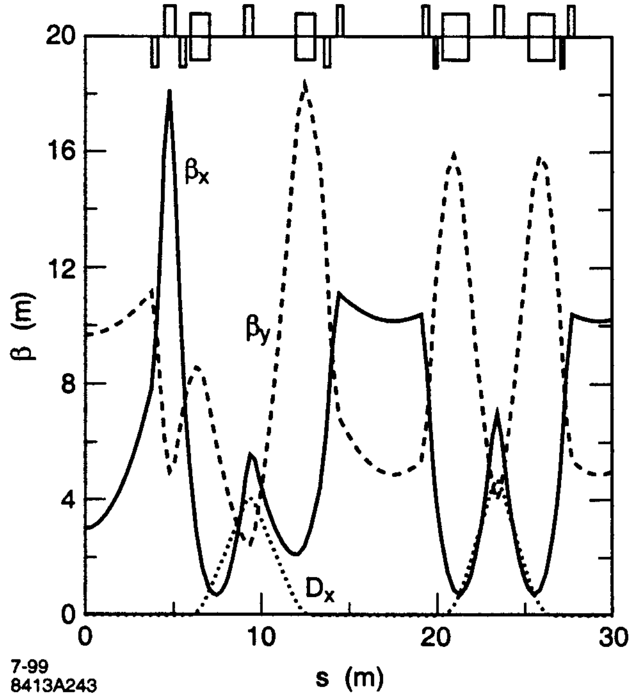

Figure 3.21 Low-β optics in the racetrack straights.

Figure 3.21 illustrates one example of low-beta optics in the matching cells, where the racetrack straight is on the left. For this case, the reduced β-functions are β_x = 3.0 m and β_y= 9.7 m. The phase advance for each matching cell is increased from the nominal values of ϕ_x=0.785, ϕ_y=0.26 to ϕ_x=0.83, ϕ_y=0.42. The peak β-functions in the matching cells are about the same as in the nominal lattice. The new quadrupole and sextupole strengths are listed in Table 3.16. Compared to the nominal lattice, only the QFY quadrupoles exhibit significant change in magnet strength. As these quadrupoles are intentionally weak in the nominal lattice, their strength remains well within the design specification of the power supply. Tracking results show the low-β lattice does not reduce dynamic aperture.

Table 3.16 Alternative lattice magnet values.

Magnet Family	Nominal Lattice	Low Emittance	Low β-function
QF (m^{-2})	1.82	1.86	1.78957
QD	-1.58	-1.59	-1.52853
QFC	1.79	1.72	1.78661
QDX	-1.42	-1.45	-1.49953
QFX	1.58	1.62	1.67629
QDY	-0.46	-0.46	-0.53120
QFY	1.47	1.41	1.47212
QDZ	-0.87	-0.83	-0.87731
QFZ	1.46	1.40	1.43391
SF (m^{-3})	30	30	30
SD	-37	-37	-37

3.1.11 Coupling and Correction

The emittance in a storage ring is determined by coupling of horizontal betatron oscillations into the vertical plane and by vertical dispersion. The coupling is primarily generated by skew magnetic gradients due to quadrupole roll misalignments and due to vertical closed orbit offsets with respect to the magnetic center of sextupoles. Vertical bending, which in turn causes vertical dispersion, arises from 1) magnet misalignments (such as dipole roll), 2) vertical-orbit steering magnets and 3) vertical quadrupole displacements. Vertical dispersion can also be caused by skew-gradient magnets at locations of non-zero horizontal dispersion.

For a storage ring without skew-quadrupole correctors, the ratio of vertical to horizontal emittance typically falls on the order of 5%. Skew quadrupole correctors will be used in SPEAR 3 to reduce that ratio to the design value of 1%. To accomplish this goal, skew quadrupole windings will be included on all 72 sextupoles. Only 14 of these skew quadrupoles will initially be cabled and powered, each with its individual power supply. The remaining 58 skew quadrupoles can be powered if further vertical beam size reduction is needed. The 14 skew quadrupoles were chosen to correct the dominant terms driving coupling–the sum and difference resonances–as well as the vertical dispersion.

The difference resonance coupling coefficient, κ, is [1]

$$\kappa = \frac{1}{4}\pi\int ds K_S\sqrt{\beta_x\beta_y}e^{i\phi_D} \tag{15}$$

$$\frac{\phi_D(s)}{2\pi} = (\mu_x(s)-\mu_y(s))-\frac{s}{C}(\nu_x-\nu_y-N) \tag{16}$$

and C is the ring circumference.

For SPEAR 3 ($\nu_x = 14.19$, $\nu_y = 5.23$), the closest difference in resonance occurs when N=9. In general, the random skew-gradient errors in the ring sum up to yield an amplitude and phase for κ. The skew quadrupole correctors should be distributed in ϕ_D so they can be powered to cancel any amplitude and phase effectively. Figure 3.22 plots phasors in the complex planc for

$\sqrt{\beta_x\beta_y}e^{i\phi_D}$ given the 14 skew quadrupole correctors chosen for SPEAR 3. This set of correctors could adjust κ to zero, regardless of phase. The maximum integrated strength of the skew quadrupoles is 0.012 m^{-1} at 3 GeV, which is similar to the maximum skew gradients at other synchrotron light sources. Also, simulations have shown this level to be more than sufficient for correcting the expected coupling error.

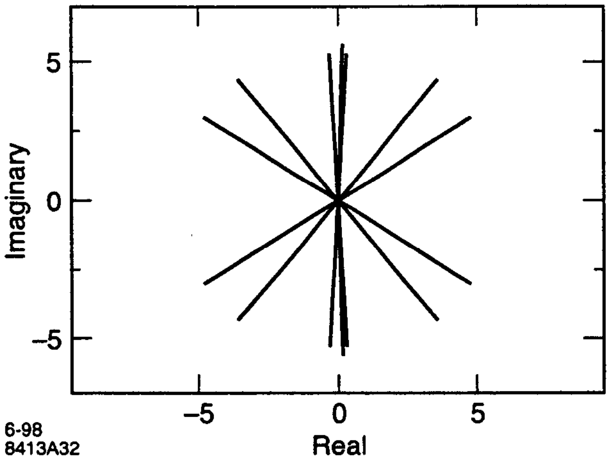

Figure 3.22 Skew quadrupole corrector distribution for difference-resonance correction.

Figure 3.23 shows a plot of phasores for the sum resonance driving term, $\sqrt{\beta_x\beta_y}e^{i\phi_s}$ from the 14 skew quadrupoles, where

$$\frac{\phi_s(s)}{2\pi} = (\mu_x(s) + \mu_y(s)) - \frac{s}{C}(\nu_y - \nu_y - 19) \tag{17}$$

Figure 3.24 shows a plot of phasors for $\eta_x\sqrt{\beta_y}e^{i\phi_{\eta_y}}$, the dominant driving term for η_y,

$$\text{where } \frac{\phi_{\eta y}(s)}{2\pi} = \mu_y(s) - \frac{s}{C}(\nu_y - 5) \tag{18}$$

The phase distribution of the 14 skew quadrupoles is effective for correcting both the sum resonance and the fifth harmonic of η_y.

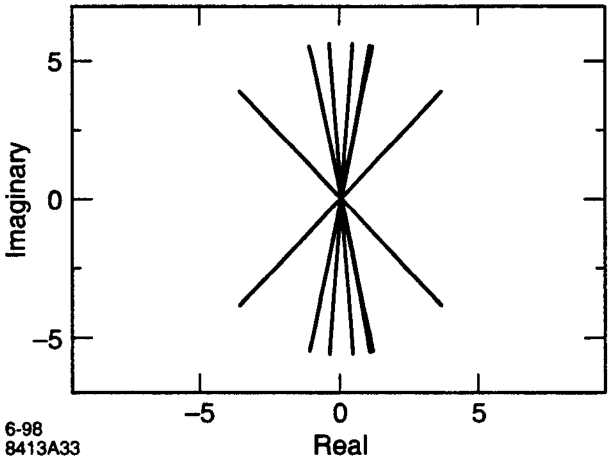

Figure 3.23 Skew quadrupole corrector distribution for sum resonance correction.

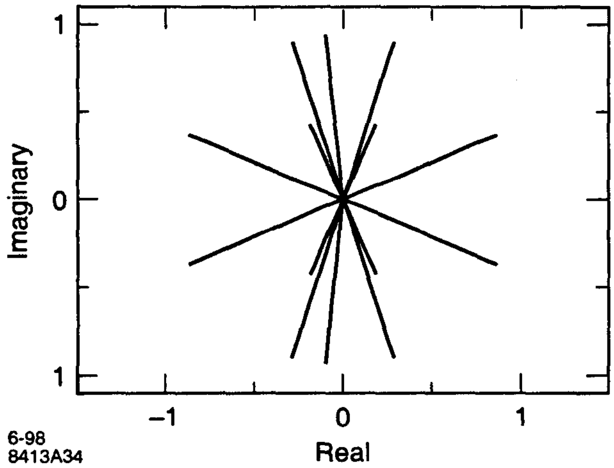

Figure 3.24 Skew quadrupole corrector distribution for η_y correction.

All of the skew quadrupoles will be at locations of non-zero η_x so they will affect both coupling and η_y. Ideally, some skew quadrupoles could be added at locations of zero η_x, so as to separate coupling correction from η_y correction. Simulations with MAD [2], however, have shown that appropriate linear combinations of the skew corrector gradients can be used to correct coupling nearly independent of η_y. Operationally, the coupling correction algorithm developed at NSLS [3] will be used to set the skew quadrupole strengths.

The 14 skew quadrupole power supplies are connected to sextupole numbers 4, 7, 11, 19, 26, 30, 33, 40, 43, 47, 54, 62, 66, and 69, where the sextupoles are numbered from 1 to 72 starting from the center of the West racetrack straight proceeding counter clockwise.

References

[1] G. Guignard, CERN 76-06 (1976).

[2] H. Grote and F.C. Iselin, The MAD Program, Version 8.1, CERN/SL/90-13, June 17, 1991.

[3] J. Safranek and S. Krinsky, Proc. 1993 Particle Accelerator Conf., 1491-1493.

3.1.12 Beam-Stay-Clear

This section discusses beam stay clear (BSC) in the horizontal and vertical planes. Factors used to determine the BSC include first pass injection, injection oscillations, and closed orbit allowance for both the injected and stored beams. The analysis shows that a 30 mm x 15 mm BSC in the arcs is adequate for both injection and stored beam conditions (half width). The actual chamber size in the arcs is 42 mm x 17 mm. In the vertical plane, the ID vacuum chambers for Beamlines 6 and 11 are only 6 mm. In the horizontal plane, the septum magnet is positioned at x = -25 mm, well outside the ~18 mm dynamic aperture.

3.1.12.1 Horizontal Beam-Stay-Clear

To accommodate the magnet layout of the existing injection transport line, SPEAR 3 will utilize a vertical Lambertson septum with inside, horizontal injection. The separation between stored beam and the injected beam is 10 mm, and the horizontal beam size at the BTS terminus is < 1.5 mm (ε_x~200 nm-rad, β_x<5). A schematic of the injection geometry for SPEAR 3 is shown in Section 3.2, Figure 3.30.

As the injected charge traverses the storage ring, it executes up to 17 mm-mrad horizontal betatron oscillations about the closed orbit (Equation 21). The envelope of betatron oscillations, including an energy error 'δ' is given by

$$\sigma(s)_{inj} = \sqrt{\varepsilon_{eff}\beta(s) + \eta(s)^2\delta^2} + x_{COD} \tag{19}$$

where β(s) is the local betatron function, η(s) is the local dispersion, x_{COD} is the closed orbit distortion and the effective horizontal emittance of the injected charge is given by

$$\varepsilon_{eff} = \frac{x^2}{\beta} \tag{20}$$

If a 5 mm horizontal steering error is included,

$$\varepsilon_{eff} = \frac{(10mm + 5mm)^2}{10.2} = 22 \text{ mm-mrad} \tag{21}$$

Based on Equations 19-20, the injected charge envelope is plotted in Figure 3.25 for one quarter of the ring. Including a 10 mm closed orbit distortion, the horizontal envelope of the injected beam is equal to the 25 mm septum radius. Since the injected charge must pass 33 mm to the inside of quadrupole magnets in Girder 15, the horizontal BSC was specified for 40 mm clearance at this girder. With ± 1 mm positional resolution from the first-turn orbit monitors and ± 5 mm closed orbit interlocks to protect the vacuum chamber, the horizontal BSC for the injected beam is conservative.

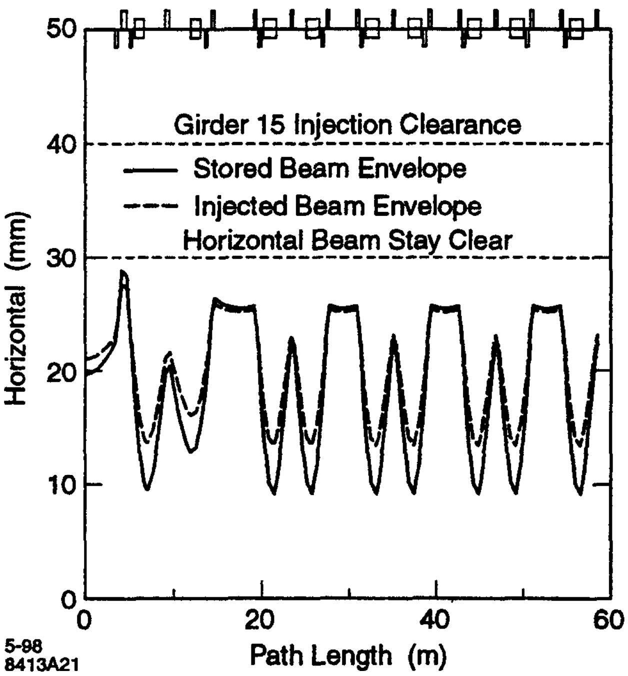

Figure 3.25 Horizontal beam stay clear.

For the stored beam, the limiting horizontal aperture is again the septum (25 mm). Assuming a closed orbit distortion of $x_{COD}= \pm3$ mm leaves 22 mm clearance to the septum, or 47 mm-mrad acceptance (about equal to dynamic acceptance). Using (Equation 19) with ε_{eff}=47 mm-mrad and a closed orbit distortion of x_{COD}= ± 3 mm, the horizontal stored beam envelope is shown in Figure 3.25.

3.1.12.2 Vertical Beam-Stay-Clear

The limiting vertical apertures occur in the ± 6 mm vacuum chambers at Beamlines 6 and 11. Despite these small local restrictions, the vertical BSC within in the arc chambers was specified at ± 15 mm. This decision was based on a compromise between the maximum dipole gap (imposed by magnet engineering constraints) and the need to maintain a large chamber aperture wherever possible. The large vertical aperture also accommodates 'worst case' conditions (β-beats, beam missteering, chamber mis-alignment, gas conductance, and chamber impedance, etc.), leaving a comfortable margin for alternative operational modes in the future.

Assuming 10% emittance-coupling on the injected beam, the effective vertical emittance of the incoming charge is 2.2 mm-mrad ($\varepsilon_y = 0.1\varepsilon_x$). Since the vertical acceptance is limited by beamlines 6 and 11 (A_y=7.7 mm-mrad) the injected charge should accumulate with ease. Application of (Equation 19) to the injected charge with 10% emittance coupling and $y_{COD} = \pm 3.1$ mm leads to the vertical injected beam envelope shown in Figure 3.26. In a worst case scenario involving 35% emittance coupling ($\varepsilon_y = 0.35\varepsilon_x$), 'perfect' steering of the vertical closed orbit is required through Beamlines 6 and 11.

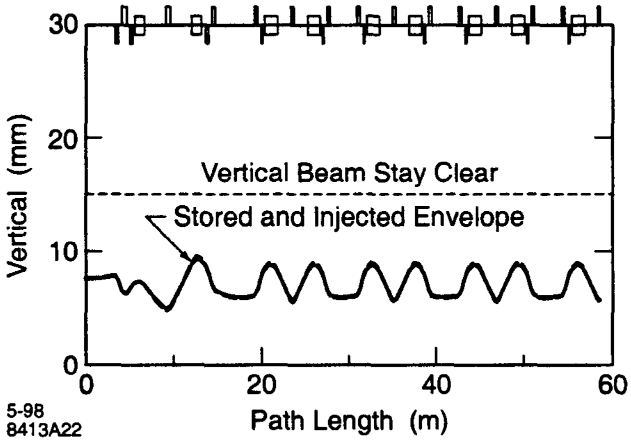

Figure 3.26 Vertical beam stay clear.

For the vertical stored-beam envelope, a closed-orbit distortion of 2 mm was assumed in the ±6 mm beamline vacuum chambers. This leaves 4 mm clearance to the ID chamber walls, or 3.4 mm-mrad vertical acceptance. These specifications (3.4 mm-mrad, $y_{COD} = 2$ mm) yield a vertical stored envelope shown in Figure 3.26 (equalling the injection conditions almost exactly). In practice, the vertical closed orbit displacement will be interlocked at values <1 mm. For 100% coupling on the stored beam, ε_y~9 nm-mrad, and the vertical size of the stored beam in the insertion-device vacuum chambers is σ_y~200 μm. In these units, the fully coupled beam has about 30-σ_y clearance to the vacuum chamber.

3.1.13 Photon Beam Steering Envelope

The intense synchrotron radiation from SPEAR 3 insertion devices (IDs) will be capable of damaging the vacuum chamber for beam currents above 50 mA. The chamber will be passively safe to dipole radiation for stored currents up to the maximum design of 500 mA. Under normal steering conditions all the radiation will hit discrete, water-cooled photon stops. Large closed orbit steering errors, however, could result in ID synchrotron radiation striking the vacuum chamber. To avoid chamber damage, SPEAR 3 will have an interlock system that aborts the beam if a large closed-orbit distortion is detected in the insertion devices at currents above 50 mA.

Thermal analysis of chamber heating due to synchrotron radiation is covered in Section 4.???, and the interlock system hardware is described in Section 4.9.2.4. This section specifies the interlock trip levels and beam steering limits.

3.1.13.1 Insertion Device Vertical Orbit Interlock

Under normal steering conditions, ID radiation exits the vacuum chamber through the 12 mm ante-chamber slot in the dipole downstream of the ID straight section. If the electron beam is vertically mis-steered in an ID, the synchrotron radiation can hit the chamber wall above or below this slot when

$$|y + Ly'| > \frac{g}{2}. \tag{22}$$

Here y and y' are the position and angle of the electron beam at the center of the insertion device, g is the ante-chamber gap, and L = 3.9 m is the distance from the center of the ID to the point where the radiation exits the chamber slot into the antechamber. Allowing ± 1 m for slot alignment tolerance gives g/2 = 5 mm.

The BPMs used in the ID orbit interlock will be on each end of the insertion device straight sections, 1.54 m from center of the ID. An orbit distortion of - 2.0 mm on the upstream BPM and + 2.0 mm on the downstream BPM would satisfy equation (Equation 22). To accommodate BPM offset errors and add tolerance for large vertical beam size, the BPM trip levels will be set to ± 1.0 mm.

3.1.13.2 Vertical Beam Size Interlock

It was found at ESRF that a vertical multibunch instability could spread the vertical fan of synchrotron radiation enough that the edge of the photon distribution hits the vacuum chamber above or below the exit slot. The fraction of the power hitting the chamber was sufficient to damage the chamber. As the closed orbit interlock did not detect the turn-by-turn oscillations, a vertical beam size interlock was developed [2].

In the worst case for SPEAR 3, with the vertical closed orbit steered to just within the closed orbit interlock trip levels and with a multibunch oscillation amplitude large enough to start scraping the ID chamber, nearly 30 percent of the synchrotron radiation could strike above the chamber slot. This power level, however, was deemed acceptable because the power is spread out vertically and such a combination of mis-steering and vertical instability would happen rarely, if ever. SPEAR 3 will therefore not require a vertical beam size interlock.

3.1.13.3 Horizontal Orbit Interlock

The BPMs used in the vertical orbit interlock will be interlocked for horizontal closed orbit distortions of ± 5.0 mm.

3.1.13.4 Beam Steering Limits

Table 3.14 summarizes the beam steering limits in SPEAR 3. Designing to these numbers is conservative because it would not be possible to simultaneously steer to both the maximum angle and position. The rest of this section will outline the derivation of these numbers. Formulae will be given for combinations of position and angle for those cases in which the vacuum chamber design requires less conservative steering limits

Table 3.17 Maximum possible closed orbit mis-steering. h is the half gap of the vacuum chamber at the insertion device, which varies from 5 to 9 mm for existing insertion devices

State	$y_{\max}$ (mm)	$y'_{\max}$ (mrad)	$\chi_{\max}$ (mm)	$\chi'_{\max}$ (mrad)
IDs, (interlocks on)	1.25	0.81	5.25	3.4
IDs, (interlocks off)	h	3.0	42	4.2
Dipole beamline source points	12	16	5.0	18
Dipoles elsewhere	18	6.8	21	19

3.1.13.4.1 ID Beam Steering Limits

Figure 3.27 shows the envelope of maximum y, y' steering in IDs with interlocks on. The mis-steering envelope in x has the same shape, with (x_{max}, x'_{max}) also listed in Table 3.14. The mis-steering in IDs is limited by the trip levels of the orbit interlock. The limits in Table 3.14 apply to vertical trip levels of ±1.0 mm, horizontal trip levels of ±5 mm, 0.25 mm uncertainty in the BPM offsets, and the BPMs ±1.54 m from the center of the insertion device. The 0.25 mm for uncertainty in the BPM offset accounts for 0.05 mm in the accuracy to which the difference of the quadrupole and BPM offsets can be determined with beam-based alignment, plus 0.20 mm quadrupole alignment tolerance. Accurately determining the offsets of the BPMs will be important for the operation of the orbit interlock system. We are also considering steering the photon beam to the top and bottom of the chamber slot (at low current) to further characterize the BPM offsets.

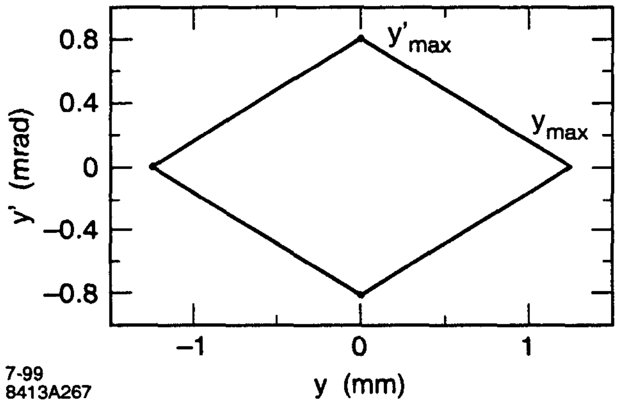

This should be figure 3.27 (A267)

Steering limits in IDs with interlocks on.

At currents below 50 mA, the interlocks may be disabled. In this case, the steering is only limited by the vacuum chamber dimensions and beam dynamics. The vertical steering is limited within the ellipse

$$\frac{y^2}{y_{max}^2} + \frac{y'^2}{y'^2_{max}} \le 1 \text{ and } |y| \le h \qquad (23)$$

$$\text{where}\, y_{\max} = \sqrt{\varepsilon_{y,\mathrm{eff}}\beta_{y,\,\mathrm{ID}}} = 14.2 \qquad (24)$$

$$y_{max} = \sqrt{\frac{\varepsilon_{y,\,eff}}{\beta_{y,\,ID}}} = 3.0\text{mrad} \tag{25}$$

for ε_y = 42 mm-mrad and $\beta_{y,ID}$ = 4.7 mm. Figure 3.28 shows an example of the steering envelope for a chamber half-gap, h of 8 mm and the interlocks disabled.

The maximum emittance of a combined global and local orbit distortion, $\varepsilon_{y,eff}$, is

$$\varepsilon_{y,\,eff} = \left(\sqrt{\varepsilon_{y,\,global}} + \sqrt{\varepsilon_{y,\,local}}\right)^2 . \tag{26}$$

Here, $\varepsilon_{y,global}$ is limited by the typical chamber gap at the insertion devices,

$$\varepsilon_{y,\,\mathrm{eff}} = \frac{h^2}{\beta_{y,\,\mathrm{ID}}} = \frac{(8\mathrm{mm})^2}{5\mathrm{m}} , \tag{27}$$

and $\varepsilon_{y,local}$ is the size of a 3-magnet local bump given the 1 mrad maximum strength of a vertical corrector magnet,

$$_{y,\,local} = \theta^2\beta_{y,\,corrector} = (1mrad)^2(8.6m/rac{=}\ 8.6\text{ mm-mrad.} \tag{28}$$

For the case with interlocks disabled in the horizontal plane, it is not possible to steer the beam all the way out to the chamber wall with a global orbit distortion as the horizontal orbit shift in the sextupoles creates enough tune shift to loose the beam before the chamber is reached. Simulations with MAD indicate that the beam becomes unstable from the vertical tune hitting the half integer when $\varepsilon_{x,global}$ = 89 mm-mrad, or about 33 mm in the β_x=10.2 m straight sections.

The horizontal correctors have a maximum strength of 1.5 mrad, so

$$_{\chi,\,\mathrm{local}} = \theta^2\beta_{\chi,\,\mathrm{corrector}} = (1.5\mathrm{mrad})^2(6.4\mathrm{m/rad}{=}\ 14.4\text{ mm-mrad..} \tag{29}$$

Combining $\varepsilon_{x,global}$ with $\varepsilon_{x,local}$ gives $\varepsilon_{x,eff}$=175 mm-mrad (42 mm at =10.2 m).

For the interlocks off case, the horizontal mis-steering is thus limited by the ellipse

$$\frac{\chi^2}{\chi^2_{max}} + \frac{\chi'^2}{\chi'^2} \le 1 , \tag{30}$$

where
$$\chi_{\mathrm{max}} = \sqrt{\varepsilon_{\chi,\,\mathrm{eff}}\beta_{\chi,\,\mathrm{ID}}} = 42\text{ mm} , \tag{31}$$

$$\chi'_{\mathrm{max}} = \sqrt{\frac{\varepsilon_{\chi,\,\mathrm{eff}}}{\beta_{\chi,\,\mathrm{ID}}}} = 4.2\text{ mrad} , \tag{32}$$

and $\beta_{x,ID}$=10.2 m.

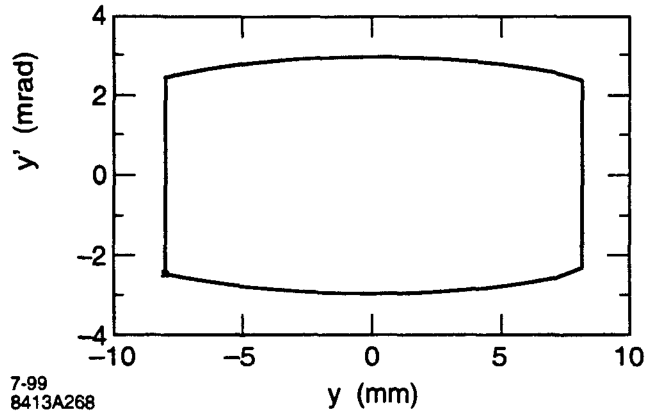

Figure 3.27 Steering limits in IDs with interlocks off and chamber half-gap of 8 mm.

Figure 3.28

3.1.13.4.2 Dipole Beam Steering Limits

Mis-steering in the dipoles is more complicated than in the insertion devices because the optical functions (α, β, and γ) vary significantly with longitudinal position. The values given in Table 3.14 are the maxima that could occur anywhere in the dipole. At most locations in the dipole, the beam has neither the maximum angle nor the maximum position, so designing the vacuum chamber to these specifications is conservative.

More accurate limits can be determined according to the following ellipses constrained by $|y| \le h$:

$$\gamma_\chi \chi^2 + 2\alpha_\chi \chi\chi' + \beta_\chi \chi'^2 \le \varepsilon_{\chi,\mathrm{eff}} \tag{33}$$

$$\gamma_y y^2 + 2\alpha_y y y' + \beta_y y'^2 \le \varepsilon_{y,\mathrm{eff}} \tag{34}$$

where $\varepsilon_{x,\mathrm{eff}} = 175$ mm-mrad, $\varepsilon_{y,\mathrm{eff}} = 42$ mm-mrad, and h = 18 mm is the half-gap of the dipole chamber. Tables 3.15 and 3.16 give the Twiss parameters α and β as a function of position through the two dipoles in each girder, as well as the maximum position and angle steering. Given α and β, γ is calculated from $\gamma = \frac{1+\alpha^2}{\beta}$.

Figure 3.29 shows a plot of the mis-steering envelope ellipse for a position 90% of the way through the first dipole (B2), which is roughly the source point for the dipole beamlines. As an example, for large positive displacements y, the angular deviation y' must be negative, so y and y' tend to cancel each other in terms of the photon beam position.

Table 3.18 Horizontal Twiss parameters and steering limits through the standard girder dipoles.

Fractional Length	β_χ(m)	α_χ	$\chi_{\max}$(mm)	χ'_{max}(mrad)
First dipole†				
0.0	2.540	2.075	21	19
0.2	1.572	1.316	17	17
0.4	0.984	0.727	13	16
0.6	0.713	0.215	11	16
0.8	0.730	-0.273	11	16

Table 3.18 Horizontal Twiss parameters and steering limits through the standard girder dipoles.

Fractional Length	β_χ(m)	α_χ	χ_{max}(mm)	χ'_{max}(mrad)
1.0	1.036	-.215	13	17
Second dipole‡				
0.0	1.036	0.803	13	17
0.2	0.730	0.273	11	16
0.4	0.713	-0.215	11	16
0.6	0.984	-0.727	13	16
0.8	1.572	-1.316	17	17
1.0	2.540	-2.075	21	19

†. The first dipole (B2) is the dipole downstream of an ID straight.

‡. The second dipole (B1) is upstream of an ID straight.

Table 3.19 Vertical Twiss parameters and steering limits through the standard girder dipoles.

Fractional Length	β_y(m)	α_y	y_{max}(mm)	y'_{max}(mrad)
First dipole				
0.0	13.567	-3.283	18	6.0
0.2	15.039	-1.901	18	3.6
0.4	15.734	-0.468	18	1.8
0.6	15.573	1.015	18	2.3
0.8	14.576	2.387	18	4.4
1.0	12.852	3.647	18	6.8
Second dipole				
0.0	12.852	-3.647	18	6.8
0.2	14.576	-2.387	18	4.4
0.4	15.573	-1.015	18	2.3
0.6	15.734	0.468	18	1.8
0.8	15.039	1.901	18	3.6
1.0	13.567	3.283	18	6.0

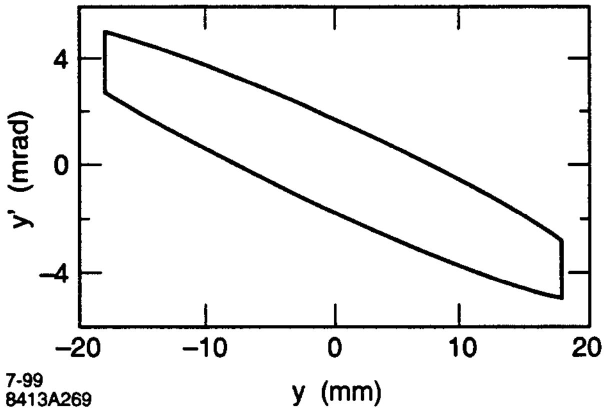

Figure 3.29 Vertical steering limit at dipole source.

References

[1] H. Grote and F.C. Iselin, The MAD Program, Version 8.1, CERN/SL/90-13, (1991).

[2] L. Farvacque and A. Ropert, ESRF Strategy for the Protection of the Vacuum Chamber, ESRF-SR/LAT-92-36, (1992).

[3] G.K. Green, Spectra and Optics of Synchrotron Radiation, BNL 50522, (1976).

3.1.14 Lattice Commissioning

Experience with SPEAR 2 has shown that following a complete re-alignment of the storage ring, the interval between electron-beam availability at the injection septum to photon-beam delivery is of order 2-3 weeks. During this time, 1) injection rates are optimized, 2) the global orbit is corrected, 3) photon beamlines are steered, 4) the orbit feedback is commissioned, and 5) initial vacuum chamber conditioning takes place. The commissioning of SPEAR 3 should proceed quickly, since we will re-use the existing LINAC, Booster Synchrotron, and BTS, as well as much of the control system, but time must be allocated to re-commission the photon beamlines. The anticipated time to fully commission SPEAR 3 and deliver the beam to users is on the order of 4-6 months.

Before delivering the beam to SPEAR 3, power supply checkouts, magnet polarity checks, vacuum checkouts, PPS & MPS checkouts, and radiation safety authorization will be finalized. During this check-out period, the LINAC will be re-commissioned, the Booster will be tuned for 3.0 GeV operation, and the beam will be steered down the BTS. Although on-energy injection will reduce the start-up schedule (less time required to develop ramp configurations), the new 3.0 GeV injection septum and kicker systems will need to be commissioned. One of several major technical complications involves the activation of the orbit interlock system, but parts of this system may be commissioned on SPEAR 2.

The commissioning procedure for SPEAR 3 will follow the same basic set of procedures used for SPEAR 2:

i. Tune LINAC
ii. Tune Booster
iii. Deliver beam through BTS to SPEAR septum
iv. Achieve first turns, store beam with RF
v. Coarse steer electron-beam
vi. Calibrate BPMs with quadrupole shunts
vii. Coarse steer photon beams
viii. Calibrate storage ring optics
ix. Fine-steer photon beams
x. Commission orbit interlock and feedback systems

The immediate goal of the commissioning period will be to deliver photon beams to users. Once the electron beam becomes available, the beamline shutters will open to facilitate photon beam steering, vacuum conditioning of the beamline components, and beamline checkouts. As system checkouts and vacuum conditioning proceed, the current will increase. Once appropriate vacuum levels are achieved, SPEAR 3 will progress from 3 fills/day to 2 fills/day to 1 fill/day. The exact schedule depends upon the outcome of negotiations with the user community. We anticipate several hundred A-hr will be sufficient to condition the vacuum chamber for 1 fill/day operations. Accelerator physics and fine lattice tuning will continue on the nominal 24 hr/week schedule.

3.1.15 Lattice Tuning

In recent years, SSRL has used an optics calibration algorithm based on fitting lattice parameters to response matrix measurements [1-3]. This method helps to identify sources of optical mis-match in the storage ring. To facilitate lattice tuning, the QF and QD quadrupole magnets have individual power supplies. Other approaches to lattice calibration include the 1) use of the orbit analysis program RESOLVE and 2) model fitting to β-function measurements obtained from quadrupole modulation data [4].

Since $d\beta/ds = 0$ at the ends of the matching cells, small tune adjustments can be performed with uniform adjustment of the QF/QD quadrupoles with minimum residual β-beats throughout the storage ring. Larger tune adjustments require that the optics be re-matched through the racetrack straights with quadrupoles in the matching cells. In practice, an eight quadrupole 'multiknob' can be used to adjust the tunes and maintain the match. As demonstrated in Section 3.1.7, the dynamic aperture remains constant for a range of tunes in the working diagram. Other quadrants of the working diagram are also accessible.

The main SF and SD sextupoles in the standard arc cells will be used to control correct chromaticity. Fine chromaticity adjustments can also be made using the matching cell sextupoles SFI, SDI.

References

[1] J. Safranek, NIM in Physics Research, Section A, 388, pp. 27-36 (1997).

[2] D. Robin, et al, Proc. 1996 EPAC, Barcelona, Spain (1996).

[3] J. Corbett, et al, Particle Accelerators, Vol. 58, pp. 193-200 (1997).

[4] W.J. Corbett, R.O. Hettel and H.-D. Nuhn, 1996 Beam Instrumentation Workshop, (1996).

3.2 Injection

The injection system will retain the present configuration with inside horizontal injection from the Booster Synchrotron. In this configuration, the beam travels along the Booster-to-SPEAR (BTS) transfer line and is deflected 8.79° vertically through a Lambertson septum into the horizontal plane of the storage ring. As Figure 3.30 demonstrates, a combination of static- and pulsed-beam bumps will move the stored beam 22 mm toward the septum.

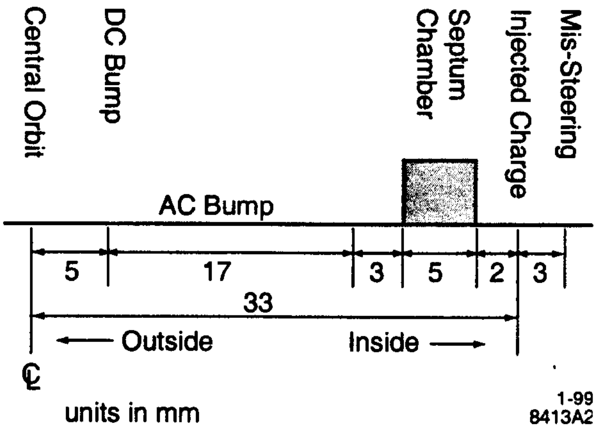

Figure 3.30 Schematic of SPEAR 3 injection geometry.

Figure 3.31 shows the initial trajectory of the injected beam as it passes through the septum magnet and Girder 15 to the third fast-kicker magnet, *K*3. The stored beam is also shown as it traverses the 22 mm injection bump. In this figure, a 3 mm steering error was included to illustrate the trajectory of the incoming beam with a 36 mm displacement from the central stored beam orbit.

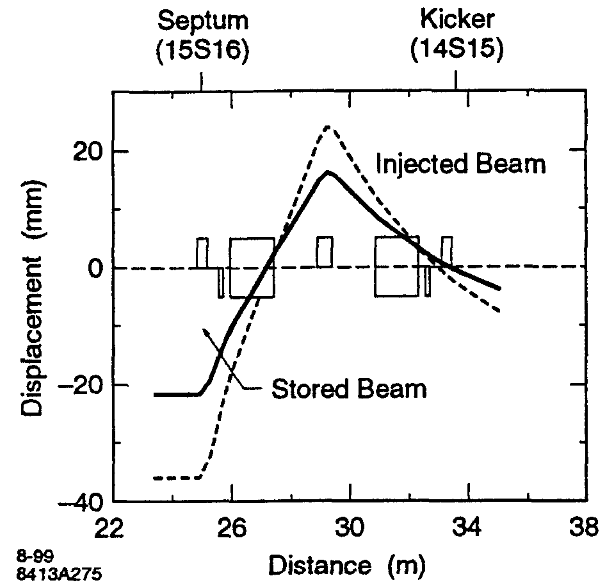

Figure 3.31 Injected and stored beam trajectories through Girder 15.

3.2.1 Beam Transfer Line

The existing BTS will be modified to:

- transport a 3 GeV beam
- move the new septum to a radius of 25 mm with respect to the stored beam
- optically match the Booster beam to SPEAR 3 at the septum

A schematic drawing of the BTS line after modifications is shown in Figure 3.32. To inject at 3 GeV, the existing injection septum will be replaced, and one of the dipoles at the end of the BTS will be relocated so that the injected beam is -32 mm from the nominal stored-beam orbit in the horizontal plane. BTS magnet B8V creates a vertical bend with the same deflection angle as the septum (8.792 degrees).

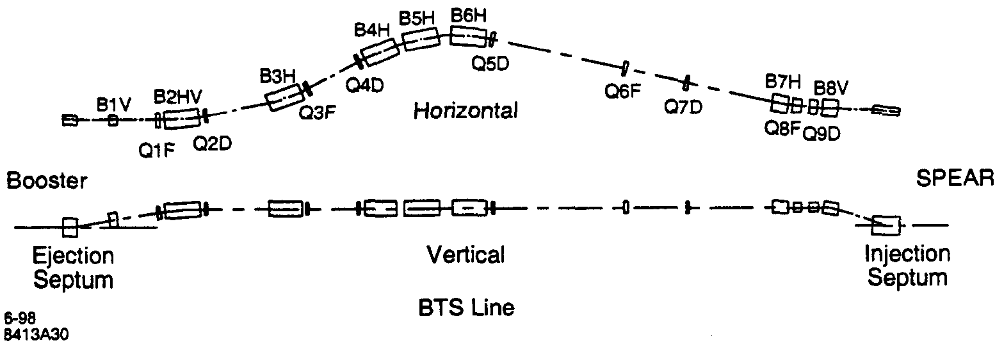

Figure 3.32 Schematic of the BTS transfer line.

As Figure 3.33 shows, the BTS contains a total of nine quadrupoles, four horizontally focusing and five vertically focusing. This configuration facilitates good control over the Twiss parameters in each plane (α, β, η, η'). A plot of the electron beam optics appears in Figure 3.34. Note that at the end of the BTS, β_x is optimized to maintain a small horizontal beam size along the length of the injection septum. Table 3.20 lists the beam parameters at the ejection septum of the booster, at the end of the BTS, and for the stored beam in SPEAR 3. Table 3.20 lists the BTS quadrupole strengths. These strengths can easily be achieved with the existing power supplies.

Table 3.20 Injection beam parameters

LOCATION	β_x [m]	α_x [rad]	η_x [m]	η'_x [m]	β_y [m]	α_y [rad]	η_y [m]	η'_y [rad]
Booster Ejection Septum	8.34	2.3	0.3	-0.02	3.4	-1.0	0.0	0.0
End of BTS	1.8	0.0	0.0	0.0	4.7	-0.1	0.0	0.0
SPEAR 3 Injection Septum	10.2	-0.06	0.0	0.0	4.7	-0.1	0.0	0.0

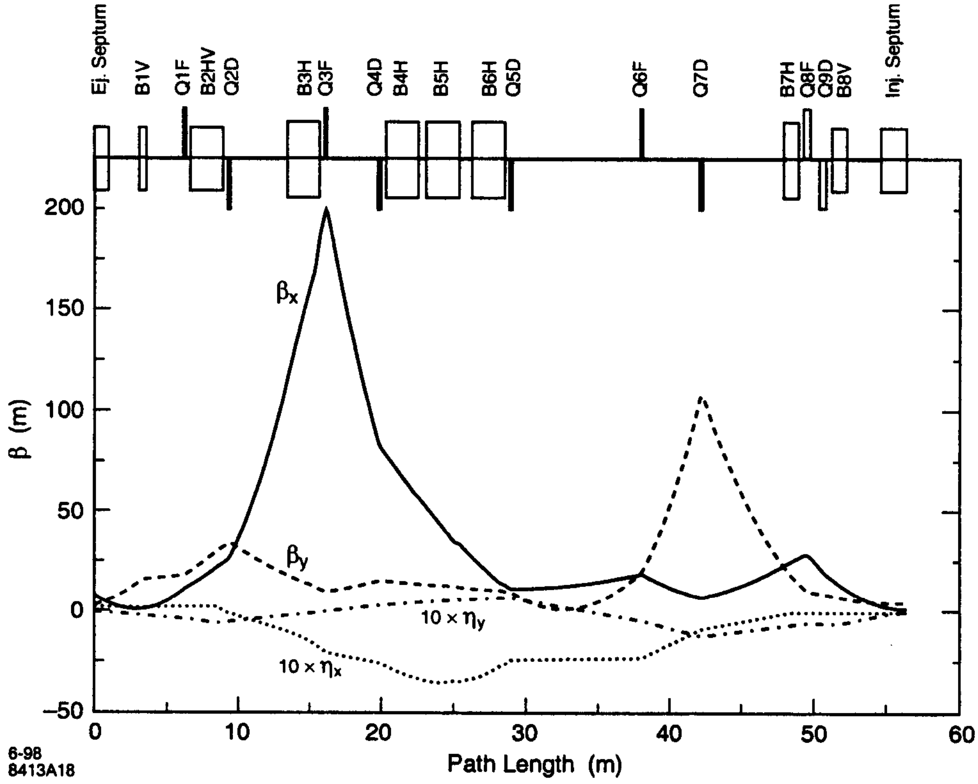

Figure 3.33 Booster-to SPEAR transport line optics.

Table 3.21 BTS quadrupole strengths

Quadrupole	Strength [m^{-2}]	Maximum Strength [m^{-2}]
BTSQ1F	+0.4580	1.700
BTSQ2-D	–0.7249	1.700
BTSQ3F	+0.8631	1.700
BTSQ4D	–0.4133	1.700
BTSQ5D	–0.9781	1.700

Table 3.21 BTS quadrupole strengths

BTSQ6F	+0.6960	1.700
BTSQ7D	-1.1119	1.700
BTSQ8F	+0.3777	0.776
BTSQ9D	-0.0158	0.776

3.2.2 Injection Bumps

Figure 3.34 shows a schematic of the injection system components in SPEAR 3. Three pulsed kickers (*K1*, *K2*, *K3*) create a 17 mm horizontal bump at the septum. By utilizing the compact, low impedance kicker design developed for DELTA [???], K2 can be placed in the 3.1 m septum straight section. This arrangement constrains the fast-kicker bump to the cells on either side of straight section 15S16. Since the horizontal phase advance per cell is nearly 3π/2, the *K2* kicker deflection is about half the value of *K1* and *K3*. The kickers will operate at 10 Hz with a half sinusoidal waveform having a base of ~750 ns. The timing system allows arbitrary bunch pattern selection.

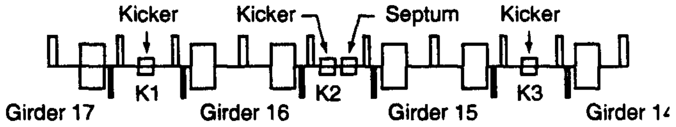

6-98
8413A27

Figure 3.34 Injection elements in SPEAR 3.

The static bump will be created using the four horizontal corrector magnets closest to the septum. Properly configured, the static bump facilitates control at the septum over the position and angle of the stored beam trajectory. The angle of the static bump will compensate the angle from the fast bump to make the injected and stored beams parallel. The static, fast, and total stored beam deflections are shown in Figure 3.35. The deflection angles of the kicks needed to create the injection bumps are listed in Table 3.21.

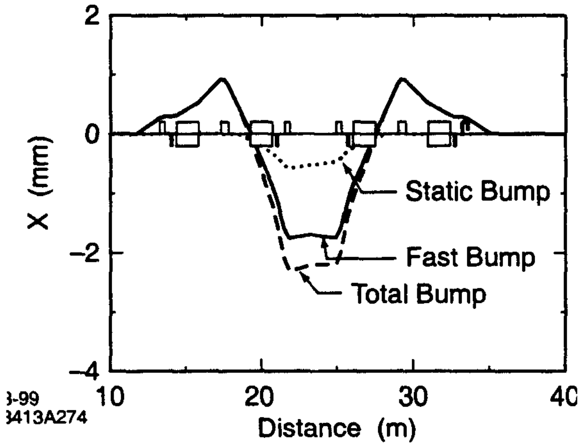

-99
413A274

Figure 3.35 Injection bumps.

Table 3.22 Deflection angles for injection components (3.0 GeV)

	Static Bump Elements	Fast Bump Elements

Table 3.22 Deflection angles for injection components (3.0 GeV)

Magnet	HCOR1	HCOR2	HCOR3	HCOR4	K1	K2	K3
Strength [mrad]	–1.14	–0.05	–1.18	–1.12	1.7	–0.75	1.7

3.2.3 Injection Analysis

As the injected beam enters SPEAR 3, it will pass through the upstream QF quadrupole on Girder 15 at a radial position of about -32 mm (Figure 3.35). A simulation of the stored and injected beams during the injection process is shown in Figure 3.36. In this Figure, the large ellipses represent the acceptance of the stored beam prior to and during the pulsed injection bump The injected beam ellipse is shown following the first five turns as it oscillates about the stored beam.

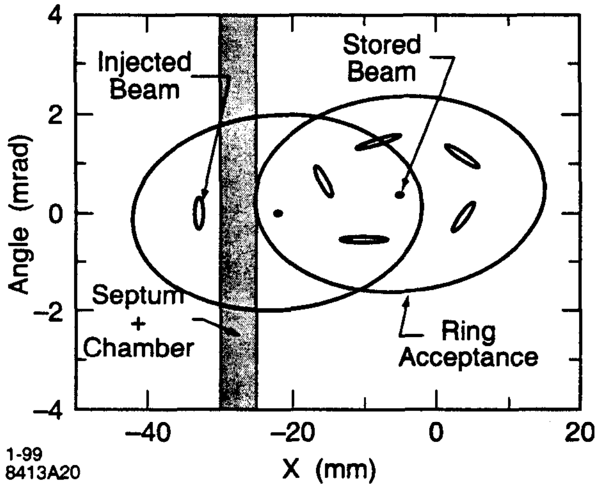

Figure 3.36 Phase space plot for stored and injected beams at septum.

In practice, the particular RF bucket being filled will traverse a locally closed bump, while other bunches will see a slightly unbalanced bump as a function of bump amplitude due to the non-linearity of the sextupole fields. Figure 3.37 shows an example of the deflection amplitude and residual oscillations for the stored bunches that experience the unbalanced bumps. This plot was made by tracking each of ten equally-spaced bunches as the pulsed kickers rise and fall through ten consecutive turns. The envelope of the residual oscillations is less than ±1 mm. Although the main bunch and injected charge will coalesce on the order of a damping time (4.2 ms), care must be taken if a wideband transverse feedback is active.

With the booster delivering about 5×10^9 e^-/sec, we anticipate injection rates comparable to the rates observed in SPEAR 2, i.e. a maximum injection rate of 50 mA/min. The capture rate is expected to improve with increased control of the BTS optics and the tuning of the injection system in SPEAR 3.

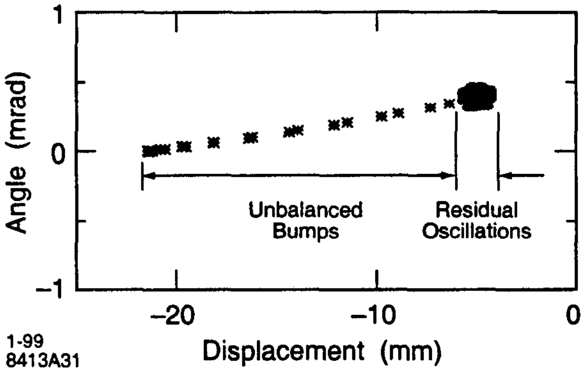

Figure 3.37 Deflection and residual oscillations of stored beam after the injection kicker pulse.

3.3 Beam Stability Requirements

The goal for transverse electron beam stability is 10% of the photon beam size and divergence at the beamline source points. Strictly speaking, 10% stability requires holding the beam position to 30-40 µm rms in the horizontal plane and 3 µm rms in the vertical plane at insertion device locations. On very long time scales (many hours or days), a positional stability of 3 µm will be difficult to achieve. In practice, the vertical position criterion can be relaxed to 5 µm since 1:1 focusing mirrors can not faithfully reproduce a 30 µm rms spot size. Future beamlines with improved focusing optics may require 3 µm rms vertical orbit stability.

The transverse stability goals will be achieved by suppressing sources of orbit motion, minimizing transverse impedance in the vacuum chamber and RF cavities andd by using feedback systems to stabilize the beam orbit (Section 4.7.1). In some cases, the photon beam will be further stabilized with feedback operating on optical components in the beamlines and/or on sample positioners.

The longitudinal phase stability requirement is on the order of 0.4° of the 476 MHz RF waveform. This requirement limits horizontal bunch motion caused by synchrotron oscillations to 10% of the beam size and reduces harmonic line-broadening in undulators. The 0.4° phase-stability requirement can also be met by minimizing vacuum chamber impedance, avoiding HOM cavity resonances,and using Mode Zero longitudinal feedback (Section 4.7.2).

3.3.1 Transverse Stability Requirements

The photon beam size for a particular beamline can be defined by the extended electron beam as viewed by the beamline optics; for optical configurations with a short depth-of-field, it equals the electron beam size. For focused beam experiments, transverse stability is determined by the motion of the electron beam at the source point. For unfocused experiments, stability is determined by the angular motion of the electron beam at the source point.

The divergence of the photon beam produced by a single electron is characterized by $1/\gamma$ for dipole and wiggler source points, and by $1/\gamma N$ for undulators, where N is the number of undulator periods. To determine the net photon beam divergence at a source point, the natural photon divergence is convolved with the electron beam divergence (Section 3.1.6). The horizontal photon beam divergence for dipole and wiggler sources is dominated by the angle of the orbit arc at the source (typically many milliradians).

The most stringent angular stability requirement occurs for undulator beamlines where diffraction effects are small. At these locations, angular stability is required to maintain the monochromator energy constant to a fraction of the 10^{-4} pass band through the diffractive crystals. For example, the change in transmitted photon energy E_{ph} from crystals with a Bragg angle θ_B due to a change $\Delta\theta_i$ in incident beam angle is given by

$$\frac{\Delta E}{E_{ph}} = \frac{\Delta\theta i}{\theta_B} \tag{35}$$

For most crystals, θ_B varies between 5° and 45°· For more sensitive cases when $\theta_B = 5°$, a 10 μrad change in incident angle causes a relative energy shift $\Delta E_{ph}/E_{ph} = 3.7 \times 10^{-5}$. A 14 μrad angular stability requirement for unfocused photon beams is therefore sufficient for photon-beam energy stability after a monochromator.

Table 3.22 summarizes the electron and photon beam properties and transverse stability requirements at the SPEAR 3 source points. For this Table, the stability requirement for vertically focused ID beams can be relaxed to 5 μm rms.

Transverse position stability is also important for steady flux transmission through aperture defining slits in front of samples. Intensity noise will affect experiments that sample or average data over periods shorter than the noise periods. For experiments that average longer than the noise period, the noise appears as an effective increase in beam size. This reduces the average intensity, but not the sample-to-sample stability. As shown in Figure 3.38, the variation in flux transmission is a strong function of transverse motion of a Gaussian beam, having rms size σ, across a small aperture. This figure shows that 0.1% flux stability, sufficient for sensitive experiments, is achieved for a 2-σ half-height aperture by limiting beam motion to 0.1 σ. Smaller apertures can require 0.05-σ stability.

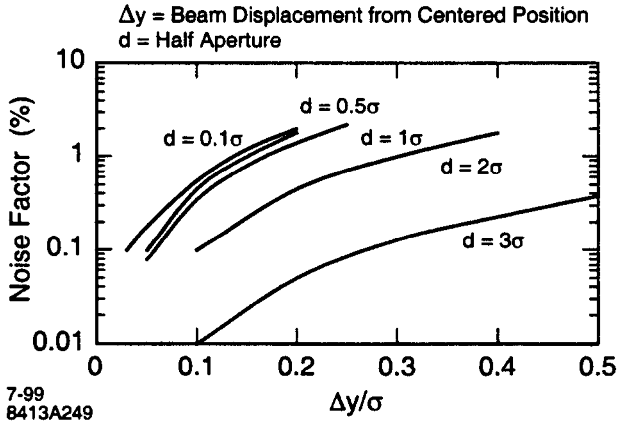

7-99
8413A249

Figure 3.38 Intensity noise as a function of off-center displacement of a photon beam having rms size in various sized apertures.

Table 3.23 RMS source point beam dimensions and stability requirements for SPEAR 3 (rms, 1% coupling).

		Electron	Photon	10%
Dipole	σ_x (μm)	160	160	16
	$\sigma_{x'}$ (μrad)	236	mrads	< mrad
	σ_y (μm)	51	51	5
	$\sigma_{y'}$ (μrad)	11	136	14
ID-Wiggler	σ_x (μm)	435	435	43
	$\sigma_{x'}$ (μrad)	43	2–20 mrad	< mrad
	σ_y (μm)	30	30	3†
	$\sigma_{y'}$ (μrad)	6	136	14
ID-100 per und.	σ_x (μm)	435	435	43
	$\sigma_{x'}$ (μrad)	43	43	4
	σ_y (μm)	30	30	3
	$\sigma_{y'}$ (μrad)	6	15	1.5

†. This requirement can be relaxed to 5 μm due to 50 μm minimum vertical spot size achieved from present focusing mirrors.

3.3.2 Longitudinal Stability

Coherent energy oscillations can cause horizontal beam motion at points with finite dispersion, diminish (and broaden) spectral peaks from undulators, and introduce variations in bunch arrival time during timing experiments. In SPEAR 3, energy oscillations occur at the ~10 kHz synchrotron frequency. Most beamline experiments acquire and average data over many synchrotron oscillation periods, so the oscillations only increase effective transverse beam size where the dispersion is non-zero. Some experiments, however, acquire data on short time scales. In this case, synchrotron oscillations of amplitude ΔE are seen as shot-to-shot jitter with transverse displacement $\eta\Delta E/E$.

From the dependence of beam size, divergence, and orbit position on energy in regions of finite dispersion the following effects can occur:

- An rms energy oscillation of amplitude ~0.1% can produce an effective 10% increase in horizontal beam size and divergence (20% emittance growth) at dipole source points (η = 0.1 m). This effective emittance growth will be observed in experiments that average data over periods longer than a synchrotron oscillation period.
- A coherent energy shift of ~0.016% produces a shift of horizontal beam position and angle equal to 10% of the beam size and divergence, respectively, at dipole source points. This motion may affect experiments that sample or average data over periods shorter than the energy fluctuation period.
- Vertical dispersion is typically non-zero, even after careful orbit correction. For example, for a 1% emittance coupling and a vertical dispersion of 0.02 m, a 0.1% electron energy spread increases the vertical beam size from 30 μm to 36 μm rms for insertion devices or from 50 μm to 54 μm rms in dipole magnets. A 0.016% coherent energy shift would move the vertical beam position by 3 μm, or 10% of the vertical beam size for this dispersion. A horizontal dispersion error of ~0.05 m does not significantly degrade horizontal beam size or stability for insertion device or dipole sources.

Another constraint on energy stability is imposed by undulator radiation properties. In this case, the wavelength of each undulator harmonic is proportional to $1/E^2$, where E is the beam energy. The relative change in photon wavelength caused by a change in beam energy ΔE is therefore

$$\frac{\Delta\lambda}{\lambda} = -\gamma \frac{\Delta E}{E} \tag{36}$$

The theoretical harmonic-line width is given by $\frac{1}{nN}\ (\frac{\Delta E}{E} = 0)$, where N is the number of undulator periods, and n is the harmonic number. The ideal line width of the 5th harmonic of a 100-period undulator (0.2%), for instance, is comparable to that caused by the 0.1% energy spread in the beam. To maintain a photon beam energy stability of 10^{-4} at the 5th harmonic, the coherent electron beam energy must be stable to 0.02%. By contrast, the coherent electron-beam energy stability required to maintain 10^{-4} energy stability at the fundamental is only ~0.1%. In the interest of exploiting higher harmonics, and to maintain position stability at dipole source points, coherent energy oscillations should be limited to the order of 0.02%.

To relate the energy stability to stability of longitudinal phase oscillations, $\Delta\phi$, we have

$$\Delta\phi(\mathrm{rad}) = \frac{h\alpha_c \Delta E}{\nu_s\ \ E} \cong 50 \frac{\Delta E}{E} \tag{37}$$

where $\alpha_c = 0.0011$ (momentum compaction), $h = 372$ (harmonic number), and $\nu_s = 0.008$ (synchrotron tune). In SPEAR 3, the longitudinal phase oscillations must therefore be limited to

$$\Delta\phi < 0.5° \text{ for } \frac{\Delta E}{E} < 0.016\%. \tag{38}$$

3.3.3 Beam Stabilization Plan

The electron beam will be subject to low frequency (< 1 kHz) closed orbit fluctuations and higher-frequency longitudinal and transverse-bunch motion (Sections 3.6 and 3.7). The source of disturbances will be minimized as much as possible through careful design of the storage ring components.

To further control beam motion, an orbit feedback system (Section 4.7.1) will be employed to reduce low-frequency orbit motion to the levels shown in Table 3.22. Mirror-angle feedback systems will also be used on focused beamlines to stabilize photon beam motion.

Mode-damped PEP-II style cavities with temperature control to < 0.5 °C will be used to minimize impedance (Section 4.7.2). HOM's in the waveguides will be damped by coupling into absorbing loads. A zero-mode RF feedback system will reduce the common mode longitudinal bunch oscillation (Section 4.7.2). With these measures, an estimated longitudinal stability of <0.4° rms or better is possible without a longitudinal multibunch feedback system. A transverse multibunch feedback system (Appendix A-4) could be needed in the future to control effective emittance growth at high currents.

3.4 Orbit Control

Successful operation of a synchrotron light source depends critically on electron beam stability. In practice, the beam must first be accurately steered through the center of the magnets to minimize non-linear optical distortions. A well-steered beam reduces coupling, emittance growth, and potential loss of dynamic aperture. The beam must also be dynamically stable to minimize fluctuations in photon beam position and intensity at the experimental stations. To address these issues, SPEAR 3 will be equipped with an orbit steering system and a digital orbit feedback control system based on electron and photon beam-position monitors (Section 4.7.1). Steering magnets mounted over CuproNickel® inserts in the copper vacuum chamber will provide wide-bandwidth actuators.

Section 3.3 summarized the overall stability plan for SPEAR 3. In this section, we discuss sources of orbit motion in greater detail and review the beam steering and Orbit Feedback systems. These systems will utilize 92 electron BPMs, 11 (or more) photon beam BPMs, and up to 54 correctors in each plane. RF frequency control will correct for energy drift. The goal of the orbit feedback system is to stabilize the electron beam over a frequency range extending to 100 Hz to within the tolerances indicated by Table 3.23.

Table 3.24 Beam stability at the BPMs necessary to meet requirements specified in Table 3.15

BPM	Horizontal Stability (μm, rms)	Vertical Stability (μm, rms)
Straight Section	< 40	< 5
Mid-Girder	< 35	< 5
Dipole	< 13	< 5

3.4.1 Sources of Orbit Distortion and Motion

In the ideal case, the electron beam position remains constant at the photon beam source points. In practice, however, many effects can cause the beam to move at the radiation source points, so a certain amount of motion is inevitable. Positional or angular photon beam motion on time scales longer than data integration times causes sample-to-sample data noise and degrades resolution. Motion on time scales shorter than the data integration time appears as an effective emittance blow-up. If the beam has a transverse dimension of σ_0, for instance, and the rms amplitude of the beam vibration is $<x_{vib}>$, the effective beam width is

$$\sigma_{eff} = \sqrt{\sigma_0^2 + <x_{vib}>^2} \tag{39}$$

On slow time scales, the tunnel temperature and the radiation-power load can cause motion among the magnets and/or BPMs. In order of increasing frequency, 1) ground vibrations take place on 1-50 Hz time scales, 2) power supplies induce beam motion at 60 Hz, harmonics thereof (or at chopper frequencies), and 3) at still higher frequencies, in the 250 kHz range, betatron motion is possible. Finally, waves in the GHz range drive single- or multi-bunch motion. All of these sources can produce noisy or reduced resolution data.

This section reviews the dominant sources of orbit perturbation, including the effects of 1) magnet mis-alignment, 2) girder motion, 3) uniform temperature excursions in the tunnel, and 4) power supply ripple. The discussion shows that 1) static-magnet alignment errors require only moderate closed-orbit correction, 2) low-frequency girder motion produces a tolerable amount of beam motion, and 3) uniform, temperature-induced motion of the storage ring can be corrected by RF frequency feedback.

3.4.1.1 Magnet Alignment

For any storage ring, magnet alignment does not remain constant over time; due to long-term ground motion, building motion, and unintentional magnet shifts during maintenance periods, the alignment slowly changes. These slow changes can be compensated through periodic re-alignment. Nevertheless, alignment can drift during extended operational periods.

Table 3.25 RMS magnet-alignment tolerance and dipole-field errors.

σ_x (μm)	σ_y (μm)	σ_ψ(μrad)	ΔB/B (%, rms)
200	200	500	0.1

To study the effects of magnet misalignments, errors were randomly distributed around the SPEAR 3 lattice (Table 3.25), and statistics were compiled for the closed-orbit perturbations. Examples of closed orbits, and their associated orbit angles appear in Figures 3.39, 3.40, 3.41, and 3.42.

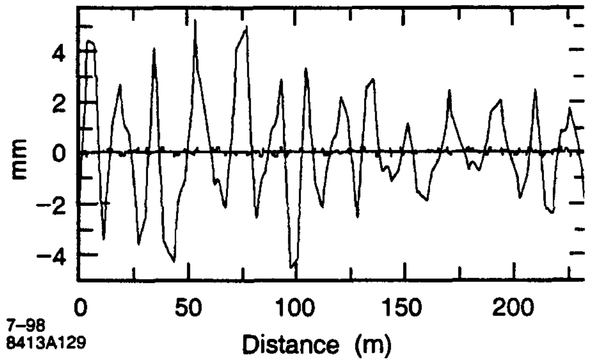

Figure 3.39 Horizontal closed orbit due to random magnet errors.

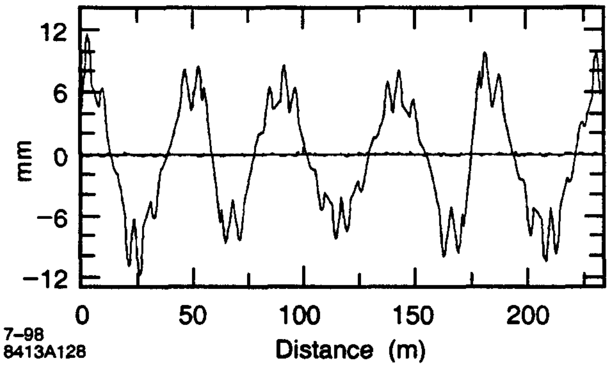

Figure 3.40 Vertical closed orbit due to random magnet errors.

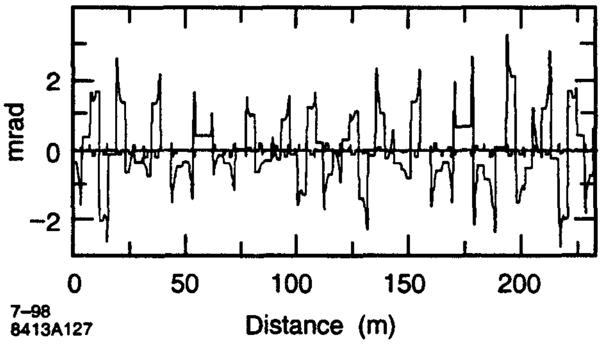

Figure 3.41 Horizontal angle error due to random magnet errors.

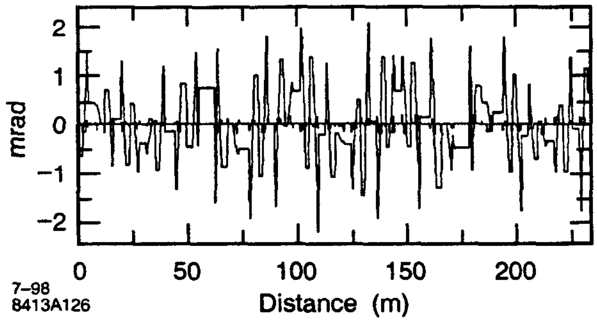

Figure 3.42 Vertical angle error due to random magnet errors.

To accumulate statistics, the rms closed orbit was calculated for 10,000 random seeds in the horizontal and vertical planes. The resulting distributions appear in Figure 3.43 and 3.45. In the horizontal plane, the rms orbit remains below 4 mm. Single orbits can have local displacements of up to 10 mm, but this falls well within the horizontal beam-stay-clear, and is easily controlled with orbit correction software. In the vertical plane, the rms orbit distortions display the same order of magnitude.

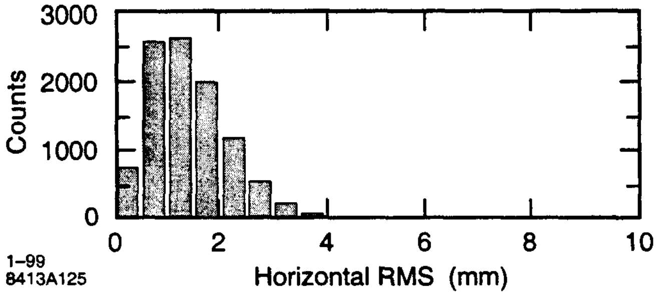

Figure 3.43 RMS horizontal closed orbit for 10,000 randomly aligned machines.

These simulations demonstrate the feasibility of storing a beam with little (or no) orbit correction, which will be an important advantage during the initial commissioning phase. Note that by scaling down 200 μm *static* alignment errors to 200 nm *dynamic* vibration errors reduces the closed orbit distortions to the order of 4 μm. Since the magnet motions are coupled to the girder and highly correlated, the resulting closed-orbit motion will be considerably less than 4 μm.

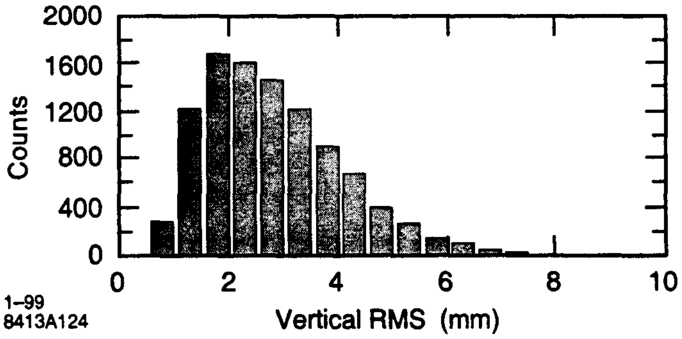

Figure 3.44 RMS vertical closed orbit for 10,000 randomly aligned machines.

The effect of alignment errors can also be estimated analytically. A distribution of quadrupoles with strength *K*, length L, and standard of deviation alignment errors σ_u has an expectation value for the orbit distortion $u_0(s)$ [4]:

$$\langle u_0(s)\rangle^{1/2} = \beta(s)^{1/2} A\sigma_u \tag{40}$$

where β(s) is evaluated at the observation point and A is an amplification factor defined by

$$A^2 = \frac{N\langle K^2 L^2 \beta_k\rangle}{8\sin^2\pi\nu} . \tag{41}$$

Here, N is the number of number of magnets in the quadrupole family, and β_k is the β-function in the quadrupoles. Table 3.26 gives the amplification factors for random misalignments of each quadrupole family.

Table 3.26 Amplification factors for dipole and quadrupole misalignments with β-functions evaluated in the center of each magnet.

Magnet	N	KL (m^{-1})	β_x (m)	A_x	β_y (m)	A_y
Full Bend	28	0.48	1.3	1.8	13.2	4.9
3/4-Bend #1	4	0.36	1.7	0.6	16.5	1.6
3/4-Bend #2	4	0.36	4.2	0.75	8.5	1.1
QF	28	0.62	9.9	6.5	5.7	4.2
QD	28	0.24	4.2	1.6	11.4	2.3
QFC	14	0.90	7.7	5.8	4.0	3.6
QDX	4	0.47	8.1	1.7	10.9	1.6
QFX	4	0.92	15.0	4.5	5.4	2.3
QDY	4	0.15	7.5	0.5	7.64	0.4
QFY	4	0.66	6.4	2.1	2.4	1.1
QDZ	4	0.27	5.2	0.75	14.0	1.1
QFZ	4	0.48	10.6	2.0	7.1	1.4

Table 3.27 lists the expectation values for orbit motion at the dipole and ID source points corresponding to a random magnet misalignment of σ_u=200 μm

Table 3.27 Expectation values at the dipole and ID source points for all magnets displaced with standard of deviation σ_u=200 μm.

Source Point	β_x (m)	β_y (m)	$<x^2>^{1/2}$ (mm)	$<y^2>^{1/2}$ (mm)
Dipole	0.80	14.05	2.9	5.28
Insertion Device	10.11	4.84	6.7	3.04

3.4.1.2 Girder Vibration

The magnet girders and associated magnet supports can vibrate in different modes. Since 1-50 Hz mechanical vibration frequencies are slow compared to the radiation damping times, the orbit tends to track magnet motion, and orbit perturbations can be calculated as in the static case.

As discussed in Section 4.1.9 , the existing magnet girders are buttressed at three support points, allowing the some vibration modes of the steel girders. The actual motion of a girder is a superposition of the modes. The magnet motions on a particular girder for a specific mode are correlated, but since the vibration modes are slightly different for each girder, the effects on closed orbit from the ensemble of girders are uncorrelated and can be investigated statistically. Where correlations may occur, the $\phi_x=3\pi/2$, $\phi_y=\pi/2$ phase-advance between girders can yield cancellation.

Prior to the decision to replace the existing concrete girders with steel girders, a study was made to assess the impact of girder vibration on orbit stability. For this case, the two main girder modes had peak vertical motion of about 200 nm and the peak horizontal motion of about 750 nm [1,2]. To simulate the effect on the closed orbit, an 18-fold, fully symmetric lattice was used. Allowing all 18 girders to vibrate out of phase produced a statistically time-independent motion of all magnets. In order to find the overall effect on the closed orbit, 10,000 different distributions of girder displacement were calculated. The results for the horizontal and vertical plane are appear in Figures 3.45 and 3.46. Clearly, the horizontal girder vibrations should not cause a problem for the horizontal beam stability. The new steel girders are expected to yield even better results.

In the vertical plane the closed orbit motion is small, but in some cases it can exceed the 5 µm limit at the photon beam source point for focused ID beamlines. With the new steel girders, and the orbit feedback system active, the vertical stability will improved.

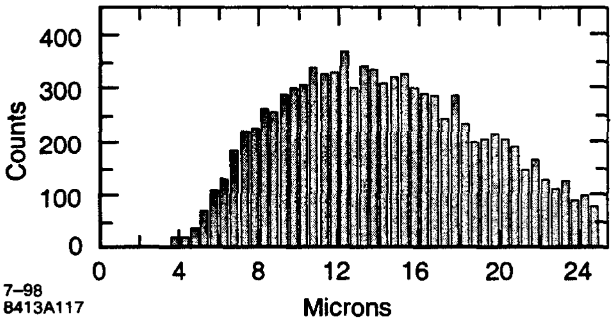

Figure 3.45 Distribution of peak horizontal orbit motion with 750 nm rms girder vibration amplitudes.

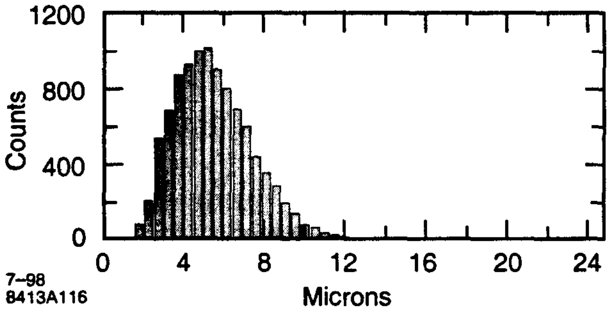

Figure 3.46 Distribution of peak vertical orbit motion with 200 nm rms girder vibration amplitudes.

3.4.1.3 Temperature Induced Motion

Temperature excursions cause longitudinal and transverse motion of accelerator components that can shift the electron orbit and photon-beam alignment. A change in the accelerator tunnel temperature, for instance, will change the mechanical dimensions of the accelerator components in proportion to the linear coefficient of thermal expansion:

$$l = l_0(1+\kappa\Delta T) \qquad (42)$$

where l_0 is the component dimension at a reference temperature, κ is the thermal expansion coefficient, and ΔT is the temperature change. The change in mechanical dimensions can move magnet axes, move BPM or vacuum chamber modules and change resonance frequencies in a cavity.

In general, if the tunnel temperature changes, the longitudinal expansion of the accelerator components will be absorbed by the compression of the vacuum bellows. Since many different materials and support structures are used in the machine, an exact calculation is difficult. In the extreme case, one can assume the storage ring is constructed from a homogeneous material without bellows so that any temperature change with alter the circumference of the ring and induce a dispersion trajectory. Assuming a temperature change ΔT would increase the storage ring circumference by $\Delta L = L_0 \kappa \Delta T$ (worst case), and using the definition for momentum compaction α,

$$\frac{\Delta L}{L} = \alpha \frac{\Delta p}{p}, \tag{43}$$

the beam momentum would change by

$$\frac{\Delta p}{p} = \frac{\kappa \Delta T}{\alpha}. \tag{44}$$

The equilibrium orbit is then shifted onto a dispersion trajectory given by

$$x_D(s) = \eta(s) \frac{\Delta p}{p} = \frac{\eta(s) \kappa \Delta T}{\alpha}, \tag{45}$$

where $\eta(s)$ is the dispersion function at position ‘s’. Based on this assumption, Table 3.28 lists the circumference change, momentum deviation, and orbit shift at the locations of peak dispersion (η_{max}=0.45) for a uniform 1° C temperature change for different materials. The corresponding RF frequency change needed to compensate the circumference change is also listed. Although this exercise only provides estimates for a uniform change in storage ring radius, we anticipate momentum deviations should remain well below 0.1%.

Table 3.28 Effect of circumference change induced by 1° C temperature rise in various materials.

Material	κ [°C^{-1}]	ΔL [mm]	Δp/p [%]	Δx [mm]	Δf [kHz]
Copper	16x10^{-6}	3.75	1.411	6.69	-5.726
Stainless steel	7x10^{-6}	3.98	1.465	6.96	-6.076
Aluminum	24x10^{-6}	5.85	2.205	10.45	-8.932
Iron	12x10^{-6}	2.81	1.058	5.01	-4.290

Thermally induced component motion can also be estimated from temperature measurements inside the tunnel (Section 6.1.3). To estimate motion in SPEAR 3, the SPEAR 2 diurnal temperature measurements were scaled down to ± 1.0° C to account for improved thermal insulation (Section 6.1.3). Monthly temperature excursions were adjusted as well. The resulting estimate for vertical girder and magnet motions are listed in Table 3.29.

Assuming the temperature variation is uniform around the ring, the net effect is to cause the uncorrected vertical beam orbit to change globally by ±??? μm/day with respect to the floor, very close to the 5 μm vertical stability specification for SPEAR 3. This excursion would only be detectable by users if the relative temperature between beamline systems and the accelerator changed diurnally. Residual photon beam drift due to differential temperature change between the accelerator and the beamlines can be reduced with feedback on the beamline mirrors. The vertical stability of the magnets and BPMs can be improved by girder floor support insulation.

To help stabilize the BPMs, each module will be supported on low thermal expansion (Invar or carbon fiber) fixtures attached to the base of the girder (Section 4.2.2.4). Longitudinal displacements of the BPMs with respect to the mid-point of the girder are given in Table 3.29.

BPM positions are also affected by changes in vacuum chamber temperature driven by changes in the resistive wall heating as the beam decays (Section 4.2.4.4). The temperature change due to resistive wall heating is estimated to be ~5 °C for a current decay from 500 mA to 350 mA. The resulting variation in vertical and horizontal BPM positions with respect to the girder are summarized in Table 3.30.

Table 3.29 Linear motion of accelerator components in the vertical plane due to temperature variations[†].

Component	Temperature Change	Vertical Motion
Girder supports (L = 17.8 cm wrt floor)	± 0.5°C/day ± 1.4°C/month	± 1.1 μm/day ± 3.0 μm/month
Girder (L = 40.6 cm wrt supports)	± 0.7°C/day ± 2.2°C/month	± 1.1 μm/day ± 3.6 μm/month
Magnet (L = 40.6 cm wrt girder)	± 0.7°C/day ± 2.5°C/month	± 3.4 μm/day ± 12.2 μm/month
Vacuum chamber (L = 1.8 cm wrt chamber support)	± 3.5°C/day ± 5.3°C/month	± 1.0 μm/day ± 1.5 μm/month
Chamber supports (Invar/carbon fiber; L = 40.6 cm wrt to girder)	± 1.0°C/day ± 2.8°C/month	± 0.4 μm/day ± 1.0 μm/month
Magnet motion with respect to floor		± 6 μm/day ± 19 μm/month
BPM motion with respect to floor		± 4 μm/day ± 10 μm/month

[†] Tunnel air temperature is expected to vary ± 1.0 °C/day, ± 2.8 °C/month.

Table 3.30 Longitudinal and horizontal bend magnet and BPM motion with respect to the girder mid-point for temperature changes given in Table 3.29.[†]

Component	Longitudinal motion	Horizontal motion
Bend magnets (L_{girder} = 2.41 m)	± 7 μm/day ± 21μm/month	± 1 μm/day ± 3.5 μm/month
BPM 1 (L_{girder} = 4.32 m)	± 12 μm/day ± 38μm/month	± 10 μm/day ± 17 μm/month
BPM 2 (L_{girder} = 4.32 m, $L_{vac.chamber}$ = 2.79 m)	± 174 μm/day ± 283 μm/month	± 10 μm/day ± 17 μm/month
BPM 3 (L_{girder} = 0.33 m, $L_{vac.chamber}$ = 0 m)	± 1 μm/day ± 3 μm/month	± 10 μm/day ± 17 μm/month
BPM 4 (L_{girder} = 4.32 m, $L_{vac.chamber}$ = 2.79 m)	± 174 μm/day ± 283 μm/month	± 10 μm/day ± 17 μm/month

Table 3.30 Longitudinal and horizontal bend magnet and BPM motion with respect to the girder mid-point for temperature changes given in Table 3.29.†

Component	Longitudinal motion	Horizontal motion
BPM 5 (L_{girder} = 4.32 m)	± 12 μm/day ± 38 μm/month	± 10 μm/day ± 17 μm/month

†. (only linear expansion considered)

3.4.1.4 Power Supply Stability

All storage ring supplies must be well regulated with low AC ripple for tune and orbit stability. To estimate the effect of quadrupole supply stability on the electron beam orbit, a statistical approach similar to that used in Section 3.4.1.1 can be applied. In this case, the angular kick at each quadrupole can be expressed as

$$\theta = (k_0 + \Delta k \cos\omega t) L \delta x \tag{46}$$

where k_0 is the nominal quadrupole strength, Δk is the power supply ripple amplitude, L is the effective magnet length and δx is the beam displacement relative to the quadrupole centers. Since the supply ripple is statistically uncorrelated to the beam offset in the quadrupoles, the time-averaged distribution of angular kicks around the storage ring is

$$\sigma_\theta^2 = (k_0 + \Delta k)^2 \left(L^2 \sigma_u^2 \infty k_0^2 L^2 \sigma_u^2 \left(1 + \frac{1}{2} \left(\frac{\Delta k}{k_0} \right)^2 \right) \right) \tag{47}$$

Calculating the rms kick value $<\sigma_\theta^2>^{1/2}$ shows the rms contribution due to the random kick distribution from quadrupole supply ripple is reduced by $\frac{1}{4}\left(\frac{\Delta k}{k_0}\right)^2$ relative to the DC orbit distortion (second order effect). While 200 μm rms static magnet misalignments would produce ~5 μm rms orbit distortion, a 1x10^{-4} quadrupole power supply ripple with σ_u = 200 μm rms orbit distortion would produce less than 1 μm rms orbit motion.

Power supply stability for the corrector magnets can also be analyzed statistically. In this case, the rms orbit motion, $\sigma_0(s)$, is given by [4]:

$$\sigma_0(s) = A(s)\sigma_\theta \tag{48}$$

where σ_θ is the rms spread of angular kicks due to the corrector magnets and the amplification factor is

$$A(s) = \frac{\sum N \beta_k \beta_0(s)}{8 \sin^2 \pi \upsilon} \tag{49}$$

The β-functions, β_k and $\beta_0(s)$, are evaluated at the corrector and observation points, respectively, and N is the total number corrector magnets at locations with the same value for β_k. Taking all corrector magnets in the storage ring into account, the corrector magnet amplification factors are listed in Table 3.31.

Table 3.31 Orbit amplification factors for random corrector kicks in SPEAR 3†.

Source Location	β_x (m)	β_y (m)	A_x	A_y
Dipole	1.86	14.6	15	43
Insertion Straight	10.1	4.8	35	25

†. $\sigma_{x,y} = A_{x,y}\,\sigma_\theta$, where $\sigma_\theta = 1$

To evaluate corrector power supply stability, we assume the vertical corrector magnets are operating with an rms value of 100 μrad. An rms power supply stability of $1\text{x}10^{-4}$ would then seed the storage ring with 0.01 μrad random deflection angles. Based on Table 3.31, the resulting rms orbit disturbance is less than 1 μm.

The dipole power supply stability is determined by tune modulation considerations. For a power supply stability of $5\text{x}10^{-5}$ and natural chromaticity of –20, the tune modulation is 0.0001.

References:

[1] G. Bowden, SPEAR Raft Vibrations, SLAC Memorandum, June 1997.

[2] G. Bowden, SPEAR Raft Vibrations, 2nd Measurements, October 1997.

[3] G. Bowden, Diurnal Heat Transfer through Concrete, NLC ME Note 14-98, May 1998.

[4] H. Wiedemann, Particle Accelerator Physics-I, Spring-Verlag, 1993.

3.4.2 BPM and Corrector Locations

SPEAR 3 will be equipped with 5 BPMs and 4 corrector magnets per cell. As indicated in Figure 3.47, the BPMs are located at each end of the cell, just inboard of each dipole magnet, and near the QFC quadrupole. The BPMs at the ends of the cell will be mechanically isolated by vacuum bellows and mounted on mechanically stable stands with low thermal expansion coefficient. The BPM in the center of the cell will also be mechanically stabilized. As the phase advance per cell is $\phi_x \approx 0.75$ and $\phi_y \approx 0.25$, five BPMs provide sufficient capability to detect local orbit distortions.

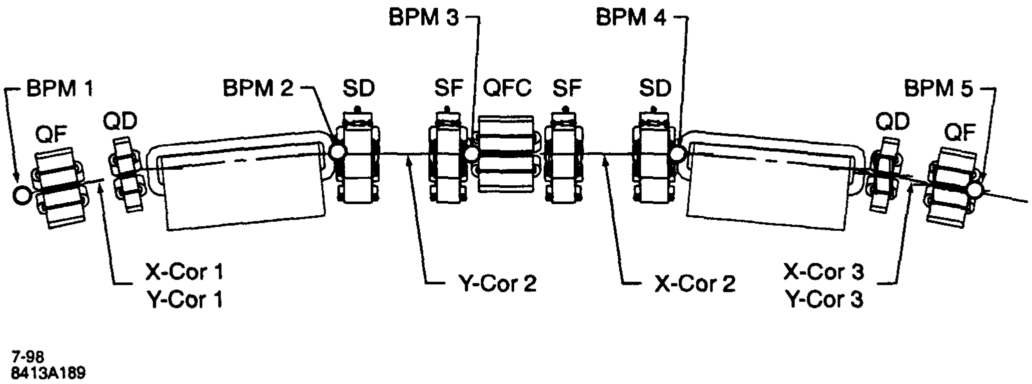

Figure 3.47 Location of electron BPMs and corrector magnets in the main cells.

The steering magnets will be made up from combined horizontal/vertical field modules that can produce up to 1.5 mrad horizontal and 1.0 mrad vertical deflection, respectively. The corrector modules will be installed between the doublet quadrupoles and between the sextupole magnets. CuproNickel® inserts are used in copper vacuum chamber to extend the -3 dB roll-off frequency of the field penetration to > 30 Hz in the vertical plane (B_y) and about 100 Hz in the horizontal plane (B_x) (Section 4.2.x)). To reduce the number of corrector power supplies, the steering coils will only be activated in the positions indicated in Figure 3.47. Calculations based on beamline steering considerations show this configuration is optimal. As demonstrated in Section 3.4.4, three steering magnets per cell in each plane is sufficient for global electron and photon beam steering. Table 3.32 lists the optical functions evaluated at the BPMs and correctors.

Table 3.32 Optical functions for BPMs and correctors in main SPEAR 3 cells.

Element	ϕ_x (phase/degree)	ϕ_y (phase/degree)	β_x (m)	β_y (m)	η_x (m)
Cell Start	0.0°/0.0°	0.0°/0.0°	10.2	4.7	0.0
BPM #1	0.024°/8.6°	0.049°/17.6°	10.3	5.3	0.0
HVCOR #1	0.034°/12.4°	0.062°/22.3°	6.4	8.6	0.0
BPM #2	0.297°/107°	0.086°/31.0°	1.0	12.8	0.14
VCOR #2	0.367°/132.1°	0.099°/35.6°	3.3	7.8	0.30
BPM #3	0.390°/140.4°	0.117°/42.1°	6.8	4.5	0.45
HCOR #2	0.424°/152.6°	0.155°/55.8°	3.3	7.8	0.30
BPM #4	0.494°/177.8°	0.167°/60.1°	1.0	12.8	0.14
HVCOR #3	0.757°/272.5°	0.191°/68.8°	6.4	8.6	0.0
BPM #5	0.767°/276.1°	0.205°/73.8°	10.3	5.3	0.0
Cell End	0.791°/284.8°	0.253°/91.1°	10.2	4.7	0.0

3.4.3 Orbit Correction Algorithms

The SPEAR 3 orbit control system will build upon a singular value decomposition (SVD) control algorithm that has operated at SSRL since 1993 [4–6]. This system has produced reliable global orbit correction, regional orbit adjustments, local beam bumps, and photon beam steering. In most instances, this system allows simultaneous control of the combined electron and photon beam postions.

Operationally, the orbit correction algorithm works as follows. First, the operator selects the set of steering magnets and BPMs for orbit control. The steering magnets can include single correctors, groups of magnets (e.g., 3-bumps or "eigenvector" patterns), and the RF frequency. The BPMs include electron and photon beam position monitors.

Orbit correction is based on measurements of the beam deflection at each BPM in response to each steering magnet. When the measured orbit shifts are arranged into columns within a matrix, the collective set of measurements forms a corresponding response matrix, **R**. For m-BPMs and n-steering magnets, **R** has dimension $m \times n$. The response matrix can also be computed numerically. Once the response matrix is determined, it is stored for future use with a compatible configuration.

In matrix notation, a corrector pattern $\Delta\theta$ creates a beam deflection $\Delta\mathbf{x}$ given by

$$\Delta\mathbf{x} = \mathbf{R}\,\Delta\theta. \tag{50}$$

Prior to matrix inversion, the monitors can be weighted individually to enhance local-orbit control, or the correctors can be weighted to control the output current. Singular Value Decomposition of **R** yields $\mathbf{R}=\mathbf{U}\mathbf{W}\mathbf{V}^T$ [7,8] where the columns of **U** form a set of orthonormal 'orbit eigenvectors' spanning the space of controllable orbit deflections (eigenvectors of $\mathbf{R}\mathbf{R}^T$), the 'singular-value' elements of the diagonal matrix **W** contain the square-root of the eigenvalues of $\mathbf{R}\mathbf{R}^T$ (same as for $\mathbf{R}^T\mathbf{R}$), and the rows of $\mathbf{V}^T$ contain a set of orthonormal 'corrector eigenvectors' (eigenvectors of $\mathbf{R}^T\mathbf{R}$) corresponding to the 'orbit eigenvectors' in **U**. It is easy to demonstrate that the vector of steering magnets $\mathbf{V}^{(1)}$ generates an orbit perturbation $\mathbf{W}^{(1)}\mathbf{U}^{(1)}$.

Using the orthogonal properties of **U** and **V** (inverse equals transpose), the inverse response matrix is readily written as $\mathbf{R}^{-1} = \mathbf{V}\mathbf{W}^{-1}\mathbf{U}^{T}$, where $\mathbf{W}^{-1}$ contains the inverse of the diagonal elements in W. The steering magnet pattern required to move the orbit by $\Delta\mathbf{x}$ is calculated by a matrix multiplication against the inverse matrix,

$$\Delta\theta = (\mathbf{V}\mathbf{W}^{-1}\mathbf{U}^{T})\,\Delta\mathbf{x}. \qquad (51)$$

When R has full rank (which requires $m \geq n$), the inverse matrix $\mathbf{V}\mathbf{W}^{-1}\mathbf{U}^{T}$ returns the standard least-squares solution for $\Delta\theta$. If R is rank-deficient (for example $m \leq n$), SVD again calculates a set of corrector eigenvectors **V** and corresponding-orbit eigenvectors **U** which span the space of controllable orbit perturbations. In the rank-deficient case, however, the extra degrees of freedom can be used to reduce the rms magnitude of the corrector strengths. Through judicious choice of the number of eigenvectors, one can balance the accuracy of the orbit correction against strength of the steering magnets. Reducing the number of eigenvectors provides an effective spatial 'low pass' filter that rejects high-frequency orbit perturbations and lowers the rms corrector strengths.

Another software tool used at SPEAR for orbit control and analysis is the interactive graphics program RESOLVE [9,10]. With RESOLVE, the operator can manually analyze a measured orbit in a particular region of the accelerator to search for BPM and/or magnet errors. As discussed in Section 3.1.15, RESOLVE or more generally response matrix-based model fitting can be used to identify quadrupole focusing errors.

3.4.4 Static Orbit Control

The orbit control system for SPEAR 3 will be based on several independent hardware and software sub-systems working in unison. The hardware systems include 1) the electron BPM processor (Section 4.8.2.1), 2) corrector magnets, 3) a DSP-based computation engine with associated A/D and D/A modules, and 4) the quadrupole shunt system (Section 4.8.3). The software systems include 1) processing algorithms for the electron and photon beam position monitors, 2) corrector setpoint and readback software, 3) orbit control programs, and 4) a beam-based alignment program to drive the quadrupole modulation supply.

The SVD matrix inversion algorithm outlined in Section 3.4.3 forms the basis for both static orbit control and dynamic orbit feedback. Adjustment of the beam position involves specification of an orbit deviation, which is then multiplied by the inverse response matrix to determine the steering-magnet pattern. Since both electron and photon beam position monitors are processed simultaneously, 'unified' orbit corrections are possible [5,11]. In SPEAR 2, for example, the unified electron/photon BPM system is used at the top of each fill to steer the photon beams. In this case, the photon BPMs are weighted by a factor of 100 to accurately steer the photon beams.

Global orbit correction is used primarily during periods of machine setup and accelerator physics experiments. To simulate orbit correction on SPEAR 3, numerical calculations were made with random orbit perturbations and random BPM noise. Similar to the analysis in Section 3.4.1.1, the orbit was perturbed by quadrupole and dipole misalignments with an rms amplitude of 200 μm. For each orbit, the electron and photon beam positions and angles were recorded at the BPMs. The photon beam positions were recorded 10 m downstream from the source points. Both the electron and photon BPM readings were then seeded with 2 μm rms readback errors to simulate electronic noise.

In these simulations, orbit correction was based on one of two algorithms: 1) only steer the electron beam position to the electron BPMs , or 2) steer both the electron and photon beams simultaneously (unified correction). For the unified steering case, a weighting factor of 100 was applied to the photon BPMs to improve steering accuracy.

Results for the case of vertical steering to the electron BPMs (case 1) are illustrated in Figures 3.48 and 3.49. These figures show the rms electron and photon beam positions as a function of the number of singular values used in the correction algorithm. Clearly, the electron beam orbit improves as the number of eigenvectors increases. Since the photon beam positions are not under direct control of the correction system in this case, photon beam steering is less accurate. The corresponding angle errors are indicated in Figure 3.49, which also shows that rms increases in corrector magnet strength as the number of eigenvectors is increased. In practice, the corrector strengths are limited by minimizing the number of eigenvectors required for acceptable orbit correction. Based on these simulations, 30-40 eigenvectors should be acceptable.

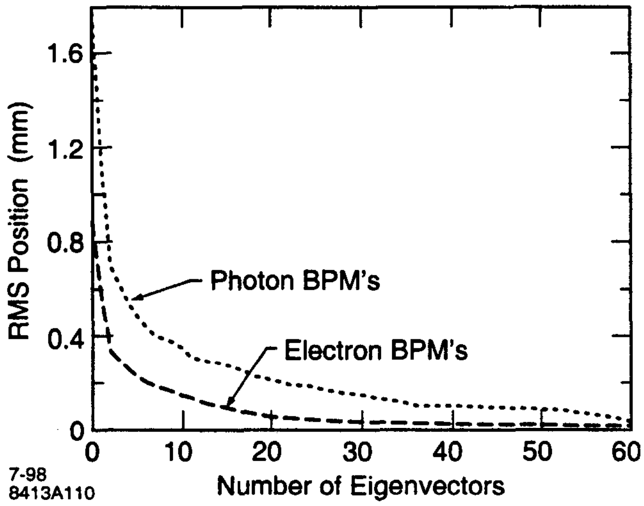

Figure 3.48 RMS orbit position for cases of correction to electron BPMs in the vertical plane.

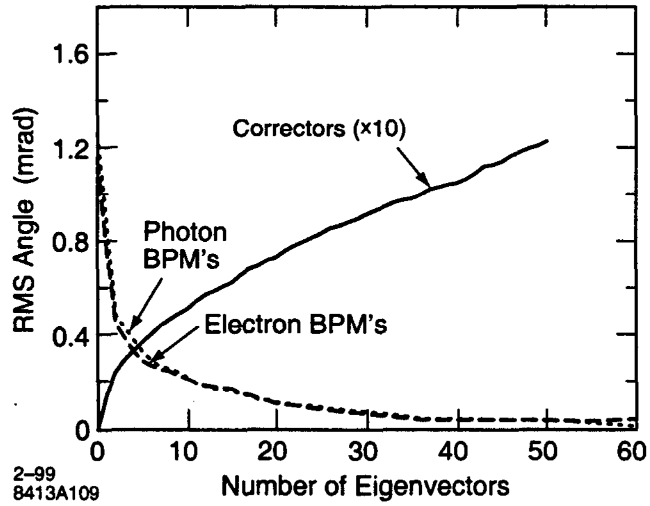

Figure 3.49 RMS orbit angle for case of correction to electron BPMs in the vertical plane.

Figures 3.50 and 3.51 illustrate the performance of the unified electron/photon-beam orbit correction system (case 2), once again for the vertical plane. For this case, a weighting factor of 100 was applied to each photon BPM to enhance photon-beam steering. As the figures indicate, the accuracy of the photon beam steering surpasses the electron beam steering under these conditions. Again, about 30-40 eigenvectors should be adequate to steer the beam.

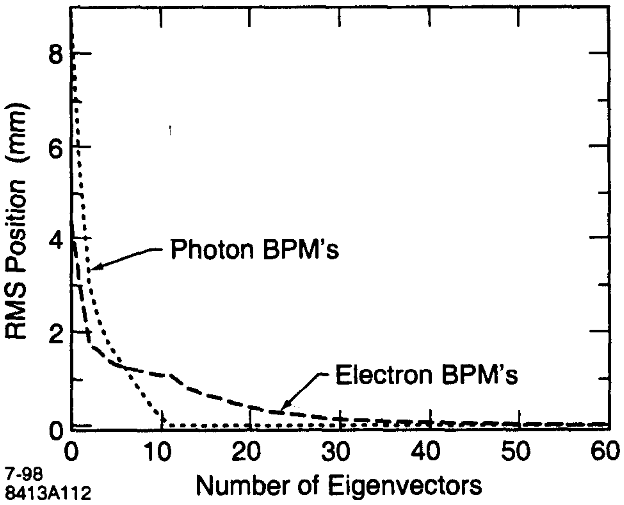

Figure 3.50 RMS orbit position for correction to photon BPMs in vertical plane.

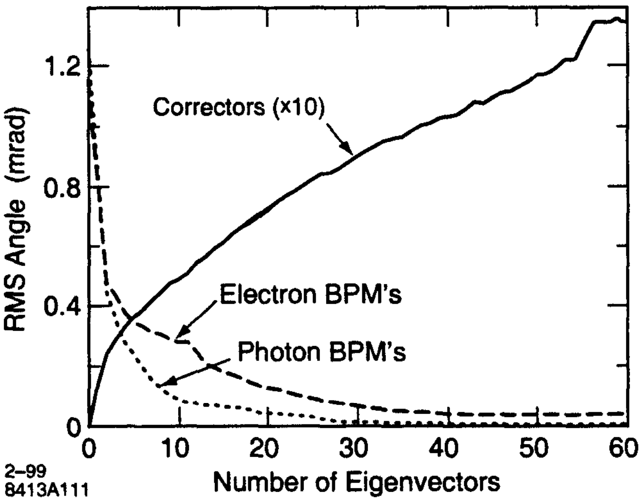

Figure 3.51 RMS orbit angle for correction to photon BPMs in vertical plane.

Another application of the SVD-based algorithm has been used to reduce the corrector strengths while holding the photon beam positions constant. This application is based on a fundamental property of SVD: any matrix R can be 'decomposed' even when the set of equations is indeterminate ($m < n$, or R is rank-deficient). For each of the n-m 'null' eigenvectors, the diagonal elements of W^{-1} are simply set to zero. This property has been used to reduce the corrector strengths while holding the photon beam positions stationary and should be a valuable tool for commissioning SPEAR 3 [12,13].

In summary, SPEAR 3 will utilize an SVD-based orbit correction algorithm using the measured corrector-to-BPM response matrix. In general, the orbit correction program can steer both the electron and photon beams to the accuracy of the BPM readings. Since the orbit control algorithm is implemented digitally, system parameters (such as the choice and weighting of the BPMs) are readily changed.

3.4.5 Dynamic Orbit Control

Similar to the static orbit correction system, the dynamic orbit-feedback system is based on SVD inversion of the corrector-to-BPM response matrix. In this case, due to the finite time-response of elements in the feedback loop (magnet supplies, magnet cores, chamber-eddy currents, BPM processor, DSP latency) the feedback algorithm requires dynamic frequency compensation (Section 4.7.1). Fortunately, a common frequency response function, H(z), factors out of the multi-input/multi-output corrector-to-BPM transfer matrix. This reduces design of the feedback compensation system to a single-input/single-output control problem.

To simplify the compensator design, the discrete transfer function H(z) is often modeled as a two-pole system. The two pole locations are identified either by direct frequency response measurements, or similar to work done at the APS, by step-function measurements, followed by DFT of the associated impulse response [14]. Based on the measured poles of the open-loop system, a digital PID control algorithm will be implemented via a DSP. Higher-order pole identification and corresponding compensator designs are also possible with either classical or state-space feedback algorithms.

In practice, the orbit feedback system utilizes much of the same hardware and software as the static orbit control system. Selection of BPMs, correctors, weighting factors, and eigenvalues is made from console menus. The console menus also permit selection of the BPM processor parameters, feedback cycle time, and compensator coefficients. A dedicated DSP processor will multiply the measured orbit perturbations against the inverse response matrix and compute the corrector outputs via the PID filter. RF frequency adjustments will correct for slow thermal expansion of the storage ring circumference. Section 3.7.1 covers the orbit-feedback hardware system.

Operationally, the orbit feedback system will be configured in the ‘unified’ orbit control mode to process both electron and photon BPMs. To emphasize photon beam stability, the photon BPMs can be given additional weight. The photon BPM signals will be equipped with front-end anti-alias filters which can also function as frequency-equalization filters. Given the anticipated <2 μm position resolution of the photon BPMs (out to frequencies beyond the girder vibrations), short-term position stability should meet or exceed user requirements. To avoid lever-arm errors, the angle of the photon beams is controlled by stabilizing the electron beam position at BPMs near the photon beam source points. Where dipole radiation interferes with variable-gap undulator beamlines, the beam position can be stabilized with electron BPMs located at either end of the straight sections.

3.4.6 Quadrupole Field Modulation

Two DC quadrupole shunt techniques have been used in SPEAR 2 [21]. The first method sweeps the beam through the quadrupole, and records the shunt-induced orbit perturbation. As shown in Figure , this ‘sweep’ method can be used to find the horizontal center of a QF quadrupole to within about 100 μm. The second technique, a derivative-based algorithm, automatically centers the beam in the quadrupole with a single corrector magnet or a closed bump.

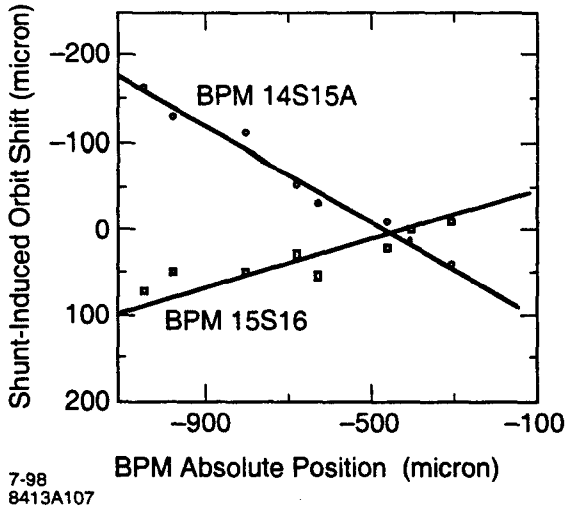

Figure 3.52 Example of DC-AC shunt-induced orbit shift as a function of BPM offset.

For SPEAR 3, an AC quadrupole modulation system will fiducialize BPM readings with respect to the quadrupole centers. The field modulation system makes use of an old, but effective beam steering method: a quadrupole shunt deflects the beam if the orbit passes through the magnet off-axis [15-20]. For quadrupole modulation to function effectively in SPEAR 3, the orbit shift should be detectable for beam displacements <100 μm from the quadrupole center. Once the quadrupole center is found, the readback offset on a nearby BPM is entered into the database. The tune shift can also be processed to estimate the β–functions at individual quadrupoles, or to calibrate the linear optics model [21].

By utilizing an AC waveform, the orbit motion can be detected synchronously at the electron or photon beam BPMs. Similar 'lock-in' detection has been successfully at LEP [ref ???] and at the SLC [ref ???]. Figure provides an example of data from an AC quadrupole modulation experiment at SPEAR 2.

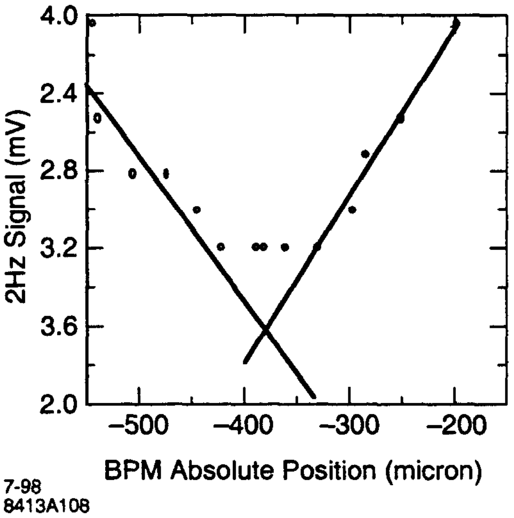

Figure 3.53 Example of AC shunt-induced orbit shift as a function of BPM offset.

The amplitude of the field modulation needed for beam centering is easily estimated. Disregarding the phase factor, the beam will move byfootnote #1

$$\Delta\chi = \frac{\Delta\theta\sqrt{\beta_{quad}\beta_{BPM}}}{2\sin\pi\nu} \tag{52}$$

where

- $\Delta\theta = \Delta kLx$ is the change in deflection angle at the quadrupole
- β_{quad} is the β-function at the quadrupole
- β_{BPM} is the β-function at the BPM
- ν is the machine tune
- Δk is the change in quadrupole strength (m^{-2})
- x is the beam offset relative to quadrupole center

Solving for the change in quadrupole strength in terms of orbit shift 'Δx' and beam offset 'x',

$$\Delta k = \frac{\Delta\chi 2\sin\pi\nu}{L\chi\sqrt{\beta_{quad}\beta_{BPM}}} \tag{53}$$

For good sensitivity, Δx/x ~0.1 (e.g. a 10 micron orbit shift for 100 micron beam displacement relative to quadrupole center).

Based on these arguments, Table 3.33 lists the field modulation needed to center the electron beam horizontally in QF magnets, or vertically in QD magnets. Approximate values for the β-functions are used throughout. The maximum horizontal and vertical β-functions at the BPM locations are 10 m and 5 m, respectivelyfootnote #2. Tune shift is given by

$$\Delta\nu = \frac{\beta\Delta(kL)}{4\pi}. \tag{54}$$

Table 3.33 Quadrupole field modulation Δk required for 10 μm orbit shift with 100 μm orbit offset in the quadrupole. For these calculations, the fractional tune is taken to be 0.2 (sinπn~0.6).

Quadrupole	β_x	β_y	Δk (m^{-2})	Δk/k (%)	$\Delta\nu_x$	$\Delta\nu_y$
QF	10	5	0.035	1.89	0.009	n/a
QD	5	10	0.111	7.3	n/a	0.013
QFC	7	4	0.028	1.57	0.008	n/a
QDX	8	10	0.049	3.6	n/a	0.013
QFX	15	6	0.016	1.0	0.011	n/a
QDY	5	8	0.055	12.4	n/a	0.012
QFY	6	3	0.03	2.3	0.007	n/a
QDZ	10	12	0.045	5.7	n/a	0.015
QFZ	10	6	0.035	2.5	0.009	n/a

footnote #1correction factors that take into account beam motion in the quadrupole self-consistently were not used for these calculations.

footnote #2Depending on the BPM configuration, one BPM in each of the matching cells will have β_y~10 m.

From Table 3.33, the maximum Δk value for QMS occurs in the QD magnet (L=0.15 m). Combined with the relatively low magnet strength ($k=-1.5\ m^{-2}$), the percentage field modulation is high (7.3%). To achieve 7.3% modulation, the main DC field coils will be used.

Figure 3.52

Figure 3.53

References

[1] G. Bowden, SPEAR Raft Vibrations, SLAC Memorandum, June 1997.

[2] G. Bowden, SPEAR Raft Vibrations, 2nd Measurements, October 1997.

[3] G. Bowden, Diurnal Heat Transfer through Concrete, NLC ME Note 14-98, May 1998.

[4] W. J. Corbett and D. Keeley, Proc. of the Brookhaven Orbit Correction and Analysis Workshop (1993).

[5] J. Corbett, et al, 1994 EPAC, London, England (1994).

[6] R. Hettel, et al, Proc. 1996 EPAC, Sitges, Spain, (1996).

[7] G. Strang, Linear Algebra and Its Applications, second ed., (Academic Press, Inc.).

[8] G. Strang, American Mathematical Monthly, Vol 100, #9, November 1993.

[9] W.J. Corbett, M.J. Lee and Y. Zambre, 1992 EPAC, Berlin, Germany (1992).

[10] M.J. Lee, Y. Zambre, and W.J. Corbett, Int. Conf. Cum Workshop on Current Trends in Data Acquisition and Control of Accelerators, Calcutta, India (1991)

[11] Y. Chung, G. Decker and K. Evans, Jr., Proc. 1993 IEEE PAC, Washington D.C. (1993).

[12] V. Ziemann, , Proc. 1993 IEEE PAC, Washington, D.C. (1993).

[13] J. Corbett, B. Fong, V. Ziemann and M. Lee, Proc. 1993 IEEE PAC, Washington, D.C. (1993).

[14] J. Cawardine, 1998 Beam Instrumentation Conference, Stanford, CA (1998), in press.

[15] Shunts were used at CEA in the 1960's. Private communication, A. Hofmann, H. Winick.

[16] D. Rice, IEEE Trans. Nuc. Sci., Vol. NS-203, No. 4, Aug. 1983.

[17] L. Arnaudon, et al, Proc. of the 1995 PAC and Int. Conf. on High-Energy Accelerators, Dallas, Texas, May 1–5, 1995.

[18] S. Herb, et al, Proc. 1st European Workshop on Beam Diagnostics and Inst. for Particle Accelerators, Montreux, Switzerland, May 3–5, 1993, pp. 120–125.

[19] P. Röjsel, NIM A, 343 (1994) 374-382.

[20] D. Robin, ALS Light Source Accelerator Physics Note-194.

[21] W.J. Corbett, R.O. Hettel and H.-D. Nuhn, 1996 Beam Instrumentation Workshop, (1996).

3.5 Storage Ring Impedance

A charged particle beam circulating in the storage ring is a source of electromagnetic fields. These fields, modified by the vacuum chamber impedance, can react on the beam and degrade its properties. The two main sources of storage ring impedance are resistive wall impedance and chamber discontinuities. Resistive impedance leads to power dissipation in the walls, which can affect beam stability. Chamber discontinuities also perturb the fields electromagnetic field, and these can also lead to beam instability. An important goal of the storage ring chamber design is to minimize these impedance effects.

In the frequency domain, the beam-chamber interaction can be modeled as an electromagnetic potential, V(ω), acting on the beam current. The ring impedance, Z(ω), is defined as

$$Z(\omega)=V(\omega)/I(\omega). \tag{55}$$

Chamber discontinuities can be subdivided into two groups. The first group consists of low-Q (wideband) devices (such as flanges, bellows, and BPMs, etc.) that can affect the single-bunch properties of the beam. These structures have discontinuities with dimensions of the order (or smaller than) the bunch length. The short-range wakefields caused by such discontinuities act on the trailing particles. Each individual structure generates very little impedance; however they can be sufficiently numerous that collectively, they produce a large impedance. The complex geometry of storage rings makes it hard to accurately quantify this cumulative impedance.

In the longitudinal dimension, short-range wakefields can lead to bunch-lengthening and energy-widening. In the transverse plane, the head-tail instability can lead to beam blow-up and particle loss. The Heifets-Bane and standard-broadband resonator models have been chosen (from among the various models available) to describe the effect of the short-range wakefields [1,2,3].

The second group of structures consists of large-volume, high-Q (narrowband) devices such as RF cavities. Fields trapped in these structures can resonate for periods of time that are long compared to the time between bunches. These high-Q structures can couple the motion of different bunches, or even the same bunch from turn to turn. Since high-Q devices may deteriorate beam quality, careful attention must be paid to these devices, eliminating them wherever possible. In SPEAR 3, the RF cavities are the main source of narrowband impedance, but the use of PEP-II, mode-damped cavities reduces the HOM resonances to benign levels.

Another source of impedance involves the resonant coupling of electromagnetic energy between the main beam chamber and the antechamber. Since the coupling slot acts as a choke to attenuate any fields built up in the antechamber, beam instabilities are not anticipated. However, fields below the cutoff frequency (which decay exponentially with distance) have been shown at other laboratories to contaminate beam position monitor readings. Given a cutoff frequency ω_c ~g/2c determined by the transverse chamber dimension, g), the evanescent length λ_{ev} is given by

$$\lambda_{ev} = \frac{c}{\sqrt{\omega_c^2 - \omega^2}} \tag{56}$$

Field leakage to the beam position monitors can be minimized by increasing the cutoff frequency in the coupling slot and/or by increasing the distance between the field energy trapped in the antechamber and the monitor locations.

3.5.1 RF Cavities

The original scope of the SPEAR 3 upgrade project was to operate with the existing 358 MHz RF system at 200 mA. The two existing five-cell RF cavities, each limited to 250 kW operation, could support a maximum current of ~250 mA at 3 GeV. A study of these cavities showed they could be tuned to operate with stable currents exceeding 200 mA without additional feedback [CDR rev 7/98].

To operate SPEAR 3 at 500 mA requires about 1.2 MW of RF power. An accelerated schedule to reach 500 mA, together with performance, cost, maintenance and reliability considerations drove the decision to replace the existing RF system with the 476 MHz PEP-II style RF system. The mode-damped PEP-II cavities provide an ~0.8 MV gap voltage-per-cell with minimum HOM impedance. SPEAR 3 will have four such cavities, thus providing a total gap voltage of 3.2 MV.

3.5.1.1 RF Cavity HOM's

To damp HOMs, the PEP-II cavities have three rectangular waveguides, each terminated with a broadband load. Table and Table , respectively, show the strongest calculated and/or measured impedances at high power levels [8]. With four cavities active, the maximum longitudinal HOM impedance, $Z_{//}(\omega)$, is close to 10 kΩ. The maximum transverse impedance is 800 kΩ/m.

The cut-off frequencies of the SPEAR 3 vacuum chamber are 4.7 GHz for TM modes and 2.1 GHz for TE modes. Above these frequencies, resonant modes will be damped in the vacuum chamber, and also by the HOM loads.

.

Table 3.34 Impedance of longitudinal HOMs for PEP-II RF cavities.

Mode	f (GHz)	R/Q(Ω)	Q	R_s (kΩ) (calibrated)	R_s (kΩ) [8] (measured)
0-E-1	0.475	117.3	14218	1654	1668
0-M-1	0.758	44.6	18	0.72	0.81
0-E-2	1.009	0.43	128	0.046	0.055
new measure	1.283	6.7	259	-	1.74
0-M-2	1.295	10.3	222	1.56	2.29

Table 3.35 Impedance of transverse HOMs for PEP-II RF cavities.

Mode	f (GHz)	R/Q(Ω)	Q	R_s (kΩ) (calibrated)	R_s (kΩ) [8] (measured)
1-E-3 V	1.327	5.58	611	58.3	76.7
1-M-4 V	1.420	5.31	1138	160.7	126.9
1-M-4 H	1.425	3.3	414	58.7	28.6
1-E-6 H	1.67	3.61	377	73.8	24.3
1-E-6 V	1.676	4.63	783	153.8	64.5

3.5.1.2 RF-Cavity Broadband Impedance

For a bunch length of 4.9 mm, simulations with ABCI [1] give a loss factor of ~1.2 V/pC for each RF cavity. Since the frequency spectrum of the bunch extends to 9.7 GHz, the reactive impedance from the cavity resonances below this frequency, when integrated over the bunch spectrum, is close to zero. The cavity broadband impedance therefore has very little effect on the single-bunch microwave instability threshold.

3.5.2 Chamber Impedance

3.5.2.1 Vacuum Chamber

SPEAR 3 will feature a copper vacuum chamber with an elliptical cross-section of radaii 42 mm x 17 mm. Its adjacent antechamber will be separated by a 12 mm-high coupling slot (Figure 3.55). Since the elliptical cross-section of the vacuum chamber keeps the majority of the image currents on the top and bottom chamber walls (Figure 3.54), the 12 mm coupling slot has a relatively small effect on the ring impedance. Calculations with GdfidL [5] give the cut-off frequencies of the dominant TM and TE modes as 4.7 GHz and 2.1 GHz, respectively, and that the TM mode is well confined to the main vacuum chamber (Figures 3.56 and 3.57). The TM mode has an evanescent length λ_{cv} of 4 mm in the chamber slot (Equation ???) so the slot prevents power transmission.

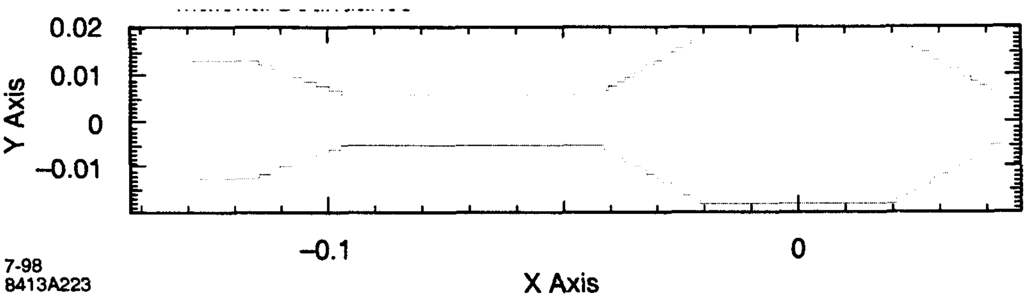

Figure 3.54 Cross-section of beam chamber and antechamber.

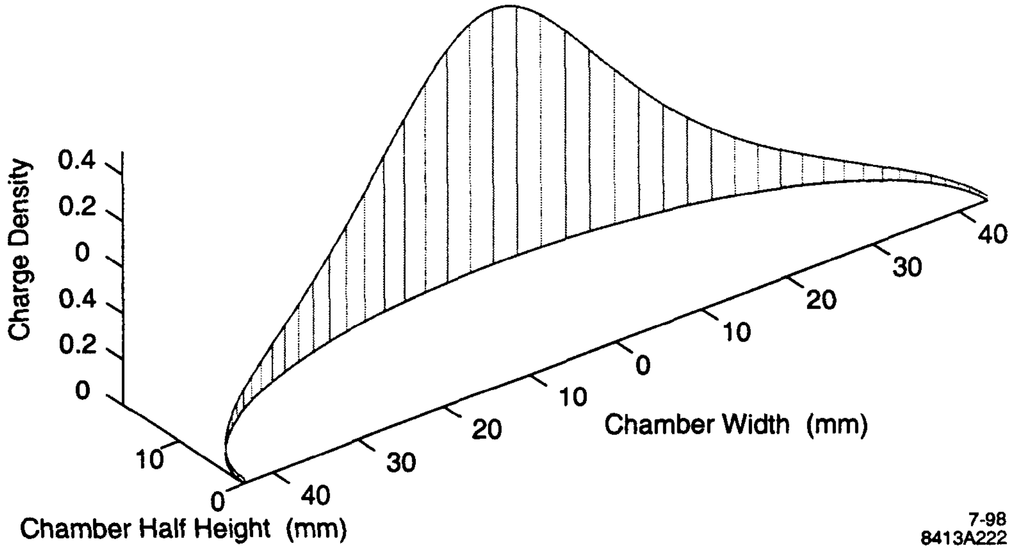

Figure 3.55 Distribution of image current in the SPEAR 3 elliptical chamber.

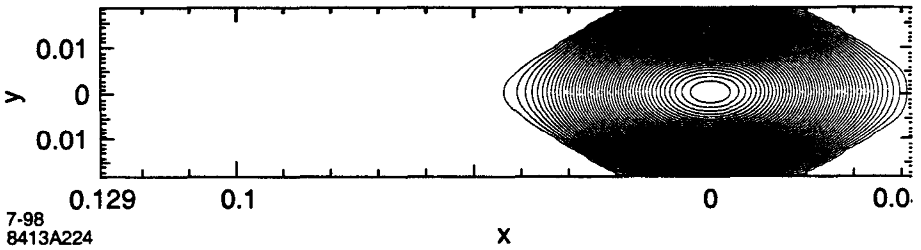

Figure 3.56 Contour plot of the longitudinal electric field E_z in the vacuum chamber.

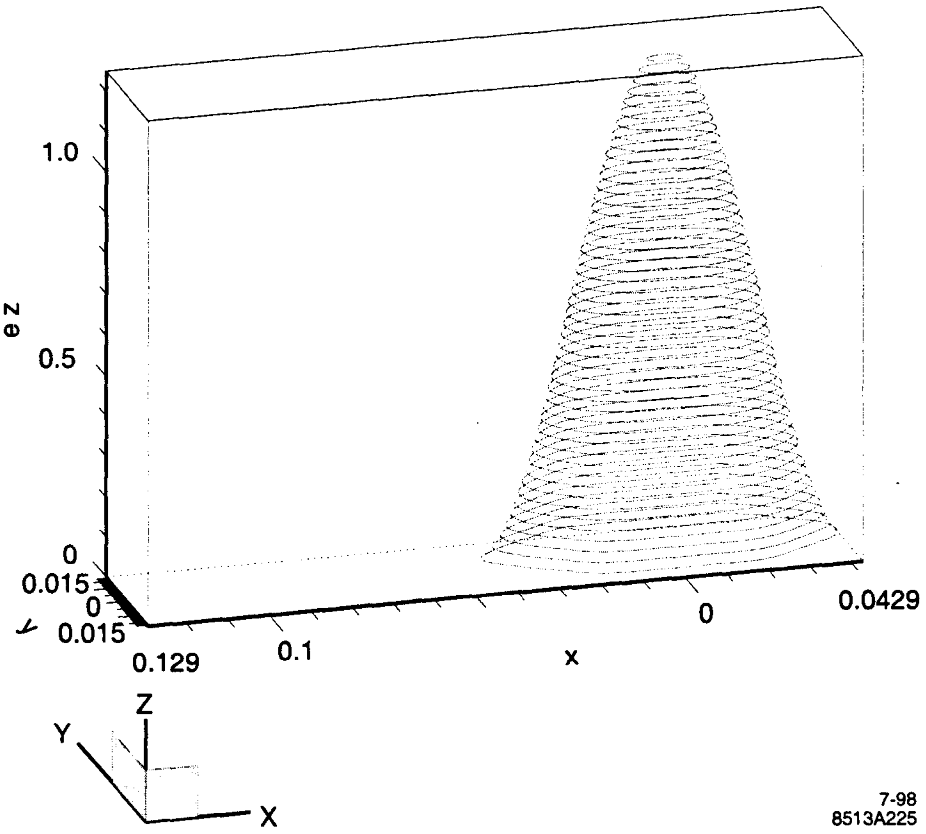

Figure 3.57 Profile plot of the longitudinal electric field E_z in the vacuum chamber.

The impedance of small gaps and discontinuities in the vacuum chamber walls can be calculated in a two-dimensional cylindrical geometry equivalent to the three-dimensional chamber geometry. For the elliptical vacuum chamber, the lowest TM cut-off frequency predicted by the 3-D code GdfidL corresponds to an equivalent 2-D radius of 23 mm. The equivalent radius calculated through normalization by the image current is 21 mm [3]. The equivalent radius for 2-D simulations was therefore chosen to be 22 mm.

3.5.2.2 Insertion Device Chambers

SPEAR 3 will use all seven existing IDs and their associated vacuum chambers. Each ID chamber has a rectangular cross-section with transitions matched to SPEAR 2. Their height is much smaller than the 47 mm vacuum chamber in SPEAR 2, so tapers are required. Unfortunately nother taper must be made to the 34 mm high SPEAR 3 vacuum chamber. These 'dual taper' transitions will create pockets within the chamber that can trap modes below the vacuum chamber cutoff frequency, $\phi_c \sim c/2g$, (where $c=3\times10^8$ m/s and g =chamber height). The new transitions will be designed so as to minimize the impedance caused by these pockets and to dampen any resonances that may be created there.

The transitions between the standard dipole vacuum chamber and the smaller insertion devices are most critical in the vertical plane where the fields are concentrated. Shallow tapers (<1:5) will help minimize the transition impedance.

The ID chambers also generate a complex resistive wall impedance per unit length

$$\frac{Z}{L} = \frac{1-i}{2\pi b^3} Z_0 \delta \tag{57}$$

where Z_0 is the free-space impedance (377 Ω), $\delta = (2/\omega\mu o\sigma)1/2$ is the chamber-wall skin depth, and b is the effective chamber radius. The complex resistive-wall impedance, which depends on $\omega^{-1/2}$ through the skin depth, is the basis for transverse beam instability calculations (Section 3.6.2.2.1). Because of the b^{-3} dependence, the vertical resistive-wall impedance is stronger in the ID chambers than in the standard arc chambers. Table 3.36 gives both the $\omega^{-1/2}$ coefficient and the impedance evaluated (at revolution frequency=1.28 MHz) for the ID chambers and for the standard vacuum chamber, respectively. For high current operation, copper plating may be needed to reduce the resistive-wall impedance in the stainless-steel ID vacuum chambers. At the frequency of interest, (0.77ωo), the skin depth of copper is 65μμ.

In summary, Table 3.36 lists the resistive wall impedances and the resistive wall power dissipation of the vacuum chamber elements

Table 3.36 Impedance properties of the ID and girder chambers

BL	Total gap (cm)	Length (m)	Material	$Z_\perp \sqrt{\omega}$ (MΩ/m/s$^{1/2}$)	$Z_\perp(\omega_o)/L$ (kΩ/m^2)	$Z_\perp(\omega_o)$ (kΩ/m)	Resistive wall power for 500 mA in 280 bunches (W)
4	1.48	2.04	Cu	40.41	6.98	14.25	7.29
5	1.96	2.04	Al	22.6	3.91	7.97	7.15
6	1.19	2.37	SS	591.17	87.94	208.42	68.97
7	1.96	2.04	Al	22.6	3.91	7.97	7.15
9	1.78	2.27	SS	169.19	26.28	59.65	44.16
10	1.96	2.25	SS	125.61	19.68	44.28	39.75
11	1.48	2.40	SS	311.19	45.71	109.71	56.15
Girder	3.4	218.88	Cu	357.57	0.58	126.06	335

3.5.2.3 Transitions

Based on a 5:1 taper from the main vacuum chamber to the smallest insertion-device chamber, the transitions into and out of the insertion devices should contribute about 1 nH per device to the low frequency inductive impedance (as computed with ABCI) [4]. Transitions to other elements (e.g., the septum and the kicker chambers) should yield comparable additional inductance.

3.5.2.4 Flanges

Each vacuum flange has an ~3 mm long RF seal recessed by no more than ~1 mm from the chamber wall. The resulting inductance, per seal, is ~18 pH with a loss factor of 4.3×10^{-4} V/pC.

3.5.2.5 Shielded Bellows

Each straight section has a bellows module to allow for longitudinal expansion of the chamber. In order to minimize impedance, RF fingers will shield the bellows corrugations. To minimize interruption of the image current, the shields will be constructed of closely-spaced longitudinal strips. Each bellows assembly will have an inductance of 73 pH and a loss factor of 1.07×10^{-2} V/pC.

3.5.2.6 BPMs

The BPM modules will have the standard elliptical cross section of the main vacuum chamber with 15 mm diameter buttons similar to those used in PEP-II. The placement of the buttons was determined by conformal mapping to give equal horizontal and vertical sensitivity. Extensive PEP-II measurements as well as simulations of the button design give an inductance of 3.7×10^{-2} nH per BPM module (i.e., four buttons) and a loss factor of 2.7×10^{-3} V/pC/module [1]. The full complement of 90 BPM's will have an inductance of 3.3 nH and a loss factor of 0.24 V/pC.

3.5.2.7 Septum Chamber

The septum chamber will conform to the elliptical cross-section of the standard-girder chamber. The injection line enters from the inboard side of the horizontal Lambertson septum, so the discontinuity there determines the impedance. Since the beam does not produce much image current on this side of the pipe, the septum will not provide a large impedance to the beam.

3.5.2.8 Kicker Chambers

The three injection kickers will be based on the slotted-pipe kicker design for the DELTA ring [6]. The copper kickers will have the same cross-section as the standard vacuum chamber, and so they will not introduce any transition impedance. Further, the kickers provide a continuous metallic path for the image currents across the top and bottom of the chamber, where they are the most concentrated. This combination of features results in a low-impedance structure. Its loss factor is more than one order of magnitude smaller than that of a conventional air coil kicker, including those used currently in SPEAR 2. The kicker-loss factor (~0.05V/pC) is extrapolated from the calculated and measured DELTA data.

3.5.2.9 Transverse Striplines

Four pairs of striplines (1 long and 1 short for the horizontal plane, with a corresponding set for the vertical plane as well) will be implemented for diagnostics and for driving the beam. To eliminate the need for transitions, the striplines will be mounted in chambers having the same elliptical cross section as the standard vacuum chamber.

The stripline design is based on a conformal map used to determine the correct positions for maximum strength and sensitivity at the center of the chamber. Since the striplines are terminated externally, they will remove power from the beam, but they not trap modes that could lead to instabilities.

The two transverse kickers (one for each plane) will each contain a 2 cm stripline. The design will derive from the ALS and PEP-II kickers. The low-frequency inductive impedance has been computed at 5.5 nH.

The two feedback pick-up modules will each have four 70 mm striplines. The impedance of each module is calculated to be 13.3 nH, assuming each stripline subtends an angle of 70°.

3.5.2.10 Scraper Chambers

SPEAR 3 will use a modified version of the existing scraper modules. Elliptical spool pieces will be extended into the scraper tanks, where they will mate with new elliptical picture-frame scrapers. Brushes on these spool pieces will act as RF seals to minimize the discontinuities. This discontinuity is more harmful in the vertical plane, where the image currents are concentrated. The loss factor for the scraper chambers is 0.06V/pC.

3.5.3 Power Loss Estimates

As the beam orbits the accelerator, it carries along with it an image current in the vacuum chamber walls. Since the SPEAR 3 chamber walls have finite conductivity, the image current generates Ohmic heating. The Ohmic power comes from the beam and must be restored via the RF cavities. This power loss can be computed as an effective voltage-per-turn supplied by the RF system, by dividing the power loss by the beam current. Each chamber component must be rated for the full 500 mA heat load and the RF system must supply the associated energy loss.

3.5.3.1 Parasitic Power Loss

The use of the frequency domain for energy loss calculations is not limited to the cavities and their high-Q modes. Any field generated by the beam can be decomposed into its frequency modes, and an energy loss for that mode can be calculated. A loss factor, k_n, is defined as the energy deposited by a unit point charge into the n^{th} frequency mode of the structure under study. The total energy deposited by the point charge is then the sum of the deposited energy for all modes. In mks units, this loss factor is commonly quoted as V/pC.

The energy lost by the actual bunch depends not only on the possible modes of the structure. It also depends on the frequency content of the bunch to excite those modes. The total energy lost by a bunch in a single pass through a structure is

$$E = \sum_n k_n |\tilde{\rho}(n\omega_0)|^2 \tag{58}$$

The finite size of the beam gives rise to an envelope in the frequency space. At frequencies above the cutoff-level of the bunch, this energy loss can be neglected . For general structures, the loss factor is typically calculated with numerical codes [4], which output the integrated energy loss over the frequency distribution of the bunch.

As with the cavity modes, the fields from each bunch must be added to obtain the total field and the energy is proportional to the square of the total field amplitude. The modes created by the majority of structures around the ring have a very low Q, the fields dissipate in a time short compared to the time between bunches. In cases such as these, the addition of fields from different bunches is negligible. As with resistive wall heating, this low-Q HOM heating can be treated as a single bunch effect.

For each mode number n, in the frequency band of the bunch, the energy lost per turn by a bunch with charge, q_b, is

$$E_n = k_n q_b^2 \tag{59}$$

The power lost by this bunch is then

$$P_n = k_n T_0 \left(\frac{I_{total}}{N}\right)^2 \tag{60}$$

and the total power lost by N bunches is

$$P_N = k_n T_0 \frac{I_{total}^2}{N} \tag{61}$$

where I_{total} [A] is the total beam current, N is the number of bunches, and T_0 [s] is the revolution period. Table 3.37 lists the power dissipation-per-unit loss factor for various currents and fill patterns. Table 3.39 lists the various discontinuities in the SPEAR 3 vacuum chamber, their loss factors, and resultant power loss at 500 mA. In this table, the HOM losses in the RF cavities have been integrated into an effective loss factor term. The total from all of the HOM losses is 5.17 kW.

Table 3.37 Power dissipated for each unit of k_{loss}.

Current (mA)	kW/V/pC for 140 bunches	kW/V/pC for 280 bunches
200	0.233	.0116
350	0.682	0.341
500	1.393	0.697

3.5.3.2 Resistive Wall Power Loss

The finite conductivity of the vacuum chamber walls creates a low-frequency, broadband impedance consisting of equal real and imaginary parts. The real part of the longitudinal impedance generates a longitudinal electric field which, for a cylindrically symmetric vacuum pipe is

$$E_z = \frac{q_b}{4\pi\varepsilon_0 b}\sqrt{\frac{1}{\pi\sigma Z_0}}\frac{1}{z^{3/2}} \qquad (62)$$

where q_b is the charge per bunch, b is the radius of the beam pipe, σ is the conductivity of the chamber wall, Z_0 is the free space impedance, and z is the distance behind the bunch. As shown by this formula, the field dies off rapidly with increasing distance from the bunch. Its strength falls fast enough that, in the case of SPEAR 3, the resistive wall loss is a single-bunch phenomenon.

For a gaussian bunch of length $c\sigma_t$, the total power loss per unit length for a single bunch can be calculated analytically. Following the same line of reasoning as when calculating the total power-loss factor, one obtains the total resistive-wall power-per-unit length, in mks units, as

$$\frac{P}{L} = \frac{1}{(2\pi)^2}\Gamma\left(\frac{3}{4}\right)\frac{T_0}{N}\frac{I_{tot}^2}{b\sigma_t^{3/2}}\sqrt{\frac{\mu_0}{2\sigma}} \qquad (63)$$

where μ_0 is the free-space permeability. Table 3.38 lists the power load, in W/m, generated by the resistive-wall impedance for various chamber materials, beam currents, and beam filling patterns. Section 3.5.3.3 summarizes total resistive-wall losses.

Table 3.38 Power dissipation (W/m) for vacuum chamber materials with different conductivity σ.

	Stainless steel $\sigma = 1.4 \times 10^6\ \Omega^{-1}\ m^{-1}$		Aluminum $\sigma = 3.5 \times 10^7\ \Omega^{-1}\ m^{-1}$		Copper $\sigma = 5.9 \times 10^7\ \Omega^{-1}\ m^{-1}$	
Number bunches	140	280	140	280	140	280
I_{tot}= 200 mA	3.01	1.49	0.6	0.301	0.464	0.232
I_{tot} = 350 mA	9.18	4.59	1.85	0.93	1.42	0.71
I_{tot} = 500 mA	18.69	9.37	3.77	1.89	2.88	1.53

For copper chambers, resistive-wall heating is minimal. The resistive-wall power dissipation per unit length along the copper chamber is 1.53 W/m.

3.5.3.3 Beam Energy Loss

The energy lost by each particle due to HOM and resistive-wall heating must be replenished by the RF cavity. The energy gain of the bunch as it travels through the cavity is $q_b V_{rf}$. The voltage the cavity needs to provide for these losses is

$$P_{loss}/I_{total}\,. \tag{64}$$

The total loss of 565 W to resistive-wall heating and 5.17 kW to HOM heating work out to a requirement for an additional 10.3 kV of RF gap voltage. Even if these numbers are too small (Section 3.5.4) and overly optimistic, the total voltage required to compensate for those losses remains very small in comparison to the total-gap voltage.

Since both power and voltage loss are proportional to the single bunch current, these values will increase dramatically for the high single-bunch currents desired for timing mode operation.

3.5.4 Impedance Budget - Conclusions

The dominant impedance sources in SPEAR 3 are the RF cavities and resistive walls of the vacuum chamber. Structures such as bellows shields, RF seals, BPMs, and tapered transitions add inductive impedance at frequencies below 15 GHz. These elements also have high-frequency resistive components generating the k_{loss} factors listed in Table 3.39. Relative to the inductive impedance of existing 3rd-generation storage rings, the total estimated inductive impedance of 0.56 Ω (70.2 nH at 1.28 MHz) is somewhat low. The discrepancy comes from small elements and transitions not accounted for in the estimates given above. As a result, conservative values will be used for all collective effect calculations which involve the broadband impedance. For bunch length and energy widening thresholds (Section 3.6.1), 1Ω will be used (1Ω is comparable to the measured value on contemporary storage rings). A value of 0.5 Ω will be used for the head-tail damping calculations (Section 3.6.2.2.3).

Table 3.39 Main contributors to impedance and chamber power dissipation in SPEAR 3.

Element	Number	Inductance / element (nH)	Total inductance (nH)	k_{loss}/element (V/pC)	Power/el (W) (200 mA in 280 bunches)	Power/el (W) (500 mA in 280 bunches)
RF cavities	4			1.120	125	784
Bellows shield	80	0.073	5.8	0.0107	1.20	7.49
RF seals	197	0.018	3.5	$4.4.10^{-4}$	0.05	0.31
BPMs	90	0.037	3.3	0.0027	0.30	1.89
Transitions	14 + 6	1	20	0.02	2.24	14.0
Transverse kickers	2	5.5	11	0.66	73.8	461
Transverse PU	2	13.3	26.6			
Girder chambers (resistive wall)					53.6	335
ID chambers (resistive wall)					36.9	231
Total			70.2		917	5734

References

[1] S. Heifets et al., "Impedance Study for PEP II B-Factory", PEP-II AP Note No. 95.02

[2] A. Chao, "Physics of Collective Beam Instabilities in High Energy Accelerators", Wiley Interscience, 1993.

[3] L. Palumbo et al., "Wake fields and impedance", 1993 CERN Accelerator School, CERN 95-06, Nov. 1995.

[4] Y. Chin, "Users' guide for new ABCI (Azimuthal Beam Cavity Interaction)", LBL-35258, CBP Note-069, 1994.

[5] W. Bruns, "GdfidL", Institut fur Theoretische Elektrotechnik Technische Universitat Berlin, Nov. 1996.

[6] G. Blokesch, M. Negrazus, K. Wille, "A Slotted-Pipe Kicker for High-Current Storage Rings", Nuclear Instruments & Methods in Physics Research, Section A 338 (1994) 151-155.

[7] J.Sebek, C.Limborg, "Characterization of RF cavity HOMs with beam", Frascati Physics, ICFA 97.

[8] R.Rimmer, "Updated impedance estimate of the PEP-II RF cavity", EPAC 96, Sitges 1996.

3.6 Collective Effects and Stabilization

To operate SPEAR 3 with high beam quality up to 500 mA, the single-bunch current and total beam current must not exceed the thresholds for single-bunch and multibunch instabilities. Given the estimates for RF cavity and vacuum chamber impedances (Section 3.5), the instability thresholds can be calculated from analytical formulae and simulation codes. The following sections discuss results for single- and coupled-bunch effects and limitations.

Broadband impedance is dominated by the vacuum chamber through the arcs, the transitions into the ID straight sections, and modular components like BPMs and bellows. As described in Section 3.5, each component has been designed to minimize broadband impedance. The resulting low value for broadband impedance (<1 Ω) provides a 4.5 mA single-bunch longitudinal instability threshold and a 28 mA transverse-mode coupling threshold.

Table 3.40 Machine Parameters for SPEAR 2 and SPEAR 3

	SPEAR 2	SPEAR 3
ρ	12.8 m	7.87 m
E	3 GeV	3 Gev
γ	5870.8	5870.8
L	234.126 m	234.126 m
f_0	1.2805 MHz	1.2805 MHz
T_0	781 ns	781 ns
Loss/turn (with SPEAR 2 IDs)	760 keV	1.12 MeV
h	280	372
V_{rf}	1.68 MV	3.2 MV
$\cos\phi_s$	0.89	0.937
α	1.5×10^{-2}	1.12×10^{-3}
dp/p (natural)	7.4×10^{-4}	9.7×10^{-4}
J_x	1	1.21

Table 3.40 Machine Parameters for SPEAR 2 and SPEAR 3

	SPEAR 2	SPEAR 3
J_y	1	1.00
J_z	2	1.79
τ_x	8.36 ms	4.24 ms
τ_y	8.36 ms	5.14 ms
τ_z	4.18 ms	2.87 ms
f_s	23.4 kHz	10.4 kHz
σ_t	75 ps	16 ps
Q_x	7.13	14.19
Q_y	5.22	5.23
$\beta_{x\ \text{straight sections}}$	20 m	10.2 m
$\beta_{y\ \text{straight sections}}$	1.8 m	4.7 m

The new RF cavities, the small momentum compaction factor, and the short radiation-damping time (Table 3.46) act favorably to increase the multibunch instability thresholds above 500mA, a level dramatically above SPEAR 2 levels. In SPEAR 3, the coupled bunch resistive wall instability occurs at about 190 mA in the vertical plane and at 683 mA in the horizontal plane for zero chromaticity. With positive chromaticity, if head-tail damping is not sufficient to damp resistive wall instabilities at 500 mA, a transverse feedback system will be installed.

3.6.1 Single Bunch Thresholds

The longitudinal (microwave) and transverse (mode-coupling) single-bunch instability thresholds are discussed below. For $\left|\frac{Z_{//}}{n}\right| = 1\ \Omega$, the microwave instability threshold is about 4.5 mA/bunch. The mode-coupling instability threshold is about 28 mA/bunch.

3.6.1.1 Longitudinal Single Bunch Instability

The longitudinal single bunch instability, known as the 'microwave instability', does not lead to a beam loss. Above threshold, however, the bunch length increases and the energy spread widens, resulting in a broadening of the undulator spectra and a reduction in the photon flux of the dipole beamlines.

3.6.1.1.1 Broadband Impedance Model

The two main contributions to the broadband longitudinal impedance come from high-Q RF cavity modes and low-Q vacuum chamber components (bellows, RF seals, transitions, etc.). In SPEAR 3, the cavity contribution can be neglected since the reactive impedance, integrated over the bunch spectrum, is close to zero and its resistive part is small.

The accuracy of the low-Q vacuum chamber model is limited by computing time and insufficient knowledge of the chamber design. From the estimate for the low frequency inductive impedance (Section 3.5.4),

$$\left|\frac{Z_{//}}{n}\right|_{\omega = 0} = \frac{R_s}{Qn_r} = 1\Omega \qquad (65)$$

where $\left|\frac{Z_{//}}{n}\right|$

is the normalized longitudinal broadband impedance, n_r is the resonator center frequency divided by the revolution frequency, f_0, and n is the frequency of interest normalized by f_0. From the lack of strong resistive peaks below 15 GHz shown by the ABCI [1] runs, and from the experience gained on other machines, the broadband model for the vacuum chamber was chosen to be:

- $R_s = 11.7\ \text{k}\Omega$,
- $Q = 1$,
- $f_r = 15$ GHz

The 11.7 kΩ shunt impedance (based on $\left|\frac{Z_{//}}{n}\right| = 1\ \Omega$ inductive impedance) will give conservative values for single bunch instability thresholds.

3.6.1.1.2 Keil-Schnell-Boussard Formulation

Keil and Schnell [2] calculated a criterion for longitudinal stability of coasting beams. Boussard [3] extended this formula to bunched proton beams. The extended formula also applies to bunched electron beams with the correct effective impedance [4]–which, in turn, depends on the bunch spectrum and on the resistive part of the broadband impedance. The Keil-Schnell-Boussard formulation gives a microwave instability current threshold I_{th}:

$$I_{th} < \frac{1.5(\omega_0\sigma_\tau)^3 V_{rf} h \cos\varphi_s}{\frac{R_{eff}}{n_r}\sqrt{2\pi}} \tag{66}$$

with

- ω_0 = ring revolution frequency ($2\pi\ 1.28 \times 10^6$ rad/s)
- σ_τ = rms bunch length (~15 ps)
- V_{rf} = RF voltage (3.2 MV)
- h = harmonic number (372)
- φ_s = synchronous phase (160 degrees).

The effective impedance,

$$\frac{R_{eff}}{n_r}\ , \tag{67}$$

as computed from [4] appears in Figure 3.58 with

$$\Delta\omega = \frac{\omega_r}{Q} = 2\pi \times 15\ \text{GHz} \tag{68}$$

and $\sigma_\omega = 1/\sigma_\tau$. Assuming the high-frequency broadband resonator model given in Section 3.6.1.1.1, the single bunch microwave instability threshold is 4.5 mA.

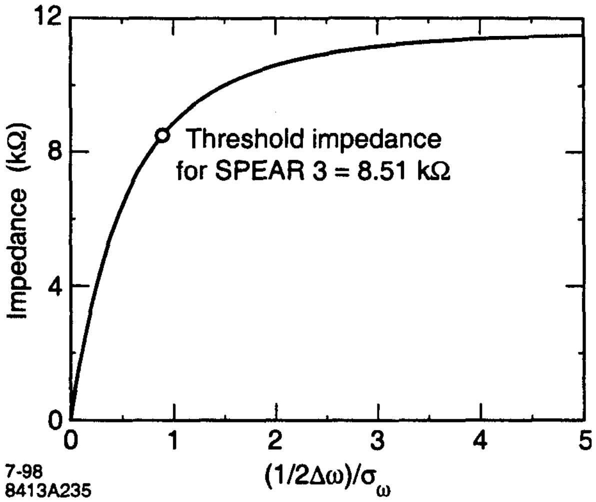

Figure 3.58 Effective impedance vs. ratio of resonance width to bunch spectral width.

3.6.1.1.3 Tracking Code Results

A multi-particle tracking code for longitudinal motion [4] was used to compute bunch lengthening and energy widening as a function of current (Figure 3.59). From 0 to 4.5 mA, the bunch lengthens by up to a factor of 1.3, while the energy spread remains at the zero-current value. Above 4.5 mA, energy-widening sets in which degrades the undulator harmonics (Section 3.3.2) and increases horizontal beam size at the dispersive bending magnet source points. The 4.5 mA microwave instability threshold given by the tracking code is consistent with the Keil-Schnell-Boussard formula. The agreement improves when the bunch-lengthening factor of 1.3 predicted by the tracking code is included in the formula. For 500 mA operation with a 280 bunch fill pattern, the 1.8 mA single bunch current is well within stable limits.

The tolerable level of energy widening can be estimated by considering its impact on the 5th harmonic line width of a 100-period undulator. The nominal line width, given by the convolution of the ideal line width of 1/nN (n = harmonic number, N = number of undulator periods) with the low-current beam energy spread of 0.1%, is ~0.28% when normalized to the wavelength of the spectral line. At a single bunch current of 18 mA, the energy spread increases to 0.15% and the line width increases by 30%. Low-harmonic line widths are less affected and can tolerate higher single bunch currents.

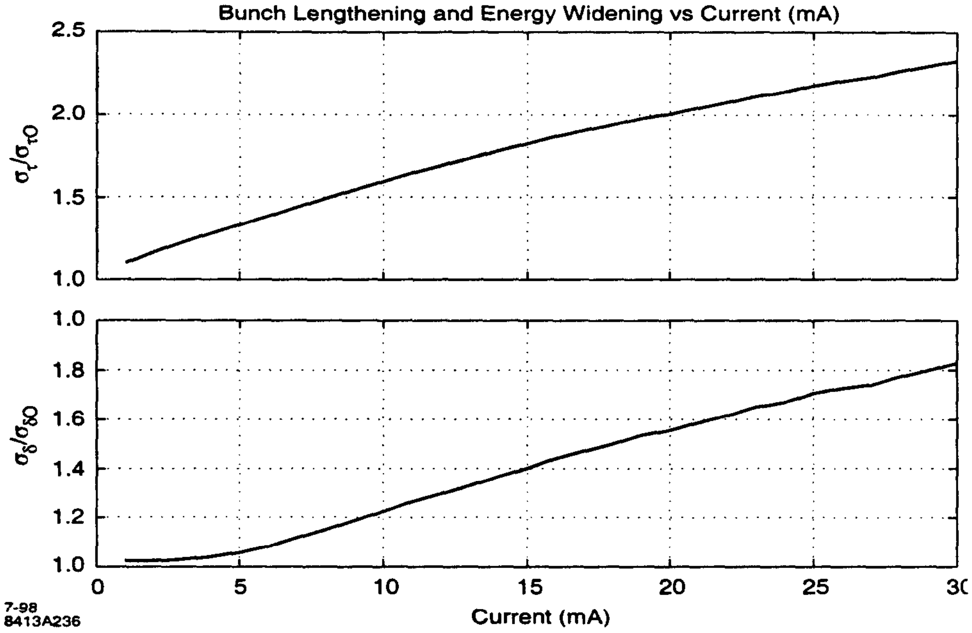

Figure 3.59 Bunch-lengthening and energy-widening as a function of single bunch current in SPEAR 3.

3.6.1.2 Transverse Single Bunch Instability

In some large electron rings, such as PEP-I, the single bunch current limit was set by transverse mode coupling. An approximation to this threshold can be calculated using a two-particle model of coupling between the transverse and longitudinal motions [5]. In this model, stability exists for bunches with fewer than N_b particles, where

$$N_b < 16\frac{\gamma Q_y Q_s \omega_o}{W_o r_o c} \tag{69}$$

and

- γ =Lorentz relativistic factor (5871)
- Q_y = vertical betatron tune (5.23)
- Q_s = synchrotron tune (0.0081)
- ω_o = ring revolution frequency (2π x 1.28 x 10^6 rad/s)
- r_o = classical electron radius (2.28x10^{-15} m)
- c = speed of light (3x10^8 m/s)
- b = chamber radius (22 mm, Section 3.???).

The short range transverse wake, W_o, is given by

$$W_o = \frac{c}{b}\left(\frac{\langle\beta_y\rangle Q_y}{R}\right)Z_\perp \tag{70}$$

where R is the ring radius, and the transverse impedance is given by

$$Z_{\perp} = \frac{2R}{b^2}\left|\frac{Z_{//}}{n}\right| \tag{71}$$

For a $\left|\frac{Z_{//}}{n}\right|$ of $1\,\Omega$, (72)

N_b is 1.4×10^{11} electrons at threshold, corresponding to a single-bunch current of 28 mA in SPEAR 3. This approximation demonstrates that transverse mode-coupling will not be a problem during normal operation.

3.6.2 Multibunch Motion and Stabilization

Longitudinal and transverse-coupled bunch-motion growth rates and stabilizing measures are addressed in the following sections.

3.6.2.1 Longitudinal Coupled Bunch Motion

Wakefields resulting from the passage of the electron beam through a high-Q resonant structure can lead to coupled bunch oscillations. The long-term wakefields provide a voltage which can excite synchrotron oscillations on subsequent bunches. For M bunches, there exist M possible modes of oscillation, labeled by a bunch number m, where $0 \le m < M$.

The current threshold for longitudinal coupled-bunch oscillations is determined by the dipole mode of the synchrotron oscillation. The dipole oscillations increase the effective energy spread and, as discussed in Section 3.3.2, degrade both undulator and dipole beamline performance. The stability threshold for quadrupole synchrotron modes is higher.

3.6.2.1.1 Longitudinal Instability Threshold Currents

A longitudinal HOM can generate an instability when the growth due to the perturbing voltage is larger than the radiation damping. The perturbing voltage is the product of the total beam current and the shunt impedance of the RF cavity HOM. The threshold is reached when

$$\frac{1}{\tau_{\mathrm{radiation}}} = \frac{1}{\tau_{\mathrm{growth}}} = 2\pi f_s \frac{p I_o e^{-\omega_p^2\left(\sigma_s^2/c^2\right)} R_s}{2hV_{rf}\cos\varphi_s} \tag{73}$$

with

- n = harmonic number of the resonance
- h = harmonic number of the ring (372)
- I_o= total beam current
- V_{rf} = RF gap voltage (3.2 MV)
- f_s = synchrotron frequency (10.4 kHz)
- φ_s = synchronous phase (160 degrees)
- R_s = resonator shunt resistance
- σ_s bunch length (15 ps)
- $\omega_p = 2\pi \times$ resonator frequency.

By using the PEP-II cavities, even the strongest longitudinal HOM is too small to excite instabilities at 500 mA. Operational experience at PEP-II has shown $R_{||} < 2.2\ \mathrm{k}\Omega$ for all modes. For the HOM with $f_r = 1.295$ GHz ($Q = 222$), the line width at -3dB is 2.9MHz. Given the large width of the low-Q HOMs, the SPEAR 3 beam spectrum will always overlap the impedance. In the worst case, however, with all four cavities tuned so that the same spectral line overlaps the 2.2 kΩ HOM, the threshold current will still be 900mA.

The high longitudinal instability threshold also comes from the favorable machine parameters of SPEAR 3 with respect to those of SPEAR 2 (Equation) the synchrotron frequency decreases from 23.4 kHz to 10.4 kHz, the RF voltage increases from 1.68 MV to 3.2 MV, and the damping time decreases from 4.2 ms to 2.87 ms. The net result is that SPEAR 3 will be stable at currents at least 9 times higher than that of SPEAR 2. Given the high coupled bunch instability threshold, no longitudinal multibunch feedback system will be needed for up to 500 mA operation.

3.6.2.2 Transverse Coupled Bunch Motion

Transverse coupled bunch instabilities come from either resistive wall impedance at the lowest betatron sidebands or from high-Q resonances in the RF cavities. Transverse coupled bunch instabilities can lead to a beam loss.

The growth rate of a transverse coupled bunch instability is given by

$$\frac{1}{\tau} = \frac{eI_o\beta_\perp}{2\pi M\sigma_\tau E}Z_{\perp_{eff}} \quad [3.6.2.2\text{-}1] \qquad (74)$$

where the effective transverse impedance, at zero chromaticity, is

$$Z_{\perp_{eff}} = \frac{\sum_{p=-\infty}^{\infty} Z_{\perp_r}(\omega_p)h_0(\omega_p)}{\sum_{p=-\infty}^{\infty} h_o(\omega_p)} \quad [3.6.2.2\text{-}2] \qquad (75)$$

with

- $\omega_p = (p\,M + m + Q)\,\omega_o$
- Q = betatron tune
- M = number of bunches
- p and m are integers, with m being the mode number
- $\beta_\perp$ is the β-function at the generated impedance
- I_o = total beam current
- σ_τ = rms bunch length (16 ps)
- E = beam energy (3 GeV)
- $Z_{\perp r}$ is the real part of the transverse impedance.

For a Gaussian bunch, the power spectrum is given by

$$h_o(\omega) = \exp[-(\omega\sigma_\tau)^2] \qquad (76)$$

The instability current threshold is usually imposed by the dipole mode, i.e. rigid body motion. Only at very high chromaticities do other modes have a faster growth rate.

3.6.2.2.1 Resistive Wall Instabilities

The resistive wall impedance for each vacuum chamber component is given in Section 3.5.3.2. For SPEAR 3, the largest impedance contributions come from the narrow-gap insertion devices (Section 3.5.1.2). Because of the dimensions of the main vacuum chamber, the effective vertical impedance is about twice the horizontal impedance [6].

Due to the $\omega^{-1/2}$ frequency dependence, the resistive wall impedance is strongest at low frequencies. As with all instability calculations, the growth or damping of each eigenmode depends on the impedance at the mode frequencies of the beam. For a uniform fill pattern, the modes most affected by the resistive wall are those with an index closest to the vertical betatron tune. These modes sample the impedance at low frequency, where the resistive wall impedance is large. For a betatron tune with its fractional part below the half-integer, the largest impedance provides damping to the corresponding mode. The mode with the next lowest index, however, will be dominated by a growth term (Figure 3.60). If this term is large enough, the mode is unstable.

For SPEAR 3, the resistive wall impedance generated by the main vacuum chamber and ID chambers is sufficiently large that the radiation damping alone cannot suppress the two most unstable modes. Additional damping must be provided by head-tail damping with positive chromaticity.

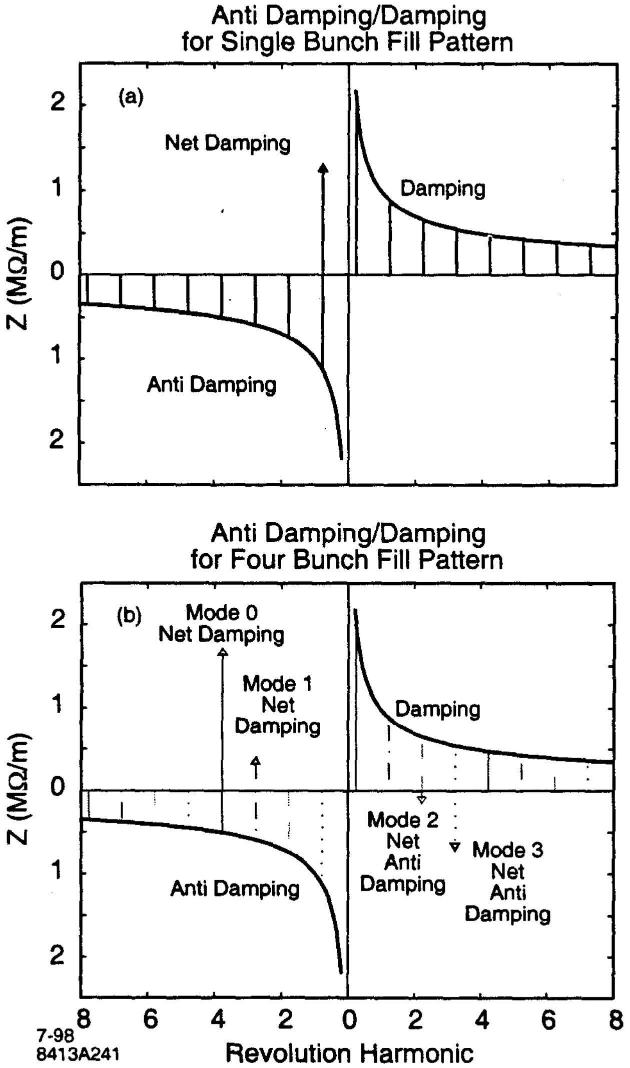

Figure 3.60 Beam spectrum and transverse resistive wall impedance for (a) single bunch and (b) 4 equally distributed bunches, mode −1.

To estimate the resistive wall instability growth rate, note that most of the SPEAR 3 ID chambers are made of stainless steel (Section 3.5.2.2). Any new IDs and the main SPEAR 3 vacuum chamber will be made of copper.

Vertical resistive wall impedance can induce coupled bunch instability in the vertical plane. The total resistive wall impedance, $Z_\perp\sqrt{\omega}$, is calculated to be 1.64 GΩ–m^{-1}-s$^{-1/2}$ or 0.36 and 1.28 GΩ–m^{-1}-s$^{-1/2}$, respectively for the main copper vacuum chamber and the stainless steel ID chambers (Section 3.5.3.2). As a result, the ID chambers dominate the resistive wall impedance.

The maximum resistive wall impedance seen by the beam is

$$Z_\perp = Z_{\perp 0}\sqrt{\frac{1}{1-f_{Qy}}}, \tag{77}$$

where f_{Qy} is the fractional part of the vertical tune and $Z_{\perp 0}$ the resistive wall impedance at f_o. With a vertical tune of 5.23, the largest anti-damping contribution occurs at $0.77f_0$, where $Z_\perp = 658$ kΩ–m^{-1}. The growth rate of the resistive wall instability is given by

$$\frac{1}{\tau} = f_o\frac{eI_0\langle\beta_\perp\rangle}{E\sqrt{\pi}}Z_\perp \tag{78}$$

At the ID locations, the vertical betatron function β_y is 4.8m while the average value $<\beta_y>$ in the ring is 8.5m. Given the transverse impedance $Z_\perp = 658$ kΩ–m^{-1}, the growth rate per mA of beam current is 0.89 $s^{-1}mA^{-1}$, shared as 0.594 $s^{-1}mA^{-1}$ and 0.294 $s^{-1}mA^{-1}$ between the ID chambers and the main copper vacuum chamber contributions.

As the vertical radiation damping rate is 181 s^{-1}, the transverse coupled bunch instability threshold is 203 mA if head-tail damping is ignored. With a normalized chromaticity of 0.16, the head-tail damping rate for 500 mA distributed in 280 bunches is 264 s^{-1}(Section 3.6.2.2.3). This computation assumes a broadband impedance peaked at 15 GHz and $\left|\frac{Z_{//}}{n}\right| = 0.5\ \Omega$. Adding the 264 s^{-1} head-tail damping to the 181 s^{-1} from radiation damping, the total damping counterbalances the 445 s^{-1} instability growth rate.

Horizontal resistive wall impedance can induce coupled bunch instability in the horizontal plane. Approximating the horizontal resistive wall impedance by half the vertical value with an average betatron function $<\beta_x>$ of 5.6 m in the girder chamber and the β_x value of 10.2 m in the IDs, the largest growth rate for a fractional tune of 0.19 is 0.7 s-mA^{-1}. The radiation damping, 4.24 ms in the horizontal plane, will damp out any horizontal resistive wall instabilities for beam currents up to 332 mA.

The horizontal damping rate is computed with a broadband impedance which is half that used in the vertical plane. A normalized chromaticity of 0.14 is required to supplement the radiation damping to stabilize a 500 mA beam distributed in 280 bunches.

In case the instability growth rate is underestimated, the damping rate could be raised by increasing chromaticity (or increasing the single bunch current), or by using a transverse feedback system (Figure 4.7.2).

3.6.2.2.2 Transverse RF Cavity HOMs

The strongest transverse HOM impedance in the PEP-II cavities is $R_\perp = 161$ kΩ–m^{-1}. In the vertical plane, for this impedance and $\beta_y = 12$ m, the current threshold will be 421 mA. In the horizontal plane as the radiation damping time is shorter, the threshold current is 513 mA for a $\beta_x = 12$m. In practice, the RF cavities will be located in the West Racetrack straight where $\beta_y = 10$ m and $\beta_x = 5$ m so the instability thresholds will be somewhat higher.

With all 4 cavities tuned on the maximum of this resonance, the current threshold would decrease by a factor of 4. Since this impedance has a Q of 1138, its width at -3dB is 0.62 MHz, or about one-half of the revolution frequency. An appropriate choice of the cavity temperature should allow this HOM cavity impedance to be tuned away from the betatron lines. Additional head-tail damping should also provide stabilization (Figure 3.6.2.2.3).

3.6.2.2.3 Head-Tail Damping

Head-tail damping is a single bunch effect which depends on the chromaticity and the current per bunch. The head-tail damping rate is given by

$$\frac{1}{\tau_{head-tail}} = \frac{ecI_0\beta}{2\pi k N_b \sigma_s E} Z_{\perp eff} \qquad (79)$$

with

- e = electronic charge ($1.6\text{x}10^{-19}$ C)
- c = speed of light ($3\text{x}10^{8}$ m/s)
- I_o = total beam current
- β= betatron function
- N_b = number of bunches
- σ_s = bunch length (15 ps)
- E = beam energy (3 GeV)
- $Z_{\perp,\mathrm{eff}}$ is discussed below.

Due to the current dependence, head-tail damping can be increased by filling more current per bunch, but high single bunch currents can deteriorate Touschek lifetime. Instead, positive chromaticity (ξ >0) can be used to enhance head-tail damping and decrease transverse oscillation growth rates.

A non-zero chromaticity shifts the power spectrum by the chromatic frequency

$$\omega_\xi = Q\omega_0\frac{\xi}{\alpha} \qquad (80)$$

where ξ is the normalized chromaticity, Q is the betatron tune, f_0 is the revolution frequency, and α is the momentum compaction factor. The effective transverse impedance, accounting for the chromatic frequency, is given by

$$Z_{\perp,\,eff} = \frac{\sum_{p=-\infty}^{p=\infty} Z_{\perp_r}(\omega_p)h_0(\omega_p-\omega_\xi)}{\sum\limits_{p=-\infty} h_0(\omega_p-\omega_\xi)} \approx \frac{\int_{-\infty}^{\infty} Z_{\perp_r}(\omega)h_0(\omega-\omega_\xi)d\omega}{\int_{-\infty}^{\infty} h_0(\omega-\omega_\xi)d\omega} \qquad (81)$$

For a broadband resonator model, the expression for $Z_{\perp,\mathrm{eff}}$ reduces to

$$Z_{\perp,\,eff} = \frac{1}{\sqrt{\pi}}R_\perp\int_{-\infty}^{\infty}\frac{x_r^3 x e^{-(x-x_\xi)^2}}{x_r^4 - x_r^2x^2 + x^4}dx \qquad (82)$$

with $x = \frac{\omega\sigma_s}{c}$, $x_r = \frac{\omega_r\sigma_s}{c}$, and $x_\xi = \frac{\omega_\xi\sigma_s}{c}$ [ref???].

The transverse broadband impedance model for SPEAR 3 has a resonant frequency f_r = 15 GHz, transverse shunt resistance $R_\perp$ = 77 kΩ–m^{-1}, and quality factor Q = 1. Based on a $\left|\frac{Z_\parallel}{n}\right|$ = 0.5 Ω impedance model, $Z_{\perp,\mathrm{eff}}$ is plotted in Figure 3.61 for f_r = 10 GHz, 15 GHz, and 20 GHz center frequencies.

Table 3.41 gives the head-tail damping rate as a function of chromaticity for the vertical broadband impedance. This broadband impedance was computed using the Panofsky-Wenzel theorem from the longitudinal impedance (while assuming a cylindrical geometry), with an effective radius of 22 mm. To compensate for the deviation from the circular symmetry, the horizontal broadband impedance has been approximated to one-half of the vertical value [6].

Table 3.41 Head-tail damping for 500mA in 280 bunches and a broadband impedance having a $Z_{//}/n = 0.5\Omega$ with $f_r = 15$ GHz, $R_\perp = 77$ kΩ-m^{-1}, Q = 1.

Chromatics	$Z_{\perp,eff}$ kΩ–m^{-1}	$1/\tau$ s^{-1}
0.1	3.4	166
0.2	6.8	333
0.3	10.2	500
0.4	13.6	666

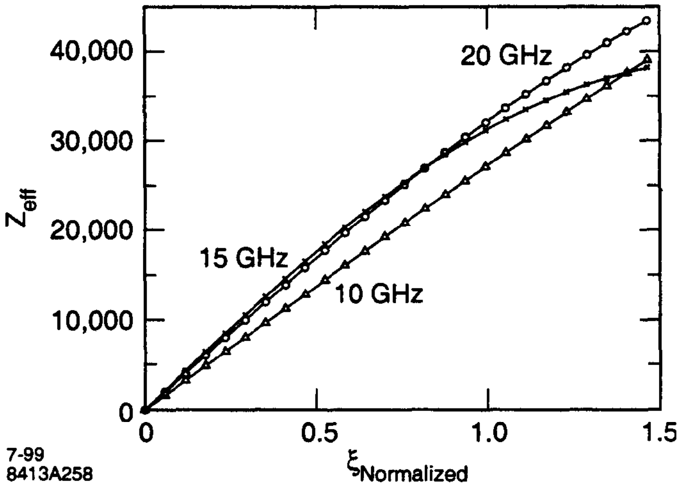

Figure 3.61 Effective transverse impedance providing head-tail damping for $f_r = 15$ GHz, $R_\perp = 77$ kΩ-m^{-1}, Q = 1

3.6.2.2.4 Transverse Feedback Requirements

Three sources of transverse instability must be counteracted: 1) resistive wall impedance, 2) cavity HOMs for the stored beam, and 3) cavity HOMs for the injected beam. The combination of radiation and head-tail damping should provide enough passive stabilization in SPEAR 3. However, since the head-tail damping is difficult to evaluate accurately before all elements are installed in the ring, specifications for a feedback system have been considered.

The transverse-feedback kicker specified in Section 4.7.2 will have a shunt resistance of R_s=7 kΩ [7] and will be driven by a 120 W amplifier. The voltage kick will be 1.3 kV. Neglecting radiation damping, this transverse kick can counteract an instability driving voltage of $V_b = I_o \Delta x Z_\perp$.

3.6.2.2.3.1 Feedback for resistive wall instability.

The vertical resistive-wall instability at 500 mA, for an impedance $Z_\perp = 522$ kΩ-m^{-1} and an average beta $<\beta_y> = 8.54$ m, has a growth rate of 475 s^{-1}. Assuming a conservative orbit offset of 2 mm with respect to the chamber axis, a kicker voltage of 447 V provides total damping. Since radiation damping will also contribute a damping rate of 181 s^{-1}, a 1.3 kV kicker voltage is more than adequate.

3.6.2.2.3.2 Feedback for cavity HOM's: stored beam.

If a 4 MΩ–m^{-1} cavity HOM drives coupled bunch motion at 500 mA, the maximum orbit offset in the cavity, which can be controlled by the feedback system (operating in the linear regime), is 650 µm. Since the orbit correction system is able to position the beam in the cavity to better than 300 µm, the feedback system will be sufficient. The strongest transverse impedance of the PEP-II cavities is 161 kΩ–m^{-1}

3.6.2.2.3.3 Feedback for cavity HOM's: injected beam.

Assuming a 10 Hz injection rate and an accumulation rate of 20 mA/min, each injected pulse carries an equivalent bunch current of I = 33 µA. The orbit offset is Δx = 10mm with respect to the stored-beam orbit. Assuming this beam interacts with a cavity impedance $Z_{\perp}$= 200 kΩ–m^{-1}, the injected bunch can be stabilized with only a 0.26 V kick from the feedback system.

3.6.3 Conclusions

The new RF cavities, the low-impedance copper vacuum chamber, the small momentum compaction, and the increased radiation damping in SPEAR 3 act favorably to increase instability thresholds with respect to SPEAR 2. For routine operation with 500 mA in 280 bunches, single-bunch instabilities are not an issue, since the microwave instability threshold is 4.5 mA, with very weak energy widening for energies above that threshold. For timing mode operation where four evenly spaced buckets are filled, the upper limit is set by the transverse mode-coupling current threshold of ~28 mA. At this current, the 0.18% energy spread is tolerable at the third undulator harmonic. The limiting factor for the timing mode is set by the resistive heat load in the ring (Section 4.2.4.4).

Transverse coupled-bunch instabilities, generated by resistive-wall impedance might require a feedback system when all IDs are installed. With both normalized chromaticities above 0.15, 500 mA distributed over 280 bunches should be stable.

When the mode-damped PEP-II style RF cavities are appropriately tuned, no horizontal or vertical coupled bunch motion driven by cavity HOM's is expected below 500mA. No longitudinal multibunch feedback system should be necessary.

Table 3.42 Table Summary of Instability thresholds

	Longitudinal	Transverse (H/V)
Multibunch	900 mA	421/ 513
Single Bunch	4.5 mA	28 mA

Table 3.43 Summary Resistive Wall Instability thresholds

	Vertical	Horizontal
Threshold when no head-tail damping	203 mA	332 mA
Normalized chromaticity for stability at 500 mA	$\xi_y = 0.16$	$\xi_x = 0.14$

References

[1] Y. Chin, "Users' guide for the new ABCI", LBL-35258, CBP Note 069, 1994

[2] E.Keil, W.Schnell, CERN report TH-RF/69-48(1969)

[3] D.Boussard, CERN Lab II/ RF/Int 75-2, 1975

[4] C.Limborg, PhD thesis, ESRF 1996

[5] A.Chao, "Physics of Collective Beam Instabilities in High Energy Accelerators", John Wiley & Sons, 1993

[6] L.Palumbo, et.al., "Wake Fields and Impedance", CERN Accelerator School, October 1993, CERN 95-06.

[7] W.Barry et.al, "Design of the ALS Transverse Coupled-bunch Feedback System" Proceedings of the IEEE Particle Accelerator Conference 1993, pp 2109-2111.

[8] A.Hofmann, C.Limborg, "Beam Instabilities in SPEAR 3", April 10, 1997, SSRL Note April 1997

3.7 Beam Lifetime

To reach the target beam lifetime of >15 hr with 500 mA stored beam, the RF gap voltage, residual gas pressure and dynamic aperture must all meet challenging standards. In this section, the particle loss mechanisms leading to finite lifetime are calculated for a 3.2 MV RF gap voltage, an average neutral gas pressure of 1.8 nT (N_2-equivalent), and a range of momentum-dependent dynamic apertures. The effect of increasing synchrotron radiation power load as more wigglers are added is also examined.

Particle losses in storage rings occur through three main processes: 1) quantum excitation, 2) elastic and inelastic collisions with background gas, and 3) intra-beam scattering (Touschek effect). The total beam lifetime, τ, is defined by the instantaneous loss rate,

$$\frac{1}{\tau} = \frac{1}{N}\frac{dN}{dt} \tag{83}$$

where N total is the total number of particles in the beam. The individual loss mechanisms contribute to the beam lifetime according to the relation

$$\frac{1}{\tau} = \frac{1}{\tau_{\text{quantum}}} + \frac{1}{\tau_{\text{elastic}}} + \frac{1}{\tau_{\text{ineleastic}}} + \frac{1}{\tau_{\text{intra-beam}}} \tag{84}$$

Using a 1.8 nT average N_2-equivalent gas pressure (Section 3.7.2.1), the elastic and inelastic gas scattering lifetimes in SPEAR 3 are 89 hr and 41 hr, respectively at 500 mA. The net gas scattering lifetime is 28 hr. The intra-beam scattering lifetime, assuming 280 bunches*, 1% coupling, ±18 mm horizontal dynamic aperture in the 3.1 m straights, and a synchrotron radiation loss of U_0=1.12 MeV/turn is 74 hr at 500 mA. The net beam lifetime is therefore 18.3 hr at 500 mA.

As more IDs are installed, the radiation power load will increase causing the inelastic gas scattering and the intra-beam scattering lifetimes to decrease. With U_0=1.61 MeV/turn (maximum projected ID load), the total estimated beam lifetime drops to about 16 hr at 500 mA with a gap voltage of 3.2 MV. Insertion devices with small vacuum chambers can further reduce beam lifetime via the large amplitude non-linear coupling process discussed in Table 3.1.7.4.

*280 bunches correspond to 3/4 of the total number of buckets. An analysis of ion effects is presented in Section 3.8.

3.7.1 Quantum Lifetime

As a result of quantum emission and radiation damping, the electron bunches have a 3-dimensional Gaussian distribution. The far tails of the distribution can be truncated by the longitudinal and transverse acceptance of the storage ring, leading to beam loss. The quantum lifetime in each dimension is given by

$$\tau_q = \frac{\tau e^{\rho}}{2\rho} \tag{85}$$

where

$$\rho = \left(\frac{1}{2}\right)\left(\frac{A}{\sigma}\right)^2, \tag{86}$$

τ is the damping time, A is the storage ring acceptance, and σ is the rms beam size in the appropriate dimension.

In the longitudinal direction, an RF voltage of 1 MV will provide a quantum lifetime of 34 h; at 1.1 MV, the quantum lifetime exceeds 10^{11} h. In the horizontal plane, the aperature limit is the 18 mm dynamic aperture in the 3.1 m straights where β_x=10.2 m. For an emittance of 18 nm-rad, the quantum lifetime is essentially infinite. In the vertical plane the limiting apertures are at the 6 mm ID chambers for Beamlines 6 and 11, but quantum lifetime is again infinite.

3.7.2 Gas Scattering Lifetime

Electrons can be lost to elastic (Coulomb) or inelastic (Bremsstrahlung) collisions with the background gas. The loss rate depends on the local β-functions, the local gas pressure, and the storage ring acceptance. In SPEAR 3, the Coulomb and Bremsstrahlung lifetimes are 89 hr and 41hr, respectively, for a 1.8 nT N_2-equivalent average gas pressure at 500 mA. Taken in combination, the total gas scattering lifetime is 28 hr at 500 mA.

3.7.2.1 Background Gas Composition

For neutral gas pressure simulations in SPEAR 3, the average CO pressure was computed for a desorption rate of 2×10^{-6} molecules/photon, three 150 l/s ion pumps and three 1000 l/s Titanium Sublimation Pumps (TSP) per standard cell. In terms of N_2-equivalent pressure (Z_{eff}=7), we have

$$P_{N_2} = \frac{1}{2(49)} \sum_{\text{atom } j} \left(Z_j^2 \alpha_j p_{sj}\right) \tag{87}$$

where Z_j is the atomic number, α_j is the number of atoms/molecule, and p_{sj} is the partial pressure for species j. Since N_2 has the same 'Z' as CO, the N_2-equivalent partial pressure is the same as the CO partial pressure.

Table 3.44 Gas composition in SPEAR 2 at 100mA scaled to P_{CO} = 0.6 nT

Pressures	P_{H2}	P_{CO}	P_{CH4}	P_{CO2}	P_{H2O}	P_{Ar}	P_{O2}	P_{N2++}	P_{NH3}
Measured P/P_{CO}	10	1	1/10	1/10	1/10	1/100	1/50	1/33	1/10
$P_{N2\text{-equivalent}}$ (nT)	0.12	0.59	0.02	0.09	0.04	0.02	0.015	0.04	0.03

Utilizing the SPEAR 2 partial pressure data shown in Table 3.44 (Equation 87) projects a 1 nT N_2-equivalent pressure for SPEAR 3. To be conservative, a 1.8 nT average N_2-equivalent pressure at

500 mA was used for all SPEAR 3 lifetime computations. This value gives gas scattering lifetimes comparable to observations made in other storage rings.

3.7.2.2 Elastic Collisions (Coulomb Scattering)

Elastic collisions between electrons and neutral gas molecules produce transverse betatron oscillations. If the oscillation amplitude exceeds the physical or the dynamic aperture of the storage ring, the particle is lost. Since the betatron oscillation amplitude is proportional to the β-function at the point of collision, the quantity to minimize is the average value, $<\beta\ p_i>$, for each gas species, 'i'. The net Coulomb lifetime can be calculated from

$$\frac{1}{\tau_{\text{elastic},\,x,\,y}} = \frac{2\pi r_0^2 c}{\gamma^2 kT}\frac{1}{A_{x,\,y}}\sum_{\text{atom}\,j}\left(Z_j^2\sum_{\text{gas}\,i}\alpha_{ij}\langle\beta_{x,\,y}p_i\rangle\right) \qquad (88)$$

with

- γ = Lorentz relativistic factor
- c = speed of light
- r_o = classical electron radius ($2.82\text{x}10^{-15}$ m)
- Z_j = atomic number
- $A_{x,y}$ = aperture normalized to local betatron function, $A_i = d_i^2/\beta_i$ where β_i is the betatron function in plane 'i' at the physical aperture d_i.
- k = Boltzmann constant ($1.28\text{x}10^{-23}$ J-K^{-1})
- T = temperature (300 °K)
- α_{ij} = number of atoms j per molecular species, i
- p_i = gas pressure (Pascal).

Figure 3.62 shows the β-functions, the pressure profile at 500 mA, and the product of the β-functions with pressure in a standard cell. In the horizontal and vertical planes, the average products are $<\beta p>_x = 3.27$ nT-m and $<\beta p>_y = 5.39$ nT-m, respectively for a cell-averaged pressure of 0.6 nT. Similar average values for $<\beta p>$ will be achieved in the matching cells where more pumping speed is available. As mentioned above, to be conservative a 1.8 nT N_2-equivalent gas pressure at 500 mA is used for beam lifetime calculations.

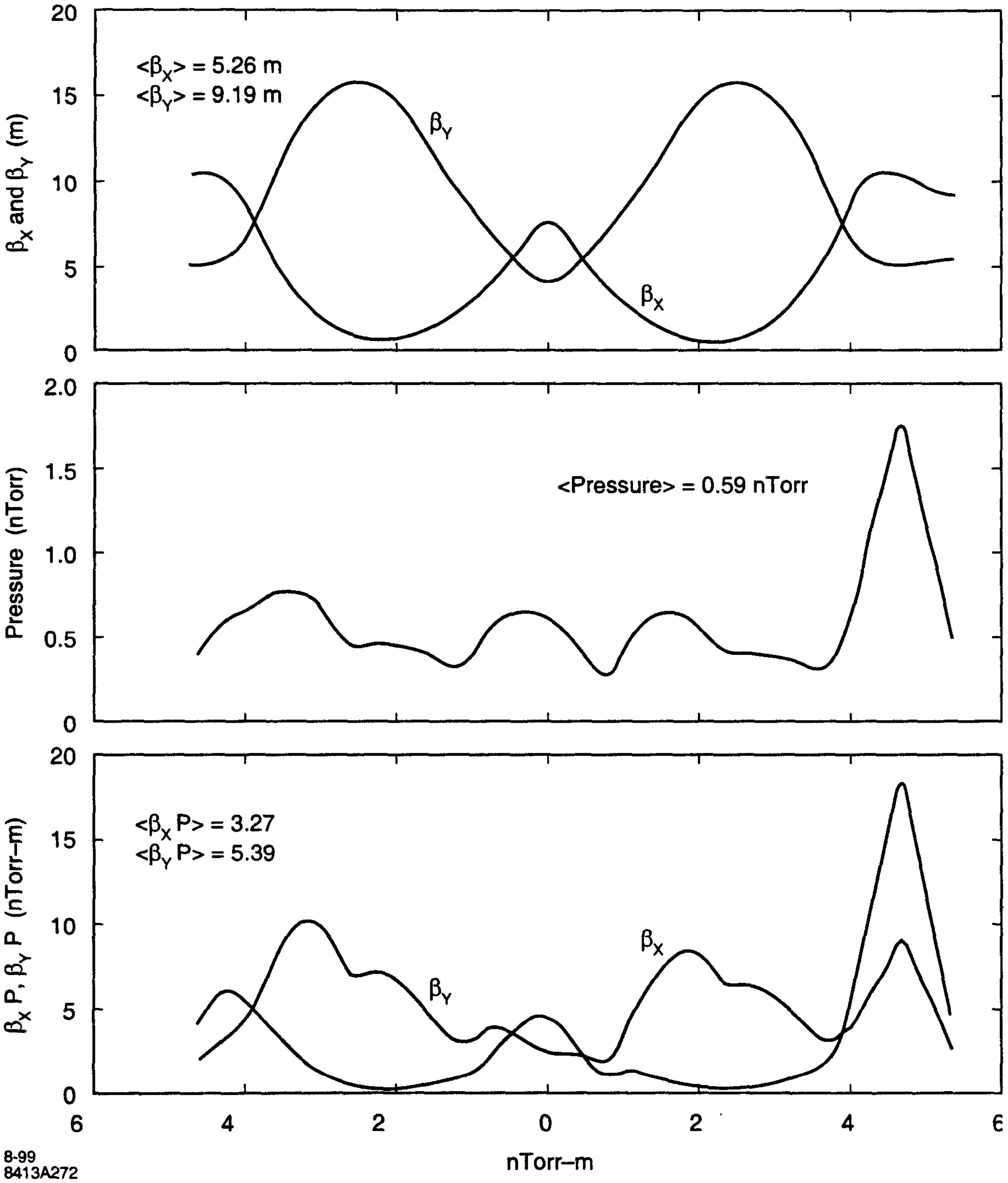

Figure 3.62 (a) Betatron functions, (b) simulated pressure profile at 500 mA, and (c) product of the (β-function)x(pressure) in a standard cell.

The vertical apertures which limit elastic scattering lifetime occur in the Beamline 6 and 11 vacuum chambers, where y = ± 6 mm and β_y = 4.7 m (A_y = 7.66 mm-mrad). Assuming an average N_2-equivalent pressure of 1.8 nT, Figure 3.63 shows the elastic scattering lifetime as a function of ID gap. Based on this plot, the vertical elastic scattering lifetime in SPEAR 3 is expected to be 96 hr at 500 mA. The horizontal acceptance is limited by the ± 18 mm dynamic aperture where β_x=10.2 m (A_x = 32 mm-mrad). The corresponding elastic scattering lifetime is about 1000 hr at 500 mA. The net elastic gas scattering lifetime is 89 hr for the 1.8 nT N_2-equivalent pressure anticipated for 500 mA.

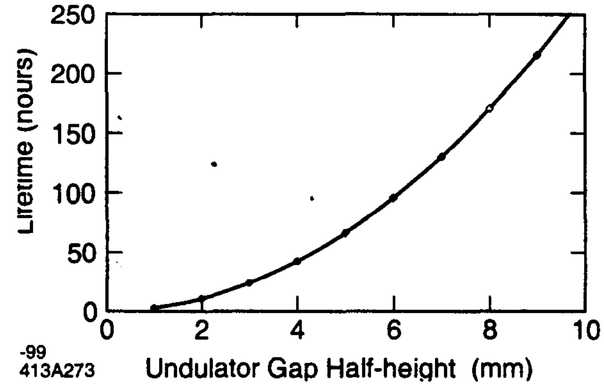

Figure 3.63 Coulomb lifetime as a function of undulator gap for 1.8 nT average N_2-equivalent gas pressure and and $\beta_y = 4.7$ m in the Insertion Device.

3.7.2.3 Inelastic Collisions (Bremsstrahlung Scattering)

Inelastic scattering of electrons on neutral gas nuclei can reduce forward electron momentum. The particle loss rate depends on the longitudinal momentum acceptance of the storage ring and the background gas pressure,

$$\frac{1}{\tau} = \frac{4r_0^2c}{137kT}\left(\frac{4}{3}\ln\left(\frac{1}{\frac{\delta p}{p}}\right)-\frac{5}{6}\right)\sum_{\text{atom},j} Z_j^2\ln\left(\frac{183}{Z_j^{1/3}}\right)\sum_{\text{gas},i}\alpha_{ij}p_i \tag{89}$$

where δp/p is the momentum acceptance of the storage ring.

Based on (Equation 89) with 3% momentum acceptance, the inelastic gas scattering lifetime is 41 hr at 500mA. For a gap voltage of 3.2 MV and synchrotron radiation power loss U_o=1.12 MeV/turn the RF bucket size is 2.9%. Fortunately, the dependence of $\tau_{\text{inelеastic}}$ on momentum acceptance is weak. With only 2% momentum acceptance, for example, the inelastic gas scattering lifetime is still 37.4 hr.

3.7.2.4 Total Gas Scattering Lifetime

The total gas scattering lifetime is plotted in Figure 3.64 as a function of average N_2-equivalent gas pressure. The total gas scattering lifetime is 28 hr at 500 mA for an average N_2-equivalent gas pressure of 1.8 nT.

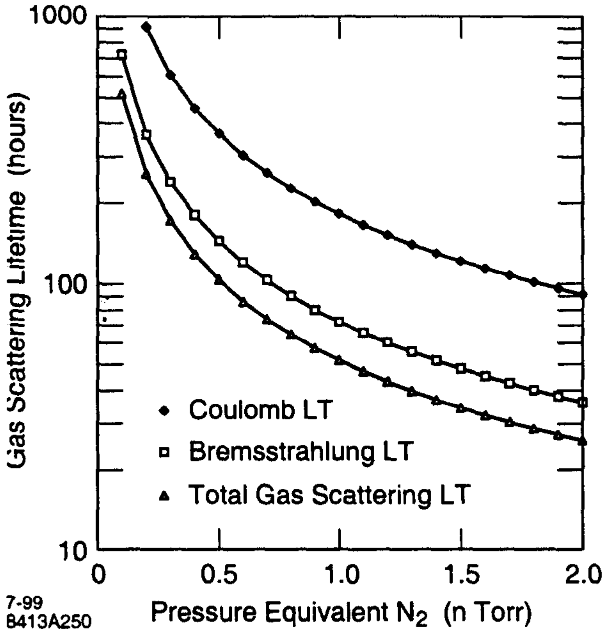

Figure 3.64 Gas scattering lifetime as a function of average N_2-equivalent gas pressure.

3.7.3 Intra-beam Scattering (Touschek Scattering)

Electrons exhibiting betatron oscillations can transfer transverse momentum into the longitudinal plane through Coulomb collisions. The longitudinal momentum variation, small in the two-particle frame, is Lorentz-boosted in the laboratory frame. If the energy transfer is sufficiently large, the particles can be lost. This 'Touschek' effect is particularly detrimental to low-energy rings (1 to 2 GeV) and has less effect in high-energy rings (6 to 8 GeV). At 3 GeV, SPEAR 3 will be moderately sensitive to Touschek scattering at the single-bunch current levels used for routine operation (I_b~1.8 mA).

For a 500 mA beam in a 280-bunch fill pattern with 1% coupling and U_0=1.12 MeV/turn, the anticipated intra-beam scattering lifetime is 52.6 hr (V_{gap}=3.2 MV). By adding more IDs to raise U_0 to 1.61 MeV/turn, the Touschek lifetime drops to 39.8 hr at 500 mA. If the momentum-dependent dynamic aperture is less than simulations predict, or if small-gap IDs are used, the Touschek lifetime will also be reduced. If intra-beam scattering proves to be a problem, the beam lifetime can be improved by increasing the emittance coupling, filling more buckets, or installing a bunch-lengthening cavity. A cavity that triples the bunch length, for instance, would triple the Touschek lifetime.

To further quantify the intra-beam scattering loss mechanisms, recall that following a scattering event, the particle-momentum deviation can exceed either the longitudinal RF acceptance, the momentum-dependent dynamic aperture or the physical acceptance in dispersive regions.

The RF acceptance is given by:

$$\frac{\Delta E}{E} = \sqrt{\frac{2U_0\left(\sqrt{q^2-1} - \operatorname{acos}\left(\frac{1}{q}\right)\right)}{\pi \alpha h E}} \tag{90}$$

where U_0 is the synchrotron radiation energy loss per turn, q = eV/ U_0 is the over-voltage factor, and α is the momentum compaction factor. Figure 3.65 shows the RF acceptance for SPEAR 3 as a function of gap voltage for U_0=0.912 MeV (dipoles only), U_0=1.12 MeV (includes present ID load) and U_0=1.61 MeV (maximum projected ID load). For a gap voltage of 3.2 MV and U_0=1.12 MeV, the RF acceptance is 2.9%. The RF acceptance as a function of U_0 is plotted in Figure 3.65 for a constant gap voltage of 3.2 MV.

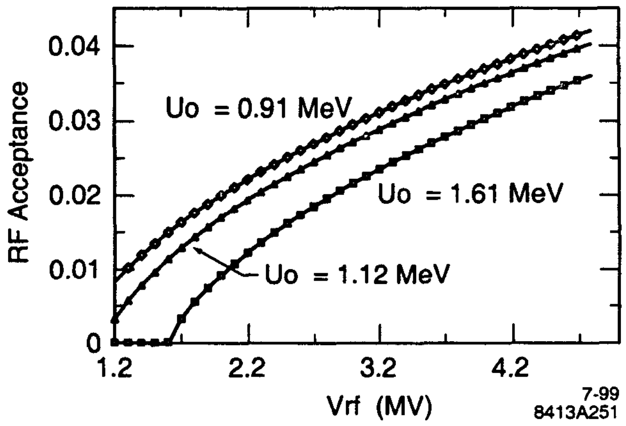

Figure 3.65 RF acceptance as a function of gap voltage for different U_0.

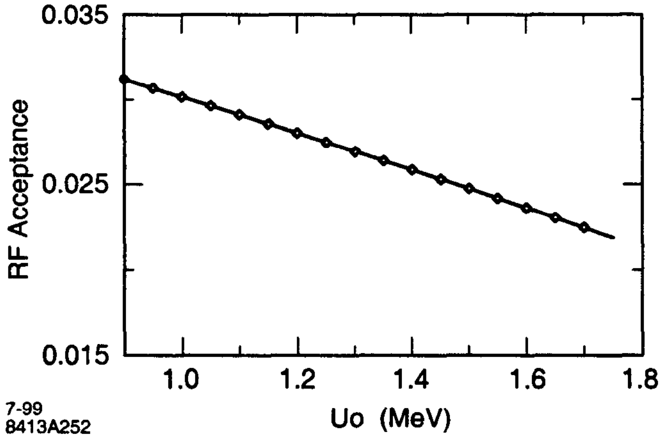

Figure 3.66 RF acceptance as a function of U_0 (V_{rf}= 3.2 MV).

The storage ring acceptance can also be limited by the momentum-dependent dynamic aperture. For a Touschek scattering event in a dispersive region at location s*, the invariant of the motion is

$$H(s^*)\left(\frac{\Delta p}{p}\right)^2 = (\gamma D^2 + 2\alpha DD' + \beta D'^2)(s^*)\left(\frac{\Delta p}{p}\right)^2 \tag{91}$$

At another location, s, the total perturbed particle amplitude is

$$\mathrm{A}(s) = \mathrm{D}(s)\frac{\Delta p}{p} + \sqrt{\beta(s)\mathrm{H}(s^*)}\frac{\Delta p}{p} \tag{92}$$

If A(s) exceeds either the vacuum chamber dimensions or the momentum-dependent dynamic aperture, the particle is lost.

Based on these principles, Touschek lifetime calculations were made with ZAP [1]. At each point in the lattice, ZAP computes the single bunch charge density and the local Touschek lifetime,

$$\tau_{Touschek} = \frac{8\pi\sigma_x\sigma_y\sigma_s\gamma^2\left(\frac{\delta p}{p}\right)_m^3}{N r_0^2 c D(v)} \tag{93}$$

where $\sigma_{x,y,z}$ are the rms bunch dimensions, γ is the Lorentz relativistic factor, N is the number of particles per bunch, r_0 is the classical electron radius, and c is the speed of light. D(v) is a form factor with a typical value of 0.2 [REF ???] $\frac{\delta p}{p}\Big|_m$ is the smallest value of the RF acceptance, the momentum-dependent dynamic aperture or the physical acceptance.

Based on the ZAP calculations, Figure 3.67 shows a plot of the 500 mA Touschek lifetime (280 bunches, 1% coupling) as a function of gap voltage for the on-momentum horizontal dynamic aperture ranging from 13 mm to 22 mm in the 7.6 m Racetrack straightsfootnote #1. For each curve, the off-momentum dynamic aperture was assumed to decrease at a rate of 1 mm per 1% normalized momentum deviation. For an on-momentum horizontal dynamic aperture of 13 mm, for instance, the Touschek lifetime is 52.6 hr for 3.2 MV gap voltage and U_0=1.12 MeV/turn. In the worst case (11 mm dynamic aperture in the Racetrack straights), $\tau_{\text{intra-beam}}$~40 hr.

footnote #1 Note: in Section 3.1.7 dynamic aperture simulations are quoted in the 3.1 m straight sections where β_x=10.2 m. In this section, Touschek lifetime calculations are performed with the Racetrack straights as the reference point (β_x=5 m). An 18 mm horizontal dynamic aperture in the 3.1 m straights corresponds to approximately 13 mm dynamic aperture.

To separate out the effect of radiative energy loss, Figure 3.68 plots the Touschek lifetime as a function of gap voltage for 13 mm horizontal dynamic aperture in the Racetrack straights and three different values of U_0. When not limited by dynamic aperture, the lifetime to increases with RF voltage. For a finite dynamic aperture, however, higher gap voltages shorten the bunch length, increase the scattering rate and decrease lifetime.

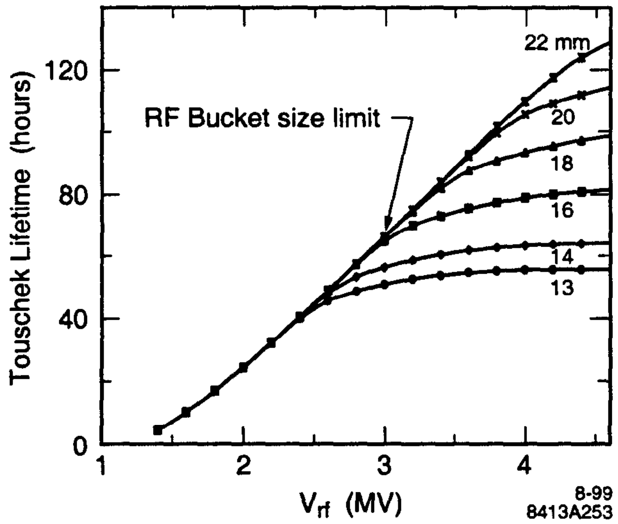

Figure 3.67 Touschek lifetime as a function of RF voltage for different values of momentum-dependent dynamic aperture.

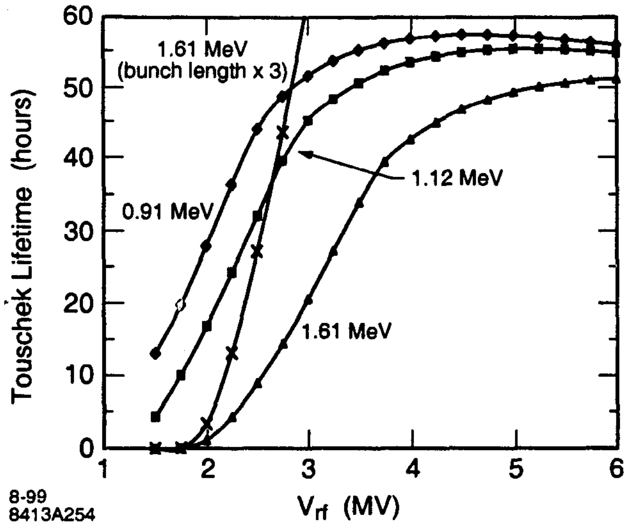

Figure 3.68 Touschek lifetime as a function of RF voltage for three different ID loads and a momentum-dependent dynamic aperture of 13 mm in the Racetrack straights. The Touschek lifetime with an ideal x3 bunch lengthing cavity is also plotted.

3.7.4 Total Electron Beam Lifetime

Table 3.45 provides a summary of the anticipated electron beam lifetime at full current (500 mA) under normal operating conditions. To achieve the projected beam lifetime of 18 hr will require careful tuning of the electron beam orbit, dynamic aperture, RF gap voltage, vacuum conditions and emittance coupling.

Table 3.45 Summary of electron beam lifetime for 500 mA distributed in 280 buckets with 1% coupling, total RF gap voltage of 3.2 MV and a total radiative loss of 1.12 MeV/turn.

	Coulomb (elastic)	Bremstrahlung (inelastic)	Touschek (intra-beam)	Total
Lifetime (hr)	89	41	74	18

Figure 3.69 shows a plot of the different contributions to beam lifetime at 500 mA as a function of the energy loss per turn, U_0. These curves show that even for large U_0 the lifetime in SPEAR 3 is dominated by gas scattering (Bremsstrahlung) under the assumption that the average N_2-equivalent gas pressure is 1.8 nT. For lower gas pressures, the Bremsstrahlung lifetime will increase and the beam lifetime will be dominated by Touschek losses. Figure 3.70 shows the anticipated current decay starting from 500 mA distributed in 280 buckets for U_0=1.12 MeV and an on-momentum horizontal dynamic aperture of 13 mm in the 7.6 m Racetrack straights. The beam lifetime of 18.3 hr is based on an average gas pressure of 1.8 nT, N_2-equivalent. For this plot, the gas desorption rate is assumed to decrease as the current decays. In practice, the Touschek lifetime would also decrease as the current decays. Based on these assumptions (initial gas scattering lifetime 28 hr, initial Touschek lifetime 52.6 hr) over 200mA stored current remains after 24 hours.

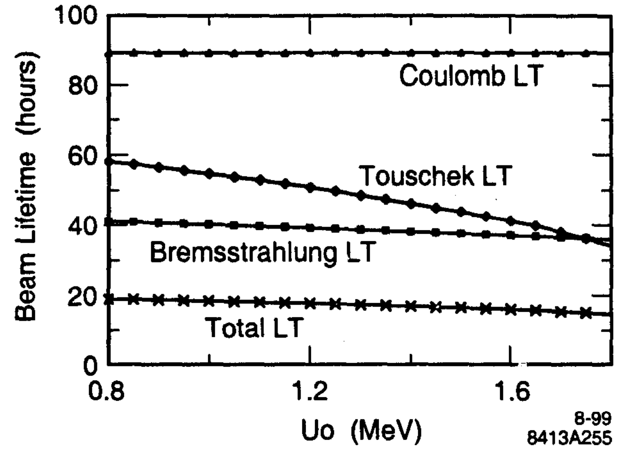

Figure 3.69 Electron beam lifetime as a function of single turn radiation loss, U_0.

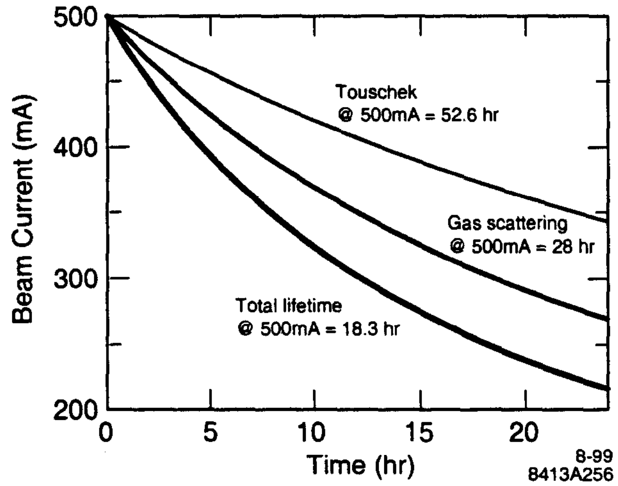

Figure 3.70 Simulation of SPEAR 3 current decay over a 24 hr period

3.8 Ion and Dust Effects

Positively charged ions trapped in the beam potential can affect the performance of electron and antiproton storage rings. The ions can be single atoms, small molecules, or micron-size 'dust' particles. Their effects on the beam include: 1) emittance increase, 2) betatron tune shifts and broadening, 3) collective instabilities, and 4) reduced beam lifetime. For high-current, low-emittance beams, even with a large clearing gap in the bunch train, ion-driven single-pass instabilities can occur.

For a uniform fill pattern, both single- and multiple-charged ions can be stably trapped in the beam potential. The total number line density for ions of all charges is about 3×10^6 per meter; the charge density is about 5 times higher. In the worst case, the trapped ions could reduce the beam lifetime due to elastic gas scattering and due to bremsstrahlung by as much as a factor of 10, and also induce a fairly large incoherent tune shift of about 0.16. The ions could also give rise to a coherent 2-beam instability, with a submicrosecond rise time.

To avoid these unwanted effects, a clearing gap is introduced in the bunch train. With a 200-ns gap, only single-ionized molecules are trapped over multiple revolutions. At most, the beam lifetime due to interaction with the residual gas could decrease by a factor of 2 with the incoherent tune spread 50 times smaller than in the case without a gap. The growth rate of trapped-ion collective instabilities is also reduced by a factor of 50. Moderate Landau damping would suffice to damp such instabilities. The one instability that still could occur is the single-pass fast-beam ion instability (FBII), with an estimated rise time of 20 ms, much larger than the radiation damping time. For the beam current levels in SPEAR 3, macro-size 'dust' particles are thermally unstable: if a dust particle is trapped by the beam, it will explode in less than 1 ms.

3.8.1 Machine Parameters

For the study of ion effects in SPEAR 3 we assume machine and beam parameters as listed in Table 3.46. All the numbers calculated in this section refer to a fixed beam current of 200 mA; they are easily scaled to different situations. The decision to utilize 476 MHz PEP-II cavities (h=372) does not change this section's qualitative results, which were calculated for a 358 MHz RF system (h=280).

Almost all the ion effects considered can be considerably alleviated by a gap of about one quarter of the ring's length. Wherever appropriate, we will give estimates for such a gap, in addition to those for the uniform fill pattern.

Table 3.46 SPEAR 3 parameters assumed for ion studies

Variable	Symbol	Value
circumference	C	234.1 m
beam energy	E	3 GeV
current	I	200 mA
bunch population	N_b	7×10^9
number of bunches	n_b	140
harmonic number	h	280
bunch spacing	t_{sep}	5.6 ns
bunch gap	n_{gap}	none†
average rms horizontal beam size	$<\sigma_x>$	350 μm
average rms vertical beam size	$<\sigma_y>$	45 μm
average horizontal beta function	$<\beta_x>$	6.7 m
average vertical beta function	$<\beta_y>$	10.6 m
carbon monoxide pressure	p_{gas}	0.6 nT
average beta product in arcs	$<\beta_x\beta_y>$	45 m^2
maximum beta product in arcs	$(\beta_x\beta_y)_{max}$	75 m^2
minimum beta product	$(\beta_x\beta_y)_{min}$	15 m^2

†. We also quote some results for a 200-ns gap ($n_{gap} \approx 35$ missing bunches).

3.8.2 Ion Production Rates and Ion Density

In a storage ring, ions are created continually by interaction of the stored beam with molecules of the residual gas. The most important ionization mechanism is direct collisional ionization of molecules by electrons passing nearby, with a typical ionization cross section, for carbon monoxide, of σ_{ion} = Mbarn [1,2]. The number of ions per meter λ_{ion} after the passage of N beam particles is

$$\lambda_{ion}[\mathrm{m}^{-1}] \approx \sigma_{ion} p_m N \approx 6 N p_{gas} \tag{94}$$

where pgas [Torr] is the gas pressure, and rm [m–3] the molecular density. For a carbon monoxide pressure of 0.6 nT, and 200 mA current, this amounts to about 15 ions per meter per revolution period.

Ions can also be generated via photo-ionization [3]. The photo ionization cross section for carbon monoxide is [4,3]

$$\sigma_{pi}[\mathrm{cm}^2] \approx 9.12 \times 10^{-14} e^{-2.48} - 4.80 \times 10^{-12} e^{-4.05} \text{ for } e > e_{th} \approx 14\mathrm{eV} \tag{95}$$

where ε denotes the photon energy and ε_{th} the threshold energy, both in eV. The total number of ions generated by photo-ionization is about 2–4 times that produced by collisional ionization. Fortunately, most of the former are created far away from the beam and thus, in first order, we may ignore their effect.

The number of ions does not grow indefinitely [5,6]. For SPEAR 3 parameters, the tightest limit on the ion density arises from multiple ionization: Since the collisional-ionization cross section for secondary and higher ionization is of similar magnitude as for primary ionization, the density of primary single-charge ions cannot exceed the residual gas density [7]. A given gas density would therefore yield an ion line density of

$$\lambda_{ion} \leq 3 \times 10^{22}\mathrm{m}^{-3} \sigma_x \sigma_y p_{gas} |Torr| \approx 3 \times 10^5 \mathrm{m}^{-1} \text{ (single charge).} \tag{96}$$

At a production rate of 15 ions per meter per revolution, the maximum density of (Equation 96) is reached after about 16 ms (20,000 turns).

For SPEAR 3, multiply ionized atoms can also be trapped by the beam. Thus in equilibrium about the same number of neutral, single ionized, double ionized, etc., molecules or atoms can coexist within the beam volume. The maximum charge a carbon monoxide molecule can acquire is about 10; this would also be a good estimate for the maximum total charge of its constituent atoms, after fragmentation.

From these considerations we expect that, in SPEAR 3, the limit on the maximum total ion density (summing over all ionization states) is about

$$\lambda_{ion} \leq 3 \times 10^6 \mathrm{m}^{-1} \text{ (all charges)} \tag{97}$$

With an average ion charge equal to a few electron charges, the maximum ion charge density is about 5 times the ion density $\lambda_{ion.}$

If a 200-ns gap is introduced in the bunch train, only single charge ions (Q = 1) are trapped from turn to turn. We then expect an ion line density equal to the single-ion density limit of (Equation 96); the charge density ($Q\lambda_{ion}$) will be 50 times lower than for a uniform fill.

There are other effects which can limit the build-up of a trapped ion cloud. An important one is charge neutralization [7]: The ions stop accumulating when their total charge density is equal to the average beam density, because at this point there is no net force left to attract the ions. The corresponding limit on the ion line density is

$$\lambda_{ion} \le \frac{n_b N_b}{C} \approx 6.5 \times 10^8 \mathrm{m}^{-1} \tag{98}$$

This limit is about 100 times higher than the limit imposed by multiple ionization. Further potentially limiting effects are the heating of ion motion by beam-gas collisions [6], and recombination with (photo)electrons. These effects are not easily quantified, but they appear to be of minor importance here.

In the following analysis, we assume that the ion density corresponds to the multiple-ionization limit of (Equation 97) (no clearing gap), and that the average ion charge is $Q \approx 5$.

3.8.3 Trapping

In the absence of a clearing gap, ions are trapped in the electric potential of the beam if their mass A is larger than the critical mass A_{crit}, [7]:

$$A \ge A_{crit} \equiv \frac{Q N_b r_p L_{sep}}{2\sigma_y(\sigma_x + \sigma_y)} \tag{99}$$

where A and A_{crit} are given in units of the proton mass, r_p is the classical proton radius, and L_{sep} the bunch spacing in length units (1.7 m). For an ion charge of $Q \approx 5$, the critical mass is $A_{crit} \approx 2$,which means that ionized carbon monoxide molecules or its constituents (after fragmentation) are trapped by the beam even if their charge is much larger than 1.

With a gap slightly larger than 200 ns (a quarter of the ring), $A_{crit} > 14$, and only single charge ions can survive.

3.8.4 Lifetime

Trapping of about 10 differently charged ion species inside the beam volume, each with a density equal to that of the residual gas, increases the effective gas density by a factor of 10. This will cause a reduction in beam lifetime due to elastic gas scattering and bremsstrahlung by a similar factor.

It is interesting that the additional contribution of trapped ions to the beam lifetime could explain large discrepancies, by a factor 10 or more, between measured and expected pressure-limited beam lifetimes, which were observed at various machines, for example at the SLC damping rings [14].

With a 200-ns gap in SPEAR 3, the total ion density is about 10 times lower than without gap. In this case, the ions could reduce the beam lifetime due to gas scattering and beamstrahlung by up to a factor of 2.

3.8.5 Tune Shift

Ions trapped by the beam induce a betatron tune shift. If the transverse ion distribution is proportional to the beam distribution, the tune shift of coherent betatron oscillations is

$$\Delta Q_{x,y;coh} \approx \frac{\beta_{x,y} r_e Q \lambda_{ion} C}{\gamma 4\pi\sigma_{x,y}(\sigma_x + \sigma_y)} \tag{100}$$

Assuming the maximum ion density of (Equation 97) (no clearing gap), and an average ion charge $Q \approx 5$, one finds

$$\Delta Q_{x;coh} \approx 0.006 \text{ and } \Delta Q_{x;coh} \approx 0.006 \tag{101}$$

There is also an incoherent tune shift, which affects the single particle motion. This incoherent tune shift is simply twice the coherent tune shift:

$$\Delta Q_{x,\,y;inc} \approx 2\Delta Q_{x,\,y;coh} \tag{102}$$

So, under the above assumptions the vertical incoherent tune shift is about $\Delta Q_{y;\mathrm{inc}} \approx 0.16$. This may still be acceptable, or even helpful, as it provides Landau damping. With a 200-ns gap, the tune shift will be 50 times smaller, as only single charge ions contribute.

3.8.6 Ion Frequencies

The single-ion oscillation frequency in the beam potential is [7]

$$f_{i;x,\,y} = \frac{c}{2\pi}\left(\frac{2QN_b r_p}{AL_{sep}\sigma_{x,\,y}(\sigma_x + \sigma_y)}\right)^{1/2} \tag{103}$$

The expected horizontal and vertical ion frequencies fall in the range between 3 MHz and 22 MHz. These are the frequencies at which one could excite the beam, for ion clearing purposes (RF knock out) [8,9]. With a 200-ns gap, the ion frequencies will be in the range 3–9 MHz.

3.8.7 Coherent Trapped-Ion Instabilities and Landau Damping

If an ion cloud interacts coherently with the beam, it can cause a collective instability. Taking into account the frequency spread of the ions but not that of the electrons, the growth rate is estimated as [10,11]:

$$\frac{1}{\tau} \approx \frac{\pi^2 f_{rev}\Delta Q_{y;inc}}{(\Delta f_i/f_i)_{FWHM}} \tag{104}$$

where f_{rev} is the revolution frequency, $\Delta Q_{y;\mathrm{inc}}$ the incoherent tune shift, and $(\Delta f_i/f_i)_{\mathrm{FWHM}}$ the FWHM spread of the ion frequencies. The latter is caused by the beam-size variation around the ring and by the nonlinear character of the beam-ion force. Assuming $(\Delta f_i/f_i)_{\mathrm{FWHM}} \approx 1$, the estimated growth time is $\tau \approx 500$ ns, less than a revolution period. However, the coherent instability is suppressed by Landau damping, if the following condition is satisfied [12,13,8]:

$$\Delta Q_y^{rms}\Delta Q_{ion}^{rms} \geq \left|\frac{Q_c^2 q}{Q_y}\right| \tag{105}$$

where ΔQ_y^{rms} denotes the rms betatron tune spread (e.g., caused by chromaticity and momentum spread or by the ion space-charge field), ΔQ_{ion}^{rms} , the rms ion frequency spread, Q_c the ion space-charge force on the electrons ($Q_c^2 = N_{tot}^{ion} r_e Q/(2\pi 2\sigma_y(\sigma_y + \sigma_y)\gamma)$), where N_{tot}^{ion} denotes the total number of ions and Q the ion charge in units of e), q the electron beam space-charge force on the ions ($q^2 = N_{tot} r_e CQ/(2\pi^2 \sigma y(\sigma_x + \sigma_y)A)$), and Q_y the betatron tune.

We again assume that the ion-frequency spread is of the same magnitude as the ion frequency itself, $\Delta Q_c \approx Q_c^2/4Q_y$ Then, expressing the coherent tune shift due to the ions in terms of Q_c and Q_y, $\Delta Q_{coh} \approx Q_c^2/4Q_y$. and (Equation 105), describing the instability threshold, can be rewritten as

$$\Delta Q_y^{rms} \geq 4\Delta Q_{coh} \approx 2\Delta Q_{inc} \tag{106}$$

According to this very rough estimate the rms betatron tune spread should be at least twice the incoherent spread caused by the ions. We expect that for a smaller tune spread, the Landau damping is insufficient and the beam becomes unstable.

However, experience at existing machines suggests [14] that the trapped-ion instability may already be suppressed by a tune spread smaller than that estimated in (Equation 106). Based on this experience, the ion induced betatron tune spread in SPEAR 3 is most likely sufficient to prevent coherent trapped-ion instabilities.

If a 200-ns gap is introduced, the instability rise time is 50 times larger, and the betatron tune spread required for Landau damping is only $\Delta Q_y^{rms} \approx 6 \times 10^{-3}$. Thus it would be possible to Landau damp the trapped-ion instability, if it should occur.

3.8.8 Fast Beam-Ion Instability

If the predicted incoherent tune shift due to the trapped ions, the beam-lifetime reduction, or coherent instabilities are a concern, one could contemplate operation with a large ion clearing gap in the bunch train. A gap of 200-ns, which was considered as an option throughout this text, would remove all ions except for the single ionized ones. The minimum gap size required to remove all carbon-monoxide ions is 400 ns, corresponding to 70 empty bunch positions (half the ring). With such a large gap, however, the ions created during a single revolution of the beam could potentially cause a different kind of instability, similar to beam break-up in a linac. This effect, called 'fast beam-ion instability' (FBII), was discussed in Refs. [15,16,17,18], and experimentally confirmed in Refs. [19,20].

In a simple linear treatment applicable for small oscillation amplitudes ($y \ll \sigma_y$) the bunch centroid at the end of the train grows quasi-exponentially as [15]

$$y \sim \exp(\sqrt{t/\tau_c}) \tag{107}$$

where the characteristic time coefficient in the exponent is

$$\frac{1}{\tau_c} \equiv \frac{4 d_{gas} \sigma_{ion} \beta_y N_b^{3/2} n_b^2 r_e r_p^{1/2} L_{sep}^{1/2} c}{\sqrt{3} 3 \gamma \sigma_\gamma^{3/2} (\sigma_x + \sigma_y)^{3/2} A^{1/2}} \tag{108}$$

with $d_{gas} = p/(k_B T) \approx 1.9 \times 10^{13}$ m^{-3} the residual gas density, $\sigma_{ion} \approx 2$ Mbarn the ionization cross section, and A the ion mass (in units of the proton mass). For the parameters of Table 3.46, but considering only $n_b \approx 70$ bunches, we find $\tau_c \approx 5$ ms.

The ion motion decoheres because the vertical ion oscillation frequency depends on the horizontal position within the bunch. The instability is further damped by the variation of the beam size and, thus, of the ion frequency around the ring. If both these effects are taken into account, the instability growth is predicted to be purely exponential [17]

$$y \sim \exp\left(\frac{t}{\tau_e}\right) \tag{109}$$

with an e-folding time

$$\frac{1}{\tau_e} \approx \frac{1}{\tau_c} \frac{c}{2\sqrt{2} l_{train} (\Delta\tilde{\omega}_i)_{rms}} \tag{110}$$

where l_{train} is the length of the train, and $(\Delta\omega_i)_{rms}$ denotes the rms variation of the (angular) ion frequency as a function of the azimuthal position around the ring. The coherent angular ion frequency is

$$\tilde{\omega}_i = c\sqrt{\frac{4N_b\tau_p}{3AL_{sep}\sigma_y(\sigma_x+\sigma_y)}} \approx 4\times 10^7 s^{-1} \tag{111}$$

with an rms variation, $(\Delta\omega_i)_{rms}/\omega_i$ of about 8%.

The e-folding rise time is then $\tau_e \approx 17$ ms. This is 4 times larger than the radiation damping time, and thus does not look like a source for concern. Note that the FBII growth rates scale between linear and quadratic with the charge per bunch and the number of bunches, respectively, and linear with the pressure.

3.8.9 Dust Trapping

Sudden drops of the beam lifetime ascribed to the capture of positively charged macroparticles ('dust') have been observed at many high-energy electron storage rings [21,22].

The thermally most stable dust particles, needle-shaped silica particles of mass $A \approx 3 \times 10^{11}$ [21], are expected to melt and explode when the average beam current flux exceeds 3.5×10^9 mA m^{-2}. For the SPEAR FODO 3 parameters this flux corresponds to a beam current of 56 mA, much below the design value. Hence, dust trapping will not be a problem.

References

[1] F.F. Rieke and W. Prepejchal, Phys. Rev. A, 6 (1972).

[2] T.O. Raubenheimer, Proc. of IEEE PAC95, Dallas, p. 2752 (1995).

[3] Y. Miyahara, Jpn. J. Appl. Phys. 26, no. 9, p. 1544 (1987).

[4] E.L. Kasarev and E.R. Dodolyak, Opt. Spectrosk. 56, p. 643 (1984).

[5] A. Poncet, CERN/US particle accelerator school, Hilton Head Island, South Carolina, Springer Verlag, Lecture Notes in Physics 400 (1992).

[6] Y. Baconnier, A. Poncet, P. Tavares, CERN/PS 94-40 (1994).

[7] Y. Baconnier and G. Brianti, CERN/SPS/80-2 (1980).

[8] R. Alves Pires et al., Proc. of 1989 IEEE PAC, p. 800 (1989).

[9] E. Bozoki, Proc. of 3rd EPAC, Berlin, p. 789 (1992).

[10] H.G. Hereward, CERN 71-15 (1971).

[11] D. Sagan and A. Temnykh, Nucl. Instr. Meth. A 344, p. 459 (1994).

[12] G. Koshkarev and Zenkevich, Part. Acc. 3, p. 1 (1972).

[13] J.M. Laslett, A.M. Sessler, D. Möhl, Nuclear Instruments and Methods 121, p. 517-524 (1974).

[14] F. Zimmermann, P. Krejcik, M. Minty, D. Pritzkau, T. Raubenheimer, M. Ross, M. Woodley, Proc. of the International Workshop on Multibunch Instabilities in Future Electron and Positron Accelerators (MBI97), Tsukuba, and SLAC-PUB-7665 (1997).

[15] T.O. Raubenheimer and F. Zimmermann, Phys. Rev. E 52, no. 5, p. 5487 (1995).

[16] G.V. Stupakov et al., Phys. Rev. E 52, no. 5, p. 5499 (1995).

[17] G.V. Stupakov, Proc. of Int. Workshop on Collective Effects and Impedance for B factories (CEIBA95), KEK Proceedings 96-6, p. 243 (1996).

[18] S. Heifets, Proc. of Int. Workshop on Collective Effects and Impedance for B factories (CEIBA95), KEK Proceedings 96-6, p. 270 (1996).

[19] J. Byrd et al., Phys. Rev. Let., Vol. 79, no. 1, p. 79 (1997).

[20] M. Kwon et al., KEK-REPORT-97-6 (1997).

[21] F. Zimmermann, J.T Seeman, M. Zolotorev, and W. Stoeffl, Proc. of IEEE PAC95, Dallas, p. 517 (1995).

[22] D.R.C. Kelly et al., Proc. of IEEE PAC95, Dallas, p. 2017 (1995).

Storage Ring Systems 4

4.1 Magnets and Supports

The SPEAR 3 storage ring magnet system, which comprises 36 gradient dipoles, 94 quadrupoles, 72 sextupoles, 72 dipole correctors (horizontal, vertical and combined function), 2 injection dipoles, 2 injection quadrupoles and 1 septum magnet (Table 4.1). The 234.126 m ring is divided into 14 standard cells and 4 matching cells each long respectively 11.691 m and 17.611 m. The magnets for each of these cells will be mounted on new steel support girders, replacing the existing concrete girders. All the magnets are optimized at 3 GeV and can be operated at 3.3 GeV. The magnet design has been performed scaling previous magnets geometries with conformal mapping [1] and computing the magnetic field with the numerical codes Ansys® for 2D analysis and Amperes© for 3D analysis.

The C-shape gradient dipoles, the Collins type quadrupoles and the closed yoke sextupoles are straight magnets and allow the synchrotron radiation to exit the ring. The yokes are made of AISI 1010 steel laminations either glued or compressed using tie rods or end plates and longitudinal plates. All the magnets are chamfered at the ends to meet the integrated field quality specifications. All the main magnet coils are made of water-cooled hollow copper conductor insulated and vacuum impregnated with epoxy. In order to avoid solenoidal fields that can couple the horizontal and vertical betatron oscillations, all the SPEAR 3 magnets will be wired without net current loop around the beam.

SPEAR 3 will use 14 new steel girders for the standard cells and 12 new steel girders for the matching cells. Each magnet will be individually supported onto the girder and separately aligned. The girder supports will be modified to decrease the vibration modes (Section 4.1.9). Before installing the vacuum chamber, the lower half of the quadrupoles and lower third segment of the sextupoles will be installed on the girders. After installing the vacuum chamber and completing the installation of quadrupoles and sextupoles, the dipoles will be inserted radially around the vacuum chamber.

All magnet families with the same excitation current will be powered in series with the exception of 20 QD and 20 QF quadrupoles that will be powered individually. The dipole trim coils, the quadrupole modulation coils, the skew quadrupoles coils inside the sextupoles and all the horizontal and vertical steering correctors will require individual power supplies.

Table 4.1 SPEAR 3 magnet inventory

Magnet type	Magnet Name	Core length (m)	Qty	Gap Height or Diameter (mm)	Design Pole Tip Field @ 3.3 GeV (T)
Gradient Dipole	FULL BEND	1.45	28	50	1.42 (+ 3.63 T/m)
Gradient Dipole	3/4 BEND	1.09	8	50	1.42 (+ 3.63 T/m)
Quadrupole	QFX	0.60	4	70	0.77
Quadrupole	QFC, QFY	0.50	18	70	0.77
Quadrupole	QF, QDX, QDY, QDZ, QFZ	0.34	44	70	0.77
Quadrupole	QD	0.15	28	70	0.77
Sextupole	SD	0.25	28	90	0.56
Sextupole	SF, SDI, SFI	0.21	44	90	0.56
H/V Correctors	H/V1, H/V2, H/V3, H/V4	0.16	72	109	0.04 (horizontal field) 0.06 (vertical field)
BTS Dipole	B7H, B8V	1.02	2	28	1.51
BTS Quadrupole	Q8, Q9	0.54	2	80	0.34
Septum	B9V	1.17	1	12	1.31

4.1.1 Summary of Magnet Parameters

The SPEAR 3 standard cell and matching cell are shown in Figures 4.1 and 4.2. The specifications for the standard cell and matching cell magnets used in the tracking studies are described in Tables 4.2, 4.3, and 4.4. The specifications include magnet length, relative position and strength. The strength of quadrupoles (or gradient dipoles) and sextupoles is defined in the following way (Section 4.1.2): $k_{quad}=b_2/(B\rho)$, $k_{sext}=2\times b_3/(B\rho)$. The good field region and multipole requirements are listed in Tables 4.5, 4.6, and 4.7. The alignment tolerances are listed in Table 4.8.

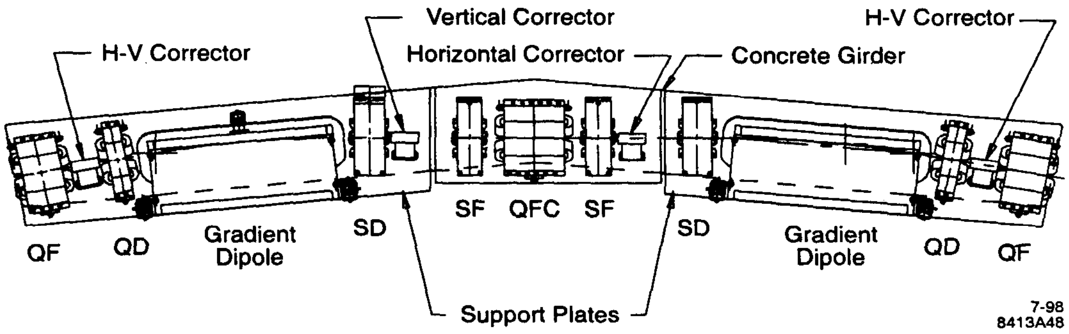

Figure 4.1 SPEAR 3 standard cell

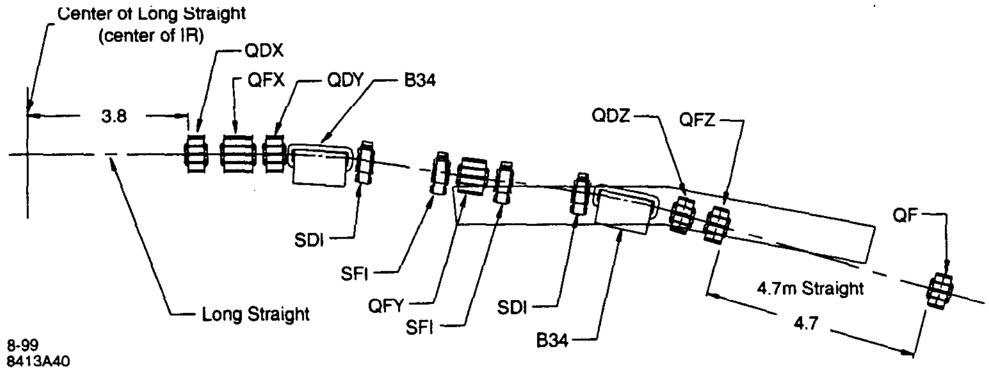

Figure 4.2 SPEAR 3 matching cell

Table 4.2 Standard cell magnet parameters - SP3V78

Magnet	Magnetic length (m)	Strength
QF	0.3400	2.00 m^{-2}
QD	0.1500	-2.00 m^{-2}
BEND	1.4521	-0.33 m^{-2}
SD	0.2500	-50.00 m^{-3}
SF	0.2100	40.00 m^{-3}
QFC	0.5000	2.00 m^{-2}
SF	0.2100	40.00 m^{-3}
SD	0.2500	-50.00 m^{-3}
BEND	1.4521	-0.33 m^{-2}
QD	0.1500	-2.00 m^{-2}
QF	0.3400	2.00 m^{-2}
Standard cell length	11.6914	

Table 4.3 Matching cell magnet parameters - SP3V78

Magnet	Length/Distance (m)	Strength
QDX	0.3400	-2.00 m^{-2}
QFX	0.6000	1.68 m^{-2}
QDY	0.3400	-1.5 m^{-2}
3/4 BEND	1.0884	-0.33 m^{-2}
SDI	0.2100	-30.00 m^{-3}
SFI	0.2100	30.00 m^{-3}
QFY	0.5000	1.50 m^{-2}
SFI	0.2100	30.00 m^{-3}
SDI	0.2100	-30.00 m^{-3}
3/4 BEND	1.0884	-0.33 m^{-2}
QDZ	0.3400	-1.50 m^{-2}
QFZ	0.3400	2.00 m^{-2}
Matching cell length	17.6115	

Table 4.4 Magnet separations (between magnetic ends) - SP3V35

Section	Length (m)
IR - QDX	3.3326
QDX - QFX	0.3900
QFX - QDY	0.2800
QDY - B34	0.2500
B34 - SDI	0.2500
SDI - SFI	1.5061
SFI - QFY	0.2500
QFY - SFI	0.2500
SFI - SDI	1.5061
SDI - B34	0.2500
B34 - QDZ	0.5000
QDZ - QFZ	0.4100
QFZ - Center of straight section	2.9600
QF - Center of straight section	1.5367
QF - QD	0.3950
QD - BEND	0.2500
BEND - SD	0.2300
SD - SF	0.6020
SF - QFC	0.1800
QFC - SF	0.1800
SF - SD	0.6020
SD - BEND	0.2300
BEND - QD	0.2500
QD - QF	0.3950
QF - Center of straight section	1.5367

Table 4.5 Size of good field region[†] (r)

	Dipole	Quadrupole	Sextupole
Horizontal (mm)	± 30 mm (relative to beam orbit)	± 11 mm	
Vertical (mm)			32 mm
Radial (mm)			32 mm

[†] radius at which $\Delta B/B$ is specified, see Section 3.1.7

Table 4.6 Allowable systematic multipole coefficients (Section 4.1.2)

Magnet	Multipole coefficients	Radius (mm) for ΔB/B	ΔB/B
Gradient dipole	b_2	30	1.00×10^{-3}
Gradient dipole	b_3-b_{14}	30	5.00×10^{-4}
Quadrupole	b_6, b_{10}, b_{14}	32	5.00×10^{-4}
Sextupole	b_9	32	4.42×10^{-3}
Sextupole	b_{15}	32	1.21×10^{-3}

Table 4.7 Allowable random multipole coefficients

Magnet	Multipole coefficients	Radius (mm) for ΔB	ΔB/B
Gradient dipole	b_2	30	1.00×10^{-4}
Gradient dipole	b_3,b_5,b_7,b_9	30	1.00×10^{-4}
Quadrupole	b_6, b_{10}, b_{14}	32	5.00×10^{-4}
Quadrupole	b_7,b_8,b_9,b_{11}	32	1.00×10^{-4}
Sextupole	b_5	32	1.00×10^{-3}
Sextupole	b_7	32	3.20×10^{-4}

Table 4.8 Alignment tolerances

	X (in µm)	Y (in µm)	Roll Angle (in µrad)
Gradient dipole	200	200	500
Quadrupole	200	200	500
Sextupole	200	200	500

4.1.2 Magnetic Field Quality

The magnetic field inside the bore of a magnet can be expressed as a power series:

$$F = B_y + iB_x = \sum_{n=1}^{n} (b_n + ia_n) r^{n-1} e^{i(n-1)\theta} \tag{1}$$

where B is the magnetic flux density, r and θ are the polar coordinates of the point at which the field is evaluated and b_n and a_n are respectively the normal and skew n-pole coefficients. In this notation n=1 is the dipole component, n=2 the quadrupole component, n=3 the sextupole component. It is important to note that $b_3=0.5\ \partial^2B_y/\partial x^2$. The multipole coefficients are usually expressed in $T/cm^{(n-1)}$ and are often normalized to the fundamental component (i.e. for a sextupole b_9/b_3 is in cm^{-6}). The field quality can also be expressed in terms of B_n/B where $B_n=|b_n+ia_n|\ r^{(n-1)}$ is the n-pole component of the magnetic field and is expressed in Tesla, r is the radius of the good field region and B is the required field.

The magnetic field has been evaluated using the numerical codes Ansys® for 2D analysis and Amperes© for 3D analysis. The multipole coefficients have been computed by Fourier analysis of the vector potential results ($B_x=\partial A_z/\partial y$, $B_y= -\partial A_z/\partial x$) around a circle with a radius greater than the specified good field region and not containing any discontinuities (i.e. coils or yoke). For the gradient dipole, since the good field region is oval and such a circle does not exists, a least square fit approach has been utilized and the normal multipole components b_n have been computed with the following matrix expression [2]:

$$b_n = ((G^T G)^{-1} G^T C)_n \times n \tag{2}$$

where C is the vector of the vector potential solution on the boundary of the region and the matrix G is such that $G_{mn}=r_m^n \cos(n\theta)$, where r and θ are the polar coordinates of the point at which the vector potential has been computed and m represents the m^th^ point along the boundary. With this approach, the polynomial terms are not orthogonal and the multipole coefficients depend on the number of terms used in the fitting.

After computing the multipole coefficients using the vector potential solution, the magnetic field can be reconstructed using Equation 1 and the error ΔB/B evaluated as follows:

$$\frac{\Delta B}{B} = \frac{\sqrt{\Delta B_x^2 + \Delta B_y^2}}{\sqrt{B_x^2 + B_y^2}} \tag{3}$$

where B is the required field and ΔB is the difference between the computed field and the required one.

The good field region is defined as the area in which the field quality meets or exceeds the specifications expressed in terms of normal and skew multipole coefficients, B_n/B or ΔB/B. The computed multipole coefficients are validated with tracking studies with the element-by-element tracking code LEGO designed to study single particle dynamics (Section 3.1.7).

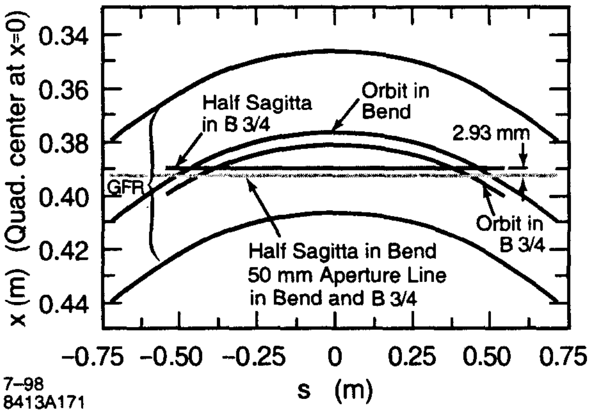

Figure 4.3 Beam orbit in the long and short gradient dipoles

The beam orbit in the gradient dipole or offset quadrupole shown in 4.3 is a hyperbolic cosine [3]:

$$\begin{bmatrix} x(s) \\ x'(s) \end{bmatrix} = \begin{bmatrix} \cosh(s\sqrt{|k|}) & \frac{1}{\sqrt{|k|}}\sinh(s\sqrt{|k|}) \\ \sqrt{|k|}\sinh(s\sqrt{|k|}) & \cosh(s\sqrt{|k|}) \end{bmatrix} \begin{bmatrix} x(0) \\ x'(0) \end{bmatrix} \tag{4}$$

in which k is the normalized quadrupole gradient ($k_{quad}=b_2/(B\rho)$), s is the arclength and x is distance from the center of the quadrupole. The reference position used to specify the multipole coefficients is the beam orbit half sagitta. The magnetic field traversed by the particles can be expressed in terms of multipole coefficients computed around the beam orbit. The off-center multipole coefficients are characterized by ‘spilldowns’ from higher order multipoles to lower order multipoles. The off-center spilldown multipole coefficients can be derived from the coefficients defined at the reference centerline using the following matrix expression:

$$b_n(x+\Delta x) = \frac{\{[T_{ij}] \cdot nb_n(x)\}_n}{n} \tag{5}$$

where $T_{ij}=k_{ij}\Delta x^{j-i}$, $k_{1j}=j$, $k_{ij}=0$ for $i>j$, $k_{ij}=1$ for $i=j$, $k_{ij}=k_{(i-1)(j-1)}+k_{i(j-1)}$ for $i>1$ and $j\geq 1$.

In the 2D analysis the core length has been conservatively underestimated as equal the specified magnetic length. Since the 3D fringe field makes the effective length longer than the core length, after chamfering the pole ends to improve the field quality the effective length will still be longer than the magnetic length specified. This way the integrated field requirements will be met with a local field less than the design value. The size of the chamfers will be determined according to the magnetic measurements of a prototype and to the 3D calculations performed with the code Amperes©.

The multipole coefficients can be separated in systematic (average) coefficients and in random (rms) coefficients. The random multipoles caused by variation of the yoke’s magnetic permeability along the magnet length can be minimized by shuffling the laminations before assembly. Errors in positioning multiple-piece yokes are another cause of random multipoles. In SPEAR 3, the gradient dipoles have very small random multipoles because they are made of one-piece laminations. The Collins quadrupoles and the closed yoke sextupoles have higher random multipoles because they are made respectively by two and three piece laminations.

4.1.3 Dipole Magnets

In the SPEAR 3 ring there are 36 gradient dipole magnets, of which 28 are full-length magnets for the standard cells and 8 are 3/4 length magnets for the matching cells. Each cell has two C-type configuration gradient dipoles that allow the synchrotron radiation to exit the ring. The C-type configuration has been chosen instead of the H-type because it simplifies the design of the magnet, the vacuum chamber and other components while provides good stiffness and field quality. The gradient dipoles are made of one-piece laminations and will be installed after the vacuum chamber is in place. The combined dipole/quadrupole function allows simultaneous bending and defocusing of the beam. The orbit of the particles through the gradient dipole is the hyperbolic cosine described by Equation 4. The half sagitta is 16.6 mm for the full-length magnet and 9.4 mm for the 3/4-length magnet. The good field region is an ellipse centered on the beam orbit with a 60 mm horizontal aperture and a 22 mm vertical aperture (Figure 4.86).

The SPEAR 3 gradient dipole is a straight magnet. The curved and segmented options were considered but discarded because of complexity of assembly and cost. The curved magnet would allow reducing the magnet pole width by 33 mm and decreasing the flux to be carried in the yoke but it requires repunching different slots in each lamination so that, after aligning the laminations and inserting the tension rods, its axis follows the arc. The coils should follow the same curve. The segmented option, for example 2 segments, would reduce the pole width by 25 mm and would still require the use of a single length coil in order to reduce the total length. In this configuration, the yoke would be made of two straight parts joined together with a wedge and supported together or individually.

The 3/4-length magnet is identical to the full-length magnet in terms of cross section and current. The two magnets differ in the position of the pole reference line with respect to the beam orbit half sagitta (0 mm for the full-length magnet and 2.69 mm for the 3/4-length magnet). All the dipole are equipped with individually powered trim coils that allow a 2% magnetic field adjustment.

4.1.3.1 Full Length Dipole

The main parameters of the full length gradient dipole are listed in Table 4.9. The magnet cross section is shown in Figure 4.4. The pole tip shape listed in Table 4.9 has been determined by conformal mapping of the ALS gradient dipole [4]. The conformal mapping transformation is composed by the following three steps:

1. Mapping the ALS gradient dipole into a dipole.
2. Scaling the dipole pole width to match the SPEAR 3 requirements.
3. Mapping the dipole into the SPEAR 3 gradient dipole.

The good field region extends horizontally from -46.6 mm to +46.6 mm in respect to the pole reference line (coincident with the full-length magnet half sagitta), and vertically from -11 mm to +11 mm (Figure 4.80). Since the beam size varies through the hyperbolic cosine beam orbit the pole width is not centered with the half sagitta. The pole width and the position of the pole bumps have been computed using the following formula:

$$\frac{\Delta B}{B} = \frac{e^{-7.17\left(\frac{a}{h} - 0.39\right)}}{100} \qquad (6)$$

where $\Delta B/B$ is 10^{-5}, a is the pole overhang and h is the half gap. This formula estimates the pole width required to achieve a given $\Delta B/B$ in a dipole which after is conformally mapped into the gradient dipole [1]. The fixed distance between the beam line and the support girders limits the height of the magnet to 0.787 m and consequently the magnetic flux the yoke can carry without saturating. The pole width is limited by the maximum flux the yoke can carry and by saturation of the inner corner. The coils are tilted to decrease the saturation in the region between the pole and the return leg.

The 2D magnetic analysis has been performed using the finite element code Ansys® version 5.4. The model shown in Figure 4.82 represents half magnet because of the magnet symmetry respect to middle plane. It uses Neumann boundary conditions at the middle plane and infinite boundary conditions at the other boundaries. The B-H curve used for the AISI 1010 steel [5] with a packing factor of 0.98 is shown in Figure 4.119. The flux lines and the flux density in the yoke at the nominal current are shown in Figure 4.86 and Figure 4.87. At the nominal current, the maximum field in the yoke is 2.1 T. Figure 4.85 shows the decrease in magnet efficiency with current caused by the saturation of the yoke. At 3.0 GeV, the efficiency is 98 %. In Table 3.16 are listed the normal multipole coefficients at different currents. Figure 4.84 shows $\Delta B/B$ along the midplane at various current levels. Figure 4.85 shows B_n/B computed with the off-center coefficients on an ellipse centered on the beam orbit with a 60 mm horizontal aperture and a 22 mm vertical aperture. Figure 4.86 shows $\Delta B/B$ computed with the off-center coefficients along the beam orbit on the same ellipse. The magnet field quality degrades rapidly beyond 110% of the nominal field. Figure 4.89

shows B_n/B computed at different currents at a radius of 30 mm from the half sagitta. The multipole component that changes the most with the current is the sextupole.

In the 2D analysis the core length has been conservatively underestimated as equal the specified magnetic length. Since the 3D fringe field makes the effective length longer than the core length, after chamfering the glued end packs to improve the field quality the effective length will still be longer than the magnetic length specified. This way the integrated field requirements will be met with a local field less than the design value. The size of the chamfers will be determined according to the magnetic measurements of a prototype and to the 3D calculations performed with the code Amperes©. The chamfering can also be used to equalize the magnetic length across the midplane. Figure 4.87 shows the 3D field distribution at the ends of the magnet with infinite permeability yoke. Further studies will be performed to assess the integrated field variation along the transversal position and the end-chamfering required to correct such a variation.

The coils are composed by three pancakes per pole and are made of a 14 mm × 12.6 mm conductor with a 6 mm diameter water-cooling channel and no internal joints. Each pancake is made of 14 turns in 2 layers. The pancake height is less than the minimum yoke gap to allow insertion onto the magnet pole. Each individual conductor is insulated with 50% overlapped Dacron tape (0.13 mm thick and 19 mm wide) and 50% overlapped Mylar tape (0.08 mm thick and 19 mm wide). Each coil pancakes is ground insulated with 50% overlapped fiberglass tape (0.25 mm thick and 38 mm wide) and then epoxy impregnated. The coils will be hipotted at a voltage 100% higher than the string voltage plus 1 kV. Each coil will be leak checked at 350 psi and must pass a water flow test. The magnet core is fabricated from thin AISI 1010 steel laminations 0.5 mm thick. After precisely stacking and aligning the laminations on a fixture, they will be compressed and the side plates will be pinned to the end plates. The voids between the side plates and the step in each lamination will be filled with a steel reinforced epoxy (Devcon). This is a fabrication technique first used for the 1.5 m and 2.0 m PEP-II insertion quadrupoles and more recently for the 0.8 m long ALS gradient dipole magnets. These magnets proved to be distortion free and magnetic measurements verified good field quality. The random multipoles are expected to be small because the yoke is made of one-piece laminations and the stamping tolerances are 25 μm. The effect of a variation of permeability is minimized by shuffling the laminations.

The magnet is supported with a six-strut system (Section 4.1.10). Because of the small clearance between magnet and girder, the supports are located on the sides. The magnet has 6 survey alignment balls (4 on top, 2 on the side) precisely indexed to the laminations. The position of the 6 survey alignment balls with respect to a set of magnet datum lines will be measured in all the magnets with a coordinate measuring machine or a laser interferometer theodolite system.

Since this magnet is a gradient dipole (or offset quadrupole), accurate positioning of its magnetic center is required. The alignment tolerances are listed in Table 4.8. The magnetic measurements will need to measure the integrated field vs. the excitation current, and to locate the center and the roll angle of the quadrupole field with respect to the alignment balls or to the magnet datum lines. The field quality will be determined by the magnetic measurement procedure described in Section 4.1.8.

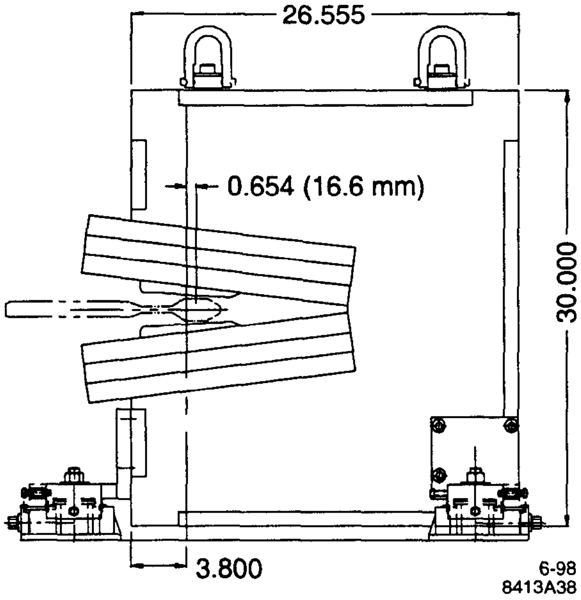

Figure 4.4 Cross section of the gradient dipole magnet (trim coils not shown).

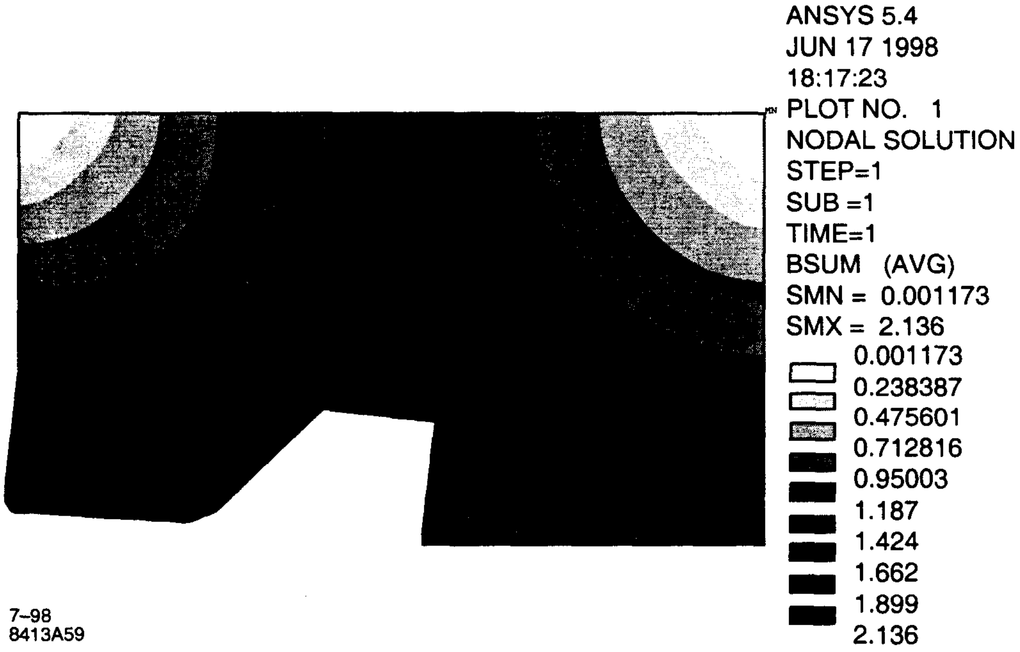

Figure 4.5 Gradient dipole magnetic induction plot (the values are in Tesla). The maximum field at the two pole bumps is 2.14 T.

	FULL BEND	3/4 BEND	Trim Coil (2%)	Trim Coil 3/4 (2%)
Number of Magnets	28	8	28	8
Quad Strength (1/m^2)	–0.3300	–0.3300	-0.00660	–0.00467
Bending Angle (rad)	0.185	0.139	0.0037	0.0028
Magnetic Arc/Straight Length (m)	1.4521/1.4500	1.0884/1.0875		
Nominal Gradient (T/m)	–3.630	–3.630	-0.0726	–0.0513
Bxρ (Tm)	11.000	110.000	11.000	11.000
X at Center/Ends/Half Sagitta (m)	0.3758/0.4089/0.3923	0.3803/0.3990/0.3896		
Pole Center - Half Sagitta Distance (m)	0.0000	–0.00269		
B at the Center (T)	-1.364	-1.380		
B at the Ends (T)	-1.484	-1.448		
B at Half Sagitta (T)	-1.424	-1.414		
Integrated Field Along Trajectory (Tm)	-2.039	-1.527		
Half Sagitta (m)	0.0166	0.0094		
Gap Height (m) @ Half Sagitta	0.0500	0.0503		
Core Length (m)	1.4500	1.0875		
Lamination Height/Width (m)	0.787/0.664	0.787/0.664		
Core Weight (kg)	5400	4100		
Ampere-Turns per Pole (98% eff.)	28912	28912	578	409
Turns/Pancakes per Pole	42/3	42/3	45/1	45/1
Conductor Size/Cooling Hole Diam (mm)	12.6/14.0/6.0	12.6/14.0/6.0	3.55/2.00	3.55/2.00
Conductor Cross-Sectional Area (mm^2)	147.27	147.27	6.74	6.74
Conductor Length/Pole (m)	54.2	44.0	174	141
Current (A)	688.4	688.4	12.8	9.1
Current Density (A/mm^2)	4.7	4.7	1.9	1.3
Inductance (mH)	67	50	77	58
Total Coils Weight (kg)	428	348	21	17
Magnet Resistance @ 40 C (mΩ)	41	33	960	780
Power/Magnet (kW)	19.4	15.8	0.159	0.064
Power/String (kW)	671 (powered in series)			
Voltage Drop/Magnet (V)	28.25	22.94	12.34	7.09
Voltage Drop/String (V)	974 (powered in series)			
Water Flow Rate/Magnet (gpm) (75 psi, 6 circuits, 21 °C)	5.2	5.8		
Water Flow Rate/String (gpm)	192			
Water Temperature Rise (°C)	14.2	10.3		
Reynold's Number	11786	13250		
Water Velocity (m/s)	1.9	2.2		
Friction Factor	0.0309	0.0301		

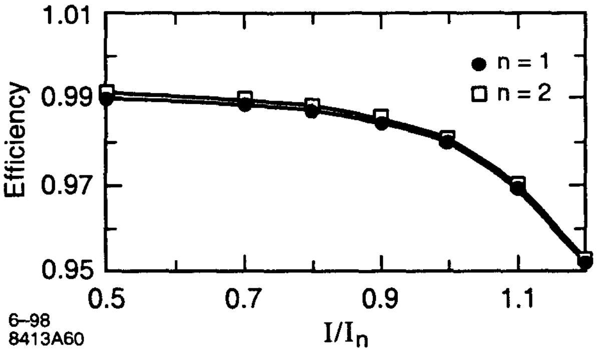

Figure 4.6 Efficiency vs. current in the gradient dipole. The dipole and quadrupole field efficiency is 98% at the nominal current and it decreases rapidly at higher currents.

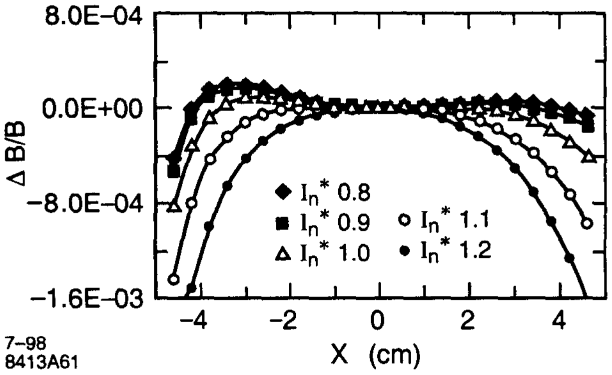

Figure 4.7 ΔB/B vs. transversal position at different currents in the gradient dipole (I_n=25757 AT). The x=0 position corrisponds to the half sagitta.

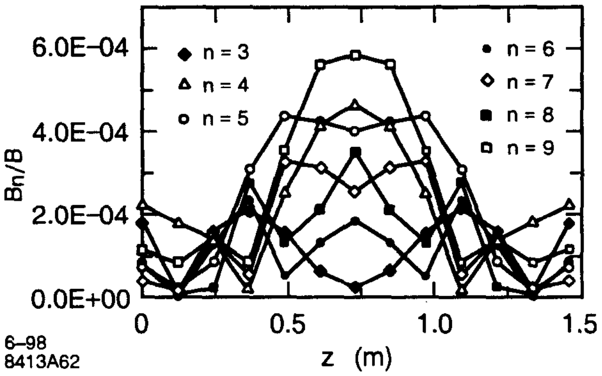

Figure 4.8 B_n/B vs. longitudinal position at the nominal current I_n=25757 AT. B_n/B is computed with the spilldown coefficients along the beam orbit on an ellipse with 60 mm horizontal aperture and 22 mm vertical aperture. The average value of B_n/B is less than the 5×10^{-4} specified in the tracking code at r=30 mm from the orbit.

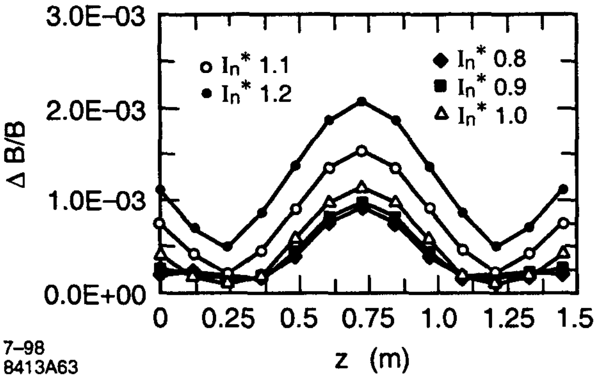

Figure 4.9 ΔB/B vs. longitudinal position at different currents in the gradient dipole (I_n=25757 A-T), ΔB/B is computed with the spilldown coefficients along the beam orbit on an ellipse with 60 mm horizontal aperture and 22 mm vertical aperture.

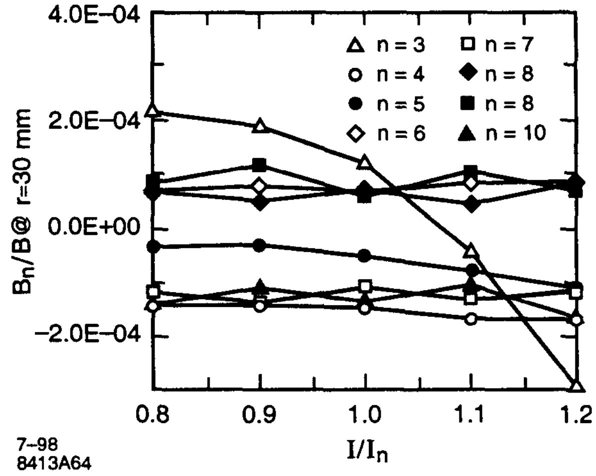

Figure 4.10 B_n/B in the gradient dipole at r=30 mm from half sagitta and I_n=25757 A-T. The yoke saturation causes a change only in the sextupole component.

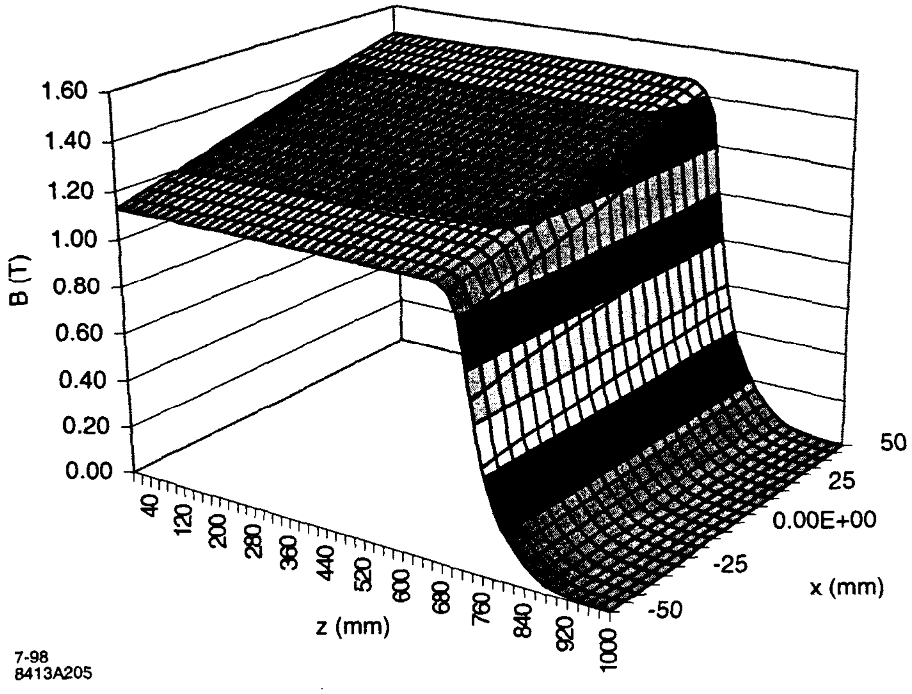

Figure 4.11 Vertical field vs. x and z in the gradient dipole at I_n=25757 A-T and infinite permeability yoke. Further studies will be performed to assess the integrated field variation along the x axis and the end chamfering required to correct such a variation.

Table 4.9 Gradient dipole pole tip coordinates.

X (mm)	Y (mm)	X (mm)	Y (mm)	X (mm)	Y (mm)	X (mm)	Y (mm)
-70.070	159.080	-54.309	28.992	-10.230	25.668	54.848	21.972
-82.400	50.600	-52.270	28.840	-8.163	25.531	56.759	21.887
-82.400	39.100	-50.220	28.669	-6.106	25.395	58.678	21.809
-82.243	37.642	-48.174	28.490	-4.060	25.261	61.362	21.642
-81.872	36.223	-45.997	28.306	-2.025	25.130	64.059	21.393
-81.296	34.874	-44.410	28.175	0.000	25.000	66.362	21.099
-80.525	33.626	-42.825	28.043	5.334	24.665	68.670	20.746
-79.576	32.507	-41.234	27.911	10.599	24.343	70.518	20.535
-78.471	31.544	-38.840	27.725	15.797	24.033	72.522	20.441
-77.658	30.999	-36.436	27.538	20.930	23.734	74.518	20.514
-75.981	29.913	-34.021	27.356	26.001	23.447	76.504	20.766
-74.163	29.117	-31.599	27.168	31.012	23.169	78.490	21.186
-72.233	28.682	-29.979	27.050	35.965	22.901	80.459	21.775
-70.263	28.620	-28.356	26.932	38.224	22.778	81.569	22.180
-68.307	28.774	-26.728	26.810	40.231	22.679	101.000	30.600
-66.337	28.961	-24.278	26.634	42.242	22.577	191.100	117.210
-64.364	29.121	-21.821	26.461	44.259	22.471	192.450	129.350
-62.377	29.223	-19.356	26.291	46.283	22.366	313.235	115.900
-60.376	29.260	-16.883	26.118	48.313	22.256	300.329	0.000
-58.367	29.225	-14.399	25.951	50.626	22.153		
-56.339	29.127	-12.309	25.809	52.945	22.057		

Table 4.10 Gradient dipole multipoles (T/cm$^{(n-1)}$) vs. current (I_n =25757 AT) at half sagitta. (Figure 4.11).

	$I_n \times 0.8$	$I_n \times 0.9$	$I_n \times 1$ (3 GeV)	$I_n \times 1.1$	$I_n \times 1.2$
b_1	1.022E+00	1.147E+00	1.268E+00	1.380E+00	1.477E+00
b_2	2.598E–02	2.915E–02	3.223E–02	3.506E–02	3.754E–02
b_3	2.722E–05	2.709E–05	2.074E–05	–2.184E–06	–4.256E–05
b_4	–5.412E–06	–6.214E–06	-7.038E–06	–8.668E–06	–9.915E–06
b_5	–2.121E–07	–2.037E–07	-5.341E–07	–9.856E–07	–1.608E–06
b_6	2.782E–07	3.617E–07	3.687E–07	3.732E–07	6.111E–07
b_7	–1.729E–07	–2.250E–07	-2.125E–07	–2.875E–07	–2.724E–07
b_8	1.435E–08	4.718E–09	1.459E–08	3.322E–08	6.815E–09
b_9	1.570E–08	2.418E–08	1.947E–08	3.330E–08	2.482E–08
b_{10}	–4.013E–09	–3.066E–09	-4.830E–09	–7.973E–09	–1.551E–09
b_{11}	–5.474E–10	–1.500E–09	-9.004E–10	–2.547E–09	–1.059E–09
b_{12}	2.922E–10	2.238E–10	3.798E–10	6.508E–10	9.132E–12
b_{13}	-1.702E–11	5.483E–11	1.242E–11	1.316E–10	–1.156E–11
b_{14}	–9.297E–12	-6.138E–12	-1.402E–11	-2.697E–11	–9.468E–12
b_{15}	2.301E–12	-1.118E–12	5.496E–13	–4.563E–12	3.205E–12
b_{16}	1.431E–13	6.610E–14	2.880E–13	6.166E–13	-4.688E–13
b_{17}	–8.695E–14	3.639E–15	-3.044E–14	8.836E–14	–1.361E–13
b_{18}	–6.646E–16	1.181E–16	-2.543E–15	–5.980E–15	7.205E–15
b_{19}	1.161E–15	1.442E–16	4.130E–16	–7.395E–16	1.939E–15

4.1.3.2 3/4-Length Dipole

The 3/4-length gradient dipole has the same gradient and magnetic field of the full dipole and 75% of its length and bending angle. The beam orbit is shown for both magnets in Figure 4.3. The half sagitta is 9.4 mm in the 3/4-length magnet and 16.6 mm in the full-length magnet. The 3/4-length magnet is identical to the full-length magnet in terms of cross section and current. The two magnets differ in the position of the pole reference line with respect to the beam orbit half sagitta (0 mm for the full-length magnet and 2.69 mm for the 3/4-length magnet). Since the sagitta and the good field region are smaller, ΔB/B is lower than in the full-length dipole.

4.1.4 Quadrupole Magnets

The 94 SPEAR 3 quadrupoles have 4 different lengths (0.60, 0.5, 0.35, 0.20 m) and 9 different excitation currents. All the quadrupoles have the same bore diameter of 70 mm. In order to reduce the number of different parts and components, they are designed with the same cross section and different lengths and excitation currents. The Collins type configuration [6] has been chosen because it allows space for the vacuum chamber and the synchrotron radiation to exit the ring. In the Collins quadrupoles the magnetic center is coincident with the geometrical center and the odd multipole components present in the C-type quadrupoles are zero. In order to accommodate the varying sizes of the vacuum chamber, non-magnetic C-shape and flat spacers of different widths are used between the upper and lower yokes. To reduce the influence of the earth magnetic field and other stray fields, the top and bottom halves can be connected by magnetic shunts. Individually powered QMS coils on each quadrupole allow ~2% beam alignment shunting. 20 QF and 20 QD are powered individually to compensate for the changes due to wigglers and undulators.

4.1.4.1 Main Quadrupoles

The main parameters of the standard cell and matching cell quadrupoles are described in Tables 4.11 and 4.12 . The magnet cross section is shown in Figure 4.97.

The pole geometry listed in Table 4.14 is conformally mapped from the ALS quadrupoles while the mechanical structure is similar to the BESSY 2 quadrupoles [8]. The yoke consists of an upper and a lower half attached horizontally and vertically with bolts to spacers. The sides of the laminations and the C-shape and flat spacers are used to align horizontally and vertically the two halves. The ears in the laminations are non-symmetrical and are alternately stacked in packs to allow space for the bolts.

The magnetic analysis has been performed for the quadrupole magnet QD that has a gradient of 22 T/m (nominal + 10% tuning), the highest gradient of all the quadrupoles in the ring, using the finite element code Ansys® version 5.4. Since the magnet is symmetrical respect to middle plane, as shown in Figure 4.14, only half of the magnet has been modeled. In the model Neumann boundary conditions are used at the middle plane and infinite boundary conditions at the other boundaries. The B-H curve used for the AISI 1010 steel [5] with a packing factor of 0.98 is shown in Figure 4.42.

The inscribed radius is 35 mm and the radius of the good field region is 32 mm. Figures 4.14 and Figure 4.91 show the flux lines and the flux density in the yoke at the nominal current. At the nominal current the maximum field inside the yoke is 1.87 T. Figure 4.92 shows the decrease in magnet efficiency with current caused by saturation. In Table 4.66 are listed the normal multipole coefficients at different currents. Figure 4.93 shows $\Delta B/B_2$ along the middle plane at various current levels. At 3.0 GeV $\Delta B/B_2$ is 5×10^{-4} and the magnet efficiency is 98.3%. Figure 4.94 shows that the main multipole components at a radius of 32 mm are b_6, b_{10} and b_{14} (allowed also in the case of a perfectly symmetrical quadrupole) and they are less than the allowable values specified in Table 4.57.

The magnet core is fabricated from thin AISI 1010 steel laminations approximately 0.5 mm thick. After precisely stacking, aligning and gluing the laminations, they will be compressed axially by tie rods. In order to avoid residual stresses and deformations of the yoke, the yoke is not split in two at the vertical plane and welded together after inserting the coil (as in the APS quadrupoles [9]). The coils are composed by two pancakes per pole because of the limited space to insert the coil onto the poles. The inner coil has 64 turns, the outer coil has 60 turns, and the QMS coil has 24 turns. The QMS coils are needed also to incremental adjust the quadrupole field and determine the alignment by monitoring the beam position with the downstream BPMs. The inner and outer coils are made of a 4.76 mm-wide square copper conductor with a 3.18 mm diameter cooling channel. Each individual conductor is insulated with a polyester glass fiber insulation (Daglass, 0.10 mm thick). Each coil pancakes is ground insulated with 50% overlapped fiberglass tape (0.25 mm thick and 38 mm wide) and then epoxy impregnated. The coils will be hipotted at a voltage 100% higher than the string voltage plus 1 kV. Each coil will be leak checked at 350 psi and must pass a water flow test.

As shown in Figure 4.90, the magnet is supported on 6 struts (Section 4.1.10). Since the quadrupole cross-section is large compared to its maximum length, the vertical deflection is small. The magnet has 6 survey alignment balls (4 on top, 2 on the side) precisely indexed to the laminations. The position of the alignment balls will be measured with respect to the magnet datum lines with a laser interferometer theodolite system.

Accurate horizontal and vertical positioning of all the quadrupoles is required. The alignment tolerances are listed in Table 4.85. The magnetic measurements will be used to locate the center of the quadrupole with respect to the alignment balls or the magnet datum lines. The quadrupole transfer function and field quality will be determined by the magnetic measurement procedure described in Section 4.1.8.

In Table 4.59 are listed the random multipoles of the two-piece quadrupole caused by errors in the assembly of the two magnet halves. These estimated multipoles are based on measurements of the PEP-II LER quadrupoles. Since the multipole spectra due to vertical, shear and rotational displacements of one magnet half with respect to the other are different and distinct, it will be easy to minimize these errors by reassembling the magnets with poor performance. The effect of a variation of permeability is minimized by shuffling the laminations. The pole asymmetries of each lamination are compensated by flipping the laminations.

In the 2D analysis the core length has been conservatively underestimated as equal the specified magnetic length. Since the 3D fringe field makes the effective length longer than the core length, after chamfering the pole ends to improve the field quality the effective length will still be longer than the magnetic length specified. This way the integrated field requirements will be met with a local field less than the design value. The size of the chamfers will be determined according to the magnetic measurements of a prototype and to the 3D calculations performed with the code Amperes©.

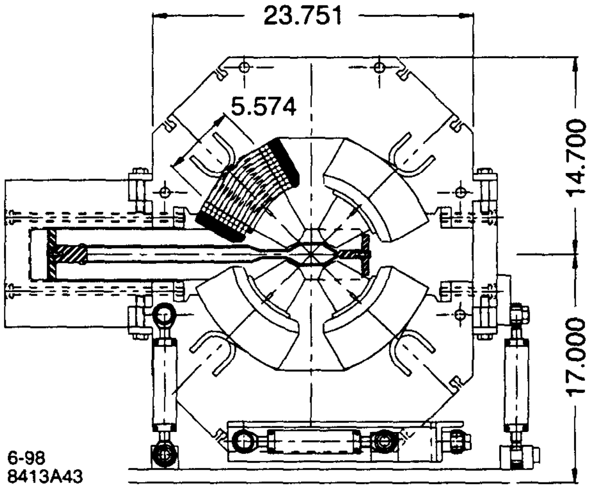

Figure 4.12 Cross section of the quadrupole magnet (magnetic shunt not shown)

Table 4.11 Standard cell quadrupole parameters.

	QF	QD	QFC	QMS coil for QD
Design Energy (GeV)	3.3	3.3	3.3	3.3
Number of Magnets	28.000	28.000	14.000	28.000
Number of Magnets/string	8	8	7	
Quad Strength (1/m^2)	2.000	–2.000	2.000	0.072 (max)
Magnetic Length (m)	0.340	0.150	0.500	0.150
Nominal Gradient (T/m)	22.000	–22.000	22.000	0.561 (r.m.s.)
Pole Tip Field (T)	0.770	–0.770	0.770	0.020 (r.m.s.)
Integrated Field (T)	7.480	–3.300	11.000	0.084 (r.m.s.)
Inscribed Radius (m)	0.035	0.035	0.035	0.035
Core Length (m)	0.340	0.150	0.500	
Yoke Height (m)	0.745	0.745	0.745	
Yoke Width (m)	0.603	0.603	0.603	
Core Weight (kg)	922	407	1356	
Ampere-Turns per Pole (98% eff.)	10942	10942	10942	279
Turns per Pole	124	124	124	240
Pancakes per Pole	2.000	2.000	2.000	1.000
Conductor Size (mm)	4.76	4.76	4.760	3.55 x 2.00
Cooling Hole Diameter (mm)	3.18	3.18	3.18	
Conductor X-Sect Area (mm^2)	13.86	13.86	13.86	6.74
Conductor Length/Pole (m)	142.5	95.4	182.2	15.82
Current (A)	88.24	88.24	88.24	11.63 (r.m.s.)
Current Density (A/mm^2)	6.4	6.4	6.4	1.7
Inductance (mH)	264	116	388	4
Resistance/Magnet (mΩ)	765	512	978	175
Power/Magnet (kW)	6.0	4.0	7.6	0.024
Power/String (kW)	47.6	31.9	53.3	
Voltage Drop/Magnet (V)	67.5	45.2	86.3	2.03 (r.m.s.)
Voltage Drop/String (V)	539	361	604 X 2	
Water Circuits	8	8	8	
Water Flow Rate/Magnet (gpm)	1.55	1.95	1.35	
Water Flow Rate/String (gpm)	12.4	15.64	9.42 X 2	
Water Pressure Drop (psi)	150	150	150	
Water Temperature Rise (o.c.) (°C)	15.5	8.7	22.3	
Reynold's Number (o.c.)	4866	6000	4263	
Water Velocity (o.c.) (m/s)	1.5	1.85	1.31	
Friction Factor (o.c.)	0.033	0.031	0.031	

Table 4.12 Matching cell quadrupole parameters.

	QFZ/QDX	QFX	QDY/QDZ	QFY
Design Energy (GeV)	3.3	3.3	3.3	3.3
Number of Magnets	4	4	4	4
Quad Strength (1/m^2)	2.000	1.680	1.500	1.500
Magnetic Length (m)	0.340	0.600	0.340	0.500
Nominal Gradient (T/m)	22.000	18.480	16.500	16.500
Pole Tip Field (T)	0.770	0.647	0.578	0.578
Integrated Field (T)	7.480	11.088	5.610	8.250
Inscribed Radius (m)	0.035	0.035	0.035	0.035
Core Length (m)	0.340	0.600	0.340	0.500
Yoke Height (m)	0.745	0.745	0.745	0.745
Yoke Width (m)	0.603	0.603	0.603	0.603
Core Weight (kg)	922	1627	922	1356
Ampere-Turns per Pole	10942	9191	8206	8206
Turns per Pole	124	124	124	124
Pancakes per Pole	2	2	2	2
Conductor Size (mm)	4.76	4.76	4.760	4.760
Cooling Hole Diameter (mm)	3.18	3.18	3.18	3.18
Conductor X-Sect Area (mm^2)	13.86	13.86	13.86	13.86
Conductor Length/Pole (m)	142.5	207.0	142.5	182.2
Current (A)	88.24	74.12	66.18	66.18
Current Density (A/mm^2)	6.4	5.3	4.8	4.8
Inductance (mH)	264	466	264	388
Resistance/Magnet (mΩ)	765	1111	765	978
Power/Magnet (kW)	6.0	6.1	3.3	4.3
Power/String (kW)	23.8	24.4	13.4	17.1
Voltage Drop/Magnet (V)	67.47	82.33	50.61	64.70
Voltage Drop/String (V)	269.90	329.31	202.42	258.79
Water Circuits	80	8	8	8
Water Flow Rate/Magnet (gpm)	1.55	1.25	1.55	1.35
Water Flow Rate/String (gpm)	6.20	5.00	6.20	5.38
Water Pressure Drop (psi)	150.000	150.000	150.000	150.000
Water Temperature Rise (o.c.) (°C)	15.5	19.1	8.7	12.6
Reynold's Number (o.c.)	4866	3976	4866	4263
Water Velocity (o.c.) (m/s)	1.5	1.23	1.5	1.31
Friction Factor (o.c.)	0.039	0.041	0.039	0.040

Table 4.13 Quadrupole pole tip coordinates

X (mm)	Y (mm)
24.750	24.750
24.998	24.503
25.124	24.382
25.254	24.256
26.485	23.129
27.758	22.068
29.063	21.075
30.390	20.152
31.731	19.296
33.076	18.505
34.429	17.798
35.793	17.192
37.159	16.679
38.519	16.251
38.959	16.097
39.374	15.897
39.768	15.647
40.141	15.351
40.494	15.006
40.832	14.615
41.171	14.227
41.529	13.894
41.905	13.615
42.296	13.389
42.700	13.215
43.118	13.094
43.544	13.022
43.984	13.001
44.436	13.001
44.881	13.001
45.318	13.001
46.321	13.001

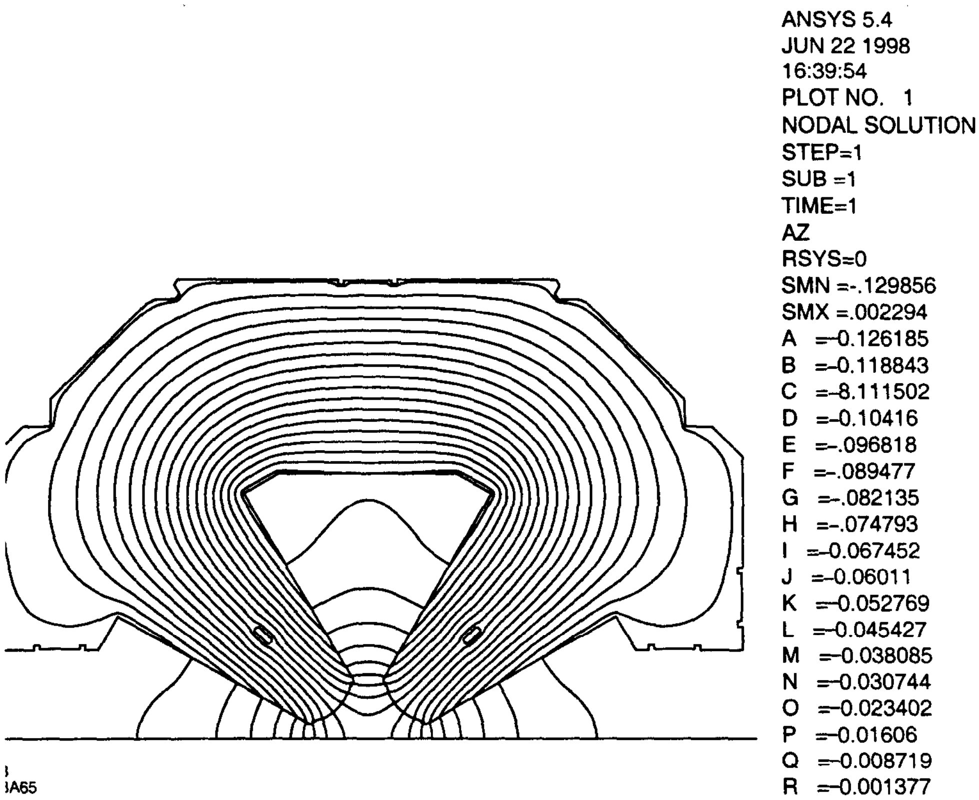

Figure 4.13 Quadrupole flux plot at I_n=9748 AT (the vector potential values are in Tm).

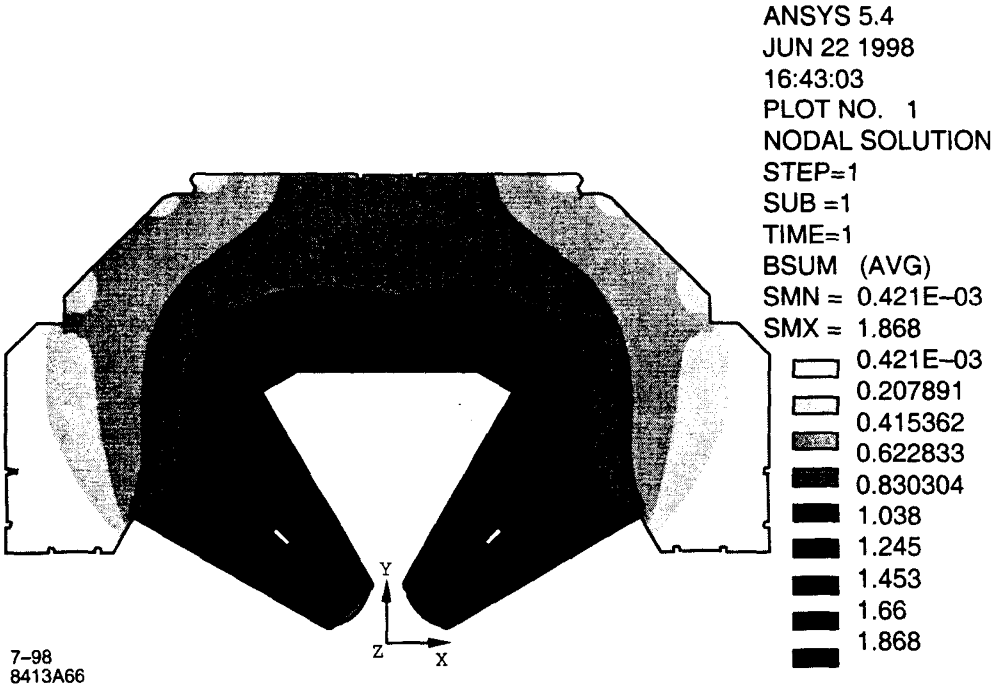

Figure 4.14 Quadrupole magnetic induction plot I_n=9748 AT (the values are in Tesla)

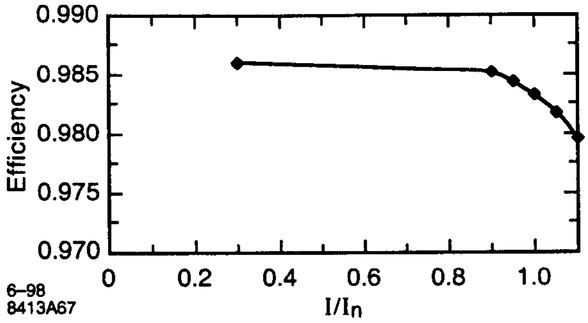

Figure 4.15 Efficiency vs. current in the quadrupole. I_n is the current at 3 GeV.

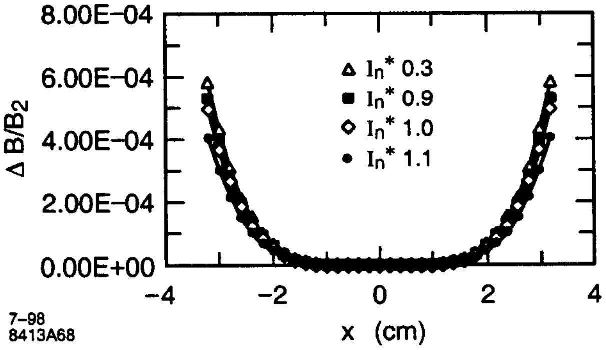

Figure 4.16 $\Delta B/B_2$ vs. transversal position at different currents in the quadrupole.

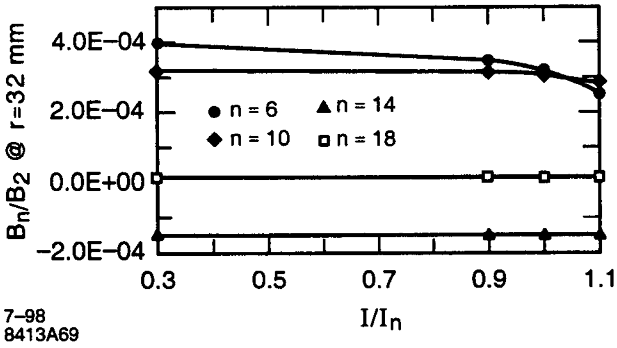

Figure 4.17 B_n/B_2 vs. current in the quadrupole at r= 32 mm.

Table 4.14 Quadrupole multipoles (T/cm(n-1)) vs. current (In=9722 AT) (Figure 4.11).

	$I_n \times 0.3$	$I_n \times 0.9$	$I_n \times 1.0$ (3 GeV)	$I_n \times 1.1$
b_1	2.59E-15	-1.05E-14	-1.90E-14	-1.78E-15
b_2	5.92E-02	0.1773	0.1966	0.2154
b_3	1.15E-16	-4.64E-16	-7.78E-16	-4.11E-16
b_4	-1.97E-08	-2.61E-10	2.13E-11	9.97E-11
b_5	-1.64E-18	2.74E-18	1.08E-17	-7.23E-18
b_6	2.83E-08	-6.56E-10	-4.80E-08	-1.74E-07
b_7	-1.77E-19	2.48E-19	1.30E-18	4.32E-19
b_8	9.94E-12	8.25E-13	8.11E-13	8.99E-13
b_9	-7.55E-21	-3.01E-20	-3.36E-20	-5.26E-20
b_{10}	-3.58E-10	-1.12E-09	-1.34E-09	-1.80E-09
b_{11}	-1.35E-21	-4.38E-21	-7.36E-21	-9.47E-22
b_{12}	1.84E-17	2.13E-15	2.54E-15	2.91E-15
b_{13}	5.89E-23	6.26E-23	-1.93E-22	1.97E-22
b_{14}	-2.91E-11	-8.70E-11	-9.63E-11	-1.05E-10
b_{15}	7.29E-24	-3.14E-23	1.15E-24	2.29E-23
b_{16}	3.30E-17	4.11E-18	4.05E-18	4.26E-18
b_{17}	-8.56E-25	-2.90E-24	-3.09E-24	-7.06E-24
b_{18}	-2.85E-13	-8.52E-13	-9.44E-13	-1.03E-12

Table 4.15 Estimated random multipole coefficients of the quadrupole magnets at 32 mm

Multipole index	B_n/B_2 normal	B_n/B_2 skew
3	5.96E-05	7.11E-05
4	7.26E-05	2.06E-05
5	9.48E-06	1.20E-05
6	1.57E-05	7.06E-06
7	3.31E-06	4.50E-06
8	3.31E-06	4.74E-06
9	1.83E-06	2.84E-06
10	2.08E-06	3.21E-06
11	1.88E-06	1.73E-06
12	2.31E-06	2.81E-06
13	33.5E-06	3.52E-06
14	3.51E-08	2.91E-06

4.1.4.2 Skew Quadrupoles

In SPEAR 3 each sextupole has a skew quadrupole coil on each one of two top and bottom poles. The sextupole magnets are described in Section 4.1.5. The main parameters of the skew quadrupole coils are listed in Table 4.11. The skew quadrupole coils are not water cooled and are individually powered. Table 4.16 shows the flux lines at the nominal current. 4.16 lists the skew multipole coefficients at the nominal current. The skew octupole component a_4 is high and it causes B_4/B_2 of 0.43 at the good field radius of 32 mm. Figures 4.27 and 4.29 show $\Delta B/B$ in the sextupole magnet SF at full current respectively without and with the skew quadrupole field. The computed multipole coefficients are validated with tracking studies with the element-by-element tracking code LEGO designed to study single particle dynamics (Section 3.1.7).

Table 4.16 Main parameters of the skew quadrupole coils.

	SD	SF, SDI, SFI
Design Energy (GeV)	3.3	3.3
Number of Magnets	28	44
Strength (1/m^2)	0.044	0.052
Magnetic Length (m)	0.250	0.210
Gradient (T/m)	0.480	0.571
Pole Tip Field (T)	0.022	0.026
Integrated Gradient (T)	0.120	0.120
Inscribed Radius (m)	0.045	0.045
Core Length (m)	0.250	0.210
Ampere-Turns per Pole (98% eff.)	843	1004
Turns per Pole	36	36
Pancakes per Pole	1.000	1.000
Conductor Size (mm)	4.76x4.76x3.18	4.76x4.76x3.18
Conductor Cross-Sectional Area (mm^2)	13.86	13.86
Conductor Length/Pole (m)	27.33	24.45
Current (A)	23.42	27.89
Current Density (A/mm^2)	1.7	2.0
Inductance (mH)	5.5	4.7
Magnet Resistance at 40 C (mΩ)	73.34	65.61
Power/Magnet (kW)	0.040	0.051
Voltage Drop/Magnet (V)	1.72	1.83
Water Circuits	1	1
Water Flow Rate/Magnet (gpm)	0.2	0.2
Water Pressure Drop (psi)	150	150
Water Temperature Rise (°C)	0.7	0.8
Reynold's Number	5800	6181
Water Velocity (m/s)	1.8	1.9
Friction Factor	0.038	0.037

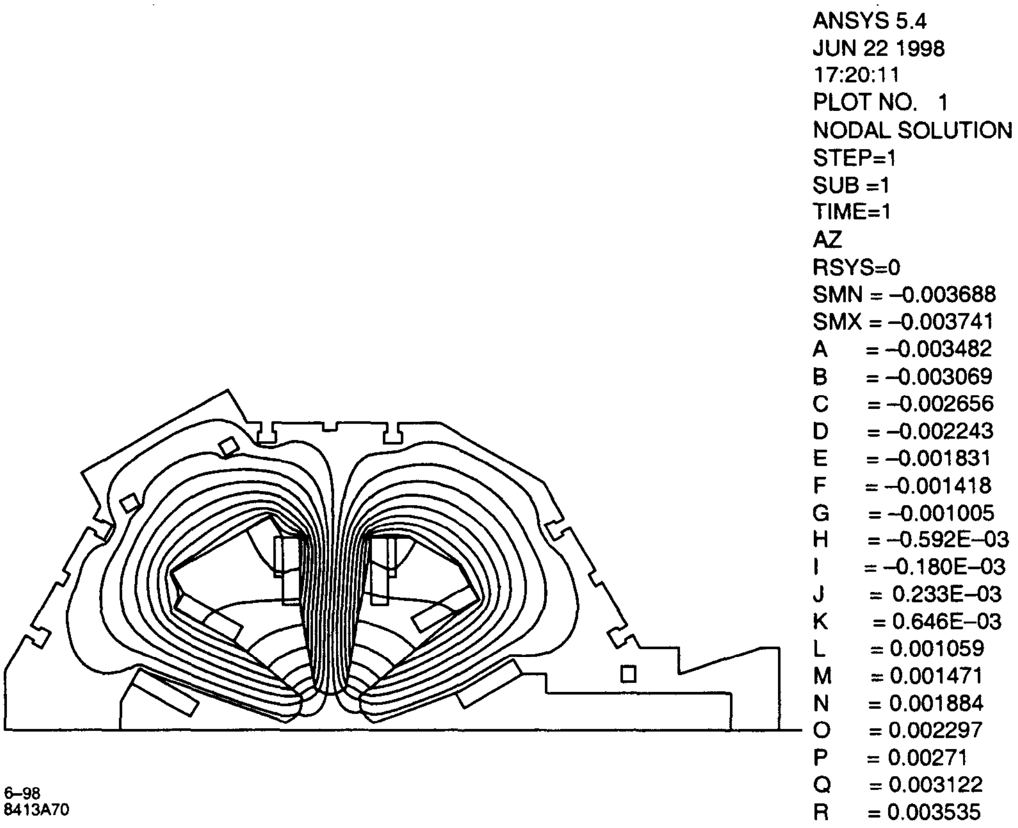

Figure 4.18 Skew quadrupole flux plot (the vector potential values are in T-m.

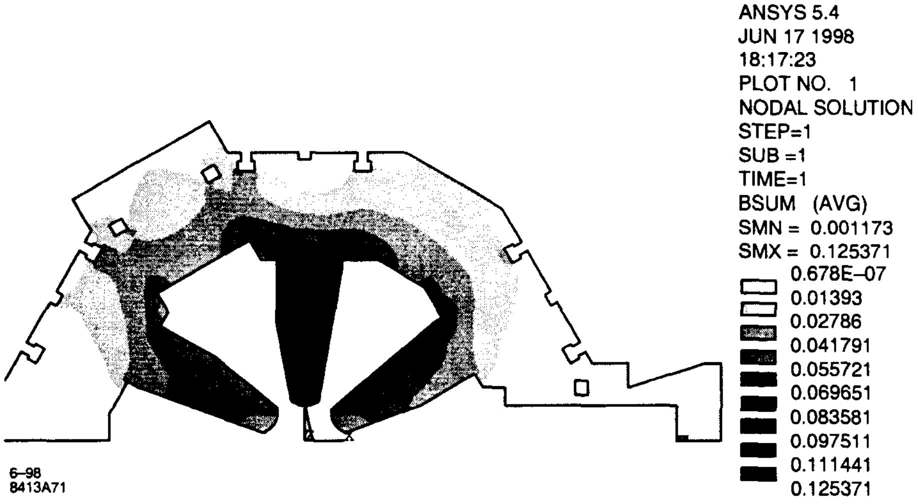

Figure 4.19 Skew quadrupole magnetic induction plot the values are in Tesla.

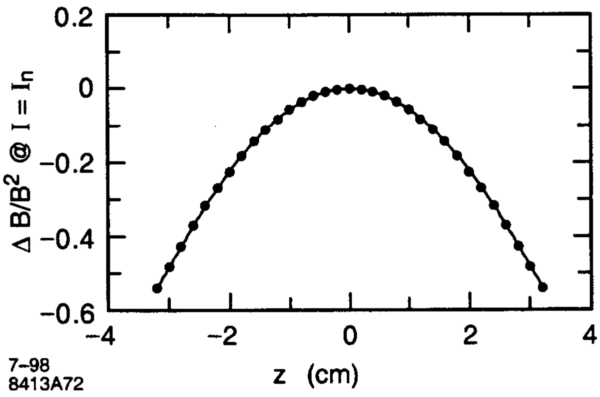

Figure 4.20 $\Delta B/B_2$ vs. transversal position in the skew quadrupole field without sextupole.

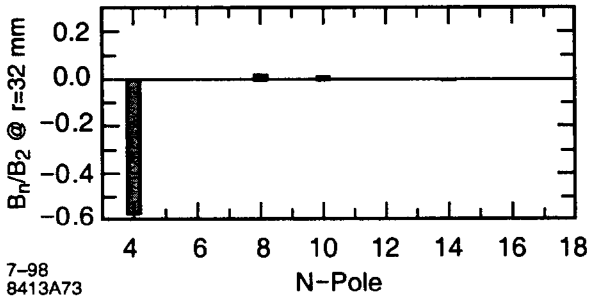

Figure 4.21 Systematic B_n/B_2 in the skew quadrupole at r =32 mm. The large skew octupole component has been validated by tracking studies.

Table 4.17 Skew quadrupole multipoles (T/cm$^{(n-1)}$) vs. current (I_n=983.8 A-T) (Figure 4.21).

a_1	1.51E-05	a_{10}	2.25E-09
a_2	5.77E-03	a_{11}	4.33E-13
a_3	2.68E-08	a_{12}	2.46E-13
a_4	-2.49E-04	a_{13}	-4.11E-14
a_5	-2.93E-08	a_{14}	-1.56E-11
a_6	4.49E-09	a_{15}	4.06E-17
a_7	2.19E-10	a_{16}	6.81E-13
a_8	5.06E-08	a_{17}	7.63E-17
a_9	4.25E-12	a_{18}	-1.19E-17

4.1.5 Sextupole Magnets

The 72 SPEAR 3 sextupoles have 2 different lengths (0.25 m and 0.21 m) and 4 different excitation currents. All the magnets have the same bore diameter of 90 mm. In order to reduce the number of different parts and components, all the magnets are designed with the same cross section and different lengths and excitation currents. The closed yoke configuration with magnetic steel spacers has been chosen over the C-type because of mechanical strength and better field quality when used with a skew quadrupole correction. The skew quadrupole parameters are described in Section 4.1.4.2.

The main parameters of the standard and matching cell sextupoles are listed in Table 4.16. The sextupole cross section is showed in Figure 4.100. The laminated core is made of a single type of laminations assembled in three sections separated by three spacers. The three sections are indexed by positioning pins and matching surfaces and bolted to the spacers. The pole tip shape (listed in Table 4.19) is flat as in the APS quadrupoles [7?]. This pole shape performs better than a quadratic hyperbola or a conformally mapped dipole profile. The pole root is asymmetrical to allow more space for the vacuum chamber and increase the excitation efficiency at higher fields.

The main sextupole coil has 33 turns of a 6.35 mm square copper conductor with a 3.15 mm diameter cooling channel. Each individual conductor is insulated with 50% overlapped Dacron tape (0.13 mm thick and 12.7 mm wide) and 50% overlapped Mylar tape (0.08 mm thick and 12.7 mm wide). The skew quadrupole coil has 36 turns of a 4.76 mm square copper conductor with a 3.18 mm diameter cooling channel, insulated with a polyester glass fiber insulation (Daglass, 0.10 mm thick). Each coil pancakes is ground insulated with 50% overlapped fiberglass tape (0.25 mm thick and 38 mm wide) and then epoxy impregnated. The coils will be hipotted at a voltage 100% higher than the string voltage plus 1 kV. Each coil will be leak checked at 350 psi and must pass a water flow test.

The magnetic analysis has been performed for the sextupole magnet SD that has a sextupole coefficient of 275 T/m^2, the highest of all the sextupoles in the ring, using the finite element code Ansys® version 5.4. Since the magnet is symmetrical respect to middle plane, as shown in Figure 4.24, only half of the magnet has been modeled. In the model Neumann boundary conditions are used at the middle plane and infinite boundary conditions at the other boundaries. The B-H curve used for the AISI 1010 steel [5] with a packing factor of 0.98 is shown in Figure 4.42.

Figures 4.24 and Figure 4.25 show the flux lines and the flux density in the yoke at 3 GeV. The maximum field in the yoke is 1.49 T. Figure 4.26 shows a slight decrease in magnet efficiency with current caused by the yoke saturation. In Table 4.25 are listed the normal multipole coefficients at different currents. Figure 4.27 shows $\Delta B/B$ along the midplane at various current levels. At 3.0 GeV, $\Delta B/B$ is 3.7 10^{-3} and the efficiency is 98.2 %. As shown in Figure 4.28 the main multipole component at the 32 mm radius is b_{15} which decays very rapidly with the radius. Figures 4.27 and 4.29 show $\Delta B/B$ in the sextupole magnet SF at full current respectively without and with the skew quadrupole coils energized. In this last case the main field error in the sextupole magnet is caused by the large octupole field generated by the skew quadrupole coils.

The yoke is made of three segments and the random multipole errors caused by the rotational, shear and vertical displacements of the core sections will be corrected by chamfering the ends. The effect of a variation of permeability is minimized by shuffling the laminations. The ears in the laminations are non-symmetrical and are alternately stacked in packs to allow space for the bolts.

The magnet core is fabricated from AISI 1010 steel laminations 0.5 mm thick. After precisely stacking, aligning and gluing the laminations, they are compressed and bolted with tie rods.

The magnet is supported on 6 struts (Section 4.1.10). Since the sextupole cross section is large compared to its maximum length, the vertical deflection is small. The magnet has 6 survey alignment balls (4 on top, 2 on the side) precisely indexed to the laminations. The position of the alignment balls will be measured with respect to the magnet datum lines with a laser interferometer theodolite system.

Accurate horizontal and vertical positioning of all the sextupoles is required. The alignment tolerances are listed in Table 4.59. The magnetic measurements will be used to locate the center of the sextupole with respect to the alignment balls or the magnet datum lines. The sextupole transfer function and field quality will be determined by the magnetic measurement procedure described in Section 4.1.8.

In the 2D analysis the core length has been conservatively underestimated as equal the specified magnetic length. Since the 3D fringe field makes the effective length longer than the core length, after chamfering the pole ends to improve the field quality the effective length will still be longer than the magnetic length specified. This way the integrated field requirements will be met with a local field less than the design value. The size of the chamfers will be determined according to the magnetic measurements of a prototype and to the 3D calculations performed with the code Amperes©.

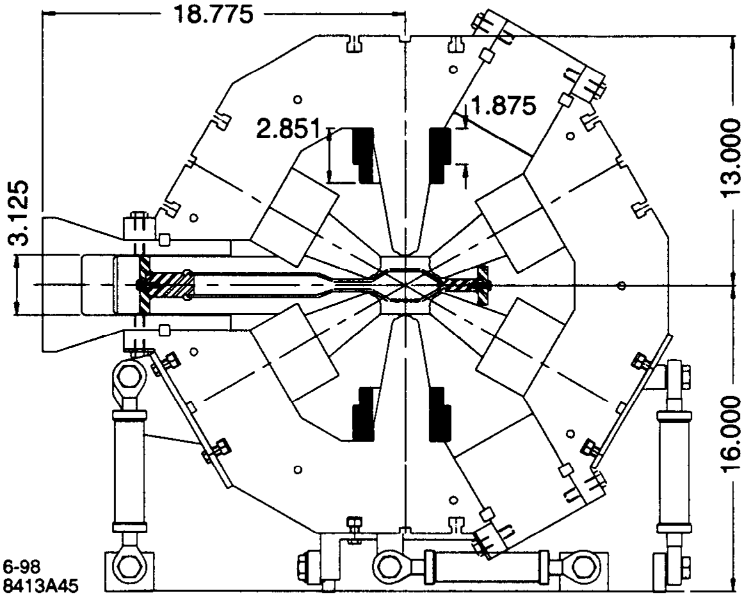

Figure 4.22 Cross section of the sextupole magnet.

Table 4.18 Standard and matching cell sextupoles parameters.[†]

	SD	SF	SDI/SFI
Design Energy (GeV)	3.3	3.3	3.3
Number of Magnets	28	28	8
Strength ($1/m^3$)	50	40	30
Magnetic Length (m)	0.250	0.210	0.210
Sextupole Coeff. $b_3=0.5\ \partial^2 B_y/\partial x^2$ (T/m^2)	275	220	165
Pole Tip Field (T)	0.557	0.446	0.334
Integrated Field (T/m)	68.75	46.20	34.65
Inscribed Radius (m)	0.045	0.045	0.045
Core Length (m)	0.250	0.210	0.210
Yoke Height (m)	0.666	0.666	0.666
Yoke Width (m)	0.730	0.730	0.730
Core Weight (kg)	515	433	433
Ampere-Turns per Pole	6783	5426	40708
Turns per Pole	33	33	33
Pancakes per Pole	1	1	1
Conductor Size (mm)	6.35	6.35	6.35
Cooling Hole Diam (mm)	3.15	3.15	3.15
Conductor Cross-SectionalArea (mm^2)	31.67	31.67	31.67
Conductor Length/Pole (m)	25.90	23.26	23.26
Current (98% eff.) (A)	205.54	164.43	123.32
Current Density (A/mm^2)	6.5	5.2	3.9
Inductance (mH)	20	16.8	16.8
Magnet Resistance (mΩ)	91	82	82
Power/Magnet (kW)	3.85	2.21	1.24
Power/String (kW)	108	62	10
Voltage Drop/Magnet (V)	18.7	13.5	10.1
Voltage Drop/String (V)	525	377	81
Water Circuits	6	6	6
Water Flow Rate/Magnet (gpm)	2.0	2.1	2.1
Water Flow Rate/String (gpm)	56.3	59.9	17.1
Water Pressure Drop (psi)	150	150	150
Water Temperature Rise (°C)	7.3	3.9	2.2
Reynold's Number	8714	9258	9258
Water Velocity (m/s)	2.7	2.9	2.9
Friction Factor	0.034	0.034	0.034

[†] For skew quad coils see Section 4.42

Table 4.19 extupole pole tip coordinates

X (mm)	Y (mm)	X (mm)	Y (mm)
38.965	22.497	44.475	13.696
39.254	21.997	45.018	13.600
39.542	21.497	45.249	13.600
39.831	20.998	45.666	13.600
40.119	20.498	46.083	13.600
40.407	19.998	46.500	13.600
40.696	19.499	46.917	13.600
40.984	18.999	47.335	13.600
41.273	18.499	47.752	13.600
41.561	18.000	47.990	13.600
41.850	17.500	48.769	13.624
42.138	17.000	49.545	13.696
42.427	16.501	50.315	13.815
42.715	16.001	51.077	13.981
43.004	15.501	51.826	14.193
43.292	15.002	133.430	40.051
43.643	14.394	195.393	75.825
43.997	13.972		

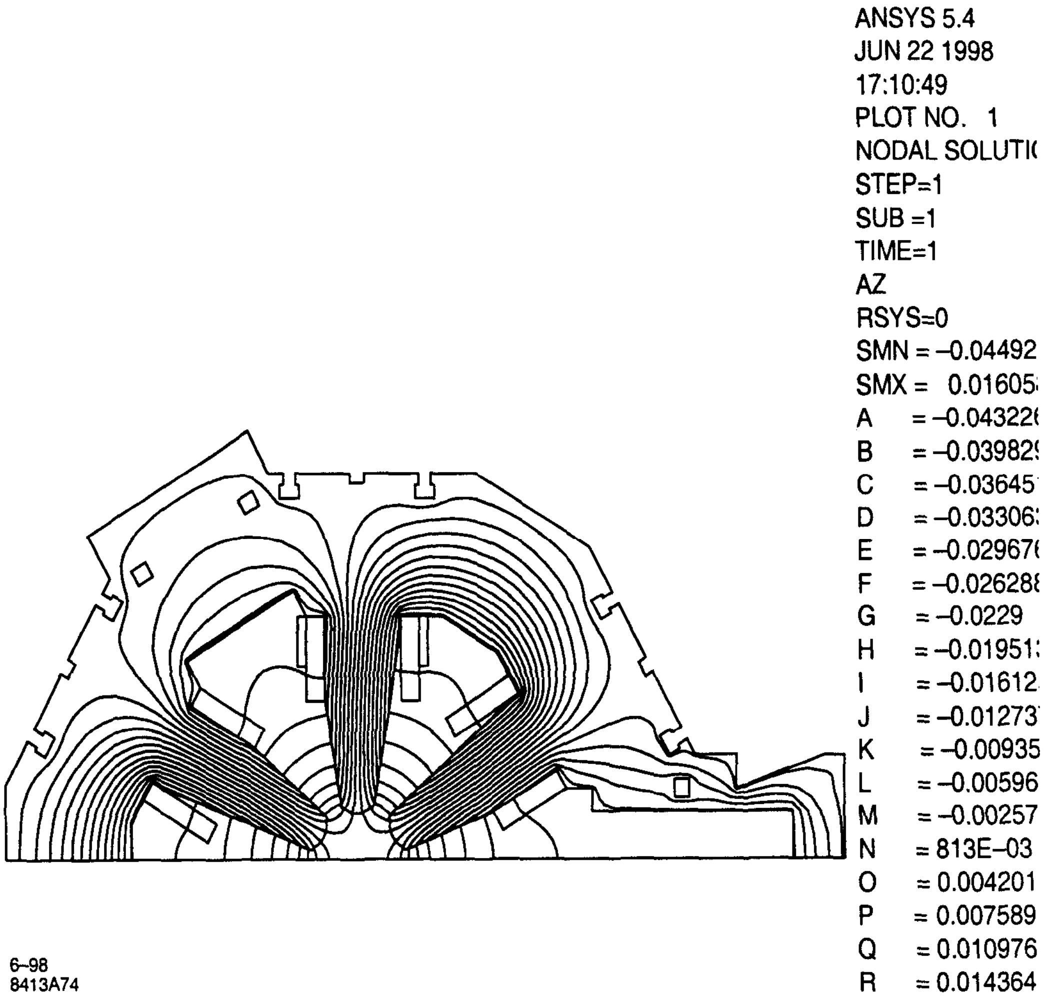

Figure 4.23 Sextupole flux plot (the vector potential values are in T-m). The pole root is asymmetrical to allow more space for the vacuum chamber and increase the excitation efficiency at higher fields.

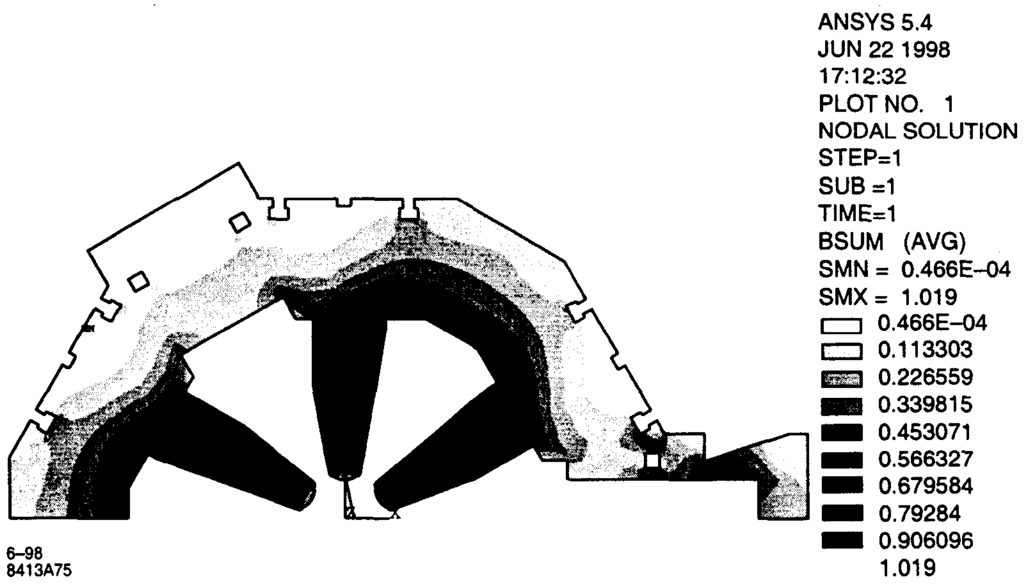

Figure 4.24 Sextupole magnetic induction plot (the values are in Tesla). The magnetic field at pole root is higher than at pole tip because of the large amount of flux entering from the sides (Figure 4.23).

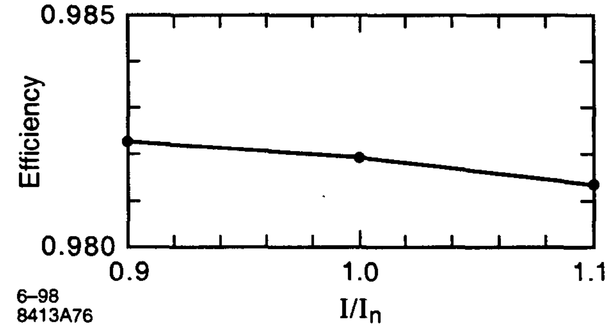

Figure 4.25 Efficiency vs. current in the sextupole

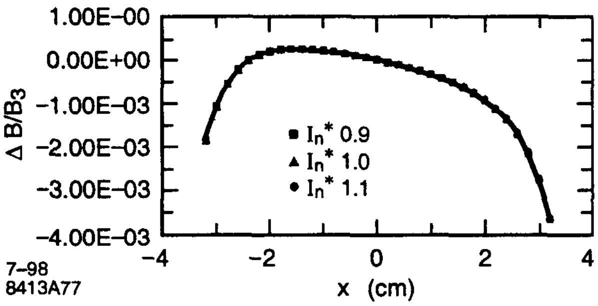

Figure 4.26 $\Delta B/B_3$ vs. transversal position at different currents in the sextupole (without skew quadrupole field).

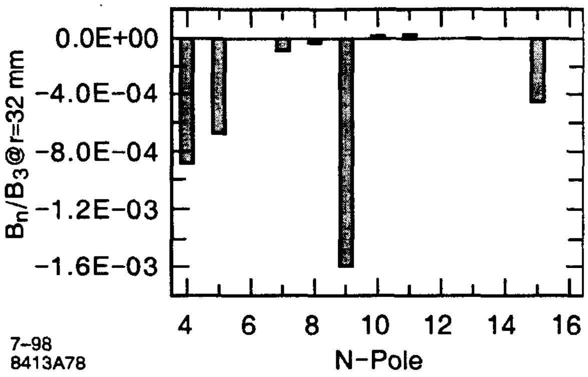

Figure 4.27 Systematic B_n/B_3 in the sextupole at r=32 mm (without skew quadrupole field)

Table 4.20 Sextupole multipoles (T/cm$^{(n-1)}$) vs. current without skew quadrupole.

	$I_n \times 0.3$	$I_n \times 0.9$	$I_n \times 1.0$ (3 GeV)	$I_n \times 1.1$
b_1	-2.22E-04	-5.12E-04	-5.79E-04	-6.52E-04
b_2	-4.62E-05	-1.06E-04	-1.18E-04	-1.31E-04
b_3	7.68E-03	2.30E-02	2.55E-02	2.79E-02
b_4	-1.99E-06	-4.55E-06	-5.11E-06	-5.66E-06
b_5	-4.13E-07	-9.53E-07	-1.08E-06	-1.21E-06
b_6	-7.17E-11	-2.29E-11	-2.32E-11	-2.47E-11
b_7	-3.96E-09	-9.12E-09	-1.03E-08	-1.16E-08
b_8	-4.11E-10	-9.39E-10	-1.05E-09	-1.17E-09
b_9	-1.82E-10	-6.23E-10	-7.23E-10	-8.36E-10
b_{10}	1.78E-11	4.08E-11	4.59E-11	5.09E-11
b_{11}	7.38E-12	1.70E-11	1.93E-11	2.17E-11
b_{12}	1.18E-15	-3.83E-15	-4.31E-15	-4.76E-15
b_{13}	5.73E-13	1.32E-12	1.49E-12	1.68E-12
b_{14}	1.25E-13	2.86E-13	3.21E-13	3.56E-13
b_{15}	-2.13E-11	-6.38E-11	-7.07E-11	-7.74E-11
b_{16}	5.48E-15	1.25E-14	1.40E-14	1.55E-14
b_{17}	1.09E-15	2.52E-15	2.85E-15	3.20E-15
b_{18}	-7.65E-20	-1.93E-19	-2.10E-19	-2.25E-19

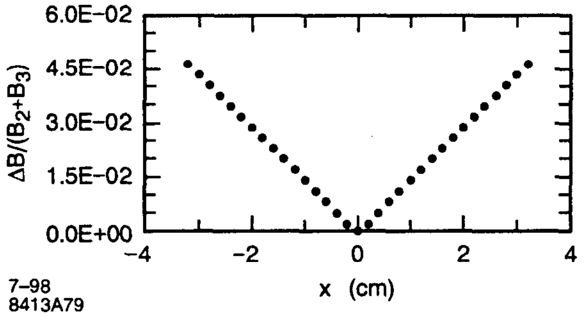

Figure 4.28 ΔB/B vs. transversal position in the sextupole with skew quadrupole field ((Equation 3)) Systematic B_n/B_2 in the skew quadrupole at r =32 mm. The large skew octupole component caused by the skew quadrupole coils (Figure 4.24) has been validated by tracking studies.

4.1.6 Corrector Magnets

The 72 SPEAR 3 combined correctors are C-shape ramped magnets for horizontal and vertical steering. On each girder there are 4 correctors located close to the absorbers. Their size is limited by the vacuum chamber, the adjacent magnets and the absorber. The beam steering needed in the horizontal and vertical direction is respectively 1.5 mrad and 1 mrad. Steering coils have not been added to the quadrupole or sextupole magnets because of the poor dipole field quality that would be generated in such geometry. The configuration chosen is shown in Figure 4.107.The two vertical steering coils are wound on the pole faces and since the horizontal dipole field is conductor dominated, the undesired multipole components caused by the C-shape yoke can be corrected by inserting spacers between turns at specific locations. The vertical dipole field can be corrected by shaping the pole. The two horizontal steering coils are located next to the vertical steering coils on the return leg of the magnet. The two types of coils can be installed together or separately on the same yoke. Although the vertical/horizontal steering magnets exhibit some field non-linearity at large beam displacement, we do not anticipate problems in the ±1-2 mm region where the fast orbit feedback system operates. The yoke is made of 0.5 mm thick laminations and the magnet inductance (47 mH for the horizontal correction and 35 mH for the vertical correction) allows fast feedback (Section 4.9.1). Each magnet is individually powered.

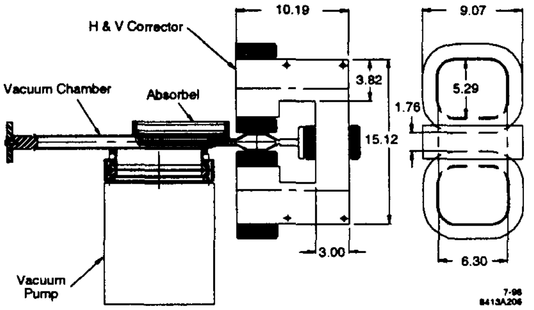

Figure 4.29 Cross section of the horizontal/vertical corrector magnet

4.1.6.1 Combined Horizontal/Vertical Correctors

The main parameters of the horizontal/vertical corrector are listed in Table 4.22. The magnetic field analysis has been performed using the 3D code Amperes© because of the magnet's low length/gap ratio and the importance of the end effects. After computing the 3D magnetic field, the vertical/horizontal field component was integrated over the magnet length, and the current adjusted to meet the required steering angle.

The vertical steering field has been computed along the x direction (transversal to the beam) and its harmonic content has been integrated in the z direction (parallel to the beam). Figure 4.32 shows the flux lines in the vertical corrector magnet at the nominal current. Figure 4.32 shows a surface plot of the magnetic field B_x at the orbit plane. The value of the integrated field along the magnet length vs. the transversal position x is shown in Figure 4.33. The multipole components of the line integral are listed on Table ???. and shown in Figure 4.34. The quadrupole and sextupole components can be minimized spacing adequately the turns.

Similarly the horizontal steering field has been computed along the x direction (transversal to the beam) and its harmonic content has been integrated in the z direction (parallel to the beam). Figure 4.35 shows the flux lines in the horizontal corrector magnet at the nominal current. Figure 4.36 shows a surface plot of the magnetic field B_y at the orbit plane. The value of the integrated field along the magnet length vs. the transversal position x is shown in Figure 4.37. The multipole components of the line integral are listed on Table 4.11 and shown in Figure 4.39. The quadrupole and sextupole components can be minimized by shaping the pole.

Table 4.21 Corrector magnet parameters.

	Vertical steering coil	Horizontal steering coil	Cooling coil
Design Energy (GeV)	3.300	3.300	
Number of magnets	72	72	
Steering Angle (rad)	0.0010	0.0015	
Integrated Field (T*m)	0.0110	0.0165	
Magnetic length (m)	0.2687	0.2687	
Magnetic field (T)	0.0409	0.0614	
Conductor Width (mm)	4.93	4.93	4.76
Conductor Height (mm)	1.80	1.80	4.76
Cooling Hole Diam (mm)			3.18
Conductor Cross-Sectional Area (mm2)	8.88	8.88	14.72
Coil/magnet	2	2	4
Turns per coil	240	120	10
Average coil width (mm)	158	158	158
Coil straight length (mm)	160	160	160
Coil length (m)	165.8	82.9	6.9
Coil resistance (mOhm)	347	174	
Coil inductance (mH)	8.6	1.8	
Coil weight (kg)	13.0	6.5	0.9
Amp Turns per coil (A)	5004	2656	
Current (A)	20.85	22.13	
Current density (A/mm2)	2.3	2.5	
Magnet Resistance @ 40 C (mOhm)	694	347	
Inductance (mH)	34.6	46.7	
Power/Magnet (kW)	0.302	0.170	0.472
Voltage drop/Magnet (V)	14.47	7.68	
Total Coils Weight (kg)	25.9	13.0	3.6
Core Length (m)	0.160	0.160	0.160
Gap Height (m)	0.109	0.109	0.109
Pole width (m)	0.108	0.108	0.108
Lamination Height (m)	0.384	0.384	0.384
Lamination Width (m)	0.246	0.246	0.246
Core Weight (kg)	86.7	86.7	86.747
Water Pressure Drop (psi)			150
Water Circuits			1
Water Flow Rate/Magnet (gpm)			0.3
Water Temperature Rise (C)			5.4
Water speed (m/s)			2.6
Reynold's number			8559

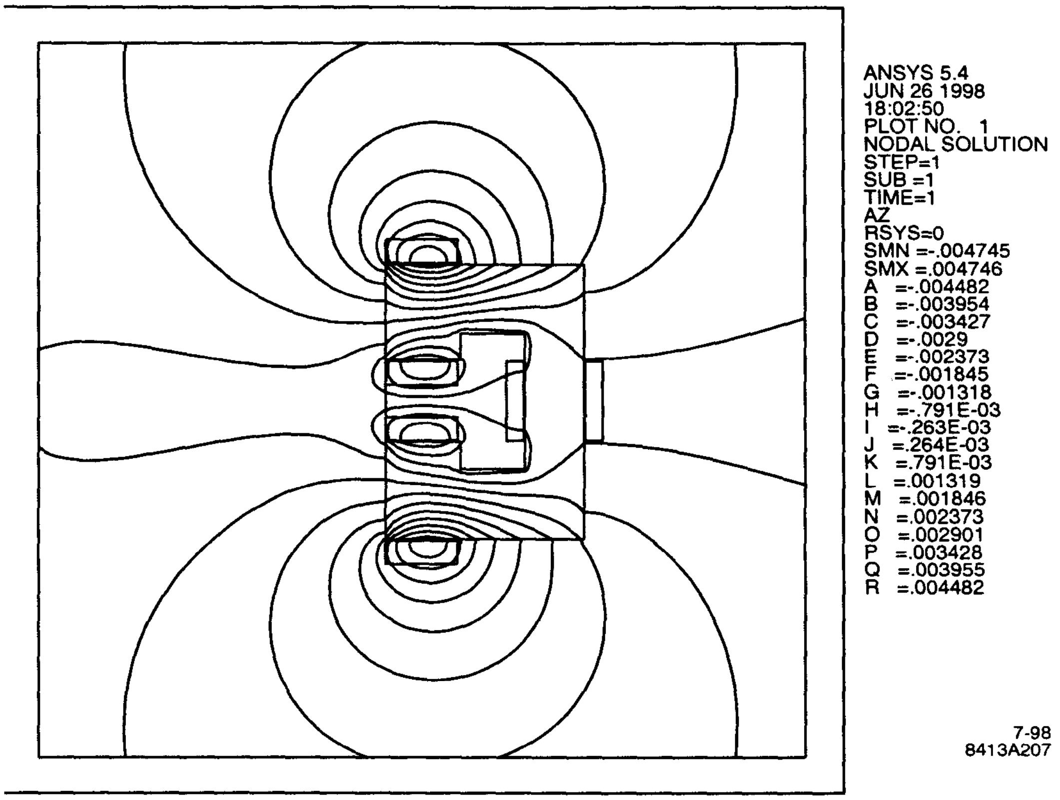

Figure 4.30 Vertical corrector flux plot
(the vector potential values are in Tm)

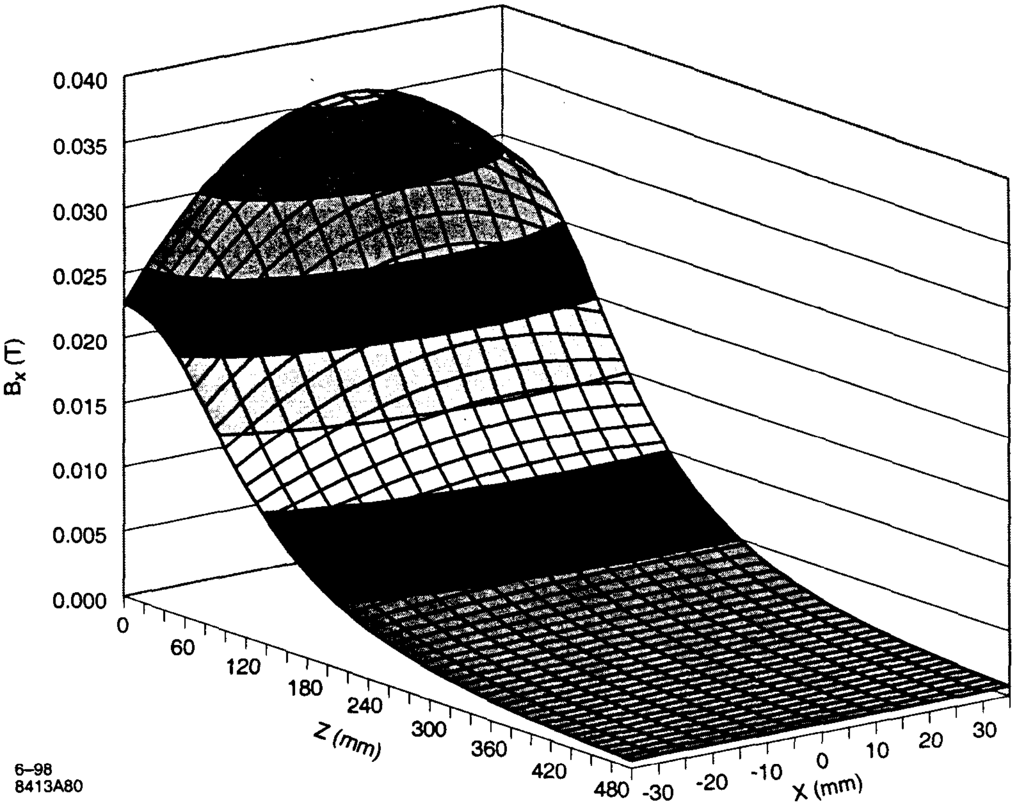

Figure 4.31 Vertical steering field vs. x and z in the H/V corrector at I_n =5004 AT. The end effects are very important because of the magnet's low length/gap ratio.

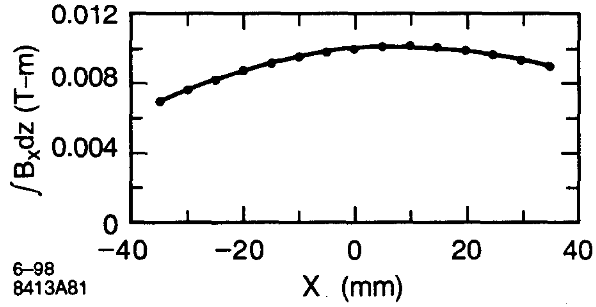

Figure 4.32 Integral of vertical steering field vs. x in the H/V corrector at In =5004 AT. The quadrupole and sextupole components can be minimized by inserting spacers between turns (the field is coil dominated). Although the vertical steering magnet exhibits some field nonlinearity at large beam displacement, we do not anticipate problems in the ±1–2 mm region where the fast orbit feedback system operates.

Table 4.22 Integrated multipoles of vertical steering field in the H/V corrector at I_n = 5004 A-T (also Figure 4.35).

n	$\int b_n dz$ (T-m/cm$^{(n-1)}$)	$\int B_n dz$ (T-m) @ r = 35 mm	$\int B_n dz / \int B_1 dz$ @ 35 mm
1	1.0005E-02	0.01000488	1
2	2.9337E-04	0.00102678	1.03E-01
3	-1.6842E-04	-0.0020632	-2.06E-01
4	-8.0793E-07	-3.464E-05	-3.46E-03
5	4.3184E-07	6.4803E-05	6.48E-03
6	5.9345E-08	3.1169E-05	3.12E-03

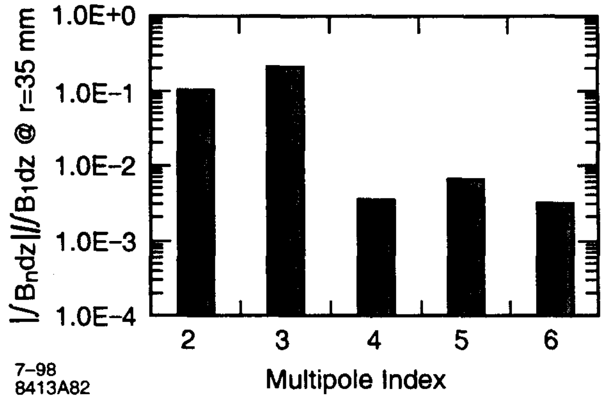

Figure 4.33 Integrated multipoles of vertical steering field in the H/V corrector

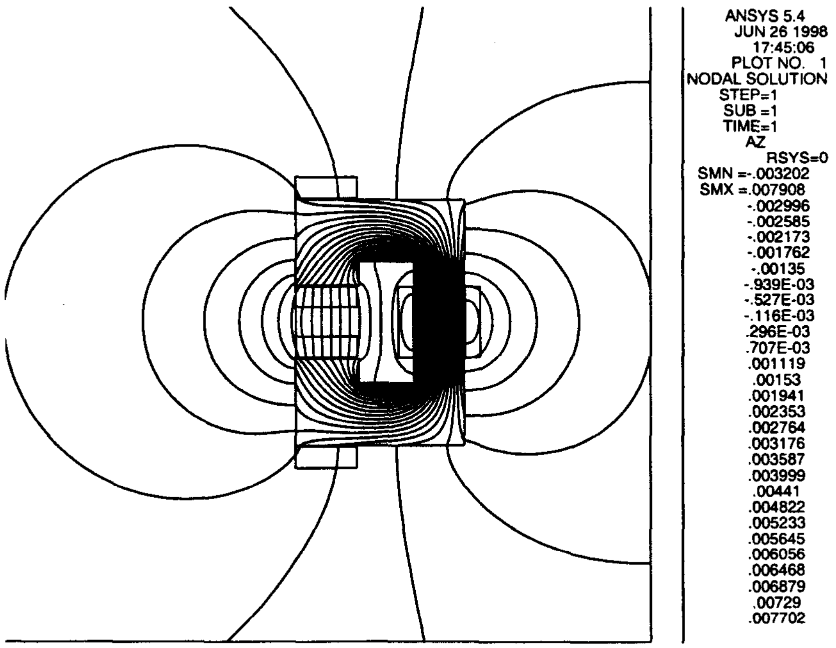

Figure 4.34 Horizontal corrector flux plot (the vector potential values are in Tm)